JOCHEN JENS HEINRICH

SEARCH FOR CHARGED STABLE MASSIVE PARTICLES WITH THE ATLAS DETECTOR

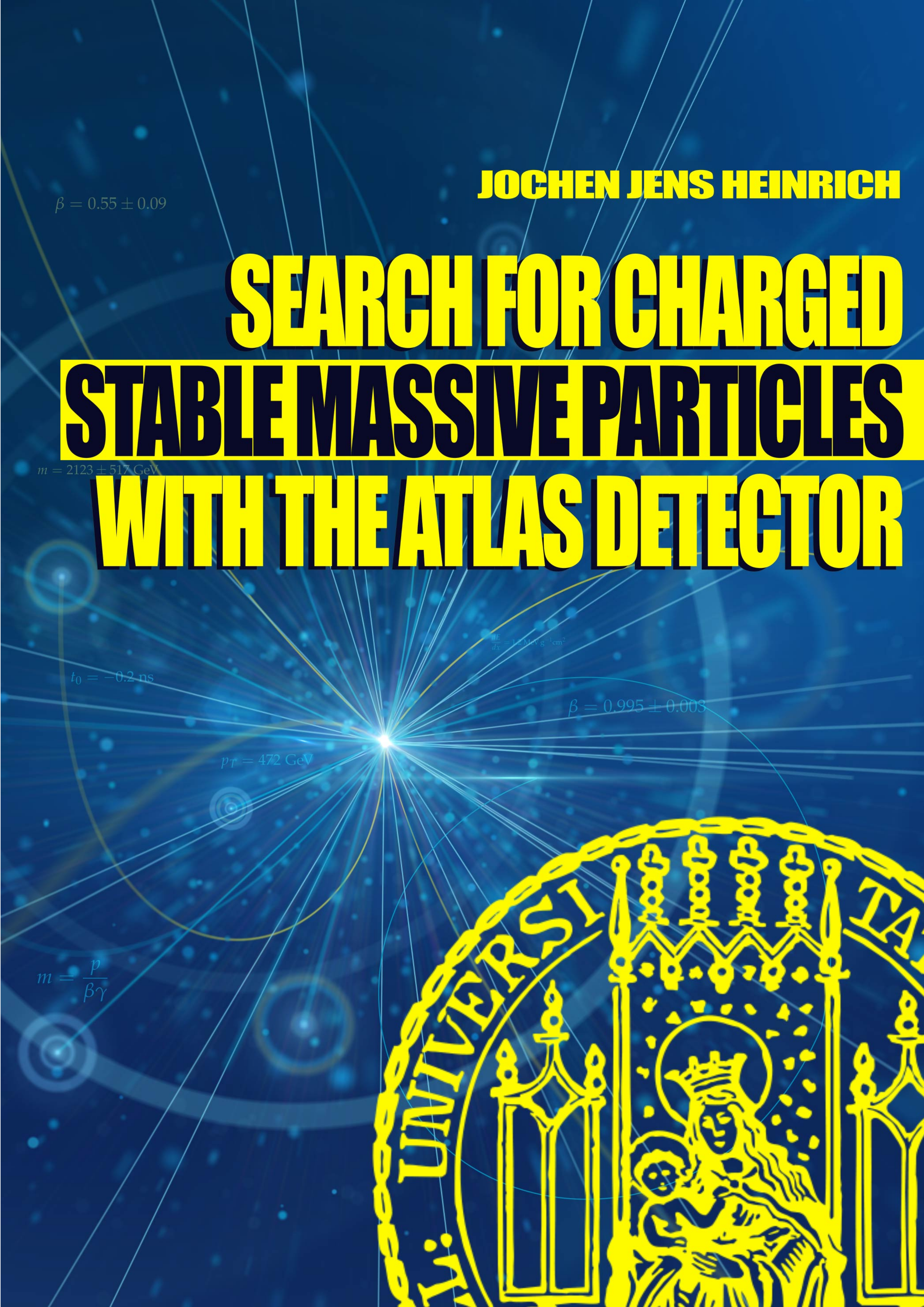
$\beta = 0.55 \pm 0.09$
$m = 2123 \pm 517$ GeV
$t_0 = -0.2$ ns
$\beta = 0.995 \pm 0.003$
$p_T = 472$ GeV
$m = \frac{p}{\beta\gamma}$

JOCHEN JENS HEINRICH

SEARCH FOR CHARGED STABLE MASSIVE PARTICLES WITH THE ATLAS DETECTOR

DOKTORARBEIT
AN DER FAKULTÄT FÜR PHYSIK
DER LUDWIG-MAXIMILIANS-UNIVERSITÄT
MÜNCHEN

VORGELEGT VON
JOCHEN JENS HEINRICH
AUS AALEN

MÜNCHEN, DEN 14. MÄRZ 2018

Erstgutachter: Prof. Dr. Dorothee Schaile
Zweitgutachter: Prof. Dr. Wolfgang Dünnweber
Tag der mündlichen Prüfung: 26.04.2018

Copyright © Jochen Jens Heinrich 2018

Search for Charged Stable Massive Particles with the ATLAS Detector

Thesis submitted for a doctoral degree in physics
at the faculty of physics of the
Ludwig-Maximilians University
Munich, Germany

Submitted by Jochen Jens Heinrich, born in Aalen, Germany
on March 14th, 2018 and defended April 26th, 2018

First printing, May 2018

Zusammenfassung

Eine Suche nach schweren, elektrisch geladenen, stabilen Teilchen mit dem ATLAS Detektor wird vorgestellt. Hierzu werden Proton–Proton Kollisionsdaten, welche einer integrierten Luminosität von 36.1 fb^{-1} entsprechen und bei einer Schwerpunktsenergie von $\sqrt{s} = 13$ TeV aufgenommen wurden, ausgewertet. Langlebige massive Teilchen werden nicht in den Kalorimetern absorbiert, demnach ist ihre Signatur äquivalent zu Myonen, die aufgrund ihrer großen Masse mit Geschwindigkeiten deutlich unterhalb der Lichtgeschwindigkeit propagieren und hoch ionisierend sind. Die Ionisationsenergieverluste werden in Pixelclustern der innersten Spurenkammern gemessen, die Ausbreitungsgeschwindigkeiten β durch Flugzeitmessungen bestimmt. Eine Zeit-Kalibrierung des Myonen-Systems wird vorgestellt, welche eine signifikante Verbesserung gegenüber früheren Kalibrierungen darstellt und die bisher beste β-Auflösung in ATLAS erreicht. Dies beinhaltet die Korrektur von zeit-abhängigen Fluktuationen und die Bestimmung von Kalibrierungskonstanten mittels Gaußschen Parameterisierungen für etwa $700\,000$ einzelne Detektorelemente. Der erwartete Untergrund wird direkt aus Daten abgeschätzt. Keine der betrachteten Signalregionen weißt einen statistisch signifikanten Ereignis-Überschuss auf. Die Ergebnisse werden in verschiedenen supersymmetrischen Modellen, welche die Existenz von langlebigen Teilchen vorhersagen, interpretiert. Langlebige Gluinos aus Split-SUSY-Modellen und langlebig Bottom und Top Squarks, welche zu R-Hadronen hadronisieren, wurden bei 95% CL bis zu Massen $m(\tilde{g}) = 2015$ GeV, $m(\tilde{b}) = 1240$ GeV und $m(\tilde{t}) = 1325$ GeV ausgeschlossen. Direkt produzierte langlebige Staus aus GMSB-Modellen sind für Massen bis $m(\tilde{\tau}) = 420$ GeV ausgeschlossen. Detektorstabile Charginos, welche in mAMSB-Modellen entstehen, können bis zu Massen von $m(\tilde{\chi}_1^{\pm}) = 1100$ GeV ausgeschlossen werden. Alle Ausschlussgrenzen stellen die gegenwärtig striktesten Einschränkungen für stabile supersymmetrische Teilchen dar und bedeuten eine signifikante Verbesserung gegenüber früheren ATLAS- und CMS-Ergebnissen. Um kürzeren Lebensdauern, Modellunabhängigkeit und möglichen ladungsverändernden Interaktionen Rechnung zu tragen, wird die R-Hadronen Suche wiederholt und alle Signale vom Myonen System ignoriert. Kein Ereignis-Überschuss wird beobachtet und 95% CL Ausschlussgrenzen werden gesetzt. Dieser ergeben sich zu $m(\tilde{g}) = 1950$ GeV, $m(\tilde{b}) = 1170$ GeV und $m(\tilde{t}) = 1220$ GeV für Gluinos, Bottom- und Top-Squarks. Schließlich wird ein neuartiger Trigger der auf langsame Teilchen spezialisiert ist vorgestellt. Hierbei werden zwei direkt aufeinanderfolgende Kollisionsereignisse berücksichtigt und der momentan existierende Effizienverlust durch verspätet im Myonensystem ankommende Teilchen minimiert.

Abstract

A search for charged stable massive particles in $36.1\ \text{fb}^{-1}$ of proton–proton collisions at $\sqrt{s} = 13$ TeV with the ATLAS detector is presented. Since stable massive particles are not absorbed in the calorimeters their signature is equivalent to muons that propagate much slower than the speed of light due to their large mass and are highly ionising. The ionisation energy losses are measured in pixel clusters of the innermost tracking chambers, the propagation velocity β is determined by performing time-of-flight measurements. An in-depth timing calibration of the muon system is presented which significantly improves previous results and achieves the best ATLAS β resolution to-date. This involves the correction of temporal effects and determination of calibration constants for about $700\,000$ detector elements individually. The expected background is estimated in a purely data-driven manner. No statistically significant excess of events was observed in any signal region. The results are interpreted in various supersymmetric models predicting the existence of long-lived particles. Long-lived gluinos, originating from Split SUSY models, and long-lived bottom and top squarks that hadronise into R-hadrons were excluded at 95% CL up to masses of $m(\tilde{g}) = 2015$ GeV, $m(\tilde{b}) = 1240$ GeV and $m(\tilde{g}) = 1325$ GeV. Directly pair-produced long-lived staus from GMSB models are excluded to masses up to $m(\tilde{\tau}) = 420$ GeV. Detector-stable charginos originating from mAMSB models can be ruled out up to masses of $m(\tilde{\chi}_1^{\pm}) = 1100$ GeV. All limits are the most stringent constraints on stable SUSY particles and are a significant improvement over previously reported ATLAS and CMS results. To account for shorter lifetimes, model independence and possible charge-flip reactions the R-hadron analysis is also done disregarding all signals stemming from the muon system including triggering. No excess of events is observed and 95% CL exclusion limits are set resulting in the limits $m(\tilde{g}) = 1950$ GeV, $m(\tilde{b}) = 1170$ GeV and $m(\tilde{g}) = 1220$ GeV for gluinos, bottom and top squarks, respectively. Lastly, a novel trigger is introduced that is dedicated to slow-particle searches by considering two consecutive collision events thereby recovering muon-trigger efficiency for particles arriving out-of-time in the muon system.

Preface

In its infancy, only a fraction of a second after the Big Bang, the Universe looked very different from what we today see as the Universe: it was small, hot and opaque. The energy density was large enough to prevent the formation of molecules, atoms and even protons. There was nothing there except a cosmic primordial soup of elementary particles that interacted with each other and which we call quark-gluon plasma. Yet, the seed for everything that ever was, is, or will ever be must already have been present then. In fact, the fundamental characteristics of the Universe were determined in this early stage by the properties of the elementary particles involved. If we want to understand how the Universe adopted the form we know today, we need to understand its origin and discover the rules that governed its evolution in its earliest stage. It might be one of the most poetic paradoxes that we have to study the smallest and most fundamental constituents of nature to answer the biggest imaginable questions about the existence of our Universe: how did it begin? What is it made of? What rules govern it? And what will its final destiny be?

For many decades, particle physicists have piled up their knowledge and developed increasingly exhaustive models of nature that were then scrupulously put to the experimental test. Our current understanding of the particle world is given by the Standard Model of particle physics. Though incomplete, it provides an accurate description within our at present accessible energy regime. It is based on quantum field theories and contains a total of twelve matter particles with an additional five particles to mediate three of the four known forces of nature. Would it not be a remarkable thought to think of every object surrounding us being composed of a set of just twelve different fundamental particles? Yet the truth is even more stunning. All but three matter particles are unstable and decay within fractions of a second to one of the stable particles. The majority of known particles are therefore short lived. It is intuitive to assume potential new massive particles to have equally short lifetimes. However, there are compelling reasons to assume that the first hints of new previously undiscovered particles might come from a different sector altogether and that those particles may in fact be long-lived.

After a two-year maintenance break, the Large Hadron Collider at CERN in Geneva began its operation again in early 2015 at an unprecedented centre-of-mass energy of 13 TeV. I consider it a stroke of luck that I was able to start my PhD project in October 2014, right in-time for the preparations for the new energy regime which had never been probed before. The prospect of searching for new long-lived charged particles was - and remains - an exciting challenge to me as the analysis has many non-commonplace demands, possesses unique requirements and uses the detector in a way it was never optimised for. It was essential to the project to develop a good understanding of both the hypothesised physics as well as the working principle of the detector from signal generation and readout to reconstruction algorithms.

This thesis summarises the work I did in the past three years and which found its way into two papers [1, 2]. The first was published in 2016. It analyses the first 13 TeV collisions recorded in 2015 and reports a simple and fast search for stable massive particles while using only parts of the detector. The second relies on data from both 2015 and 2016 and gives a complete update on searches for different models using the entire detector for its maximal sensitivity. It is to be published in 2018. Since the search reported in the first paper is contained and expanded within the second, the text of this thesis considers only the second paper. I presented the results of the first paper at an international conference [3] and introduced the analysis strategy of both the first and the second paper at several national workshops and conferences.

Within a collaboration like ATLAS where more than 3000 physicists work together, no analysis effort can be done by one individual alone. A few words on my own contribution to the work presented here might be in order. I have split my work into three chapters which are found as chapters 4-6 in this thesis and contain the timing calibration of the Muon Spectrometer, a description of the analysis effort and a short account on the work done for the late-muon trigger. Being the dedicated analysis expert for the Muon Spectrometer, the results and investigations reported in the timing calibration chapter are exclusively my contributions. A small exception from this is marked in the text and I am thankful to Massimiliano Bellomo for sparing me a lot of work there. For this reason I have put great emphasis on this self-contained chapter. The following chapter contains an account of the analysis effort. The principle analysis team is small, the main work load being shared between three people. It is thus unavoidable that I had contributions to nearly all stages of the analysis and took part in discussions about the remaining topics. The definition of the data format, event reweighting based on the amount of occurring initial-state radiation and due to wrongly simulated muon-trigger efficiencies, as well as the estimation of many different systematic uncertainties were some of my main contributions. In the text I have tried to reflect the amount of my own contributions during a particular analysis step in the level of detail of its description. Lastly, the late-muon trigger was a project which I started on in 2014 and liked to keep returning to all throughout the last three years. Some of the most time-consuming work has not found its way into this thesis, even though I do remember quite vividly many weeks of digging through the code of trigger software in order to get the trigger simulation running. I will however not claim that my contributions were more than a footnote in this process. The implementation of the trigger on Level 1 was done by Susan Cheatham, the HLT implementation was started by Enrique Kajomovitz and finalised by Massimiliano Bellomo. Among other things, I have at various points during development supplied samples with artificially shifted timing information for testing purposes. In the text of this thesis I have highlighted my own contribution in the commissioning process of the trigger which led to its activation for physics-data taking. A long list of dedicated trigger experts have contributed in these discussions. I also want to mention Marc Berndl, who estimated the late-muon trigger rate under my supervision.

Obviously, many projects I have worked on in the past three years, whether small or big, I could not include in this thesis. Some for quite obvious reasons, others because the work was superseded by new considerations and it became superfluous (as an example I will name an optimisation of the analysis pre-selection, the result of which was later put into disuse by the intention of harmonising the selection with another similar analysis effort). I have also refrained from going into detail about several small projects I designed for students to work on. The experience of supervising a project was, however, very instructive to me, as were the teaching duties I had during the project. Further, having spent about eight months of my time at CERN, I took on additional responsibility by becoming a software release coordinator for the trigger group. Compatibility of new packages, release building and distribution were amongst my tasks.

The most gratifying and rewarding side-project I took on during the last three years, however, was unquestionably my work in outreach as an ambassador for particle physics at many schools, as a guide at CERN and at various public events. The opportunity to excite the minds of promising students to challenges and fascinations in the field of particle physics and to try explaining complex scientific concepts in an approachable manner has been an utmost pleasure to me. Though of course not an official part of my PhD project, I nevertheless considered it my duty to engage in discussions and advocate an undirected fundamental research that is driven by our curiosity and thirst for knowledge and understanding.

After much discussion with many of my colleagues I feel also compelled to give a few words of justification on the thesis style I have chosen. I hope nobody is led to believe the main motivation was to fill pages more quickly by using only two thirds of each page. On the contrary: especially the timing-calibration chapter with its different calibration steps requires the reader to have a clear and precise picture of the underlying timing distributions and results in mind, to be able to follow the arguments made. Instead of writing long descriptions, I decided to give as many plots as necessary and rather one too many than to leave out a crucial piece of information. The two-column approach allows me to include all plots, while still keeping the thesis structured and easy to read. The reader is further spared to search for the corresponding figure as it is usually found right next to the text where it is first referenced. The 167 figures and 39 tables included in the main body of this thesis will hopefully aid me in making my arguments. Whether I have succeeded in this, I will leave for the reader to judge. In the theory and detector chapter I have used margin notes to also give explanations for readers who do not have a background in particle physics.

I wrote this thesis with myself at the beginning of my project in mind. It contains all the information and references I wished to have had back then. My hope is this thesis will be of assistance to everybody carrying on the search for stable massive particles and prevent them running into a few of the blind alleys that I sometimes explored. Hopefully they will find answers to many of the questions I was unable to. But then again, if Robin Ince and Brian Cox are right and science can be defined as "the desire to stay confused", this project really was - without a doubt - in the best scientific spirit.

JOCHEN JENS HEINRICH
Munich, Decembre 2017

Acknowledgements

More than three years have passed in the blink on an eye. Looking back, I stand amazed at how many people had a hand in the work presented here. They all have my deepest gratitude.

Foremost, I want to thank my supervisor Sascha Mehlhase for his guidance throughout the past three years. Not only have your suggestions, honest feedback and help been invaluable to me, but you also gave me the chance to pursue my own ideas which I am sure required a good deal of patience every once in a while. I am much obliged for your encouragements to get myself engaged in outreach activities and allowing me to take the time to do so. And of course I am appreciative of your lesson in time management by red-carding me for running 15 seconds overtime at a conference talk.

I am further thankful to Dorothee Schaile for giving me the opportunity to work in her group with many talented colleagues. Not only did you support me for schools, conferences and an eigth-month stay at CERN, but you also gave me the feeling that you always had my best interest at heart. I am sure I am not your only student feeling this way.

To my colleagues in the SMP analysis, Michael Adersberger, Massimiliano Bellomo, Sascha Mehlhase, Troels Petersen and Shlomit Tarem, I am grateful for many discussions, ideas and advice which helped me a lot in countless analysis problems I encountered over the years.

I want to especially mention Shlomit Tarem again, who has been my first contact for any questions I had related to the Muon Spectrometer or the late-muon trigger. Thank you for always taking the time to answer my questions.

The path to understanding the timing information in the RPC system was painful. I would not have been able to without the help of Massimo Corradi, Stefania Spagnolo and others, whom I annoyed at regular intervals with my inquiries.

I enjoyed a very pleasant, productive and social working environment at the LS Schaile. This is due to all my colleagues with whom there was always room for discussions, whether they were related to particle physics or not. I would also like to give thanks to the members of the helpdesk for keeping the IT system running, despite my best efforts to ruin it, and Elke Grimm-Zeidler, without whom I would surely have lost track of my holidays and travels,

Without my office colleagues, foremost Michael Adersberger, Vincent Kitali, Ferdinand Krieter and Martin Habedank, I would have probably finished this thesis five months earlier, but it would have been only half the fun. Coming into the office never felt like work with you guys!

To Alexander Mann ("Wochenende klettern?"), Daniela Köck ("Ping Pong?") and Michael Adersberger ("Mach’ mer ne Runde?!") I am grateful for the occasional distractions that were especially necessary during the write-up.

I want to thank all my friends for continuing to ask me how the writing is going and staying interested in my work. You have kept me motivated all this time! My thanks are also to Laura Oestreich for the encouragement and the support in finding my motivation.

Last, but surely not least, I want to thank my family both near and far and especially my parents, who supported me no matter what.

Contents

Zusammenfassung iii

Abstract v

Preface vii

Acknowledgements x

Contents xi

1 Introduction 1

2 The Standard Model and beyond 3

2.1 The Standard Model of particle physics 3
- 2.1.1 Particle content 4
- 2.1.2 Electroweak theory 5
- 2.1.3 Quantum Chromodynamics 6

2.2 Particles with long lifetimes 7
- 2.2.1 Why particles are long lived 7
- 2.2.2 Long-lived particles in the Standard Model 7

2.3 Shortcomings of the Standard Model 7

2.4 Physics beyond the Standard Model 10

2.5 Supersymmetry 10
- 2.5.1 Soft supersymmetry breaking 12
- 2.5.2 R-parity 12
- 2.5.3 Minimal Supersymmetric Standard Model 13
- 2.5.4 Supersymmetry at the LHC 14
- 2.5.5 Split SUSY 15
- 2.5.6 Gauge-mediated supersymmetry breaking 15

2.5.7 Anomaly-mediated supersymmetry breaking 16
2.6 Theories involving extra dimensions 16
2.7 Stable Massive Particles 16
2.7.1 Interaction with matter 17
2.7.2 Cosmological constraints on SMPs 20
2.7.3 Constraints from searches on SMPs 20
2.8 Summary 23
3 The ATLAS Experiment at the Large Hadron Collider 25
3.1 The Large Hadron Collider (LHC) 25
3.1.1 Luminosity and pileup 26
3.1.2 Acceleration chain and filling scheme 27
3.2 The ATLAS detector 29
3.2.1 The Inner Detector 31
3.2.2 Calorimeters 33
3.2.3 Muon Spectrometer 35
3.2.4 Trigger System 38
3.3 Event data and simulation 39
3.4 Summary 40
4 Timing calibration of the ATLAS Muon Spectrometer 41
4.1 Uncalibrated data 41
4.1.1 Uncalibrated timing distributions 42
4.1.2 Uncalibrated β distributions 43
4.1.3 RPC-timing bug 44
4.2 RPC online-timing correction 45
4.3 MDT detector-element calibration 46
4.3.1 Chamber calibration 46
4.3.2 Run-wise chamber calibration 48
4.3.3 Drift-tube calibration 49
4.4 RPC detector-element calibration 51
4.5 Time-dependent phase-shift correction 54

4.6 Order of calibrations 56

4.7 Pull correction of σ_β 57

4.8 Combination of β estimates 58

4.9 MDT simulation timing smearing 61

4.9.1 Underestimation of data resolution 61
4.9.2 Drift-tube smearing 64
4.9.3 Chamber-based smearing 65

4.10 RPC simulation timing smearing 66

4.11 Application to signal MC 70

4.12 Summary 70

5 Search for Stable Massive Particles 73

5.1 Data and Monte Carlo samples 73

5.2 Object reconstruction 76

5.3 Measurement of Pixel dE/dx 76

5.3.1 Pixel dE/dx measurement 76
5.3.2 $\beta\gamma$ and mass determination 77

5.4 Measurement of β via time-of-flight 78

5.5 Online event selection 80

5.5.1 Missing-transverse-energy trigger 80
5.5.2 Single-muon trigger 81

5.6 Offline event selection 84

5.6.1 Pre-selection 85
5.6.2 Signal region definitions 88

5.7 Background estimate 90

5.8 Systematic Uncertainties 97

5.8.1 Theoretical cross sections 97
5.8.2 E_T^{miss} trigger efficiency 97
5.8.3 Single-muon trigger efficiency 99
5.8.4 Initial-state radiation 100
5.8.5 Measurement of Pixel dE/dx 102
5.8.6 β estimation in signal MC 102

5.8.7 MuGirlStau reconstruction efficiency 103
5.8.8 Pileup 103
5.8.9 Luminosity 104
5.8.10 Background estimate 104
5.8.11 Summary of systematic uncertainties 104
5.9 Results 105
5.10 Summary 109
6 Late-muon trigger for slow-particle searches 111
6.1 Concept of the late-muon trigger 111
6.2 Trigger thresholds 112
6.3 L1 rate estimation 113
6.4 Expected efficiency 114
6.5 Summary 115
7 Conclusion and Outlook 117
Appendices 121
Appendix A Definition of an SMP specific derivation 123
Appendix B Further Muon Spectrometer Calibration Plots 125
Appendix C Decomposition of the simulated RPC timing distributions 135
Appendix D Shifted means and large widths in RPC MC timing 139
Appendix E Supplementary material for SMP searches 143
Appendix F Layout of the Muon Spectrometer 149
List of Figures 153
List of Tables 159
List of Abbreviations 161
Bibliography 165

CHAPTER 1

Introduction

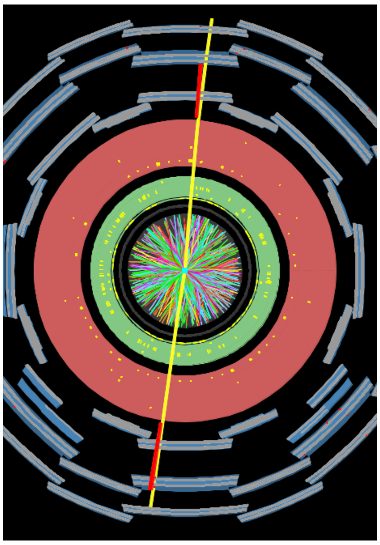

An ATLAS collision event display giving rise to two muons. Image adapted from [4].

Throughout the last decades research in particle physics has been conducted in the framework of one dominant theory called the Standard Model of particle physics. With only a handful of elementary particles known at the time the complex mathematical foundation of the model seemed like an utter theoretical overkill. Yet, after extensive efforts and the construction of more and more powerful particle accelerators the energy frontier has been pushed forward and all of the predicted particles have emerged, completing the model. But the job of a particle physicist is far from done. The Standard Model leaves many questions unanswered and cosmological measurements demand the existence of physics beyond current knowledge. But on what energy scale is this new physics to appear? There are many reasons (see chapter 2.3) to believe new particles may turn up on the TeV scale and are thus accessible to experiments at the Large Hadron Collider. The exact properties of such new physics are in the absence of concrete measurements left to guesswork. From the theoretical side a whole plethora of proposed models exist, but none could be verified so far. This generates an exciting prospect for an experimental particle physicist: every new study that is being conducted could uncover the longed for new physics.

Many of the proposed new models predict a set of new particles of which one or more are long-lived. In this work, the term long-lived particle is used as follows:

> **Definition: Long-lived particle (LLP)**
> A particle with a lifetime long enough to allow it to travel a measurable distance from the point of production before its decay.

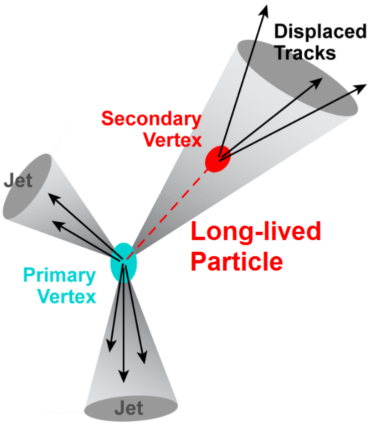

Figure 1.1: A long-lived particle was produced in the primary vertex and subsequently decays after travelling some distance giving rise to a displaced vertex signature. The figure was adapted from [5].

Typically this means a lifetime $\tau > 0.1$ ns which results in a flight distance of ≈ 3 cm (figure 1.1). This is enough to cause standard track reconstruction to fail. At longer lifetimes the LLP might reach the first detector layer and decay within the tracking chambers. It is thus required to perform dedicated analyses depending on the lifetime of the particle.

If the lifetime is long enough for the particle to traverse at least one subdetector altogether before decaying the LLP is called metastable[1]. Such hypothetical metastable massive particles (mSMPs) open up the prospect of a direct search, as opposed to the identification of decay products as done in most generic new particle searches. For even longer lifetimes the particle is able to leave the detector before decaying. Such particles are called detector-stable. In this thesis the term stable[2] massive particle is used as follows:

---

[1] This definition is only used within the context of this study to allow an easy differentiation between signatures.

Definition: Stable massive particle (SMP)
A particle with a mass considerably larger than known Standard Model particles, a lifetime long enough to reach at least the ATLAS hadronic calorimeter before decaying and an electric charge while traversing the tracking chambers.

In this definition the implicit assumption of an electric charge in the tracking chambers is made to accommodate the possibility of charge-flip interactions for composite particles (see chapter 2.7.1) and is necessary in order to perform a direct search, which offers many benefits: it can be constructed to be nearly model independent and through the absence of known particles with comparable characteristics and large masses, the search can be designed close to free of physical background. Indeed, in the search presented here the background is caused by instrumental effects. It is therefore required to develop a thorough understanding regarding hardware and data acquisition as the detector is used for a purpose which was not its primary design objective. It further demands dedicated calibration procedures that are not covered by detector performance task forces and instead left to the analysers themselves. Additional challenges arise on the triggering of candidate events, where particles may arrive "out of time" at the trigger chambers.

This thesis provides documentation for the considerations and investigations leading towards a search for SMPs in proton–proton collisions at a centre-of-mass energy $\sqrt{s} = 13$ TeV with the ATLAS detector.

The thesis is structured as follows: chapter 2 lays the theoretical groundwork to motivate the search for SMPs, describes how they might turn up in a detector and gives a brief overview of previously published search results. The experimental setup at CERN with focus on the Large Hadron Collider and the ATLAS experiment is introduced in chapter 3. The individual characteristics of the relevant subdetectors are discussed in some detail as required for the understanding of the timing calibration of the ATLAS muon system, which is detailed in chapter 4. The SMP search itself is described in chapter 5 and walks the reader through all stages of the analysis from event selection to the results. Future iterations of the analysis will suffer from increasingly difficult trigger conditions, which is why chapter 6 introduces a conceptually new trigger dedicated for slow-particle searches. Lastly, chapter 7 summarises the work presented here and gives a brief outlook into the future.

[2] Since the exact lifetime of the particle is of no concern as long as it is long-lived enough to leave the detector, the term 'stable' instead of 'detector-stable' is used throughout this thesis.

CHAPTER 2

The Standard Model and beyond

The Standard Model of particle physics is the established centrepiece of modern particle physics. It is therefore prudent to start by introducing the model and list its particle content in chapter 2.1. Different mechanisms which can render a particle long-lived are discussed in chapter 2.2 and a list of known long-lived particles is given. If the theory of the Standard Model was complete and flawless, particle physics would be at an end. This is not the case and different shortcomings of the model are discussed in chapter 2.3. As a result, physics beyond the Standard Model has to exist and chapter 2.4 will give an introduction into the framework of one hypothetical expansion called supersymmetry. A group of other new models which involve extra dimensions and can give rise to SMPs are briefly discussed in chapter 2.6. Chapter 2.7 contains a basic description of the properties of SMPs, their interactions in matter and introduce approaches how the behaviour can be correctly modelled. as well as summarise previous search efforts. Lastly, the chapter summarises previous search efforts for SMPs.

Particle physics in a bubble chamber. Image adapted from [6].

2.1 The Standard Model of particle physics

The aim of particle physics is to gain a better understanding of the fundamental building blocks of the Universe and their interactions. A series of ground-breaking theoretical works like the unification of the electromagnetic and weak interactions into one combined electroweak interaction by Glashow [8] in 1960 and the formulation of the Higgs mechanism [9–12] and its incorporation into electroweak theory by Weinberg [13] and Salam [14], let to the creation of the Standard Model of particle physics (SM) in the mid 1970s. It includes descriptions of three of the four known fundamental forces of nature[1] and describes the interactions of all known particles with each other. Not only does the SM provide a natural order to the fundamental particles, it also predicted the existence of additional particles upon its formulation. Since then all predicted particles have been successfully searched for, completing the SM with the discovery of the Higgs boson in 2012 [15, 16].

Force	Range [m]	rel strength
Gravity	∞	1
Weak	10^{-18}	10^{24}
Electromagn.	∞	10^{35}
Strong	10^{-15}	10^{37}

Table 2.1: The four fundamental forces of nature, their range and relative strength. The strength is taken as the relative magnitude of the force acting on proton pairs with a distance of 10^{-15} m. Adapted from [7].

[1] electromagnetic, strong and weak forces. Not included is gravity which in comparison is on this scale orders of magnitude weaker than the other forces (table 2.1) and can thus safely be ignored. See chapter 2.3 for more details.

2.1.1 Particle content

All known matter is composed of a very limited set of fundamental particles. These matter particles are categorised into two very different particle groups which consist of three generations of particle doublets each. The first group are the quarks. Here the up quark u and the down quark d constitute the first generation. Their electric charges are $(2/3e, -1/3e)$, where e is the elementary charge[2]. Charm quark c and strange quark s form the doublet of the second generation, the third is composed of top quark t and bottom quark b. They are both copies of the first generation but with much larger particle masses. Quarks are confined to colourless hadronic bound states and can only be observed in baryons (qqq) and mesons $(q\bar{q})$.

The electron e^- is the representative of the first generation of the lepton family. Together with the electrically neutral electron neutrino ν_e it forms the doublet (e, ν_e). Muon μ^- and tau τ^- with their corresponding neutrinos ν_μ and ν_τ are the second and third generation. Again the masses of the particle increase with the generation number[3] while other physical properties are identical to the first generation. Quarks and leptons are collectively called fermions and carry an half-integer spin. Measurements place strong exclusions on the existence of a fourth generation of fermions [19].

Besides the matter particles there exist the force-carrier particles. They are bosons carrying an integer spin. Electromagnetic interac-

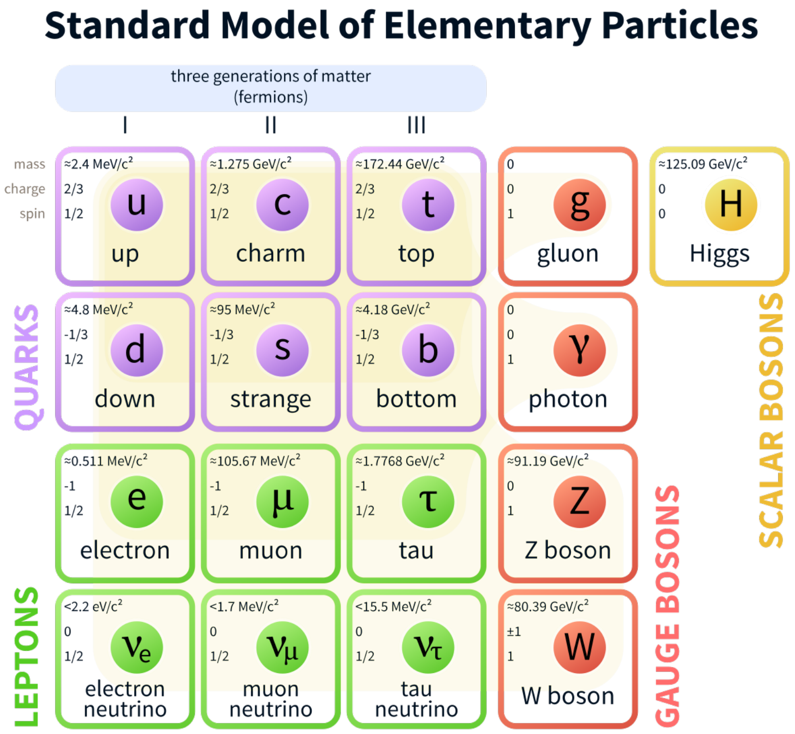
Standard Model of Elementary Particles
three generations of matter
(fermions)
I
II
III
mass
charge
spin
≈2.4 MeV/c²
2/3
1/2
u
up
≈1.275 GeV/c²
2/3
1/2
c
charm
≈172.44 GeV/c²
2/3
1/2
t
top
0
0
1
g
gluon
≈125.09 GeV/c²
0
0
H
Higgs
≈4.8 MeV/c²
-1/3
1/2
d
down
≈95 MeV/c²
-1/3
1/2
s
strange
≈4.18 GeV/c²
-1/3
1/2
b
bottom
0
0
1
γ
photon
≈0.511 MeV/c²
-1
1/2
e
electron
≈105.67 MeV/c²
-1
1/2
μ
muon
≈1.7768 GeV/c²
-1
1/2
τ
tau
≈91.19 GeV/c²
0
1
Z
Z boson
<2.2 eV/c²
0
1/2
νe
electron neutrino
<1.7 MeV/c²
0
1/2
νμ
muon neutrino
<15.5 MeV/c²
0
1/2
ντ
tau neutrino
≈80.39 GeV/c²
±1
1
W
W boson
QUARKS
LEPTONS
GAUGE BOSONS
SCALAR BOSONS

Figure 2.1: Overview of all particles contained in the Standard Model. The mass of each particle, its charge and spin is listed in the top left corner. Quarks and leptons form the fundamental matter particles, the gauge bosons mediate three of the four fundamental forces of nature, the Higgs boson arises from the Higgs mechanism. The figure was taken from [20].

[2] The electric charge of a proton, $e = 1.6021766208(98) \times 10^{19}$ C [17]

[3] The observation of neutrino oscillations show that neutrinos require a non-zero mass. However, so far no measurement of neutrino masses was successful and only upper bounds are known. See for example [18].

tions are mediated by the massless photon γ. The weak force is transmitted by the massive gauge bosons W^+, W^- and Z^0, which couple to every particle in the SM. The massless gluon g mediates the strong interaction and couples only to colour-charged quarks and itself[4].

The last particle in the SM is the Higgs boson. It is an electrically neutral, colour neutral, scalar (spin-0) particle which couples to all massive particles.

All electrically charged SM particles also possess antiparticles with opposite electric charge. They are denoted by either a bar above the particle (anti-up quark $\bar{u}$) or by reversing the superscript indicating the electric charge (positron e^+). Electrically neutral particles are said to be their own antiparticles.

An overview of the particle content of the SM is given in figure 2.1.

2.1.2 Electroweak theory

Electroweak theory (EWT) is the unification of Quantum Electrodynamics (QED), which is the underlying theory of photon-mediated electromagnetic interactions, and weak interaction theory. Although the two interactions seem fundamentally different at low energies, they can be treated on an equal footing at the unification scale at energies $\mathcal{O}(100 \text{ GeV})$. EWT forms a gauge theory based on the $SU(2)_L \otimes U(1)_Y$ symmetry group[5].

All electrically charged particles participate in electromagnetic interactions and thus couple to the photon. An example for a fundamental interaction vertex in QED is depicted in figure 2.2.

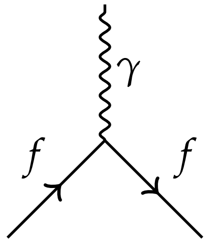

Figure 2.2: A fundamental electromagnetic interaction vertex where a fermion radiates a photon.

In weak interactions on the other hand, there are both neutral and charged particle exchanges. In neutral interactions a particle radiates a Z^0 boson which can then decay into a pair of neutral or charged particles (figure 2.3a). Charged-current interactions mediated by the $W^\pm$ bosons deserve some special attendance. The $W^\pm$ bosons can decay into a charged and an uncharged lepton, as happens for example in the classical β-decay $p \to n + W^+ \to n + e^+ + \nu_e$. In exchange interactions it thus allows leptons to change into the other state within the generational doublet (an example would be electron–neutrino scattering $e^-\nu_\mu \to \nu_e\mu^-$ in which a W^- boson is exchanged). It is not possible to cross generational borders (i.e. $e^- \to \mu^-$) via weak interactions in the lepton sector. However, the situation is different in the quark sector. Here the generational doublets do not correspond with the eigenstates of the weak interaction, which take the form

$$\begin{pmatrix} u \\ d' \end{pmatrix}, \begin{pmatrix} c \\ s' \end{pmatrix}, \begin{pmatrix} t \\ b' \end{pmatrix} \tag{2.1}$$

where the lower components are linear combinations of the physical d, s and b quarks related via the mixing coefficients in the CKM

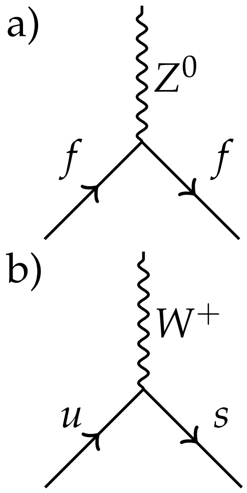

Figure 2.3: Two fundamental weak interaction vertices. a) shows the radiation of a Z^0 boson and b) the radiation of a W^+ boson which crosses a generational border changing an up quark into a strange quark.

---

[4] As a consequence the gluon itself carries two colour charges: a colour and an anti-colour.

[5] The index L accounts for the fact that weak interaction is a "left-handed" theory, i.e. maximally parity violating, the index Y refers to the weak hypercharge. For further reading [21, 22] is suggested.

matrix

$$\begin{pmatrix} d' \\ s' \\ b' \end{pmatrix} = \begin{pmatrix} V_{ud} & V_{us} & V_{ub} \\ V_{cd} & V_{cs} & V_{cb} \\ V_{td} & V_{ts} & V_{tb} \end{pmatrix} \cdot \begin{pmatrix} d \\ s \\ b \end{pmatrix} \quad . \tag{2.2}$$

An example for a resulting vertex is depicted in figure 2.3b. For more details on electroweak interactions [23] is recommended.

2.1.3 Quantum Chromodynamics

The theory describing strong interactions is called Quantum Chromodynamics (QCD) [24][6]. It can be seen as an expanded version of the same pictorial machinery used in QED. But whereas there is only one charge in QED, there is three different ones in QCD. They are called colour charges and need to be preserved at every interaction vertex. Very much like the photon, there is a massless gauge boson mediating the force, but unlike the photon, which is neutral with respect to the charge it couples to, the gluon carries two colour charges itself: a colour and an anti-colour charge. This has interesting phenomenological consequences: The spectrum of possible QCD interaction vertices is much richer since the gluon can couple to itself and even form bound states called glueballs, consisting exclusively of gluons. A few examples of interaction vertices are depicted in figure 2.4, where without loss of generality the three colour charges are called blue, red and green, as is common in current literature.

Evaluating all possible colour-charge combinations the gluon can take on, one concludes the existence of 8 physical gluon states. This colour-octet is described by an $SU_C(3)$ symmetry group.

To this day, nobody has directly observed a particle with fractional electric charge, or discernible colour charge. This is commonly known as the confinement problem. Its solution constitutes another major discrepancy from QED and intuition. When the distance between two particles is increased, the strong force acting in between them gets stronger, much like the force of a spring increases when the ends are pulled. Yet, at small distances quarks and gluons can still be treated as free particles. This is called asymptotic freedom and allows QCD to be treated as a perturbation theory. If the field between two particles gets strong enough, a new $q\bar{q}$ pair is created from the energy of the interaction field to counteract the colour forces in between as shown in figure 2.5. In practice this means coloured particles will immediately after creation form colour-neutral bound states which can then be observed. States of the form $q\bar{q}$ are called mesons and carry a colour and its anticolour, qqq states exhibit all three different colour charges and are called baryons (or antibaryons in the $\bar{q}\bar{q}\bar{q}$ case). Collectively mesons and baryons are called hadrons.

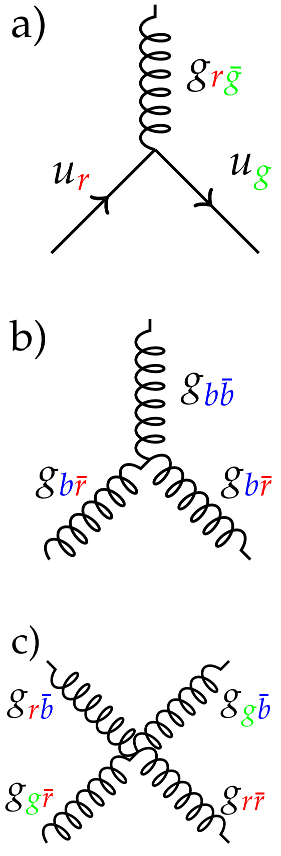

Figure 2.4: a) an up quark radiating a gluon and thus changing its colour charge. b)+c) the gluon self-coupling leads to vertices in which three or four gluons couple to each other.

[6] For an interesting easy-to-read, yet somewhat dated compendium on QCD see [25].

2.2 Particles with long lifetimes

This study describes a search for new heavy long-lived particles. The SM itself offers a series of elementary particles and bound states with long lifetimes.

2.2.1 Why particles are long lived

Many different mechanisms can influence the lifetime of a particle and render it detector-stable.

- If the system at hand exhibits a (nearly) conserved quantum number, there has to be a particle that finds no lighter particle to decay to without violating the conserved quantity. There are several examples from the SM: the electron cannot decay to any lighter charged particles without violating conservation of lepton number or electric charge. It is thus stable. The same way one can argue the stability of the proton: as the lightest baryon there is no possibility for it to decay without breaking the conservation of baryon number[7].
- If there is a weak coupling in the decay chain, the decay is suppressed and the parent particle becomes long lived. In the SM this is the case for the muon. Its long lifetime of $\tau_\mu = 2.197\ \mu\text{s}$ [27] is caused by its decay being a purely weak process via a heavy W boson as depicted in figure 2.6.
- If the available phase space for a decay is limited. This is the case if the sum of the masses of the decay products are very close to the mass of the parent particle. In the SM the neutron is only about 0.08% heavier than the sum of the decay products p, e^- and $\bar{\nu}_e$. The β-decay is thus further suppressed by phase space limitations resulting in the lifetime of the neutron of $\tau_n \approx 880$ s [28].

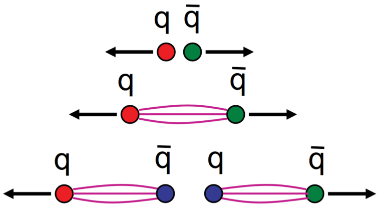

Figure 2.5: Results of colour confinement in QCD. Two quarks are pulled apart, the strong force in between them increases and to counteract the field in between them two new quarks are created. Figure taken from [26].

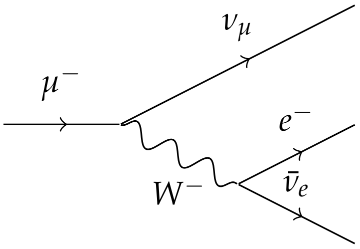

Figure 2.6: The decay of the muon is suppressed because of the weak coupling to the heavy W boson.

2.2.2 Long-lived particles in the Standard Model

The SM offers a range of particles that can be considered long-lived. In figure 2.7 all SM particles with mean lifetimes larger than 10^{-20} s are plotted. Further, for a particle boost of 200 GeV the time interval in which the particle travels through the ATLAS detector have been included. As can be seen, particles with lifetimes $\tau > 0.1$ ns are able to decay within the detector itself.

2.3 Shortcomings of the Standard Model

Since its formulation different aspects of the SM have been experimentally tested over and over again. One of the most impressive

---

[7] This of course only holds for the free particle. A proton bound in a nucleus can "borrow" energy from the binding energy to decay to a neutron, positron and neutrino.

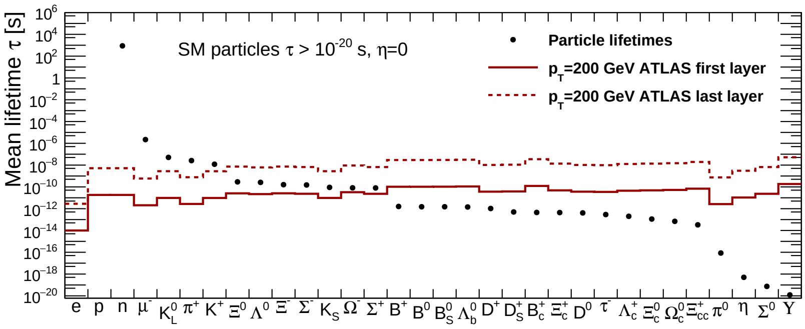

Figure 2.7: All known particles of the SM with lifetimes larger 10^{-20} s. Since electron and proton are stable no data point can be seen. Assuming a particle boost of 200 GeV, the two red lines indicate the time interval during which the particle would travel within the active layers of the ATLAS detector (without being stopped). Particle lifetimes and masses have been extracted from [29].

examples is the measurement of the anomalous magnetic moment of the electron $a_e = (g-2)/2$, where g is the so called g-factor[8]. The theoretical prediction was calculated up to tenth order in perturbation theory and arrived at the value of [30]

$$a_e(\text{theory}) = 159652181.78(77) \times 10^{-12} \quad . \tag{2.3}$$

The measurement arrived at a value of [31, 32]

$$a_e(\text{exper.}) = 159652180.73(0.28) \times 10^{-12} \quad . \tag{2.4}$$

Theoretically calculated and measured values agree to more than 10 digits. This is an astonishing precision and an impressive achievement for the SM. Further, the model also predicted new particles that were still undiscovered at the time. Massive search efforts however lead to the experimental verification and the discoveries of the $W^{\pm}$ [33, 34] and Z^0 [35, 36] bosons at CERN's SPS in 1983, of the top quark at Fermilab in 1995 [37, 38] and of the Higgs boson at the LHC in 2012 [39, 40].

The SM itself is a remarkable success. Yet, despite everything there are many serious shortcomings of the model which are briefly discussed here.

Gravitational force The SM does not attempt to give an accurate description of gravity as the fourth known fundamental force of nature. Because of its relative weakness on energy scales probed so far[9], this has not posed a problem and is unlikely to do so in the foreseeable future. It is however expected that this will change when moving to higher and higher energies and the SM will become invalid when gravity ceases to be negligible[10]. The best current description of gravity is given by general relativity which seems to be fundamentally incompatible with the SM [41]. Many attempts have been made to construct a theory of quantum gravity, yet, they have proven unsuccessful so far [42, 43]. As an analogue to the other three forces, an additional force carrier called the graviton could be assumed which mediates gravitational force. The physics program at the LHC in-

[8] The anomalous magnetic moment originates from quantum mechanical effects which can be expressed by Feynman diagrams with an arbitrary number of loops. The "g-factor" corresponds to the classical result, i.e. only the tree-level contribution, for which the Dirac equation predicts $g = 2$.

[9] compare to the relative strengths of the forces listed in table 2.1

[10] A rough estimate on where this happens is given by the Planck scale which can be calculated by equating the Compton wavelength $\lambda_C = h/m$, at which quantum effects start to be relevant for an accurate description of particle behaviour, with the Schwarzschild radius $r_S = 2Gm$ which describes a particles maximal confinement before collapsing into a black hole. This yields $m_P = \sqrt{h/2G} \approx 1.22 \times 10^{19}$ GeV.

cludes searches for gravitons, however no evidence of their existence has been found so far, e.g. [44, 45].

Dark matter Cosmological observations including galactic rotation curves [47], stellar velocity dispersions [48], as well as observations of gravitational lensing effects [49] lead to the conclusion that ordinary matter as described by the SM makes up only 4.9% of the mass in the Universe (figure 2.9). Recent measurements by the Planck satellite [50] suggest a significantly larger portion of 26.8% is dark matter, which is assumed to be of particle nature. Dark matter does not interact with ordinary matter via the strong or electromagnetic force and is thus limited to gravitational and weak interactions. After the discovery of neutrino oscillations it was speculated whether dark matter could be composed of SM neutrinos, however, the measured upper limits on neutrino masses and their cosmic abundances seem to rule out that interpretation [51]. Many much discussed hypotheses involve WIMPs (weakly interacting massive particles) with masses on the TeV scale. Therefore, the SM does not offer a suitable candidate to explain dark matter. The remaining 68.3% of the Universe is called dark energy, which counteracts the gravitational pull of the matter and is responsible for the accelerated expansion of the Universe. Dark energy remains one of the most mysterious observations in contemporary physics [52].

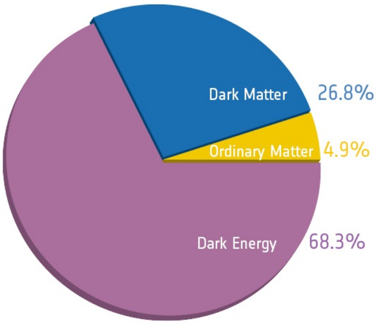

Figure 2.8: Content of the Universe as measured by the Planck satellite. Figure taken from [46].

Neutrino oscillations In the SM neutrinos are massless. However, the observation of neutrino oscillations [54] demands neutrinos to have mass, albeit a small one. Adding neutrino mass terms to the SM leads to further theoretical problems as it is not clear whether neutrino masses stem from the same mechanism as all the other masses in the SM.

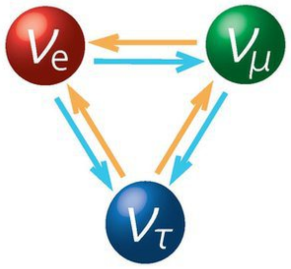

Figure 2.9: Neutrinos oscillate between their flavours. Figure taken from [53].

Baryon asymmetry The Universe seems to be composed of matter particles with almost no antimatter around. Yet, the Big Bang theory predicts matter and antimatter to be created in equal abundances. In order for such an asymmetry to appear a process needs to discriminate between matter and antimatter allowing for matter to become dominant over antimatter[11]. Such a process is called a charge-parity (CP) violating process. The dominant interactions in the SM, however, are CP invariant. The small CP violations that have been measured in the hadronic electroweak sector are far too small to explain the lack of baryonic antimatter in the Universe [56–58].

Hierarchy problem The SM is a low-energy approximation only valid on the order of the electroweak unification at energies $\mathcal{O}(100 \text{ GeV})$, which is considerably lower than the Planck scale at $\mathcal{O}(10^{19} \text{ GeV})$. The inconsistencies introduced by the different scales become apparent when considering the Higgs mass. Its measured value m_H is in fact the sum of its bare mass m_0 and the quantum corrections it

[11] This is one of the three Sakharov conditions for generating baryon asymmetry. The others are the existence of baryon number violation and departure from thermal equilibrium [55].

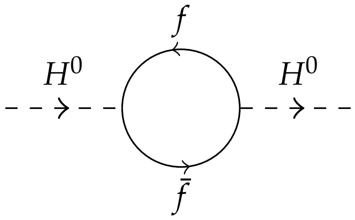

Figure 2.10: One-loop quantum corrections to the physical Higgs mass coming from virtual fermion loops, most dominantly the top quark.

receives through loop diagrams like the one depicted in figure 2.10

$$m_H^2 = m_0^2 - 6\lambda_f^2 \int \frac{d^4k}{(2\pi)^4} \frac{1}{k^2} \quad , \tag{2.5}$$

where λ_f is the coupling constant of fermions to the Higgs field (most dominantly the top quark because of its large mass). As can be seen, the integral diverges quadratically and the computation is only possible by defining a cut-off Λ up to which the integration is carried out and the theory looses its validity [59]. If Λ is taken to be the Planck scale[12], the loop correction become enormous and about 34 orders of magnitude larger than m_H [60]. To get the observed value of a mere ≈ 125 GeV the quantum corrections have to cancel with the bare Higgs mass to an astonishing precision. This fine tuning between the two large and uncorrelated parameters is considered unnatural [61, 62].

	Number of parameters
Coupling constants	3
Higgs potential	2
Fermion masses	9
CKM matrix (quark mixing)	4
No CP-violation in strong interactions	1
Neutrino masses	3
Mixing angles	≥ 4

Table 2.2: The free parameters of the SM. Below the line are the additional free parameters necessary for the neutrino sector. The listed neutrino mixing angles include three angels and at least one CP-violating complex phase stemming from the PMNS matrix [63].

Number of free parameters The SM has 19 numerical parameters that are not determined within the theory and can only be measured in an experiment. The discovery of non-zero neutrino masses adds even further free parameters to the list as given in table 2.2. Some find so many free parameters disquieting and search for a more fundamental theory.

2.4 Physics beyond the Standard Model

Because of the many shortcomings associated to the SM and discussed in the previous chapter, it has become general consensus that some form of physics beyond the framework of the SM has to exist. Many such suggested expansions invoke new fundamental symmetries of the Universe, new particle fields or place the perceivable surroundings of physical existence within a much more complicated structure of space-time. While they set out to solve many of the aforementioned shortcomings of the SM, they must also respect existing measurements. A common prerequisite of all new models is therefore the incorporation of the SM within the context of new and expanded phenomenology, rather than replacing it. In the following a prominent set of beyond the SM theories which involve a new fundamental symmetry called supersymmetry is described. The parameter spaces of such theories can offer some degree of freedom to allow for the existence of new massive long-lived particles.

2.5 Supersymmetry

Recall the hierarchy problem as described in chapter 2.3. The Higgs mass receives quantum corrections Δm_H from loop diagrams. For the fermion loop in figure 2.10 the correction is of the form

---

[12] since a complete theory is required to be valid all the way up to the Planck scale

$$\Delta m_H^2 = -\frac{|\lambda_f|^2}{8\pi^2} \cdot \Lambda^2 + \cdots \quad , \tag{2.6}$$

where the ellipsis involves terms at least proportional to the fermion mass that grow logarithmically in Λ. On the other hand, corrections coming from the diagram in figure 2.11, where a Higgs boson radiates and reabsorbs a hypothetical massive scalar particle that couples with coupling constant λ_S to the Higgs, yield quantum corrections of the form

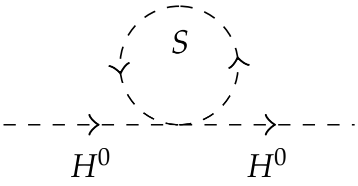

Figure 2.11: A hypothetical heavy scalar particle coupling to the Higgs boson.

$$\Delta m_H^2 = \frac{|\lambda_S|^2}{16\pi^2} \cdot \Lambda^2 - \cdots \quad . \tag{2.7}$$

Comparing equations 2.6 and 2.7 one can draw the following conclusion: If there is a fundamental new symmetry which associates fermions to bosons and vice versa, one can have systematic cancellations of the quantum corrections because of the relative minus sign[13] [64]. This fundamental symmetry is called supersymmetry (SUSY). A tremendous amount of work has been put into the development of models incorporating this symmetry [65–70].

The generator Q of this transformation is a fermionic operator which carries a half-integer spin and maps bosonic states onto fermionic states and vice versa

$$Q\,|\text{boson}\rangle = |\text{fermion}\rangle \quad , \quad Q\,|\text{fermion}\rangle = Q\,|\text{boson}\rangle \quad . \tag{2.8}$$

It has the properties of an anticommutating Weyl spinor[14]. For further details on the algebra of supersymmetry [72–75] are recommended.

SUSY affects all fields (and thus particles) in the SM. Much like the symmetry between particle and antiparticle it predicts a superpartner for every known particle with the same mass and internal quantum numbers but opposite spin statistics that form a so-called supermultiplet. Obviously, this prediction is refuted by the striking absence of discoveries of superpartners. SUSY therefore has to be a broken symmetry which causes a splitting of the masses of a supermultiplet and causes the mass of superpartners to be much higher than their SM counterparts.

Supersymmetric particles in the TeV range would allow for a unification of the gauge couplings of the three SM gauge groups at large energy scales as sketched in figure 2.12. This is one of the conditions for the construction of a Grand Unified Theory (GUT) [76–78]. Gauge coupling unification cannot be achieved in the pure SM and needs extra multiplets between the weak scale and the scale of the GUT [79].

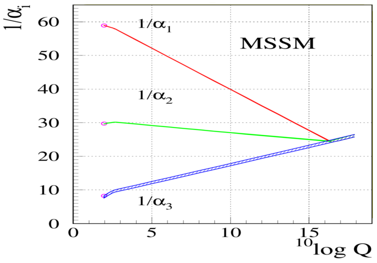

Figure 2.12: Running coupling constants in a SUSY extension of the SM. Figure adapted from [80].

In order to keep the attractive features of the theory the breaking is not arbitrary, but of a certain type called soft breaking [81, 82].

---

[13] The scalar potential is demanded to be bound from below which renders λ_S automatically positive.

[14] The generator satisfies the following anticommutator $\{A, B\} = AB + BA$ relations

$$\begin{aligned} \{Q_\alpha, Q^\dagger_{\bar\beta}\} &= 2\sigma^\mu_{\alpha\bar\beta} P_\mu \quad , \\ \{Q_\alpha, Q_\beta\} &= 0 \quad , \\ \{Q^\dagger_{\bar\alpha}, Q^\dagger_{\bar\beta}\} &= 0 \end{aligned}$$

where the indices α, β and $\bar\alpha$, $\bar\beta$ for Q and $Q^\dagger$ respectively take the values 1 and 2, P_μ is the four-momentum and $\sigma^\mu = (\mathbf{1}, \sigma_i)$ with the Pauli matrices σ_i. The SUSY algebra is consistent with Lorentz covariance [71].

2.5.1 Soft supersymmetry breaking

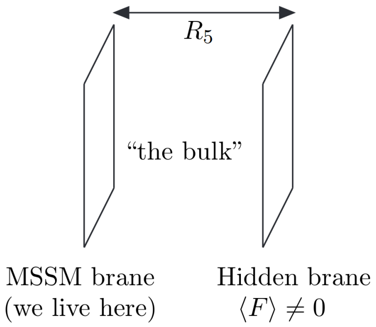

Figure 2.13: A separation of the hidden sector from the observable sector of SUSY takes place. The hidden sector might be an additional spatial dimension. Here the branes are 4D hypersurfaces in 5D spacetime. The figure is taken from [74].

To achieve soft SUSY breaking the Lagrangian is expanded by additional terms which do not satisfy SUSY transformation invariance but have a negligible effect at large energies where the symmetry is unbroken. Similar to the Higgs-mechanism in the SM, the superpartners gain their mass through direct couplings to these new terms.

There is an abundance of possible mechanisms proposed to achieve soft SUSY breaking. In fact, very often SUSY models are distinguished from each other by the breaking mechanism. In many cases this is achieved by postulating a separation of the observable SUSY sector from a hidden SUSY-breaking sector (figure 2.13). This could for example be realised by assuming additional spacetime dimensions [83, 84]. Different mechanisms of mediation between the visible and the hidden sector through messenger fields take place. Common models include gauge-mediated supersymmetry breaking (GMSB), anomaly-mediated supersymmetry breaking (AMSB) or minimal supergravity (mSUGRA).

2.5.2 R-parity

Supersymmetry adds a new multiplicative quantum number called R-parity[15] [85]

$$P_R = (-1)^{2S+3(B-L)} \tag{2.9}$$

Here S is the spin of the particle, B is the baryon number and L the lepton number. All SM particles and the Higgs boson have $P_R = +1$, while all superpartners have odd R-parity $P_R = -1$. In most SUSY models R-parity is promoted to a fundamental conserved quantity. This has striking phenomenological consequences. All supersymmetric particles decay to a state which contains at least one other sparticle with odd R-parity. Thus, the lightest supersymmetric particle (LSP) cannot decay to any lighter particle without violating R-parity conservation. If it is electrically neutral and only weakly interacting, the LSP functions as an ideal candidate for dark matter. In fact most SUSY models are designed to satisfy the dark-matter requirements. Depending on the model, WIMP candidates are usually the gravitino or the lightest neutralino [86][16].

Further, it can be concluded that sparticles are always produced in pairs and each one of them decays to a state that consists of an odd number (oftentimes just one) of LSPs.

The original motivation for R-parity was to prevent proton decays [89, 90]. It is however possible to also construct models that do not conserve R-parity and nevertheless contain a quasi-stable proton with lifetimes many times the age of the Universe [91].

---

[15] sometimes also equivalently used 'matter parity'

[16] The sneutrino is another possibility which was excluded by measurements [87, 88].

2.5.3 Minimal Supersymmetric Standard Model

The Minimal Supersymmetric Standard Model (MSSM) considers only the minimal number of additional particle fields and interactions still consistent with phenomenology [92]. This results in a superpartner for every SM fermion that is itself of bosonic character. The name of the new particle is prefixed by an 's' and its symbol canopied by a $\sim$. This way, top quark t and bottom quark b have superpartners top squark $\tilde{t}$ and bottom squark $\tilde{b}$. Further, there is a fermionic superpartner for every boson in the SM. Here the naming scheme dictates the suffix '-ino' and a $\sim$ above the symbol. Thus, the superpartner of the gluon g is the gluino $\tilde{g}$. To accommodate electroweak symmetry breaking, the Higgs sector of the MSSM needs to be enlarged with respect to the SM to prevent gauge anomalies. The simplest approach is to add two scalar Higgs doublets. The resulting higgsinos are allowed to mix with the gauginos and form six observable mass eigenstates[17]. Four of them are electrically neutral and called neutralinos $\tilde{\chi}_i^0$, the electrically charged ones are called charginos $\tilde{\chi}_i^{\pm}$. A similar mixing can be observed in the sfermion sector where the gauge eigenstates mix to form mass eigenstates. For example the $\tilde{\tau}_L$ and $\tilde{\tau}_R$[18] form mass eigenstates called $\tilde{\tau}_1$ and $\tilde{\tau}_2$.

An overview of all the predicted supersymmetric particles, which are collectively called sparticles, is given in table 2.3.

Particle name	Spin	P_R	Gauge eigenstate	Mass eigenstate
Higgs bosons	0	+1	$H_u^0\ H_d^0\ H_u^+\ H_d^-$	$h^0\ H^0\ A^0\ H^{\pm}$
squarks	0	−1	$\tilde{u}_L\ \tilde{u}_R\ \tilde{d}_L\ \tilde{d}_R$	same
			$\tilde{s}_L\ \tilde{s}_R\ \tilde{c}_L\ \tilde{c}_R$	same
			$\tilde{t}_L\ \tilde{t}_R\ \tilde{b}_L\ \tilde{b}_R$	$\tilde{t}_1\ \tilde{t}_2\ \tilde{b}_1\ \tilde{b}_2$
sleptons	0	−1	$\tilde{e}_L\ \tilde{e}_R\ \tilde{\nu}_e$	same
			$\tilde{\mu}_L\ \tilde{\mu}_R\ \tilde{\nu}_\mu$	same
			$\tilde{\tau}_L\ \tilde{\tau}_R\ \tilde{\nu}_\tau$	$\tilde{\tau}_1\ \tilde{\tau}_2\ \tilde{\nu}_\tau$
neutralinos	1/2	−1	$\tilde{B}^0\ \tilde{W}^0\ \tilde{H}_u^0\ \tilde{H}_d^0$	$\tilde{\chi}_1^0\ \tilde{\chi}_2^0\ \tilde{\chi}_3^0\ \tilde{\chi}_4^0$
charginos	1/2	−1	$\tilde{W}^{\pm}\ \tilde{H}_u^+\ \tilde{H}_d^-$	$\tilde{\chi}_1^{\pm}\ \tilde{\chi}_2^{\pm}$
gluino	1/2	−1	$\tilde{g}$	same
gravitino	1/2	−1	$\tilde{G}$	same

Table 2.3: Overview of the particles predicted by the Minimal Supersymmetric Standard Model. The Spin and R-parity state of the particles are listed. The mixing of the sfermion states in the first and second generation is assumed to be small, so mass eigenstates different from the gauge eigenstates are only given for the third family. The table has been reproduced from [74].

In total, the MSSM offers more than 120 free parameters which are largely related to CP-violating phases and flavour-changing neutral currents. Since experiments put strong constraints on those, some scenarios try to reduce the number of free parameters by at least a factor of six through experiment-motivated assumptions and by constraining parameters to each other [93]. Those models are called constrained minimal supersymmetric Standard Models (CMSSM).

[17] The neutral eigenstates result from the mixing of the neutral higgsinos ($\tilde{H}_u^0$, $\tilde{H}_d^0$) with the neutral gauginos ($\tilde{B}$, $\tilde{W}^0$). The charged ones are a mixing of charged higgsinos ($\tilde{H}_u^+$, $\tilde{H}_d^-$) and winos ($\tilde{W}^+$, $\tilde{W}^-$).

[18] The index L and R do not refer to the helicity of the SUSY particle which has spin 0, but to that of the SM partner.

Some CMSSM or mSUGRA models require as few as five parameters[19] [94].

It should be noted that the MSSM is under severe constraints due to the discovery of the Higgs boson with $m_H = 125$ GeV [95]. However, as a simple model which is (historically) available for many generators and software packages for quantitative predictions, that nevertheless correctly describes many effects of still viable supersymmetric models, it remains a much discussed and studied scenario.

2.5.4 Supersymmetry at the LHC

At the LHC SUSY particles are predominantly produced through strong processes like gluon–gluon fusion. In figure 2.14 the cross sections for several production processes are drawn. They were calculated using the PROSPINO2 [96] software and include next-to-leading order (NLO) loop corrections matched with resummed results at next-to-leading-logarithmic (NLL) accuracy.

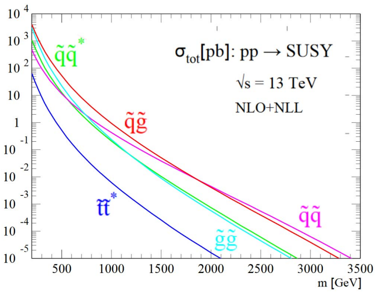

Figure 2.14: Total cross section in pb for SUSY production in proton–proton collisions as a function of mass for different production channels. The calculation was carried out including first order loop corrections. Here equally degenerate squark and gluino masses are assumed. The figure was adapted from [97].

Sparticles typically decay through long decay chains with possibly multiple promptly decaying intermediates which can give rise to a large multiplicity of jets and/or leptons in an event. In R-parity conserving models, the decay cascade terminates when the LSP is reached. Since this particle is stable and leaves the detector it will give rise to missing transverse momentum, a momentum imbalance within the detector that can be quantified by calculating the vectorial sum of the momenta of all particles in the plane transverse to the beam pipe. Since the LSP is electrically neutral it will not leave a measurable track and thus prohibit the sum from vanishing. It is often expressed in terms of missing transverse energy E_T^{miss}. Because of this most generic SUSY searches use E_T^{miss} as their primary signature.

The sparticles which are of special interest for the present study are the gluino, the third generation squarks, staus and charginos. Gluinos decay either via squark–antisquark production $\tilde{g} \to \tilde{q}\bar{q}/\bar{\tilde{q}}q$ (if $m_{\tilde{g}} > m_{\tilde{q}}$) or via $\tilde{g} \to q\bar{q}\tilde{\chi}_1^0$ (if $m_{\tilde{g}} > m_{\tilde{\chi}_1^0}$). The squarks decay to a gluino and a SM quark $\tilde{q} \to \tilde{g}q$ (if $m_{\tilde{q}} > m_{\tilde{g}}$) [98]. For sleptons like the stau, the allowed decays involve charginos and neutralinos as well as a lepton $\tilde{l} \to \tilde{\chi}^0 l/\tilde{\chi}^{\pm}\nu$. Lastly, chargino decays are much more complicated and model dependent since they result out of the mixing of higgsino and gaugino fields [99].

Example Feynman diagrams of the decay of a gluino, squark and slepton are drawn in figure 2.15.

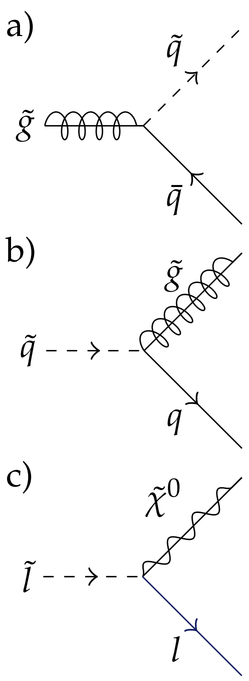

Figure 2.15: Examples for the decay of a (a) gluino, (b) squark and (c) slepton.

The general search strategy at the LHC and the ATLAS experiment is to cover as large a portion as possible of the available parameter space. To this end most analyses rely on large quantities of E_T^{miss}, a large multiplicity of jets and an analysis-dependent number of leptons in the event. This approach has been shown to work well in phenomenological MSSM model space and suggests an equally good coverage for all LHC SUSY searches [100].

---

[19] m_0 - mass scale of scalars
$m_{1/2}$ - mass scale gauginos/higgsinos
A_0 - common trilinear coupling
$\tan\beta$ - Higgs vacuum expectation value ratio
sign$\mu = \pm 1$ - sign of SUSY conserving mass parameter

Many different supersymmetric models can give rise to SMPs. In the following Split SUSY and gauge-mediated supersymmetry breaking are introduced as benchmark models used in this analysis.

2.5.5 Split SUSY

Split SUSY (SSUSY) [101, 102] models follow a slightly different motivation than laid out here. So far the main driving force for SUSY was the solution of the hierarchy problem. However, the nature of the hierarchy problem is very similar to the cosmological constant problem as it is also related to ultraviolet power divergences and gives rise to suspiciously fine-tuned parameters at low energies. Yet, one can "solve"[20] this by invoking the anthropic principle [103] as suggested by Weinberg [104]. It is now argued to adopt the same justification to the hierarchy problem and instead focus on a model providing gauge-coupling unification, a viable dark-matter candidate and a Higgs boson in agreement with observation.

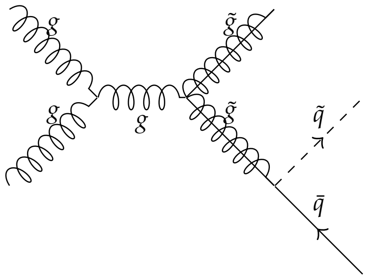

Figure 2.16: Pair production of gluinos and subsequent decay to a much heavier squark, resulting in a long gluino lifetime.

To accomplish this, SSUSY has two different intrinsic mass scales. The sfermions (squarks and sleptons) have large masses, while the other particles including the Higgs boson can be light and accessible at the LHC. This has an important consequence for the lifetime of the gluino. Since its decay involves a massive squark the decay is heavily suppressed and the gluino becomes long-lived. The process is sketched in figure 2.16. The lifetime of the gluino is determined only by its mass and the magnitude of the splitting between mass scales, i.e. the scale of supersymmetry breaking [105].

The discovery of the Higgs boson puts restrictions on the scale of SUSY breaking as can be seen from figure 2.17 and therefore on the lifetime of the gluino. Depending on the parameters of the model (especially $\tan\beta$) the maximal allowed breaking scale is 10^7 GeV which results in a gluino lifetime of $\tau_{\tilde{g}} \approx 40$ ns for $m_{\tilde{g}} = 1$ TeV, enough to qualify as an SMP.

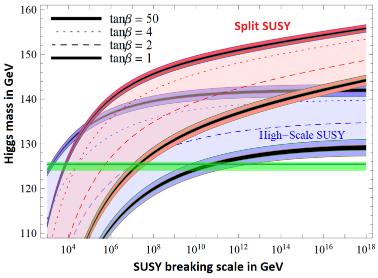

Figure 2.17: Allowed SUSY breaking scale as a function of Higgs mass for different $\tan\beta$. The green line describes the experimental value. Figure adapted from [106].

Gluinos, just like their SM counterparts, carry colour charge and are therefore subject to confinement. Gluinos will therefore hadronise immediately and form a combined state called R-hadron[21]. In this thesis gluino R-hadrons from a Split SUSY scenario are frequently used as a benchmark to study SMP behaviour.

2.5.6 Gauge-mediated supersymmetry breaking

In gauge-mediated supersymmetry breaking (GMSB) models, the breaking is mediated by the common gauge interactions in QCD and electroweak theory [74, 107]. The model can be fully described by specifying only five different parameters (see footnote in chapter 2.5.3). The gravitino $\tilde{G}$ is the LSP, which has important implications. The next-to-lightest supersymmetric particle (NLSP), for which no astrophysical constraints exist, can be charged or coloured and decays to the gravitino and its SM partner. Because the gravitino only interacts very weakly it implies a long-lived NLSP, usually the stau $\tilde{\tau}$ or neutralino $\tilde{\chi}^0$ [108]. Here only models in which the $\tilde{\tau}$ is the long-lived NLSP will be considered.

---

[20] The anthropic principle is more a cop-out than a solution, admitting our ignorance and shifting the burden of explanation to future generations with access to new experimental facilities.

[21] The same applies of course for squarks. In general: a colour-triplet C_3 hadronises either to form a meson-like object $C_3\bar{q}$ or a baryon-like one $C_3 q_1 q_2$. A colour-octet C_8 has three possible states: the meson-like $C_8 q_1 \bar{q}_2$, the baryon-like $C_8 q_1 q_2 q_3$ (or antibaryon-like $C_8 \bar{q}_1 \bar{q}_2 \bar{q}_3$) or a glueball $C_8 g$.

For further reading on GMSB [109] is recommended.

2.5.7 Anomaly-mediated supersymmetry breaking

Another group of SUSY models assumes the hidden sector to have a structure which fails to provide mass terms through either gauge interactions like in GMSB or through gravity like in SUGRA models. Instead the breaking is conveyed via the superconformal anomaly[22]. Such models are therefore termed anomaly-mediated supersymmetry breaking (AMSB) [111–113] and predict an alternative set of signatures and masses [114]. In such models one could have a near mass degeneration between the neutralino as the LSP and the lightest chargino. Such a chargino would then become long-lived.

Pure AMSB predicts negative mass squares for sleptons. This can be solved by adding a constant term to squared scalar masses. The model is then called minimal AMSB (mAMSB) [115].

2.6 Theories involving extra dimensions

An abundance of models involving additional dimensions have been proposed. Many of them can give rise to long-lived particles. In Universal Extra Dimension (UED) models there exist additional compactified spatial dimensions beyond the known three dimensions that are accessible to all SM fields [116] (figure 2.18). Similarly to R-parity one can define a new quantum number called Kaluza-Klein (KK) number which has to be conserved at each vertex. This way UED provides a viable dark-matter candidate [117]. UED could further deliver a mechanism for gauge-coupling unification [118], SUSY breaking [119] and for the fermion mass hierarchy [120].

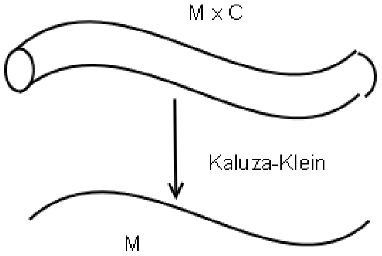

Figure 2.18: An additional dimension C is wrapped around itself and compactified enough not to be noticed. Taken from [121].

The signatures of UED are similar to those of SUSY: E_T^{miss}-based searches which can potentially contain several leptons and jets originating from cascade decays in the event [122]. The parameters of the model can be chosen to make the lightest and the next-to-lightest KK particle long-lived [123]. Such long-lived states require dedicated searches which are beyond the scope of this work.

2.7 Stable Massive Particles

In chapters 2.5 and 2.6 a few examples of models that give rise to LLPs have been discussed. Obviously they only function as benchmark models and are by no means a full list of LLP providing scenarios. As a matter of fact, since most BSM hypotheses rely on a multitude of parameters it is often possible to select a set of parameters that renders one or more particles long-lived. Consider a CMSSM

[22] Also referred to as Weyl anomaly. It is a quantum phenomenon which allows the breaking of the theorie's conformal symmetry. An example for such a type of anomaly is the trace anomaly found in QCD. The anomaly introduces the scale at which colour confinement occurs and thus determines the sizes and masses of all hadrons. [110]

model with a mass degeneration between the lightest neutralino and the stau with $m_{\tilde{\tau}_1} - m_{\tilde{\chi}^0} < m_\tau$. Depending on the model parameters m_0 and $m_{1/2}$ the lifetime of the $\tilde{\tau}_1$ now ranges from $\mathcal{O}(1\ \text{ns})$ to $\mathcal{O}(1\ \mu\text{s})$ as plotted in figure 2.19. It becomes apparent that the search strategy must heavily depend on the choice of model parameters. In models with detector-stable particles the typical long cascade processes are interrupted and do not yield large missing energy. Hence, the generic E_T^{miss}-based analyses are blind to such scenarios.

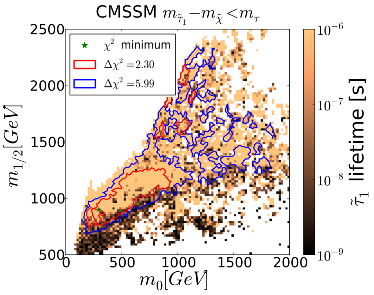

Figure 2.19: Lifetime of the $\tilde{\tau}_1$ in the m_0-$m_{1/2}$ parameter space of a CMSSM model. m_0 is the mass scale of the scalars of the model, $m_{1/2}$ that of the gauginos and higgsinos. For details on the coloured markings see source of the figure in [124].

SMPs are predicted by many supersymmetric models regardless of whether the violate R-parity [125–127] or conserve it [85, 101, 107, 128–131].

While the potential signals studied here are mainly singly-charged particles with a small fraction of doubly-charged R-hadrons, a different kind of SMP can be imagined that exhibit electric charges many times the elementary charge $|q| \gg e$. Such hypothetical particles are collectively called highly ionizing particles (HIPs). Examples are Q-balls [132, 133], dyons [134], magnetic monopoles [128] or remnants of microscopic black holes [135].

The distinctiveness of SMP topologies offer both challenges and benefits for search efforts. The long lifetimes allow for a direct detection as opposed to reconstruction through decay products. Since the SM offers no particle with similar characteristics the search is free of physical background with small backgrounds due to detector effects. It is therefore necessary to have a good understanding of the detector itself.

2.7.1 Interaction with matter

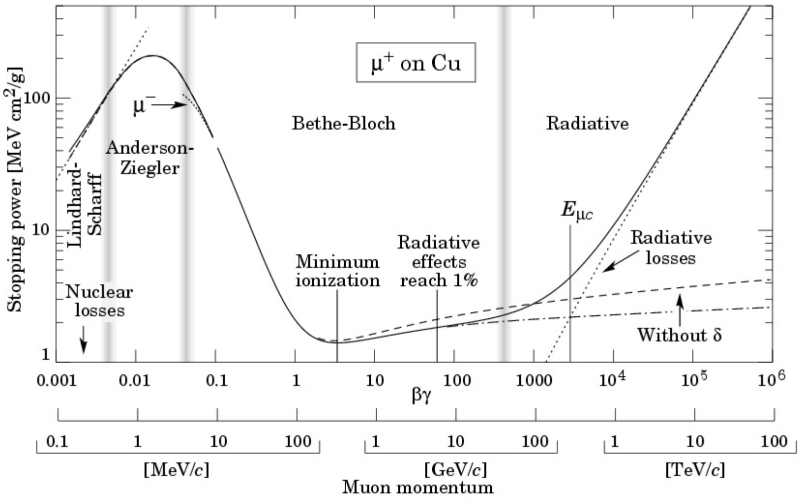

Figure 2.20: Stopping power as a function of $\beta\gamma = \beta/\sqrt{1-\beta^2}$ where $\beta = v/c$ and the momentum p for antimuons propagating through copper. The stopping power translates to ionization energy losses dE/dx. The figure was taken from [136].

The possible interactions of SMPs depend on the kind of long-lived particle. While all SMPs interact through electromagnetic effects, hadron-like SMPs like R-hadrons can also interact via the strong interaction. In comparison to electromagnetic effects they are significantly less understood. Because of their large masses all SMPs

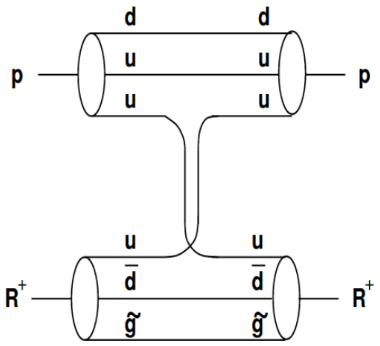

Figure 2.21: Elastic scattering of an *R*-hadron and a proton. The *R* stands for the *R*-hadron. Figure taken from [128].

have in common that their propagation velocity can be significantly smaller than the speed of light $\beta < 1$, where $\beta = v/c$. Since all light SM particles are expected to propagate with the speed of light it is possible to detect SMPs by performing time-of-flight measurements. The following chapter gives a summary of the possible interactions within the detector. For a more complete overview [137] is recommended.

Lepton-like SMPs The main electromagnetic effects are Coulomb scattering and continuous energy losses through ionisation in the detector material. The scattering processes influence the trajectory of the particle. Since the scattering angle is proportional to $1/p\beta$ one can at first assume a large effect because of the small β. However, since most SMPs exhibit a considerable momentum, the slow velocity is compensated for and the deflection angle is in fact small. The ionisation-energy losses dE/dx[23] are well described by the Bethe-Bloch equation and proportional to $1/\beta^2$ in the relevant energy regime, as can be judged from figure 2.20. It can therefore be expected to observe large dE/dx for SMPs [138]. The passage of particles through matter and the resulting ionisation-energy losses are well understood [29, 139]. The main background in this study originates from muons. Since they are light compared to the SMP and thus travel close to the speed of light, the dE/dx can be used to discriminate between signal and background.

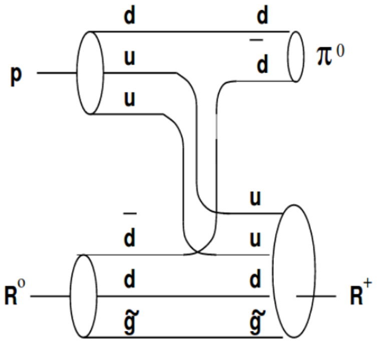

Figure 2.22: Conversion of an *R*-meson into an *R*-baryon. Figure taken from [128].

For HIPs the ionization energy losses are enormous and can even lead to the particle stopping in the detector creating unique signatures [140, 141].

Hadron-like SMPs In addition to Coulomb scattering and ionization energy losses, heavy *R*-hadrons can undergo scattering processes with nuclei resulting in parton exchange. The interaction probability of a specific parton with mass m_p and another parton in a nucleus is proportional to $1/m_p^2$ and consequently very low for the heavy supersymmetric parton considered here, which also carries most of the momentum. The majority of interactions are executed by the lighter SM constituents which are dragged along by the heavy sparton as shown exemplary in figure 2.21. Every time a parton looses some energy through scattering it is "replenished" from the vast energy carried by the massive constituent. The energy losses are thus determined by the kinetic energy of the parton cloud. A back-of-the-envelop calculation reveals that the energy scales which need to be considered are indeed low[24] [142].

By scattering off a nucleus an *R*-meson can convert into an *R*-baryon. A possible interaction is shown in figure 2.22 where a neutral *R*-meson exchanges one quark for two quarks from a proton resulting in a neutral pion and a charged *R*-baryon. The reverse of this process, however, is suppressed kinematically and by the absence of pions in the detector material [137]. It is therefore valid to assume most detectable *R*-hadrons to be of baryonic character. This is im-

[23] In a rigorous notation one would write $-dE/dx$ to describe the energy losses. However, the 'minus' sign is omitted here and throughout the remainder of this thesis

[24] Consider an *R*-hadron with an energy of 1.5 TeV and a mass of the heavy constituent of 1000 GeV. This gives the *R*-hadron a kinetic energy of 500 GeV and results in a Lorentz-factor of $\gamma = 1.5$. Assuming now further the remaining constituents are a u and a d quark yields a kinetic energy $E_{q\bar{q}} = m_{q\bar{q}}(\gamma - 1) \approx$ 0.3 GeV for the interacting system.

portant to consider since baryons carry the larger scattering cross sections. The present study is mainly interested in gluino, sbottom and stop R-hadrons. From the SM quark mass hierarchy it can be derived that the squark R-hadrons will predominantly end up in $\tilde{q}ud$ states. This results in a neutral sbottom R-hadron and a charged stop R-hadron. The present analysis can therefore be predicted to have a slightly larger sensitivity to stop based R-hadrons than to sbottom R-hadrons.

The experimentally most challenging feature of figure 2.22, however, is the change of electric charge of the R-hadron. While it was produced neutral and therefore invisible to the searches presented here, it becomes charged and visible at some point in the detector. A similar process is depicted in figure 2.23, where a gluino R-hadron scatters inelastically with a proton resulting in a change of the electric charge of the system from neutral to positive. Obviously the reverse of the reaction is possible as well and a formerly charged R-hadron performs a charge flip and becomes invisible, mimicking the signature of a decay to invisible particles in the detector. It can be estimated that charge-flip reactions contribute substantially to all interactions [128]. This can lead to peculiar R-hadron signatures in the detector with segmented tracks and (possibly several) changes of sign[25].

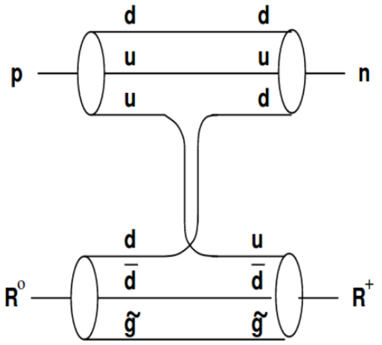

Figure 2.23: Inelastic scattering of an R-hadron resulting in a charge flip. Figure taken from [128].

Different models have been developed to correctly model the R-hadron behaviour in matter [137, 138, 145–147]. In this study two different models have been used: the generic and the Triple-Regge model.

The generic model assumes a flat geometric scattering cross section of 12 mb per light quark and a heavy spectator constituent. This is the pragmatic approach given the fundamental uncertainty regarding R-hadron interaction. For R-meson to R-baryon conversion processes phase-space factors are considered. The generic model predicts most R-baryons to be electrically charged. In this work, the generic model is used to describe the interaction of gluino R-hadrons within the detector. For this it is also necessary to specify the fraction of gluinos which hadronise into a $g\tilde{g}$-system. This fraction is referred to as the f-parameter.

The Triple-Regge model employs insights gained from low-energy hadron–hadron scatterings and estimates R-hadron interaction cross sections and energy losses from the Triple-Regge formalism [146]. Contrary to the generic model, this results in interaction rates depending on the Lorenz factor γ, as can be seen in figure 2.24, where the interaction cross sections of stop and gluino R-hadrons with a nucleon that is part of a nucleus consisting of an equal number of protons and neutrons, are plotted. The model was initially formulated for squark-based R-hadrons, but later extended to include gluino R-hadrons. It predicts a larger fraction of neutral R-hadrons than the generic interaction model. The Triple-Regge model is used in the present study to describe sbottom- and stop-based R-hadron interaction in the detector.

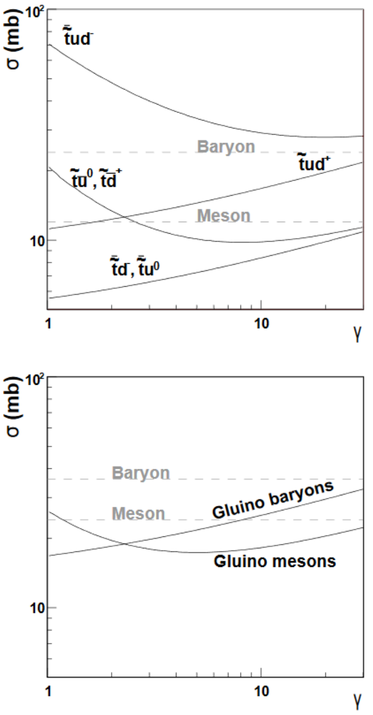

Figure 2.24: Cross sections for interactions of a stop (top) and gluino (bottom) R-hadron with a stationary nucleon for the Triple-Regge model (solid lines) and the generic model (dashed lines). Figure taken from [145].

[25] It has also been speculated about the observability of mesino-antimesino oscillations in which a neutral R-meson oscillates into its own antiparticle [143, 144]

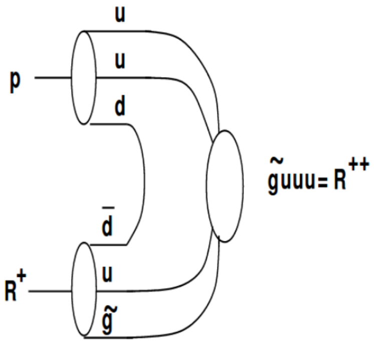

Figure 2.25: Formation of an R-hadron resonance. Figure taken from [128].

In principle it is also possible to form resonant R-hadron states as depicted in figure 2.25. Such processes are currently not implemented in any model and thus constitute a source for uncertainty on the interaction model. In [137] it is argued that the negligence of such possible resonances does not have a significant impact.

Because the energy lost through hadronic interactions is small, the passage of an SMP through a detector will not be accompanied by hadronic showers in the calorimeter systems. It follows that an SMP mimics the experimental signature of a muon, albeit with a much larger mass.

Because the interaction of R-hadrons in matter is highly uncertain, there exist also models predicting the SMP to loose almost all their momentum mainly though ionisation-energy losses and come to a stop within the detector. Such stopped particles can be found by detecting out-of-time decays. Such scenarios are not within the scope of the present work but are well covered by other analysis efforts [148–150].

2.7.2 Cosmological constraints on SMPs

A stable or quasi-stable[26] particle that is accessible to experiments at modern colliders would also have been produced during the Big Bang. If their quantity was large enough the particle would thus influence the cosmological evolution of the Universe. A quasi-SMP (qSMP) has implications on the era of nucleosynthesis. During that epoch the first light elements and isotopes like deuterium, helium-3, helium-4, etc. have been formed at a very specific ratio that can be measured today. A qSMP that decays during nucleosynthesis will affect those ratios[27]. Especially the ratio of deuterium and helium-3 has strong implications on the decay of the qSMP [153, 154].

Further constraints originate from observations on the cosmic microwave background (CMB). The decay of qSMPs injects highly energetic photons into the plasma which leads to characteristic spectral distortions that should be measurable today. The absence of such distortions allows for some conclusions on the mass of the qSMP [128, 155].

For an absolutely stable gluino it is possible to derive mass limits of a few TeV from the relict density [151].

In summary, cosmological constraints are present but weak in the mass and lifetime regime studied at present colliders.

2.7.3 Constraints from searches on SMPs

SMPs have been actively searched for in many different collider experiments. The following chapter gives a short overview over lower mass limits placed on SMPs prior to publication of results presented

[26] When speaking about cosmological timescales the usage of the label 'stable' can be tricky. Since constraints on absolute stable particles are different than those on metastable ones, the term quasi-stable is used here to avoid confusion with the regular definitions of SMP and mSMP.

[27] The decay releases energetic particles into the plasma which could lead to reactions like $p + {}^4\text{He} \rightarrow {}^3\text{He} + \text{D}$ increasing the abundance of deuterium in the Universe [151, 152].

here.

At LEP, searches for SMPs have been conducted by looking at high-momentum charged-particle tracks that are heavily ionising or produce no Cherenkov light because of their reduced velocity, whereas specific searches for neutral R-hadrons were based on topology constraints, missing energy and jets.

The $D0$ and CDF experiments at the Tevatron tagged candidates by performing time-of-flight measurements and detection of anomalous dE/dx of high-momentum tracks.

At the LHC the strategies have remained the same. While ATLAS and CMS rely on dE/dx and time-of-flight measurement, $LHCb$ employs mainly the response from Cherenkov detectors to distinguish SMPs from muons.

Long-lived sleptons Table 2.4 gives the lower mass limits on sleptons from LEP and LHC experiments.

experiment	machine	$\sqrt{s}$ [GeV]	comment	limit [GeV]	Ref.
ALEPH	LEP	184	$\tilde{\tau}_R$, $\tilde{\mu}_R$	$m_{\tilde{l}} > 81$	[156]
DELPHI	LEP	189	$\tilde{\tau}_R$, $\tilde{\mu}_R$	$m_{\tilde{l}} > 87.5$	[157]
L3	LEP	183	$\tilde{\tau}_R$, $\tilde{\mu}_R$	$m_{\tilde{l}} > 81.2$	[158]
OPAL	LEP	130-209	$\tilde{\tau}_R$, $\tilde{\mu}_R$	$m_{\tilde{l}} > 98$	[159]
ATLAS	LHC	8000	direct $\tilde{\tau}$ production	$m_{\tilde{\tau}} > 286$	[160]
ATLAS	LHC	8000	GMSB, $M = 250$ TeV, $N_5 = 3$, $\mu > 0$, $C_{grav} = 5000$, $\tan\beta = 10$	$m_{\tilde{\tau}} > 440$	[160]
ATLAS	LHC	8000	GMSB, $M = 250$ TeV, $N_5 = 3$, $\mu > 0$, $C_{grav} = 5000$, $\tan\beta = 50$	$m_{\tilde{\tau}} > 385$	[160] [160]
CMS	LHC	13000	long-lived $\tilde{\tau}$ from inclusive production	$m_{\tilde{\tau}} > 490$	[161]
CMS	LHC	13000	long-lived $\tilde{\tau}$ from direct pair production	$m_{\tilde{\tau}} > 240$	[161]
LHCb	LHC	7000-8000	long-lived $\tilde{\tau}$ in mGMSB	$m_{\tilde{\tau}} > 309$	[162]

Table 2.4: Summary of slepton lower mass limits prior to this study. The $D0$ collaboration did not quote any mass limits on long-lived staus but instead provide upper limits of $0.04 - 0.008$ pb on the cross section of scalar taus in the mass range $100 < m_{\tilde{\tau}} < 300$ GeV [163].

Measurements of the absolute decay width of the Z boson performed at LEP allow to rule out the low-mass region of $m_{\tilde{l}_R} < 40$ GeV. The limits quoted at LEP are furthermore independent of lepton flavour and are thus listed here for staus and smuons simultaneously. Limits on selectrons however differ at e^+e^- colliders because of the additional contribution from possible neutralino exchange.

Mass limits quoted at the LHC depend highly on the parameters of the benchmark models. As an example the ATLAS results are quoted in more detail to allow for an easier comparison with the results presented here. The limits by the CMS collaboration at $\sqrt{s} = 13$ TeV were published while the work on the present study was ongoing.

Long-lived squarks Table 2.5 lists the lower mass limits on squark masses from LEP, Tevatron and the LHC.

The most stringent lower limits on long-lived squarks were given by the CMS experiment in their analysis of $\sqrt{s} = 13$ TeV LHC data placing a lower limit on the top-squark mass of $m_{\tilde{t}} > 1.0$ TeV.

Table 2.5: Summary of squark lower mass limits prior to this study. Note that the limits at LEP experiments were derived for scenarios in which either the gluino or the top squark is the LSP.

experiment	machine	$\sqrt{s}$ [GeV]	comment	limit [GeV]	Ref.
ALEPH	LEP (e^+e^-)	88-209	$\tilde{g}$ and $\tilde{t}$ as LSP	$m_{\tilde{t}} > 95$ $m_{\tilde{b}} > 92$	[164]
DELPHI	LEP (e^+e^-)	189-208	purely $\tilde{g}_L$	$m_{\tilde{t}} > 90$ $m_{\tilde{b}} > 96$	[165]
CDF	Tevatron ($p\bar{p}$)	1960	stable $\tilde{t}$ squark	$m_{\tilde{t}} > 249$	[166]
ATLAS	LHC (pp)	8000	$\tilde{t}$ & $\tilde{b}$ R-hadrons	$m_{\tilde{t}} > 900$ $m_{\tilde{b}} > 845$	[160]
CMS	LHC (pp)	13000	$\tilde{t}$ R-hadrons	$m_{\tilde{t}} > 1000$	[161]

In the table only those limits which were derived for experimental signatures similar to this study have been listed. However, both ATLAS and CMS have also covered scenarios in which the SMP is either meta-stable and potentially decays after traversing the first layers of the detector [167–169], or is stopped in the detector and decays out-of-time up to many minutes after production [148, 170].

Long-lived gluinos Table 2.6 lists the lower mass limits on gluino masses derived from measurements at LEP and the LHC.

Table 2.6: Summary of gluino lower mass limits prior to this study. The CMS $\sqrt{s} = 13$ TeV results were interpreted in a cloud interaction model (CIM) and a charge-suppressed interaction model (CSIM) with different probabilities f of a gluon-gluino bound state.

experiment	machine	$\sqrt{s}$ [GeV]	comment	limit [GeV]	Ref.
ALEPH	LEP (e^+e^-)	88-209	$\tilde{g}$ is the LSP	$m_{\tilde{g}} > 26.9$	[164]
DELPHI	LEP (e^+e^-)	189-208		$m_{\tilde{g}} > 18$	[165]
ATLAS	LHC (pp)	8000	generic model	$m_{\tilde{g}} > 1270$	[160]
CMS	LHC (pp)	13000	CIM with $f = 0.1$	$m_{\tilde{g}} > 1610$	[161]
CMS	LHC (pp)	13000	CSIM with $f = 0.1$	$m_{\tilde{g}} > 1580$	[161]
CMS	LHC (pp)	13000	CIM with $f = 0.5$	$m_{\tilde{g}} > 1520$	[161]
CMS	LHC (pp)	13000	CSIM with $f = 0.5$	$m_{\tilde{g}} > 1540$	[161]

During the course of the present analysis the CMS collaboration placed the most stringent limits on the gluino mass at the time excluding masses of up to $m_{\tilde{g}} \leq 1610$ GeV. They supplied exclusion limits for two R-hadron interaction models: the cloud-interaction model (CIM), which corresponds to the generic interaction model and a charge-suppressed interaction model (CSIM), which corresponds to the Triple-Regge model as discussed in chapter 2.7.1.

The previously existing limit from ATLAS stems from an $\sqrt{s} = 8$ TeV analysis resulting in a lower gluino mass limit of $m_{\tilde{g}} > 1270$ GeV.

long-lived charginos The lower mass limits on long-lived charginos from LEP, Tevatron and the LHC prior to the present analysis are summarised in table 2.7.

The analysis of $\sqrt{s} = 8$ TeV data in ATLAS allowed to place a lower chargino mass limit of $m_{\tilde{\chi}^{\pm}} > 620$ GeV. CMS reported limits for chargino lifetimes of $3 < \tau_{\tilde{\chi}^{\pm}} < 100$ ns ranging between $100 < m_{\tilde{\chi}^{\pm}} < 800$ GeV.

Further searches Besides the searches listed above it is also possible to probe for SMPs outside the energy regime available at current

Table 2.7: Summary of chargino lower mass limits prior to this study.

experiment	machine	$\sqrt{s}$ [GeV]	comment	limit [GeV]	Ref.
DELPHI	LEP (e^+e^-)	189	$m_{\tilde{H}^\pm}/m_{\tilde{\nu}} > m_{\tilde{\chi}^\pm}$	$m_{\tilde{\chi}^\pm} > 93$	[171]
L3	LEP (e^+e^-)	189	CMSSM	$m_{\tilde{\chi}^\pm} > 76.8$	[172]
OPAL	LEP (e^+e^-)	130-209	$m_{\tilde{\nu}} > 500$ GeV	$m_{\tilde{\chi}^\pm} > 102$	[159]
D0	Tevatron ($p\bar{p}$)	1960		$m_{\tilde{\chi}^\pm} > 171$	[173]
ATLAS	LHC (pp)	8000	stable $\chi^\pm$	$m_{\tilde{\chi}^\pm} > 620$	[160]
CMS	LHC (pp)	8000	$\tau_{\tilde{\chi}^\pm} > 100$ ns	$m_{\tilde{\chi}^\pm} > 800$	[174]
			$\tau_{\tilde{\chi}^\pm} > 3$ ns	$m_{\tilde{\chi}^\pm} > 100$	

collider experiments. In most cases the SMP is required to have been produced during the Big Bang and is thus absolutely stable. Searches for new heavy stable particles trapped in matter have been performed via mass spectroscopy in water [175, 176], rare gases [177], lunar rocks [178, 179] and meteorites [180] allowing to reach masses beyond 10^8 GeV.

An extensive summary of non-collider SMP searches including cosmic-ray facilities and searches for macroscopic composite objects is given in [181]. No indications on the existence of absolutely stable massive particles have been found in any of the conducted studies[28]. However, the reach for metastable particles is extremely limited in such experiments.

2.8 Summary

The Standard Model of particle physics is a highly successful theory containing a finite set of 25 elementary particles[29] and describes their interactions through three of the four known fundamental forces of nature. Yet, the model is incomplete and physics beyond the Standard Model has to exist. One of those proposed expansions introduces a new fundamental symmetry between bosonic and fermionic particles called supersymmetry. It predicts the existence of supersymmetric partners for every Standard Model particle with the same properties except spin. Since no such particles have been found so far it can be assumed the symmetry is softly broken and the superpartner particles have masses considerably larger than their Standard Model partners. Depending on the parameters of the chosen supersymmetric model it is possible to create charged stable massive particles. Such massive particles would interact in the detector with the same signature as a much heavier copy of the muon. Colour-charged supersymmetric particles hadronise into R-hadrons. While the heavy constituent of the hadron can be treated as a spectator in most interactions with matter, the lighter particles are allowed to be interchanged resulting in charge-flip processes. Searches for stable massive particles have been carried out at most major energy-frontier collider experiments but have remained unsuccessful so far and stringent limits have been placed on their minimal masses.

---

[28] Some searches have reported the observation of exotic events in cosmic rays, however the results were never confirmed, e.g. [182].

[29] The number includes 8 gluons, 3 weak gauge bosons and the photon thus creating a symmetry of 12 fermions and 12 bosons plus one scalar Higgs boson.

CHAPTER 3

The ATLAS Experiment at the Large Hadron Collider

The LHC tunnel. Adapted from [183].

In the following chapter the experimental apparatus is introduced. Highly energetic proton–proton interactions are delivered to the experimental facilities by the Large Hadron Collider, which is described in chapter 3.1. For the present study the data recorded with the ATLAS detector is used. The detector, its relevant subdetectors, the working principle and the readout-system are described in chapter 3.2. Lastly, chapter 3.3 gives a very brief overview of the event data model and treatment of simulated collisions to make them correspond to experimental data as closely as possible.

3.1 The Large Hadron Collider (LHC)

The Large Hadron Collider (LHC) [184–186] is a proton–proton collider located just outside Geneva below the Franco–Swiss border operated by the European Organisation for Nuclear Research (CERN[1].). The machine occupies the same 27 km long tunnel which was previously housing CERN's Large Electron–Positron Collider (LEP) [187]. While the history of LHC can be traced back to 1984 [188], principle construction took place between 1998 and 2008, its physics programme starting in 2009. With a design collision energy in the center-of-mass frame of $\sqrt{s} = 14$ TeV[2] it is the most powerful particle accelerator built by mankind, leaving the previous record holder, Fermilab's TeVatron [190] with maximal energies of $\sqrt{s} = 1.96$ TeV in $p\bar{p}$-collisions, far behind. However, following a major electrical accident during initial commissioning [191], the beam energy has not been raised to design energy yet. Instead, data was taken at lower energies, as indicated in table 3.1. The data analysed for this study was taken in 2015 and 2016 at $\sqrt{s} = 13$ TeV.

In addition to its proton–proton physics program, LHC is also employed for special heavy-ion runs, in which lead-nuclei are accelerated and made to collide, in order to produce among others a quark–gluon plasma [192].

LHC has two separate beam pipes (see figure 3.1), which allow for beam crossings at four distinct points around the circumference to enable interactions of the beams. The four main experiments are

Year	$\sqrt{s}$
2009	≤ 7 TeV
2010-2011	7 TeV
2012	8 TeV
2015-2017	13 TeV

Table 3.1: LHC beam energies since begin of physics operation

[1] The acronym stems from "Conseil Européen pour la Recherche Nucléaire". The council was dissolved in 1954 to give rise to the organization but the acronym was kept

[2] In collider experiments the center-of-mass energy is given by the square root of the Mandelstam variable s, which is a measure of the incoming or outgoing particle four-momenta. An accessible motivation is given in [189]

located at those crossing points. They include two multi-purpose detectors ATLAS (A Toroidal LHC ApparatuS) [193] and CMS (Compact Muon Solenoid) [194], designed to cover the widest possible physics range. And further two specialised detectors ALICE (A Large Ion Collider Experiment) [195], focusing on heavy-ion physics, and LHCb (LHC-beauty) [196], an asymmetric experiment dedicated to measurements involving the b-quark. Furthermore, the experimental facilities are expanded by three smaller experiments sharing the experimental caverns with one of the major experiments: LHCf (LHC forward) [197] in the ATLAS cavern, TOTEM (TOTal Elastic and diffractive cross section Measurement) [198] sharing with CMS and MoEDAL (Monopole and Exotics Detector At the LHC) [199] with LHCb.

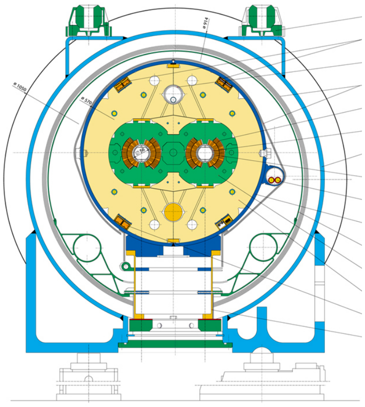

Figure 3.1: Cross section of an LHC dipole magnet. The two beam pipes surrounded by the superconducting coils and the cold mass can clearly be discerned. The figure was adapted from [200].

While lepton colliders like LHC's predecessor LEP provide clean measuring conditions to perform high-precision measurements of particle properties, this is not the case for a hadron collider. Since composite particles are being collided, we have a very incomplete understanding of the complex initial and final states of the collision. As a result experiments suffer from large measurement uncertainties. On the other hand, hadron colliders allow for a much larger discovery reach, due to the larger centre-of-mass energy. Such accelerators are therefore often referred to as 'discovery' machines. Metaphorically speaking, a hadron collider is the sledgehammer to probe for new physics, while lepton colliders are the scalpel, allowing a detailed dissection of the properties of new physics.[3] The physics agenda at the start of LHC has been extensive and included the investigation of the origin of particle mass, baryon asymmetry, dark matter and much more, with the possibility of discovering additional spatial dimensions or symmetries of nature still possible. Therefore, the experiments have to cover an immense physical spectrum and need to ensure sensitivity to as many proposed models as possible.

3.1.1 Luminosity and pileup

Besides the beam energy the most important quantity for a collider is its instantaneous luminosity L, since it provides a link between the cross section σ_P of some physical process P and the observed interaction rate $\frac{dn}{dt}$

$$\boxed{\frac{dn}{dt} = L \cdot \sigma_P} \quad . \tag{3.1}$$

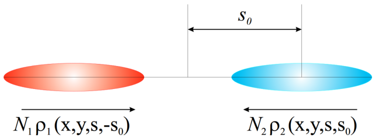

Figure 3.2: Two bunches with distribution functions ρ_i and number of protons per bunch N_i collide. s_0 is defined as the distance from the central collision point. Figure taken from [202].

The instantaneous luminosity itself depends on many different beam parameters. A generic approach to get an estimate for head-on pp collisions requires detailed knowledge about the distribution functions ρ_i of the proton bunches within the machine, as well as the number of protons N_i in bunches of both beams $i = 1, 2$ (figure 3.2). For the general approach of two identical, round beam-bunches with

[3] For completeness it can also be mentioned that various experiments exploit the best of both worlds, by performing lepton–hadron collisions in order to investigate the structure of the hadron. Such deep-inelastic-scattering experiments are for example carried out at HERA [201].

width R and $N_1 = N_2 = N_p$ [203], one can express the instantaneous luminosity with a simple relation

$$L = \frac{N_p^2 f N_b}{4\pi R^2} \tag{3.2}$$

where N_b is the number of colliding bunches and f the frequency of collisions. The LHC design goal was to reach an instantaneous luminosity of $1.0 \times 10^{34} \mathrm{cm}^{-2}\mathrm{s}^{-1}$. This goal was reached in June 2016 and later surpassed when LHC achieved an unprecedented instantaneous luminosity of $1.38 \cdot 10^{34} \mathrm{cm}^{-2}\mathrm{s}^{-1}$ [205].

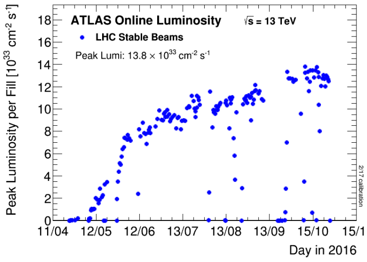

Figure 3.3: Instantaneous luminosities in ATLAS during 2016 *pp* data-taking. The figure was taken from [204].

Since the luminosity depends on quantities that are changing for different data-taking runs[4], also the luminosity is changing over time.

In figure 3.3 the peak instantaneous luminosities of the 2016 *pp* data runs measured in ATLAS are plotted. For machine protection, an intensity ramp-up is performed at the beginning of the year or after major maintenance breaks. This causes the sharp rise of intensity at the beginning of the year. The much slower, but nevertheless well discernible rise throughout the year is due to adjustments of beam properties to gain the largest possible intensity. Integrating the luminosities over time yields a measure for the actual amount of collected data. It is given in units of fb^{-1}. In 2015 LHC delivered an integrated luminosity of $\mathcal{L}_{2015} = \int L\,dt = 4.2\ \mathrm{fb}^{-1}$ to the ATLAS experiment, of which $3.2\ \mathrm{fb}^{-1}$ were deemed good for physics analysis. During the 2016 data-taking LHC delivered $\mathcal{L}_{2016} = 38.5\ \mathrm{fb}^{-1}$ to the ATLAS experiment of which $32.9\ \mathrm{fb}^{-1}$ are used for physics analysis. As an example figure 3.4 shows the accumulated integrated luminosity over the 2016 data-taking period.

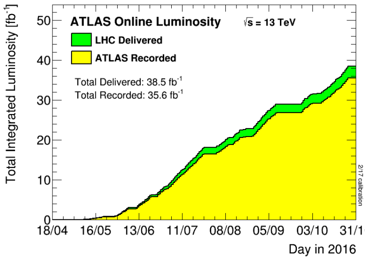

Figure 3.4: Integrated luminosity in ATLAS during 2016 *pp* data-taking. The figure was taken from [204].

However, while a large instantaneous luminosity increases the rate at which data is taken, a price has to be paid: since bunches of protons are collided, the probability of more than one proton-pair interaction increases. These additional interactions are called pile-up.

Over the 2015 and 2016 data-taking periods an average number of simultaneous collisions of $< \mu >= 23.7$ has been measured, with values ranging between 7 and 50 interactions. This is plotted in figure 3.5. The larger the number of simultaneous interactions, the more challenging the event topology for later analysis, as many interesting physical processes get drowned in additional detector activity caused by pileup.

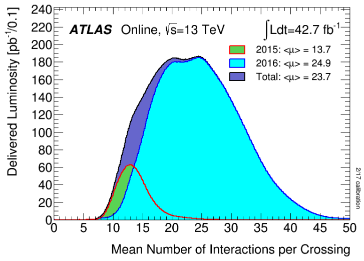

Figure 3.5: Pileup profile in ATLAS for the 2015 and 2016 data-taking periods. The figure was taken from [204].

3.1.2 Acceleration chain and filling scheme

As with all circular colliders, they cannot accelerate particles from rest, but require pre-acceleration. At the LHC protons have to pass through a whole chain of accelerators, each one more energetic (and larger) than its predecessor. Figure 3.6 gives a schematic representation of the LHC acceleration chain. Hydrogen gas is stripped of its electron in a duoplasmatron, before entering the first linear accelera-

[4] A data run usually refers to one fill of the LHC that lasts until the beam is dumped.

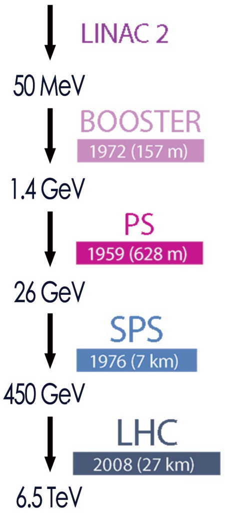

Figure 3.6: The LHC acceleration chain. Protons are accelerated in each machine, before being injected into LHC where they reach their final energy and are made to collide.

tor (LINAC). From there protons have to pass the Booster (PSB), the Proton Synchrotron (PS) and the Super Proton Synchrotron (SPS), gaining more and more energy at each step. Lastly, they are injected into the LHC. The proton bunches are accumulated and produced during the injection to the PS from the PSB [206, 207]. On arrival at the ATLAS cavern, they are heavily collimated with a transverse spread of about 15 μm and a length of 7 cm [203]. Every bunch contains 1.15×10^{11} protons [208].

With the revolution time of a proton bunch around the LHC ring of 88.924 μs and the nominal bunch spacing of 24.95 ns, this allows for a principal 3564 bunches in each beam. However, the filling scheme has to take various constraints into account: The beam-dump kicker requires a load gap to allow for the magnet rise time of around 3 μs. The injection kicker system limits in a two-fold way: first, as for the dump kickers, a gap is needed to allow for the rise time of the kicker magnets, which is given by 0.95 μs, and second, after the rise, the kicker is operated in flat-top mode, where it can remain for a maximum of 7.86 μs, giving a limit of how many bunches can be injected in one batch (also called 'bunch train'). Besides additional constraints imposed from the acceleration and injection chain, there are also experimental limitations. For example, LHCb requires offset collisions while during regular physics data-taking the number of pacman-bunches[5] are kept to a minimum to provide the necessary four-fold symmetry of the bunch structure. The initial filling scheme assumed 39 bunch trains coming from the SPS, each containing 72 proton bunches[6]. In between the trains larger spaces have to account for the rise time of the kicker magnets (mainly in SPS and LHC). This results in an effective maximum of 2808 bunches in the machine. The structure is concluded by the beam-dump gap of 119 consecutive empty bunches. For later identification, bunches are labelled continuously with the 1 being the first after the beam-dump gap [212]. An example for the LHC filling scheme is shown in figure 3.7.

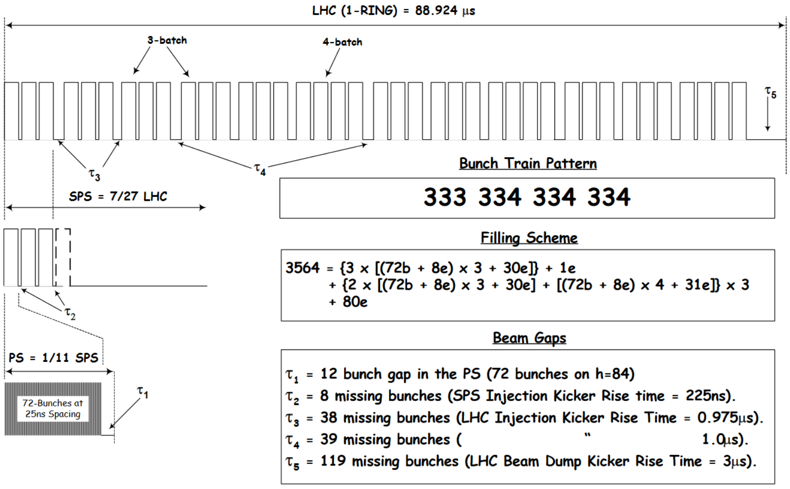

333 334 334 334

3564 = {3 x [(72b + 8e) x 3 + 30e]} + 1e
+ {2 x [(72b + 8e) x 3 + 30e] + [(72b + 8e) x 4 + 31e]} x 3
+ 80e

τ_1 = 12 bunch gap in the PS (72 bunches on h=84)
τ_2 = 8 missing bunches (SPS Injection Kicker Rise time = 225ns).
τ_3 = 38 missing bunches (LHC Injection Kicker Rise Time = 0.975µs).
τ_4 = 39 missing bunches (" 1.0µs).
τ_5 = 119 missing bunches (LHC Beam Dump Kicker Rise Time = 3µs).

Figure 3.7: Schematic representation of the LHC filling scheme with 25 ns bunch spacing. The bunch gaps τ_1 to τ_5 are marked in between the bunch trains and originate from magnet rise times in the PS (τ_1), the SPS (τ_2) and the LHC (τ_3,τ_4 and τ_5). The figure was taken from [212].

---

[5] Unpaired bunches in which a bunch of one beam encounters a bunch gap in the other beam at one or more collision points. See e.g. [209].

[6] It is possible to inject trains with 144, 288 or even up to 320 bunches [210]. However, to limit the heat load during injection and due to problems with the SPS beam dump only 72 and 96-bunch trains were used throughout most of 2015 and 2016 [211].

The acceleration is done in 16 radio-frequency (RF) cavities. To bend the beams to their circular trajectory 1232 NbTi superconducting dipole magnets, each 14.3 m long and weighing 35 tons, have been placed in the tunnel. They create a magnetic field of 8.33 T. To keep the quality of the beams 392 quadrupol magnets and additional higher-order multipol magnets have been installed. To ensure all magnets operate within their superconducting phase, the LHC is cooled to 1.9 K using 150 tons of liquid helium [213].

Table 3.2 summarises the basic machine properties of the LHC and contrasts the design values with the actual operational values during the 2015 and 2016 data-taking campaign.

	unit	design value	2015	2016
proton energy	GeV	7000	6500	6500
peak luminosity	$\mathrm{cm}^{-2}\mathrm{s}^{-1}$	1.0×10^{34}	0.5×10^{34}	1.38×10^{34}
protons per bunch		1.15×10^{11}	1.2×10^{11}	1.1×10^{11}
maximal number of bunches		2808	2244	2220
beam optics β^* in ATLAS	m	0.55	0.80	0.40
bunch spacing	ns	24.95	24.95	24.95
simultaneous collisions		23	13.7	24.9

Table 3.2: Summary of the basic characteristics of the LHC. Listed are both, the design values according to [184, 208, 214] and the values during machine operation in 2015 [215] and 2016 [216].

3.2 The ATLAS detector

The ATLAS detector [217, 218] is a multi-purpose particle detector optimised for high-precision measurements and searches for a broad spectrum of new particles. It is the largest of the four principal experiments at the LHC and has a cylindrical shape with a length of 44 m aligned along the beam axis and a diameter of 25 m. The weight of the detector can be estimated to be around 7000 tons.

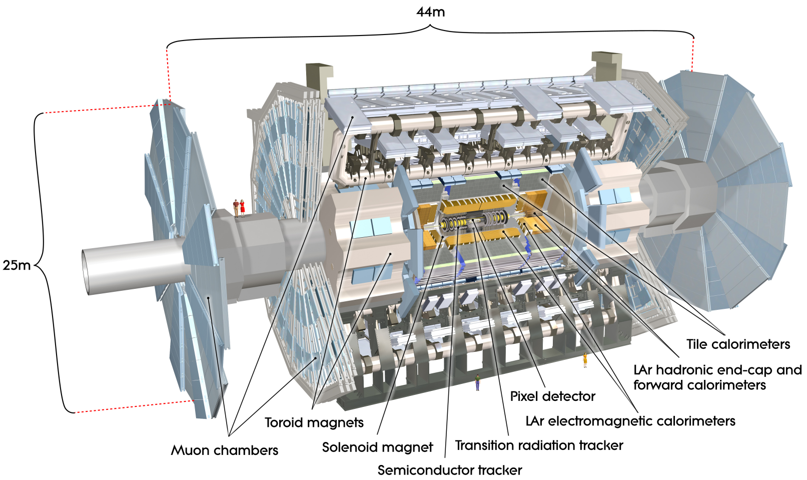
44m
25m
Tile calorimeters
LAr hadronic end-cap and forward calorimeters
Pixel detector
LAr electromagnetic calorimeters
Toroid magnets
Muon chambers
Solenoid magnet
Transition radiation tracker
Semiconductor tracker

Figure 3.8: Computer-generated representation of the ATLAS detector. The subdetectors and magnet systems are labelled. The figure was taken from [219].

ATLAS consists of concentric layers of subdetectors arranged around the primary interaction point (IP) at which the proton collisions occur. The detectors have different orientations depending on the position within the detector. In the central region (called the barrel), they are parallel to the beam pipe, while they are perpendicular in the forward region (end-caps). Figure 3.8 shows a computer-generated illustration of the full detector. Moving outward from the IP, particles will first traverse the Inner Detector (chapter 3.2.1), which consists of multiple tracking detectors for charged particles, next the electromagnetic and hadronic calorimeters (chapter 3.2.2) in which most particles get absorbed and their energy evaluated, and finally, if not stopped in the calorimeters, they reach the Muon Spectrometer (chapter 3.2.3). Before discussing the individual subdetectors in some detail, a few general aspects are mentioned.

The different subdetectors not only aim at measuring different properties of a traversing particle, but also at particle identification. Not all particles leave the same signature in all subdetectors, thereby allowing to identify a particle by combining its signal from all subdetectors. This is illustrated in figure 3.9. As e.g. a photon and an electron interact the same way in the electromagnetic calorimeter, they would be practically indistinguishable if we only had this detector information available. Through combination with the tracking detectors where an electron contrary to a photon leaves a track leading to the energy deposit, it is easy to tell them apart. The only known particles passing through the calorimeters are the muon, which leaves a distinct track in the muon spectrometer, and the neutrinos. Because of the small interaction cross section of neutrinos it is impossible to get a measurement in the detector. However, due to energy and momentum conservation it is usually possible to deduce their presence in an event as missing energy. It is not possible to distinguish light quarks or gluons in the detector. Because of their colour charge they

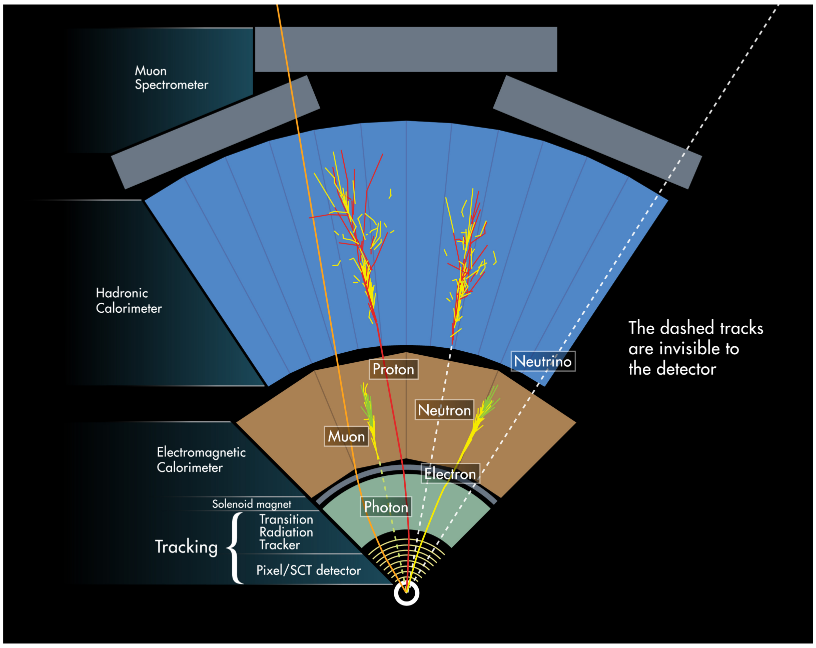

Figure 3.9: A slice of the ATLAS detector showing how different types of particles interact in the subdetectors. One note of caution, however, the schematic draws a rather unrealistic picture of interaction of hadrons in the detector. Contrary to the depicted they deposit a large fraction of their energy in the electromagnetic calorimeter as well. The figure was taken from [219].

immediately hadronise and form a string of coloured particles in between them, which manifests itself as a collimated spray of hadronic particles. This is called a jet.

In order to measure the momentum of charged particles, ATLAS measures the Lorentz-force-induced bending of particle tracks in the detector. This requires to submerge the tracking detector in a strong magnetic field. To achieve this, ATLAS has two superconducting magnet systems [220].

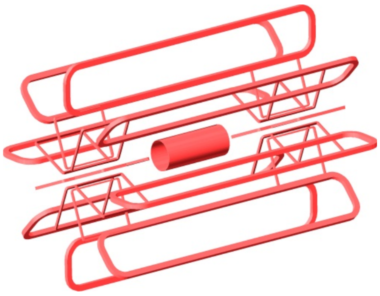

Figure 3.10: The ATLAS magnet system. The solenoid magnet in the middle is surrounded by 8 large toroids in the barrel and 8 more in each end-cap. The figure was taken from [221].

The inner tracking chambers are addressed by a superconducting solenoid magnet [222] which is housed in a cryostat between the Inner Detector and the electromagnetic calorimeter. It provides a nearly homogeneous magnetic field of 2.0 T throughout its center, with field-strengths up to 2.6 T directly on the windings. The second and much larger magnet system consists of eight air-core barrel toroid magnets[7], located within the Muon Spectrometer submerging it in a magnetic field of up to 3.9 T. In the end-caps two smaller air-core toroids reach field strengths of up to 4.1 T [223, 224]. The momentum of muons can therefore be measured twice, ensuring an excellent resolution for muon momenta spanning several orders of magnitude.

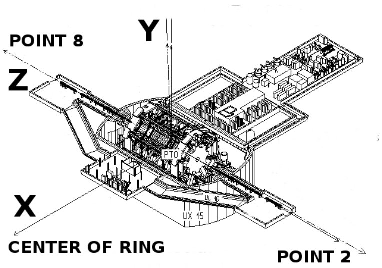

Figure 3.11: Positioning of the coordinate system at point 1 where the ATLAS detector is installed. The figure was adapted from [225].

The coordinate system used in ATLAS is a right-handed (x, y, z) coordinate system with its origin in the nominal interaction point in the center of the detector. The z-axis is aligned along the beam pipe, the y-axis is pointing upwards and the x-axis is therefore pointing towards the center of the ring (figure 3.11). Of a more practical use in data analysis is a spherical coordinate system with polar angle θ, azimuthal angle ϕ and radial distance r.

However, since θ is not invariant under boosts in z-direction, the approximately invariant quantity[8] pseudorapidity (see figure 3.12) is defined as

$$\eta = -\ln\left(\tan\left(\frac{\theta}{2}\right)\right) \quad . \tag{3.3}$$

While the momentum of the proton is known from the beam energy, it is impossible to quantify the exact longitudinal momentum carried by the parton taking part in the hard interaction. The momenta perpendicular to the beam axis, however, have to add up to zero. Thus, conservation of energy and momentum can only be applied in the transverse plane and it is prudent to work henceforth with transverse quantities. For the transverse momentum, for example, holds $p_T = p \cdot \sin\theta$.

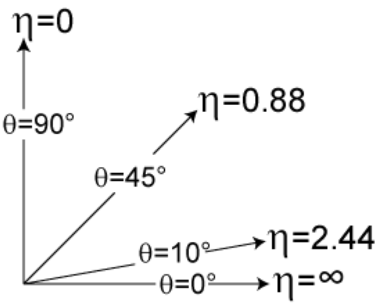

Figure 3.12: Pseudorapidity and its relation to the polar angle θ. $\eta = 0$ is perpendicular to the beam pipe which is located at $\eta \to \infty$. Figure taken from [226].

3.2.1 The Inner Detector

The ATLAS Inner Detector (ID) [227, 228] consists of three tracking detectors for high-precision tracking of charged particles with $p_T \gtrsim 0.4$ GeV in proximity to the IP [229]. It covers an acceptance range of $|\eta| < 2.5$. Charged particles passing through a tracking layer cause

[7] Hence the name 'A Toroidal LHC ApparatuS'

[8] It is only invariant for relativistic particles where the particle masses are much smaller than their momentum.

ionisation in the active cells and the created charges can be read out. This way a series of discrete points along the particle trajectory are formed. Those points are then fitted and basic properties of the particle deduced from it. The direction of bending in the magnetic field determines the charge, while the magnitude of bending is an estimator for the particle momentum. The ID has a cylindrical shape with a total length of 6.2 m and a radius of 1.15 m. The tracking efficiency for muons with $p_T = 5$ GeV is $> 98\%$ throughout the ID with the amount of dead material in the detector having little effect on the efficiency [230].

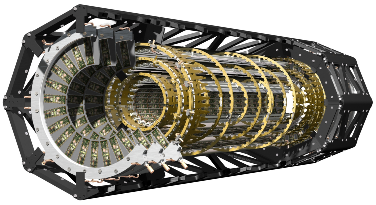

Figure 3.13: Schematic of the ATLAS Pixel Detector. Three layers of silicon-based detectors are mounted on the supporting structure drawn in golden colour. Not displayed is the IBL which was inserted in the centre of the detector. Figure taken from [219].

The innermost subdetector is the Pixel Detector [231]. A schematic illustration is given in figure 3.13. In its original design it consisted of three silicon-detector layers at radial distances of 50.5, 88.5 and 122.5 mm. The acceptance in η is expanded by three discs at each end of the barrel. It achieves a resolution in ϕ direction of 10 μm and 115 μm in z-direction. In order to judge whether a particle originates from the primary collision vertex or of a subsequent decay of a particle with a long lifetime (displaced vertex), it is essential to have an excellent vertex reconstruction capability. The installation of a smaller beam pipe within the detector allowed the Pixel Detector to be upgraded in May 2014 by an additional layer, the Insertable B-Layer (IBL) [232, 233] (see figure 3.14). The IBL delivers an additional measurement at only 33 mm radial distance from the IP, greatly improving the tracking performance [234]. All components have to be radiation hardened to withstand operation in the extreme environment close to the IP, where they are subject to doses exceeding 5×10^5 Gy [235], to ensure optimal performance throughout the detector lifetime.

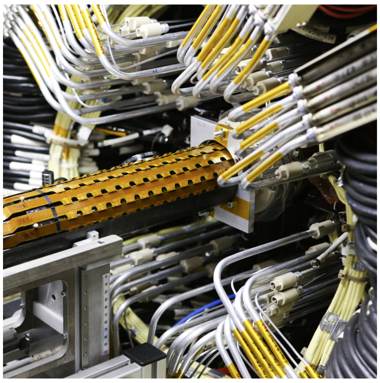

Figure 3.14: Installation of the Insertable B-Layer within the Pixel Detector. The figure was adapted from [219].

In this study, the Pixel Detector is employed for particle identification through measurement of its ionisation-energy losses. A minimum ionizing particle (MIP) generates ≈ 80 electron–hole pairs for every μm of detector material. The deposited charge is read out via a time-over-threshold method [236]. If more than 8.5 times the MIPs charge is deposited the pixel is saturated and the charge information is lost [237][9]. In most cases, however, the charge is deposited not in a single pixel, but within a cluster of several pixels. While the three layers of the original Pixel Detector have an 8-bit readout, the IBL offers only a 4-bit readout, resulting in a lower dynamic range and saturation at already 1.5 times the MIP charge. It is therefore equipped with an additional bit indicating that saturation of the pixel has occurred.

The Semiconductor Tracker (SCT) [238, 239] is another silicon-based detector that is composed of double-layers of micro-strips, which are mounted with a small stereo angle of 40 mrad in between them. The barrel consists of four cylinders at radii between 30.0 and 52.0 cm, the end-caps of 9 disks each. On average eight precision measurements can be expected for each track. The spatial resolution of the SCT in the $r - \phi$ plane is 16 μm and around 580 μm in z direction. In total there are 6.4 million readout channels in the SCT.

[9] The detector was calibrated to yield a time-over-threshold (ToT) count of 30 for a MIP traversing the nominal 250 μm of sensor material. An overflow corresponds to a ToT count of 255.

The outermost system of the ID is the Transition Radiation Tracker (TRT) [240]. It consists of 370 000 straws with lengths of up to 144 cm that detect transition radiation which is produced in polypropylene foils around the straws by a traversing relativistic particle. Each straw is 4 mm thick, filled with gas[10] and has a 30 μm gold-plated tungsten wire acting as anode in its center. The straws are read out on both ends and achieve a spatial resolution of 170 μm perpendicular to the straw direction. Along the direction of the straw (i.e. along z in the barrel and along r direction in the end-caps), no measurement can be made. On average 36 hits are expected for a traversing particle. The TRT allows a limited particle identification by exploiting the different strengths of transition radiation that depend on the velocity of the particle. It is therefore possible to distinguish between light electrons and charged hadrons. The TRT electronics contain a low-level discriminator for tracking and a high-level discriminator for the detection of transition radiation [241].

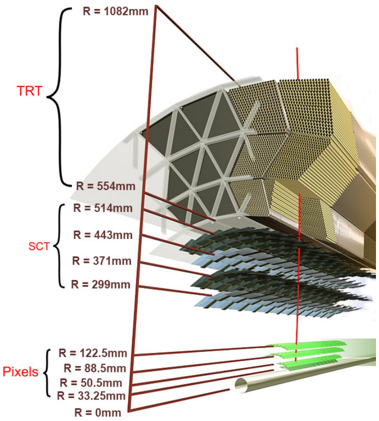

Figure 3.15: Schematic view of a barrel segment of the ID. The distances of the detector layers are marked. Figure adapted from [242].

3.2.2 Calorimeters

The purpose of the cylindrical ATLAS calorimeter system [243–245] is to measure the energy of a particle by analysing the particle shower it created. Since particles like electrons and photons interact predominantly electromagnetically, while hadrons interact also through the strong force, two different calorimeters are needed. First in line is the electromagnetic calorimeter, which is nested inside the larger hadronic calorimeter. Both are sampling calorimeters of the non-compensating type[11] and designed to have a large angular coverage to minimise the chance of particles escaping the detector outside its acceptance. This allows an excellent reconstruction of missing energy, which hints at the presence of neutrinos or other invisible particles in an event. A schematic view of the ATLAS calorimeter system is given in figure 3.16.

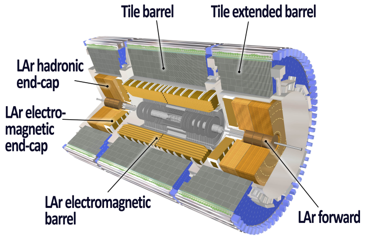

Figure 3.16: Schematic view of the calorimeter system and the position of calorimeters within the detector. The figure was adapted from [219].

In the dense passive layers of the electromagnetic (EM) calorimeter, charged particles are subject to bremsstrahlung, i.e. the emittance of a photon, while highly energetic photons on the other hand can undergo a pair creation process in the presence of a heavy nucleus. Since the two processes feed each other as depicted in figure 3.17a, an electromagnetic shower is formed which terminates only when the available energy is too small to keep it alive. The total charge produced in such a shower is proportional to the energy of the initial particle. It is measured from the active layers. The denser the passive material, the faster the shower forms and the smaller the necessary dimensions of the system.

The EM calorimeter consists of a barrel with acceptance range $|\eta| < 1.475$ and an end-cap on each side extending the pseudorapidity range to $1.375 < |\eta| < 3.2$. Liquid argon functions as the active material[12], while lead is used as the passive absorption material. To prevent 'dead towers' in the detector, its layers have an

[10] 70% Xe, 27% CO_2, 3% O_2, in some leaking straws the Xenon has been replaced by cheaper Argon.

[11] In a sampling calorimeter the layers of passive and active materials which create and detect the shower respectively, are placed alternatingly. A compensating calorimeter has an equally strong response for electromagnetic and hadronic particles of the same incident energy

[12] which is why the ATLAS electromagnetic calorimeter is sometimes only referred to as the "Liquid argon" or LAr.

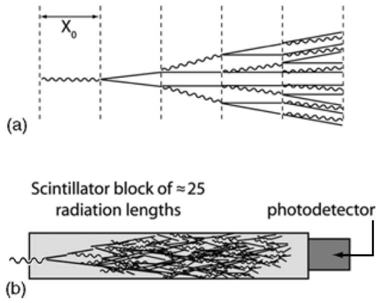

Figure 3.17: (a) shows the development of an electromagnetic shower with the definition of one radiation length. (b) shows how the shower from a photon is contained within one detector block of a fictional calorimeter tile. The figure was adapted from [246].

accordion shape (figure 3.18) with axial foldings in the barrel and radial foldings in the end-caps. The resolution varies with η and reaches a granularity of $\Delta\eta \times \Delta\phi = 0.025 \times 0.025$ in the barrel and $\Delta\eta \times \Delta\phi = 0.1 \times 0.1$ in the end-cap region. The three barrel layers of the EM calorimeter are at least 22 radiation lengths thick. In the end-cap region the thickness increases to 24 interaction lengths. Measured particle energies have to be corrected for losses experienced while the particle traversed the ID, the cryostat and the solenoid magnet before reaching the calorimeter. To aid this, a presampler was installed in the range $|\eta| < 1.8$. The design energy resolution of the EM calorimeter is given by

$$\frac{\sigma(E)}{E} = \frac{10\,\%\sqrt{\text{GeV}}}{\sqrt{E[\text{GeV}]}} \bigoplus 0.7\,\%\sqrt{\text{GeV}} \quad , \tag{3.4}$$

where the first term is called the stochastic term, the second one the constant term and the symbol '$\bigoplus$' denotes the quadratic sum. Measurements with test beams [193] and cosmic muons [247] have shown that the ATLAS EM calorimeter achieves this resolution.

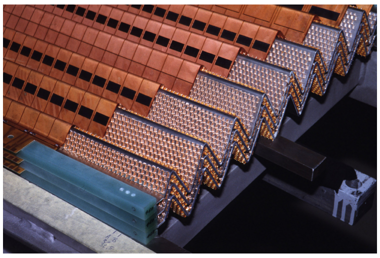

Figure 3.18: Section of the LAr electromagnetic calorimeter to reveal the accordion structure. Figure taken from [219].

In the hadronic calorimeter showers are created through strong interactions of the particle in the passive layers. While the mechanisms of shower formation are by nature more complicated than in the EM calorimeter, the working principle remains the same. The hadronic calorimeter has a granularity of $\Delta\eta \times \Delta\phi = 0.1 \times 0.1$ in the barrel which consists of a barrel segment with $|\eta| < 1.0$ and an extended barrel with $0.8 < |\eta| < 1.7$. Active layers of scintillating tiles are alternated with passive iron layers. In the end-cap region $1.5 < |\eta| < 3.2$ the hadronic end-cap calorimeter achieves a granularity of $\Delta\eta \times \Delta\phi = 0.2 \times 0.2$. Here again liquid argon is used with interjacent lead absorption layers. In the very forward region of $3.1 < |\eta| < 4.9$ the liquid argon forward calorimeter (FCal) consisting of concentric copper and tungsten tubes extends the coverage. The maximum thickness of the hadronic calorimeter are eleven interaction lengths, which is enough to prevent a punch-through into the Muon Spectrometer and contains all hadronic-shower end-products well within the calorimeter system, while only allowing muons, neutrinos and other hypothetical long-lived particles to pass.

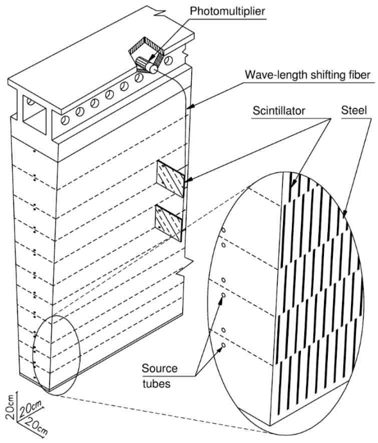

Figure 3.19: Schematic of a scintillating wedge of the barrel tile calorimeter. Figure taken from [248].

Measurements with pion test-beams have shown the energy resolution of the tile calorimeter is given by [193, 249]

$$\frac{\sigma(E)}{E} = \frac{(56.4 \pm 0.4)\,\%\sqrt{\text{GeV}}}{\sqrt{E[\text{GeV}]}} \bigoplus (5.5 \pm 0.1)\,\%\sqrt{\text{GeV}} \tag{3.5}$$

while the resolution

$$\frac{\sigma(E)}{E} = \frac{(70.6 \pm 1.5)\,\%\sqrt{\text{GeV}}}{\sqrt{E[\text{GeV}]}} \bigoplus (5.8 \pm 0.2)\,\%\sqrt{\text{GeV}} \tag{3.6}$$

is stated for the hadronic end-caps [250].

At a radial distance of up to 4.2 m the tile calorimeter provides a very good timing measurement. In this study it is used to perform time-of-flight measurements to calculate the propagation velocity of a traversing particle. One scintillating wedge containing many tiles is sketched in figure 3.19.

3.2.3 Muon Spectrometer

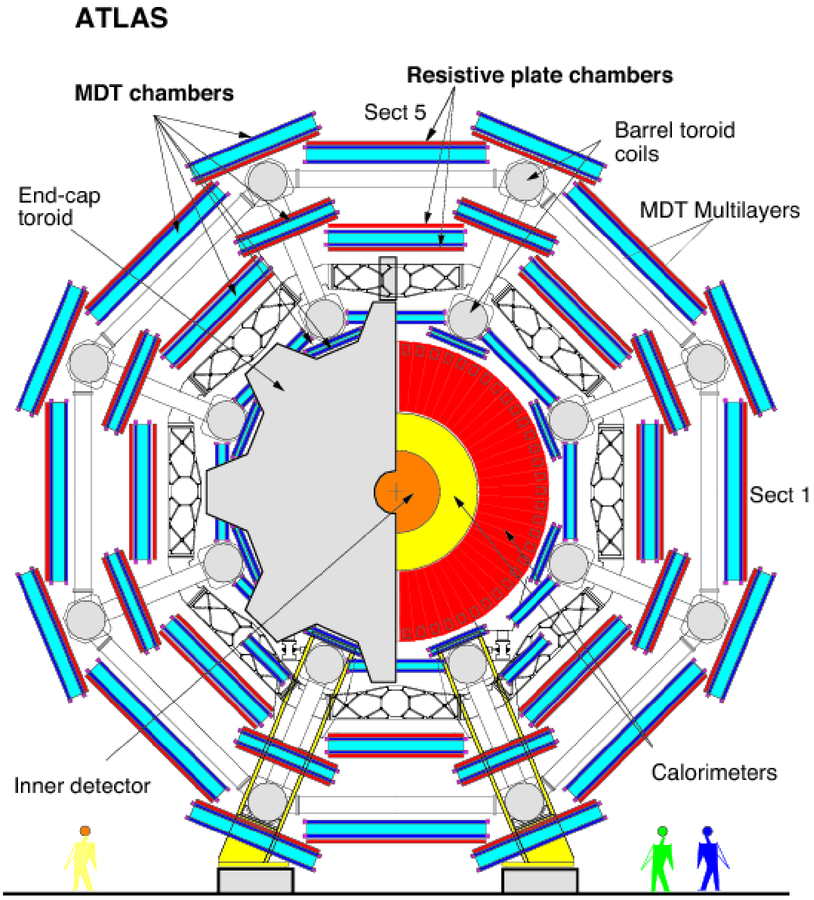
ATLAS
MDT chambers
Resistive plate chambers
Sect 5
Barrel toroid coils
End-cap toroid
MDT Multilayers
Sect 1
Inner detector
Calorimeters

Figure 3.20: Schematic representation of the ATLAS Muon Spectrometer in the x–y projection. Three layers of Monitored Drift Tubes are drawn in light blue, Resistive Plate Chambers are drawn in red. The chambers in the inner, middle and outer layers in the barrel of the detector are labelled BI, BM and BO. Those in the end-caps are called EI, EM and EO. There are sectors with large and short chambers. The magnet system is drawn in grey colour and shows the end-cap toroid and a cross-sectional view of the barrel toroid coils. The figure was taken from [251].

The outermost subdetector is the Muon Spectrometer (MS) [252]. Submerged into the magnetic field of the toroid magnets, the MS allows to accurately measure the momentum of muons with $3 < p_T < 1000$ GeV in the pseudorapidity range $|\eta| < 2.7$ [230]. The necessary size of the system determines the characteristic shape of the ATLAS detector. The MS has a twofold purpose: high-precision tracking of passing muons and delivery of a fast trigger signal for studies involving muons. To accommodate the two a variety of different technologies are employed in the MS. Monitored Drift Tubes (MDTs) are used for high-precision tracking. In the innermost layers of the end-caps where higher counting rates are expected they are complemented by Cathode Strip Chambers (CSCs). CSCs are multi-

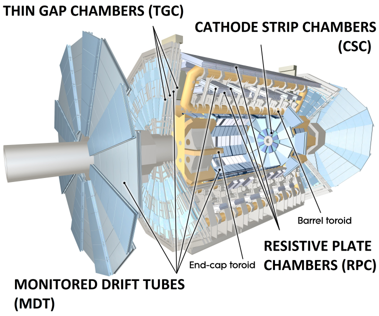
THIN GAP CHAMBERS (TGC)
CATHODE STRIP CHAMBERS (CSC)
Barrel toroid
RESISTIVE PLATE CHAMBERS (RPC)
End-cap toroid
MONITORED DRIFT TUBES (MDT)

Figure 3.21: Schematic view of the MS showing the position of the individual technologies within the detector. The figure was adapted from [219].

wire proportional chambers well suited for the forward region where they cover $2.0 < |\eta| < 2.7$. For triggering Resistive Plate Chambers (RPCs) are installed in the barrel of the detector where $|\eta| < 1.05$ and Thin Gap Chambers (TGCs) in the end-caps with $1.05 < |\eta| < 2.4$. Figures 3.20, 3.21 and 3.22 give an overview of the MS and the positions of each technology within the detector.

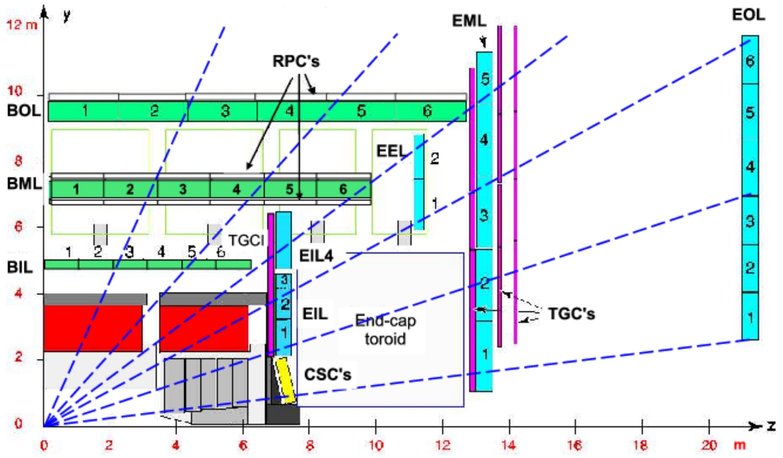

Figure 3.22: Profile of the ATLAS detector in the r–z projection at $\phi \approx \pi/2$. The MDT chambers in the barrel are drawn in green, those in the end-caps are shown in blue. RPCs are marked in black and found in the barrel, TGCs are drawn purple and exclusively in the end-caps of the detector. The CSCs are marked yellow. The figure was taken from [253].

Each MS station is named with three letters describing its exact position within the detector in terms of region, layer and sector. An overview of the station naming is given in table 3.3.

	Symbol	Meaning
Region	B	Barrel
	E	End-cap
Layer	E	Extra layer
	I	Inner layer
	M	Middle layer
	O	Outer layer
Sector	F	Feet region
	L	Large sector
	S	Small sector

Table 3.3: Overview of the naming of stations in the MS. Each station name consists of three letters describing the region, the layer (sometimes called super-layer) and the sector. A BIL station is thus located in a large sector of the inner layer in the barrel.

Since MDTs and RPCs are employed for time-of-flight measurements in the present study and require extensive calibration. A good understanding of the working principle of both detectors is required. In the following they are discussed in some depth.

Monitored drift tube (MDT) chambers Key element of the MDT chambers are the gas-filled[13] and pressurised aluminium drift tubes with a diameter of 29.970 mm and a length of up to 6 m. At the center of the tube a 50 μm gold-plated tungsten-rhenium wire acts as anode. The wire is held in position relative to the tube with an accuracy < 10 μm [193]. A passing particle ionises the gas and the free charges drift to the wire. Depending on the distance from the wire, drift times of up to 700 ns are possible. The radius of the drift-circle is thus determined by the arrival of the first charges from the track-segment closest to the wire, which is indicated as R_{min} in figure 3.23.

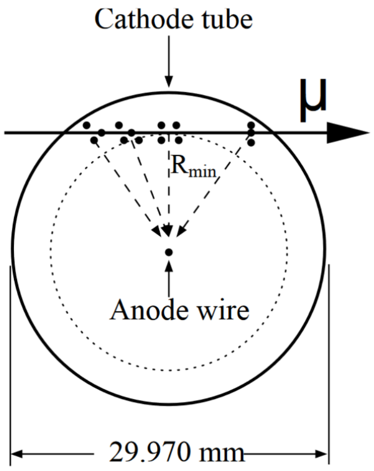

Figure 3.23: Cross section of a drift tube. Figure taken from [193]

Three layers of MDT chambers have been installed in the MS. Each chamber consists of two multilayers of drift tubes that are separated by a mechanical spacer (figure 3.24). In the middle and outer chambers, a multilayer is composed of three layers of drift tubes, while in the inner chambers, where the pattern-recognition performance needs to be highest, a fourth layer has been added. The space between the multilayers varies between chambers from 6.5 mm up to 317 mm. In total, there are 1150 MDT chambers, comprised of 354 000 tubes [254].

[13] The gas consists of 93% argon and 7% carbon dioxide

Since the reconstruction of the hit in the tube depends solely on the radius of the drift-circle around the wire, the precision of the measurement is to good approximation independent of the incidence angle of the traversing particle, which reaches values $> 45^\circ$ at the outermost edges of the barrel chambers. The resolution of a single tube is around $\approx 80\ \mu$m, for a multilayer $\approx 50\ \mu$m and for a whole chamber $\approx 35\ \mu$m [255].

The signal readout is done via a mezzanine card which is connected to up to 24 drift tubes by a signal distribution (hedgehog) board as depicted in figure 3.25. The whole MDT system is served by $\approx$ 15 000 mezzanine cards, every chamber containing up to 18 which are connected to the Chamber Service Module which acts as the local processor [257]. Knowledge about the chamber readout provides several 'natural' levels for timing corrections to act on.

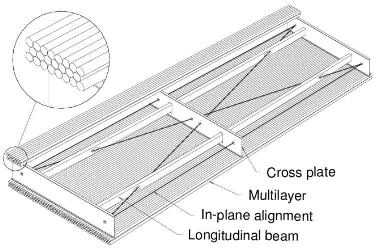
Cross plate
Multilayer
In-plane alignment
Longitudinal beam

Figure 3.24: MDT chamber with two multilayers consisting of three drift tube layers each. Figure taken from [256]

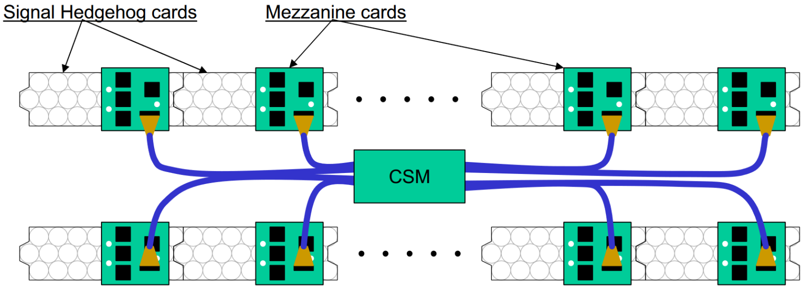
Signal Hedgehog cards
Mezzanine cards
CSM

Figure 3.25: 24 MDT tubes are read out via mezzanine cards mounted on the chambers. The chamber service module (CSM) serves up to 18 mezzanine cards. The figure was taken from [254].

Resistive Plate Chambers (RPC) The RPCs are part of the ATLAS trigger system and arranged in three layers as indicated in figure 3.26.

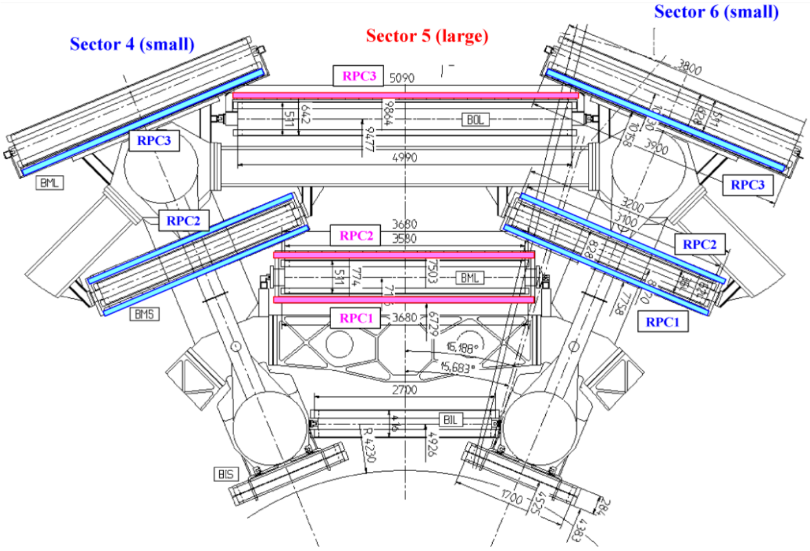
Sector 4 (small)
Sector 5 (large)
Sector 6 (small)
RPC3
RPC2
RPC1
RPC3
RPC2
RPC1
RPC3
RPC2
RPC1
BML
BMS
BIS
BOL
BML
BIL
5090
4990
3680
3580
3680
2700
3800
3900
3200
3100
15,188°
15,683°

Figure 3.26: Cross section through a standard barrel sector of the ATLAS detector showing the RPC chambers marked in colour. The inner and middle RPC layers (RPC1 and RPC2) are positioned below and above the middle MDT stations. The position of the third RPC layer varies depending whether the corresponding chamber is in a small (e.g. sector 4 and 6) or a large sector (e.g. sector 5). RPC chambers can thus be distinguished into short and long modules. The round structures are cross sections of the barrel toroid magnets. The figure was taken from [193].

A coincidence between the two inner chambers (RPC1 and RPC2) allows to select low-p_T muons in the range $6 - 9$ GeV, while the large lever arm of the third layer (RPC3) with one or two of the inner layers provides the trigger for high-p_T muons with $9 - 35$ GeV [258]. Every chamber consists of two independent detection layers where orthogonally placed strips measure the position in η and ϕ. Hence, the RPC system provides a nominal of six spatial position measurements for a muon passing through all three RPC layers[14].

The chambers consist of two rectangular resistive phenolic-melaminic plastic laminate plates that are held at a distance of 2 mm. The gap is filled with gas[15] at a voltage gradient of about 4.9 kV/mm. A passing particle causes an avalanche within the gas gap that can be read out through metallic strips that are attached to the outside and capacitively coupled to the plates. The orthogonally placed η and ϕ strips are 2.3 – 3.5 cm wide and up to 3.2 m long. For chambers with larger sizes the gas gaps are segmented and two units attached to each other as shown in figure 3.27. The same charge is thus read by both an η and a ϕ strip. In total there are about 3600 gas volumes and 370000 individual readout strips [259].

The internal logic of the RPC systems uses a 320 MHz clock as compared to the 40 MHz of proton collisions. This means every bunch crossing (BC) is divided into 8 separate ticks of an equal spacing of 3.125 ns at which the readout is happening [260]. The intrinsic timing granularity of the detector has to be considered during track reconstruction and calibration.

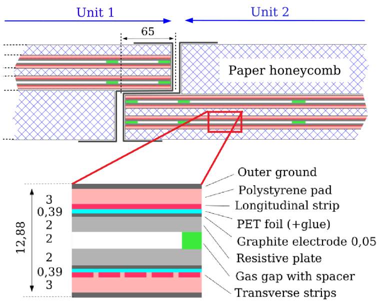
Unit 1
Unit 2
65
Paper honeycomb
3
0,39
2
2
2
0,39
3
12,88
Outer ground
Polystyrene pad
Longitudinal strip
PET foil (+glue)
Graphite electrode 0,05
Resistive plate
Gas gap with spacer
Transverse strips

Figure 3.27: Overlap region of two RPC units and how they are assembled together. Figure adapted from [261]

3.2.4 Trigger System

With a proton–proton interaction rate of 40 MHz delivered by the LHC, disk space and offline computing becomes a limiting factor. To reduce the data-taking rate to a more manageable ≈ 1 kHz, ATLAS uses a dedicated two-level trigger system [263]. The first stage is the hardware-based Level-1 (L1) trigger system [264, 265] that reduces the event rate to ≈ 100 kHz. Its key element is the Central Trigger Processor (CTP) which is fed by dedicated trigger hardware in the calorimeters (L1Calo) and MS (L1Muon), or from a new set of topological triggers (L1Topo). The latter allows to exploit kinematic and topological information of L1 objects like angular separation, invariant mass or sums of transverse masses. If an event satisfies the predefined selection criteria a 'Level-1 Accept' (L1A) is issued. The L1 takes around 2 μs before reaching a decision. To prevent the overlap of readout windows, the CTP applies a dead time[16] which was set to 100 ns during 2015 data-taking [266]. After the L1A is issued, the event information is temporarily stored in the Read-Out System, which hands over a Region-of-Interest (RoI) to the High Level Trigger (HLT), which incorporates the software-based trigger stages and constitutes the second trigger layer composed of the Level-2 trigger and the Event Filter.

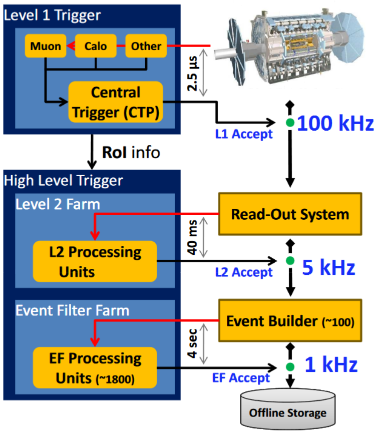
Level 1 Trigger
Muon
Calo
Other
Central Trigger (CTP)
2.5 μs
L1 Accept
100 kHz
RoI info
High Level Trigger
Level 2 Farm
L2 Processing Units
40 ms
Read-Out System
L2 Accept
5 kHz
Event Filter Farm
Event Builder (~100)
4 sec
EF Processing Units (~1800)
EF Accept
1 kHz
Offline Storage

Figure 3.28: Illustration of the ATLAS trigger system. Figure taken from [262].

The Level-2 trigger is using customised fast selection algorithms on partial event data in a RoI received from L1 which during Run 1 reduced the rate to a maximum of 5 – 6 kHz with processing times

[14] Depending on the layer this allows the trigger to use a 3-out-of-4 coincidence for low-p_T muons and a 1-out-of-2-OR for high-p_T ones [258].

[15] 94.7% $C_2H_2F_4$, 5% Iso-C_4H_{10}, 0.3% SF_6

[16] This is called a simple dead time. An additional complex dead time limits the number of L1As in a certain number of BCs to avoid an overflow of the front-end buffers.

averaging at 75 ms/event [267, 268].

The last stage is the Event Filter (EF), where algorithms are mostly following the offline object reconstruction on full granularity detector data in the RoI. The HLT is designed for an event output rate of 1000 Hz (400 Hz during Run 1). The processing time of a single event is of the order ≈ 1 s. A schematic illustration of the ATLAS trigger system is given in figure 3.28.

The selection algorithms take a threshold value (typically the transverse momentum of a detector object) as an input. The trigger rate can be controlled by either adjusting the threshold value, or prescaling the trigger chain, i.e. limiting the number of events read out even if the trigger issued an accept[17]. If the trigger rate is too high, the HLT computing farm is not able to keep up with the stream of incoming events and some will be lost. It is therefore crucial to limit the rate to the read-out and computing capabilities.

3.3 Event data and simulation

The data that is read out from the ATLAS detector is not yet ready for analysis. It undergoes a multi-staged process of reconstruction transforming the raw data content into analysable physical-object collections, ultimately reducing the disk size of a single event. The ATLAS event data model during LHC Run 2 is depicted in figure 3.29. An innovation for Run 2 is the introduction of the derivation stage. The Analysis Object Data (xAOD) is undergoing an analysis-specific reduction. The thus produced derivations or derived xAOD (DxAOD) contain only the information relevant for a specific analysis (or group of related analyses) resulting in much faster processing times and reduced disk space storage [269]. More details about the ATLAS event-data model can be found in [270].

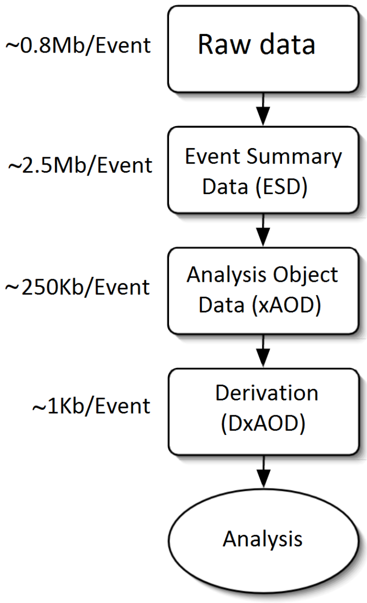

Figure 3.29: Sketch of the event data model in ATLAS. Figure adapted from [271]. The disk sizes per event have been extracted from [272].

In order to get a physically meaningful result of a hypothesised new particle signal over background, the measurement is compared with the expected background and its deviation assessed. Thus, it is necessary to have an excellent understanding of how complicated final states would look like in the complex machinery that is the particle detector. An analytical treatment of such a process is virtually impossible. Instead, irreducible backgrounds and desired signals are simulated by elaborate software packages. Since the accuracy of their predictions have a direct impact on the quality of the analysis, an extensive amount of work is invested into maintenance and development of such event generators and detector simulation packages. A variety of generators are currently available, each yielding slightly different results as they use different approximations and models. To a certain degree the result of an analysis always depends on the choice of event generator used [273][18]. Usually the differences between generators are accounted for by estimating a systematic uncertainty on the MC modelling.

The simulated event is then passed through a detailed and constantly refined simulation of the detector to mimic its response to the simulated final states. This requires to take dead material and detector inefficiencies into account. Because of the complexity of the process huge computing clusters are required as the full detector simulation of one event requires up to about 20 minutes [275]. Several millions of events are required for a typical analysis.

---

[17] A trigger with prescale 10 will on average only accept one in ten events in which the trigger has fired.

[18] Some of the most common generators are listed in [274] along with comparisons and explanations about their working principle.

Finally, the simulated samples are overlaid by several minimum-bias[19] collisions to mimic the influence of pile-up and underlying event[20]. The pile-up distribution in data (figure 3.5) determines how many collisions are overlaid.

3.4 Summary

The Large Hadron Collider is a proton–proton collider which delivers collisions at $\sqrt{s} = 13$ TeV every 25 ns to the experiments. During operation in 2015 and 2016 the machine has delivered data corresponding to around 36.1 fb^{-1} to the ATLAS experiment that were deemed good for physics analysis. On average 23.7 individual proton–proton interactions have taken place during every event in the dataset.

The ATLAS detector consists of several concentric subdetectors nested inside each other and focused around the primary interaction point. The first subdetector is composed of several tracking chambers which track the position of charged particles to determine the sign of their charge and their momentum via the Lorentz-force induced bending of the particle track in the external magnetic field of the solenoid magnet. The Pixel Detector, which is the innermost detector, can be used to measure the ionisation-energy losses of a traversing particle. In the electromagnetic and hadronic calorimeter particles are stopped and their energy is measured. The intrinsically good timing resolution of the hadronic Tile calorimeter allows to employ it for time-of-flight measurements for charged stable massive particle identification. Lastly, muons and neutrinos penetrate the calorimeters and reach the Muon Spectrometer where muons are tracked inside a toroidal magnetic field. Monitored drift tubes and resistive plate chambers exhibit good timing resolutions suitable for time-of-flight measurements. Neutrinos are the only known particles to leave the detector without being detected.

To trigger events, ATLAS employs a two-stage trigger system that reduces the 40 MHz collision rate to a mere 1 kHz for storage.

[19] Inelastic collision events which are selected with as little bias as possible.

[20] Interaction of additional partons of the same proton undergoing the hard scattering and beam remnants.

CHAPTER 4

Timing calibration of the ATLAS Muon Spectrometer

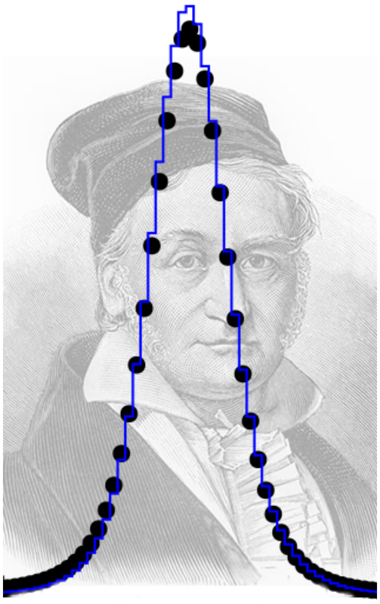

Figure adapted from [276]

The Monitored Drift Tubes (MDTs) and Resistive-Plate Chambers (RPCs) have sufficiently good timing resolution to allow to determine the propagation speed of a particle through precision time-of-flight measurements and discriminate between highly-relativistic SM particles and SMPs propagating considerably slower due to their large mass[1]. In order to maximise the sensitivity it is necessary to perform a multi-stage timing calibration of both systems. This includes individual corrections for every detector element, as well as the correction of time-dependent overall phase-shift variations and online-timing changes. The ATLAS Muon Spectrometer, including MDT and RPC systems, is described in detail in chapter 3.2.3. Since the timing is not well modelled in simulation, it is further necessary to establish a strategy for the treatment of MC to match the timing information in data.

4.1 Uncalibrated data

The calibration is done using the full 2015 and 2016 datasets corresponding to an integrated luminosity of 36.1 fb^{-1}. The SUSY8 data format defined in appendix A is used, where events are selected by requiring either an E_T^{miss}, single-muon, di-muon or E_T^{miss}+jet trigger. All events are required to pass a good-runs-list (GRL) selection, which rejects luminosity blocks[2] during which individual components of the detector were not fully operational and are thus considered bad for physics. Further, an event cleaning is applied in which individual events which are plagued by some detector problem[3] in one or more of the subsystems are likewise rejected.

The calibration relies on hit information from muons. This information is only written into xAOD data files for muons which were reconstructed using the MuGirlStau algorithm (see chapter 5.2). In order to ensure there is no possible signal contamination or low-β tracks caused by detector noise in the calibration dataset, all MuGirlStau muons are $\Delta R = \sqrt{\Delta\eta^2 + \Delta\phi^2}$ matched to a muon reconstructed with any other reconstruction algorithm that assumes the particle to be propagating with the speed of light. The matching is successful for more than 99.7% of the MuGirlStau muons. All

[1] TGCs have an intrinsic resolution that rivals the RPC system, however, the timing is lost after the trigger decision since only the BC information is passed on. It is thus not possible to use TGCs for time-of-flight measurements. CSC's are located outside the pseudorapidity range relevant for analysis.

[2] One luminosity blocks typically consists of $1-2$ minutes of data-taking and contains thousands of recorded events.

[3] This could be for example if the event was not properly recorded after a partial restart of the detector

muons used possess reconstructed tracks in the MS and the ID. Because of the online p_T threshold of the MuGirlStau algorithm the selected muons have $p_T^{\text{online}} > 60$ GeV[4] in the first 14 fb^{-1} of data, while the cut was lowered to $p_T^{\text{online}} > 30$ GeV for the remainder of data taking. In addition a cut of 20 GeV is applied on the offline transverse momentum. The p_T distribution of muons used for calibration is depicted in figure 4.1. In total, the calibration uses timing information from $\approx 1.86 \times 10^8$ muons.

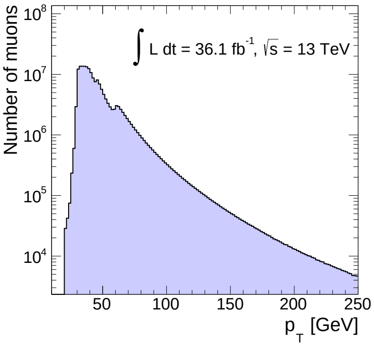

Figure 4.1: Transverse momentum of muons used for calibration. The bump at $\approx$ 60 GeV is caused by the changed online p_T threshold.

4.1.1 Uncalibrated timing distributions

The time-of-flight (ToF) is measured with respect to the ATLAS clock, where the nominal proton–proton interaction is defined to occur at $t = 0$. After the successful reconstruction of a muon, the track fit determines the precise position of a hit within a drift tube or on a readout strip. The ToF of a speed-of-light particle from the IP to the reconstructed hit can be calculated and is denoted by t_c. The relation

$$\text{ToF} = t_0 + t_c = t_0 + \frac{d}{c} \tag{4.1}$$

holds for all particles regardless of their velocity. Here, t_0 can be interpreted as the delay of a particle with respect to a speed-of-light particle and is the quantity that is measured in the detector, d is the distance of the hit from the IP and c the speed of light. The ToF distributions in the MDT and RPC system are drawn in figure 4.2.

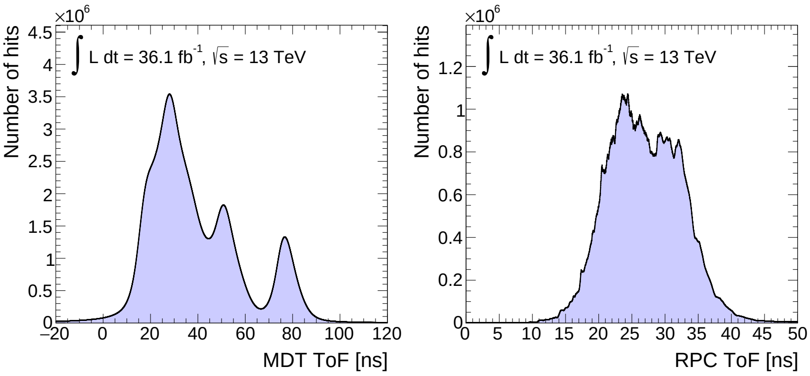

Figure 4.2: The uncalibrated ToF distributions are drawn for MDTs (left) and RPCs (right). In the MDT distribution the three end-cap layers are clearly visible as three distinct peaks in the timing distribution. The three barrel layers are merged into the first peak, while the two outer layers in the MS end-caps show as two separate peaks. Since the RPC system is only installed in the central part of the detector the spread is smaller for RPCs.

For speed-of-light particles t_0 describes the measurement resolution and potentially contains systematic effects. In a perfectly calibrated detector, the calculated t_0 values should be distributed according to a Gaussian function around $t_0 = 0$. Figure 4.3 shows the uncalibrated t_0 distributions for MDTs and RPCs.

While the MDT t_0 distribution looks close to expectation with the mean slightly shifted towards larger values, the expected Gaussian shape is absent from the RPC t_0 distribution. This is largely due to the functionality of the detector itself. The timing granularity of

---

[4] The online p_T is calculated before the reconstruction of the muon and relies only on a very crude geometrical momentum estimation. It is therefore possible to nevertheless get a small fraction of muons with offline p_T below the threshold.

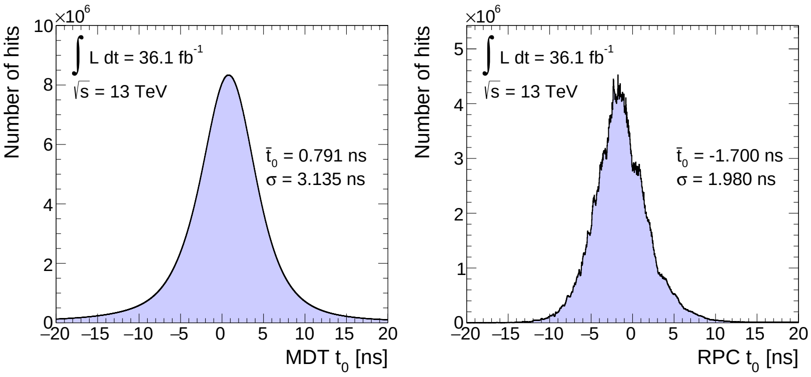

Figure 4.3: The uncalibrated t_0 distributions are drawn for MDTs (left) and RPCs (right). Mean t_0 (denoted by a bar above the symbol: $\bar{t_0}$) and standard deviation σ of a Gaussian functional parameterisation to the data are given. The roughness of the RPC distribution originates from the timing granularity of the detector.

3.125 ns results in discrete values for every readout strip that then get smeared out by the propagation time, i.e. the time the charges take to arrive at the readout electronics from the point of creation on the strip[5]. Since not all strips have the same intrinsic calibration or resolution, the features in figure 4.3 emerge.

Because η and ϕ strips of the RPC system possess individual readout electronics with possibly different delays through optical links or cable lengths, it is useful to treat them as two separate systems that require slightly different calibration constants. Figure 4.4 shows the uncalibrated t_0 distributions for RPC η and ϕ strips separately. The differences in shape confirm the approach of a separate treatment.

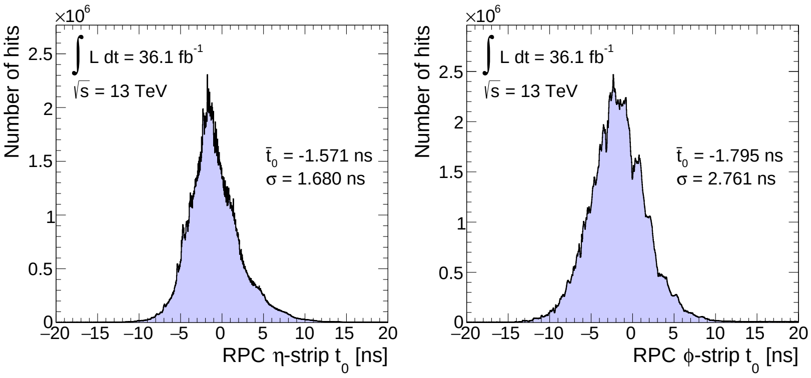

Figure 4.4: The uncalibrated t_0 distributions separately for RPC η strips (left) and RPC ϕ strips (right). Mean $\bar{t}_0$ and standard deviation σ of a Gaussian functional parameterisation to the data are given. The differences in the shape of the distribution suggest that η and ϕ strips need to be treated individually during calibration.

4.1.2 Uncalibrated β distributions

The measured ToF and reconstructed distance[6] from the IP of a hit i can be used to calculate the velocity of the passing particle via the simple relation

$$\boxed{\beta_i = \frac{d_i}{c \cdot \text{ToF}}} \quad . \tag{4.2}$$

Since the MDTs deliver an average of 20 hits per muon and the RPC system gives a nominal of 12 hits, the β measurements are combined system-wise into a weighted average according to[7]

---

[5] Typical propagation velocities are 0.208 m/ns [277, 278], which results in propagation times of up to several nanoseconds.

[6] The distance is always taken to be a straight line. The true track of a particle is of course bend due to the magnetic fields, however at the large momenta considered here the bending is minimal and the error is negligible.

$$\beta^{-1} = \frac{\sum_{i=1}^{N} \beta_i^{-1}/\sigma^2_{\beta_i^{-1}}}{\sum_{i=1}^{N} 1/\sigma^2_{\beta_i^{-1}}} \quad , \tag{4.3}$$

where $\sigma_{\beta_i^{-1}}$ is the uncertainty on the individual $1/\beta$ measurement β_i^{-1} of hit i. The uncertainty on the weighted β^{-1} is given by

$$\sigma^2_{\beta^{-1}} = \frac{1}{\sum_{i=1}^{N} 1/\sigma^2_{\beta_i^{-1}}} \quad . \tag{4.4}$$

The uncalibrated β distributions are drawn in figure 4.5. Since the uncertainty $\sigma_{\beta_i^{-1}}$ is unknown at this stage, all β_i^{-1} receive the same weight for the calculation of the weighted average.

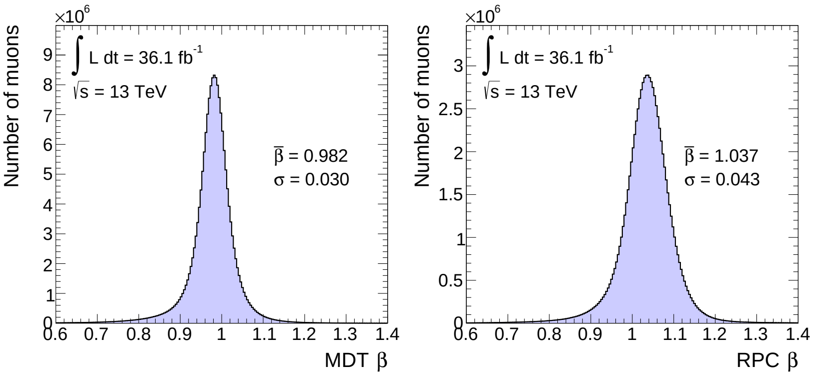

Figure 4.5: Uncalibrated β distributions for MDTs (left) and RPCs (right). As could have already been judged from the t_0 distributions in figure 4.3, the MDT β is a sharp Gaussian peak shifted towards $\beta < 1$. The RPC β distribution is much broader when compared to the MDT distribution and shifted towards $\beta > 1$. The mean $\bar{\beta}$ and standard deviation σ of a Gaussian functional parameterisation to the data are printed in the plots.

It is the goal of the calibration to get the β distributions as sharp as possible and centred around $\beta = 1$.

4.1.3 RPC-timing bug

During the initial review of timing distributions, an anomalous shape in the RPC distributions has been observed. The t_0 distributions exhibit a strong asymmetric tail towards negative values. Such an initial distribution is shown in figure 4.6. Further investigations revealed a strong correlation between the reconstructed z-position of the hit and its measured t_0, as depicted in figure 4.7. Searches for the origin of the observed features within the MuGirlStau algorithm were carried out by Massimiliano Bellomo. It was found that for RPC hits the distance of the hit to the IP was erroneously calculated in the transverse plane only, neglecting the hit displacement along the z-axis.

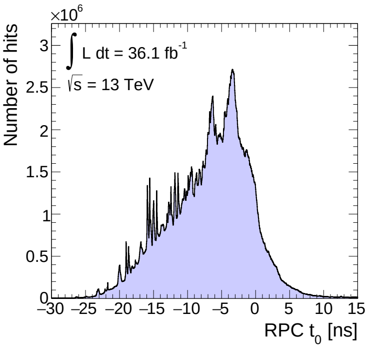

Figure 4.6: RPC t_0 distribution including a bug in the calculation resulting in long asymmetric tails.

Since this also affects the reconstruction of muons, the impact on this analysis is two-fold.

---

[7] The inverse of β is considered for the weighting as the quantity is directly proportional to the measured ToF. However, it would also be feasible to do the weighted combination with β directly.

First, all calculations of d need to account for the missing z component when determining t_0. The solution is trivial and corrects the bug completely with no further corrections being necessary.

Second, the wrong calculation of the ToF during reconstruction could lead to a reduced efficiency of the MuGirlStau algorithm for signal. This hypothesis was checked by comparing the efficiencies for simulated stable $\tilde{\tau}$ signal[8] with and without the bug. It was found that the bug reduces the sensitivity by about 1.5% in the barrel region of the detector. Since the effect is marginal, no computing-intensive reprocessing of all data has been conducted.

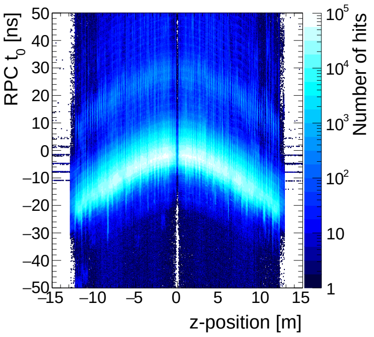

Figure 4.7: RPC t_0 with timing bug as function of the z coordinate.

4.2 RPC online-timing correction

Since the RPCs are part of the trigger system, their timing is evaluated scrupulously. The readout window of an RPC signal is 8 BCs long. With the intrinsic timing granularity of the detector, this translates into 64 readout ticks, where the trigger BC is defined from tick 26 to 33 [279]. The readout is done via coincidence matrices (CMs) that allow the application of delays to the signal. It is possible for a CM to be centred in the wrong BC. In such a case the CM delay is adjusted in between LHC runs to centre the timing distribution to tick 29. The online-timing adjustments applied to a CM and therefore to a number of readout strips can be several BCs large and consequently strongly non-negligible. However, the specific changes applied to a CM are not well documented and a retracing of the applied changes therefore difficult. Since a change of > 1 BC in timing results in prominent double-peak structures in the t_0 distributions, a strip which has received such a correction can be identified and rejected for β measurements. This is described in more detail in chapter 4.4.

In addition to corrections on individual CMs a global timing adjustment can be applied. This was done at the beginning of datataking in 2015 and 2016, as well as four more times during 2016. As a consequence the RPC timing information is split up into six periods. For each period the t_0 distributions are evaluated. The mean of a Gaussian functional parameterisation to the peak of the data can be used as a correction constant for this period. Table 4.1 lists the six periods, the corresponding integrated luminosities and the derived calibration constants $\Delta t_0^{\text{online}}$.

Period	$\int L\,dt$	$\Delta t_0^{\text{online}}$
1	3.2 fb^{-1}	-0.008
2	$<$ 0.1 fb^{-1}	-0.302
3	0.3 fb^{-1}	-1.438
4	3.4 fb^{-1}	-1.603
5	10.1 fb^{-1}	-1.619
6	19.1 fb^{-1}	-1.611

Table 4.1: The data was split up into six periods with constant global online calibration. Listed are the calibration constants $\Delta t_0^{\text{online}}$ for each period alongside the corresponding integrated luminosities.

All periods are shifted from $t_0 = 0$ and approach a central value of $t_0 \approx -1.60$ ns. This shift is most likely caused by the different level of detector information exploited in the online and offline calibrations. While reconstructed MuGirlStau muons are used here, the online-timing calibration relies on L1 trigger hit information where no muon reconstruction is run. Since periods 4 to 6 contain most of the data and exhibit very similar online-calibration, the online-timing correction mainly corrects the shift between online and offline calibration and controls minor asymmetries introduced by the data in

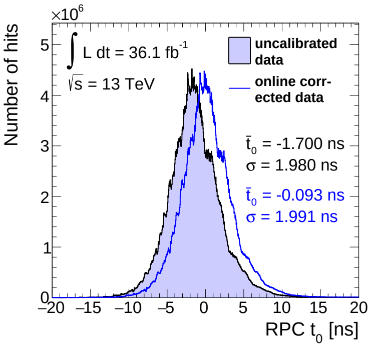

Figure 4.8: RPC t_0 distribution before and after online-timing correction.

---

[8] A detailed description of the simulated signal samples used for the test is given in chapter 5.1

period 1, which corresponds to the 2015 data. The effect of the correction on the overall t_0 distribution can be seen in figure 4.8.

Figure 4.9 shows the t_0 distributions normalised to unity for all periods before and after the online-timing correction was run. After application timing distributions of all periods are centred around the same common value of $t_0 = 0$ as expected.

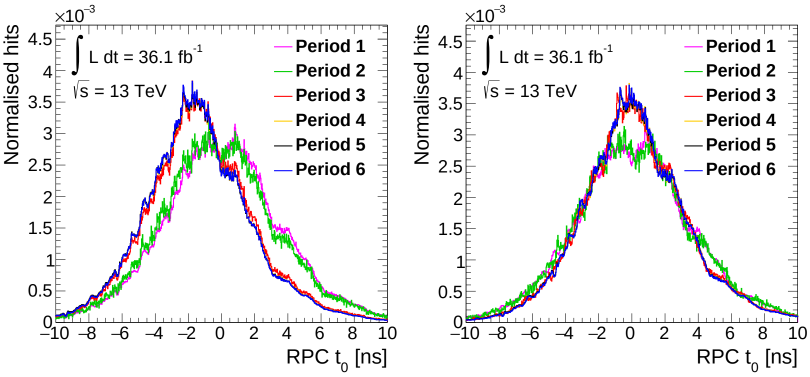

Figure 4.9: The RPC t_0 distributions are plotted for the six periods of constant global online calibrations. The left plot shows the uncalibrated distributions, while the right plot shows them after the calibration constants were applied. All distributions have been normalised to allow for an easier comparison.

The β distribution calculated after online-timing correction has gained in sharpness and is now more closely centred around $\beta = 1$. A comparison between the uncalibrated and the online-timing corrected β distributions is given in figure 4.10, where again the same weights were attributed to each β measurement.

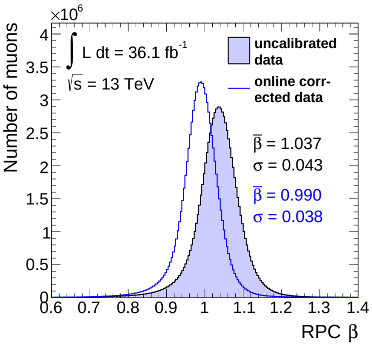

Figure 4.10: RPC β distribution before and after online-timing correction.

4.3 MDT detector-element calibration

Because of the complexity of the detector each detector element can possess a slightly different calibration through detector individualities like small differences in cable lengths, different adjustable time delays, inaccuracies during manufacturing, etc. It is therefore necessary to derive a calibration constant for each detector element. The following chapter documents the development of a calibration strategy which started by considering only the MDTs[9].

4.3.1 Chamber calibration

As discussed in chapter 3.2.3, each MDT chamber is read out via the chamber service module (CSM), which combines the signal from up to 432 drift tubes. Every drift tube has a unique identifier which is written into the data together with the position and timing information. The t_0 distribution for all 1070 CSM encountered in data are plotted separately in histograms and a Gaussian functional parameterisation is used to determine the mean and the width of the distributions. As an example, the t_0 distribution for a randomly chosen CSM has been plotted in figure 4.11. The chamber number 18 is located in the inner MDT layer of the barrel and is installed in one of the large sectors (BIL station). The red Gaussian parameterisation is

[9] This was due to a bug which was found in the calculation of the signal propagation time on RPC strips that needed to be corrected in a time-consuming reprocessing of the data. This left only the MDT information to work with. The calibration steps detailed in chapter 4.3.1 and 4.3.2 are thus only done for the MDTs.

used to determine the calibration constants printed in the plot.

The CSM calibration does not suffer from low statistics with $\mathcal{O}(10^6)$ entries in all histograms. The inverse of the standard deviation σ of the Gaussian can be used as a weight for the combination of β measurements. This way measurements from chambers with broad β distributions receive a small weight, while a β from a chamber with a better resolution gets a larger weight.

An overview over all calibration constants is given in figure 4.12. The variation between different CSMs is small, which shows that the online calibration is uniform for all chambers and spatial variations are small. Some minor structure is visible in the plot, most notably between chambers with ID 847-936 which correspond to all chambers in the outermost layer of the end-caps.

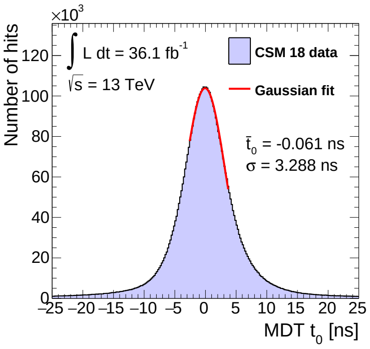

Figure 4.11: t_0 distribution of MDT CSM 18 over the full dataset. Mean and width of a Gaussian parameterisation of the data are printed.

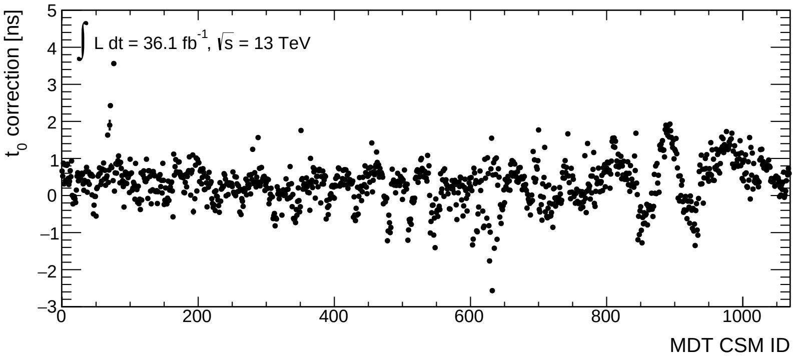

Figure 4.12: Overview of calibration constants for each MDT CSM. The calibration constants are derived from the mean of a Gaussian functional parameterisation to the timing distribution of the chamber.

The MDT chamber calibration results in the timing distribution to be shifted towards $t_0 = 0$, however the width of the distribution is not improved. This could either be due to time-dependent effects rather than chamber-specific features limiting the resolution, or that the calibrations of individual drift tubes of one chamber vary enough to render the chamber-based approach meaningless. The chamber-corrected β distribution reflects the effects observed in the timing distribution. A comparison of t_0 and β distributions before and after application of the calibration is depicted in figure 4.13.

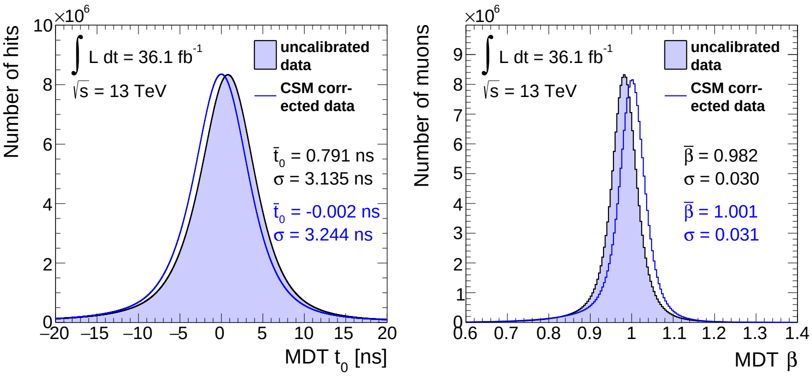

Figure 4.13: MDT t_0 and β distributions before and after the chamber calibration was performed. The mean and width of the distributions are printed and are taken from Gaussian functional parameterisations to the data.

The corrected β distribution is calculated as a weighted mean using the squared inverse of the standard deviation of the Gaussian function as weight.

4.3.2 Run-wise chamber calibration

In order to clarify why the chamber-based calibration from the previous chapter does not meet expectations, a possible time-dependent effect is investigated. The data of 2015 was collected in 65 runs, the 2016 data-taking period consists of 150 runs. Timing distributions for each chamber and run are created, yielding a total of 230 050 histograms. Since the amount of data within a single run varies strongly, the number of entries in each histogram can reach up to $\mathcal{O}(10^4)$. However, a significant fraction of histograms for short runs contain very limited statistics, as shown in figure 4.14. All histograms with more than 100 entries are parameterised by a Gaussian function. The range in which the χ^2 minimisation is carried out is defined by a window of three times the RMS (root mean square) of the histogram with the histogram mean in the centre of the window. Should a first attempt of the parameterisation fail, the fitting range is reduced to twice the RMS and the χ^2-minimisation repeated. This way all but two histograms are successfully described through a Gaussian. Mean and standard deviation are used to generate a pair $(\Delta t_0, \sigma_{t_0})$ of calibration constants. For the histograms in which the fit failed and histograms with less than 100 entries (corresponding to $\approx 7.7\%$ of histograms) the mean and standard deviation of the histogram are taken as calibration constants instead of the ones from the parameterisation. Histograms with less than 15 entries ($\approx 3.3\%$) are not corrected at all. The distribution of the correction constants Δt_0 is shown in figure 4.15. The spike at $\Delta t_0 = 0$ is originating predominantly from low-statistics histograms.

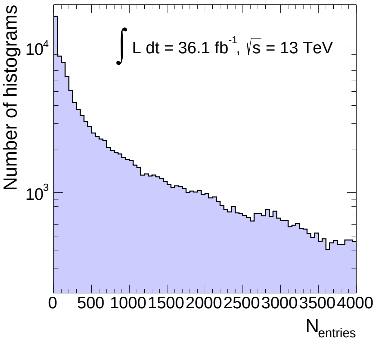

Figure 4.14: Number of entries in all run-wise chamber calibration histograms.

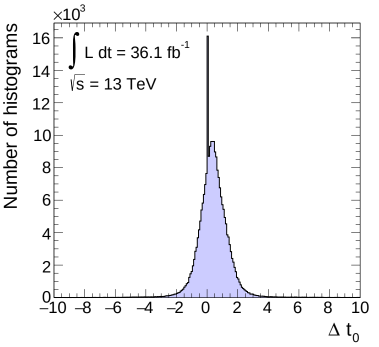

Figure 4.15: Distribution of timing corrections Δt_0 from all run-wise chamber calibration histograms. The spike at $\Delta t_0 = 0$ originates from histograms with low statistics.

Just like in the previous chapter, $1/\sigma^2_{t_0}$ is used as weight for the calculation of β in a weighted average. Comparisons between the uncalibrated and the run-wise chamber corrected t_0 and β distributions are plotted in figure 4.16.

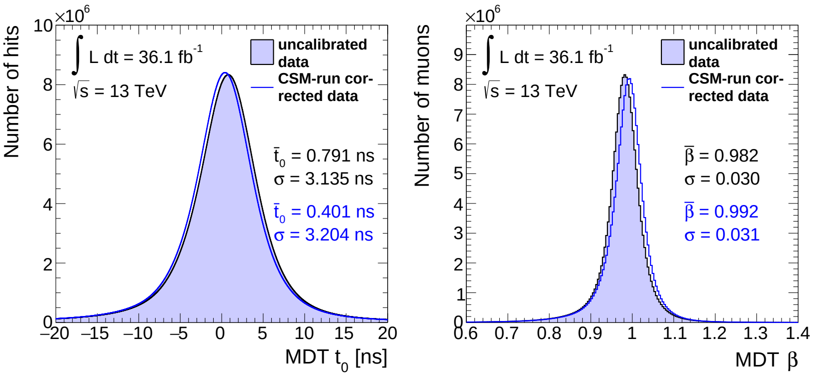

Figure 4.16: MDT t_0 and β distributions before and after the run-wise chamber calibration was performed. The mean and width of the distributions are printed and are taken from Gaussian functional parameterisations to the data.

Just like for the chamber calibration, the run-wise chamber calibration has no beneficial effect on the resolution of the β measurement. Comparing figures 4.13 and 4.16 it is possible to conclude that temporal effects do not dominate the inefficiency of the CSM-based calibration.

4.3.3 Drift-tube calibration

Since the CSM-based calibration has not yielded significant improvements, one needs to find a more detailed approach to account for finer differences between detector elements. This could either be done by performing calibrations on the mezzanine-card level, where each mezzanine card combines the signal from 24 drift tubes, or by deriving pairs of calibration constants for every drift tube should the available statistics allow it. The frequency of a drift tube being hit by a passing muon strongly depends on the position of the tube in the detector. A tube in the innermost layer in the central region of the barrel will get more hits than an otherwise equivalent tube in the outermost layer of the end-cap. Figure 4.17 visualises the available statistics.

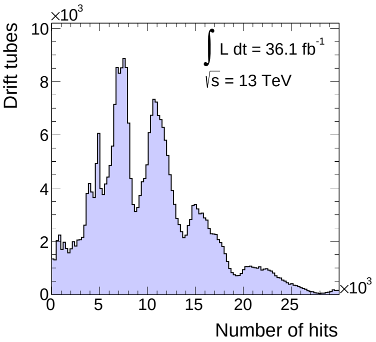

Figure 4.17: Plotted are the number of hits per drift tube for the full 2015 and 2016 datasets.

With on average 10^4 hits per tube the available statistics is large enough for an individual treatment of each drift tube. Since this requires the functional parameterisation of 323 799 distributions, a stable and automated χ^2-minimisation procedure needs to be developed. Tubes with less than 40 hits are rejected. They correspond to $\approx 0.1\%$ of the drift tubes and have negligible influence on the β estimate since a nominal 19 layers of drift tubes are passed by each muon. The remaining tubes are fitted in a two-stage process. First, the mean and width of the tube t_0 histogram are calculated. Then the fit is carried out in a fitting window of three times the width centred around the mean. In a second stage, the window is constructed again, this time however using the mean and width obtained from the first fit. Should the first fit not converge, which is likely due to statistical fluctuations in histograms with a low number of entries, the histogram is re-binned combining the content of neighbouring bins and the whole procedure repeated. For 90 drift tubes (corresponding to 0.03% of all tubes) the re-binning and retrying approach fails. Those tubes are rejected for the β estimate.

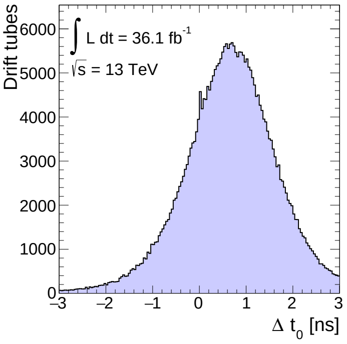

Figure 4.18: Distribution of drift tube timing corrections Δt_0.

The calibration constants Δt_0 are visualised in figure 4.18. An overall timing shift towards large t_0 is corrected while the corrections follow a Gaussian distribution as expected. The small spike at $\Delta t_0 = 0$ is due to rejected drift tubes.

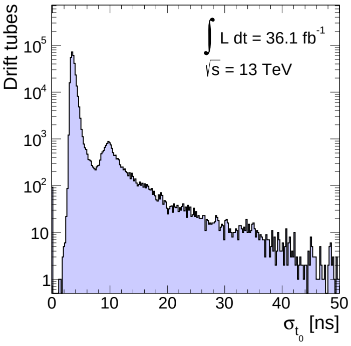

Figure 4.19: Distribution of the timing resolution σ_{t_0} for all drift tubes defined as the standard deviation of the Gaussian fit.

The standard deviation of the Gaussian parameterisation is a measure for the resolution of the drift tube. The distribution of tube resolutions is given in figure 4.19. Here, a peculiar feature is observed. While most drift tubes possess a resolution of $\sigma_{t_0} \approx 3.5$ ns, the subsequent continuous falloff in resolution is interrupted by a second accumulation of drift tubes with $\sigma_{t_0} \gtrapprox 10$ ns. As an example timing distributions of two random drift tubes with good and bad resolution are shown in figure 4.20.

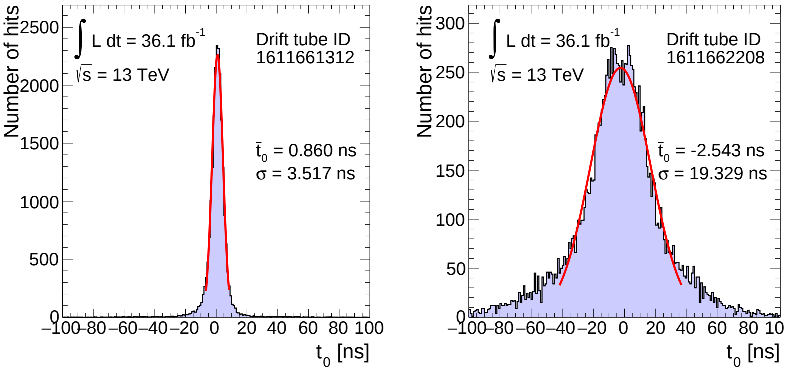

Figure 4.20: Examples of timing distributions for two random drift tubes with very different timing resolutions. Note that the scale of the x-axis is the same in both plots. The red line shows the Gaussian parameterisation of the data. Mean and standard deviation of the fit are printed next to the distribution.

Given the small fraction of $\approx 3.5\%$ of hits occurring in drift tubes with resolution $\sigma_{t_0} > 7.5$, which corresponds to resolutions worse than the local minimum in figure 4.19, it seems suggestive to reject tubes with bad resolution. However, this is only viable if the "bad" tubes are distributed randomly throughout the detector. To verify this requirement all hits that occur in tubes with $\sigma_{t_0} > 7.5$ are projected into the z–y plane of the detector and plotted in figure 4.21.

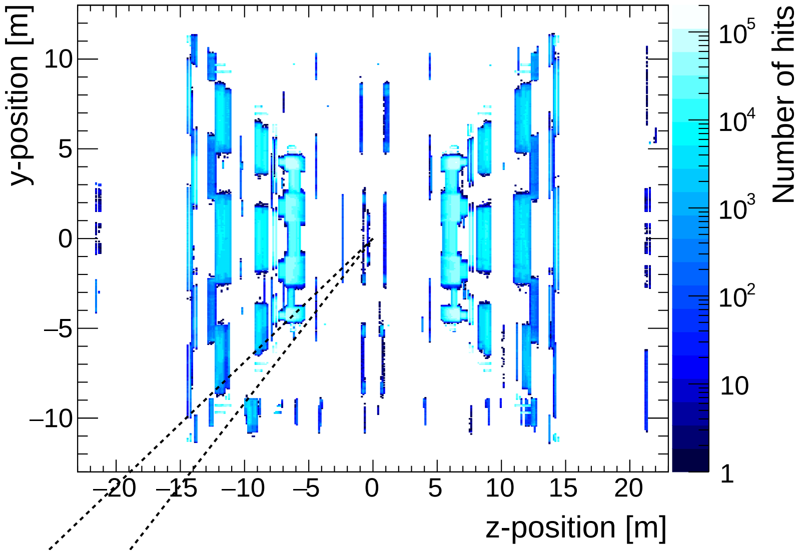

Figure 4.21: The number of hits in drift tubes with a resolution $\sigma_{t_0} > 7.5$ is shown in a projection into the z–y plane of the detector. Clearly "bad" tubes are not distributed randomly as symmetric features of the detector are clearly visible. Especially noteworthy are the transition regions between the barrel and the end-caps were all detector layers are clearly recognisable. For the lower left-hand sector this region has been highlighted by black dashed lines. The same feature can however be observed in all four sectors.

It becomes clear that low-resolution tubes are not randomly distributed. There are almost none in the central region of the barrel, while the outermost barrel chambers are entirely composed of low-resolution tubes. A plot in the x–y projection and corresponding plots for the high-resolution tubes are given in figures B.1 to B.4 in appendix B.

The transition regions between the MS barrel and end-caps seem to be especially affected, as can be seen from the region marked by dashed lines in figure 4.21. Here all detector layers consist of low-resolution tubes. A rejection of those tubes would thus be equivalent to a rejection of muons in the transition region of the MS and effectively an η-region veto. Since even a MDT β estimate composed of low-resolution hits is a powerful tool for analysis, no tubes are rejected.

Lastly, a truncation of the β estimate is performed. This is less motivated by an improvement in resolution, but rather to increase the internal consistency of the measurement. After the weighted average $\bar{\beta}$ has been calculated the averaging is repeated and all hits with $|\bar{\beta} - \beta_i|/\sigma_{\beta_i} > 5.0$ are rejected. This results in a loss of $\approx 1.1\%$ of hits. The internal consistency κ is defined as the χ^2 probability

$$\kappa = \mathrm{Prob}\left(\sum_{i=1}^{N} \frac{(\beta_i^{-1} - \bar{\beta}^{-1})^2}{\sigma^2_{\beta_i^{-1}}}, N-1\right) \quad , \qquad (4.5)$$

where the sum runs over all N hits used for the calculation. The effect of the truncation cut on κ is shown in figure 4.22.

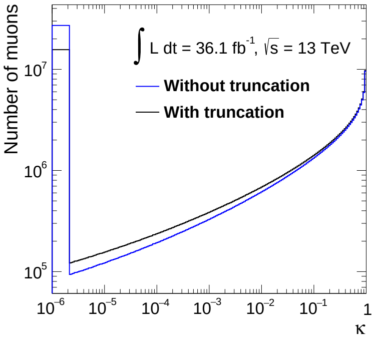

Figure 4.22: Comparison of the internal consistency κ of the MDT β estimate before and after truncation. The first (broader) bin contains all the underflow of the histogram. It corresponds roughly to the 5σ percentile. It can be clearly seen that the truncation shifts many muons from the underflow bin into the plotting range.

The effects of the drift-tube calibration on the overall MDT timing distribution are mainly visible in a shift of the central value towards $t_0 = 0$. The width of the distribution is only changed marginally. The resulting β distribution, however, is slightly improved both in terms of central value and resolution. Most of the improvements are likely due to more meaningful uncertainties on individual β estimates through the accurate parameterisation of the tube distributions. MDT timing and β distributions are compared to the uncalibrated data in figure 4.23.

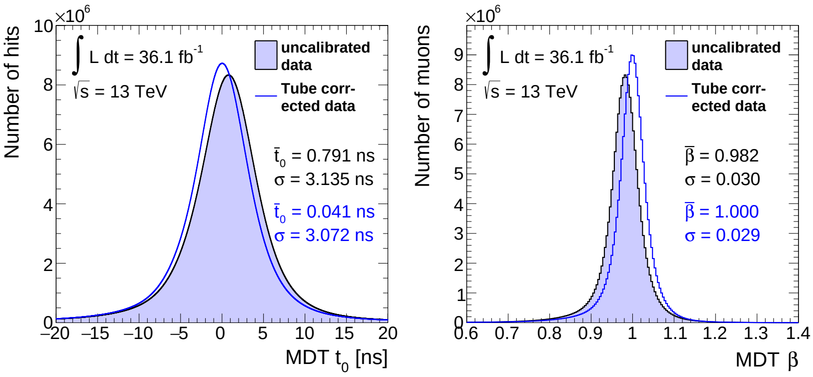

Figure 4.23: Comparison of MDT t_0 and β distributions before and after drift-tube calibration. Distributions are parameterised by a Gaussian function and mean and standard deviation are given. The β for each muon is calculated in a weighted average where $1/\sigma^2_{t_0}$ is used as a weight.

Since the drift-tube calibration yields the best results it is preferred over calibrations on chamber-level.

4.4 RPC detector-element calibration

The RPC system consists of 3 600 gas gaps in which the signal is read out via metallic strips that are oriented to either get a measurement in η or ϕ direction. A total of 113 478 η strips and 248 784 ϕ strips have registered hits in data. The number of detector elements to calibrate is thus comparable to the number of drift tubes, however less hits are registered per readout strip. Figure 4.24 shows the distribution of the number of hits separately for η and ϕ strips.

On average one can expect $\approx 4\,200$ hits on an η strip, while only about $2\,900$ hits are expected for an arbitrary ϕ strip. Both sets of strips show a large number of readout strips with very low statistics of < 40 hits[10]. One way to explain this is through a peculiarity of the RPC readout. During muon reconstruction consecutive strips are put into an "OR". This is either achieved by wiring in the same chamber or via a "logical OR" between nearby chambers. Reconstruction only knows that one of a set of strips has fired and then tries to pick up the correct one. However, this procedure sometimes fails and the wrong strip is associated [280]. It is therefore possible that a dead strip could get associated hits over a longer time period. The low-statistics strips in figure 4.24 are thus likely dead channels and all strips with < 40 hits are rejected for β estimation. While this results in a loss of 2.3% of η and 3.4% of ϕ strips, it accounts for $< 0.01\%$ losses in the total number of hits used.

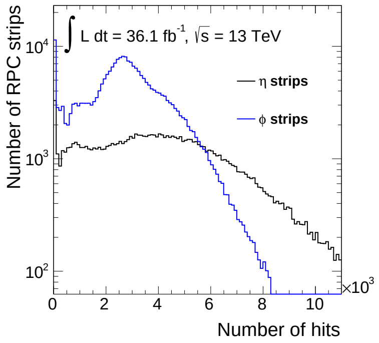

Figure 4.24: Number of hits on RPC η and ϕ strips.

Distributions of the rejected low-statistics strips in the detector and comparisons with high-statistics strips are given in figures B.5 to B.8 in appendix B. The plots confirm the statistically expected random distribution throughout the detector.

The fitting procedure for RPC strips is slightly different than the one for drift tubes in the previous chapter. Many readout strips show timing outliers that often form tails towards large t_0. A randomly chosen example for such a strip is shown in figure 4.25. Since the mean of the distribution is taken as an input for the definition of the fitting range, outliers can bias the fitting. In order to minimise their influence a truncated mean is calculated which disregards the 10% largest and 10% smallest measurements. Since the tails are asymmetric, this will still contain a bias, which is however small enough for the definition of the centre of the fitting range. The size of the fitting window is given by five standard deviations σ_{t_0}, which were taken from the untruncated timing distribution. If the fit is successful, the mean and standard deviation of the fit are stored as a pair of calibration constants. Several criteria have been defined to prevent pseudo-fits which contain:

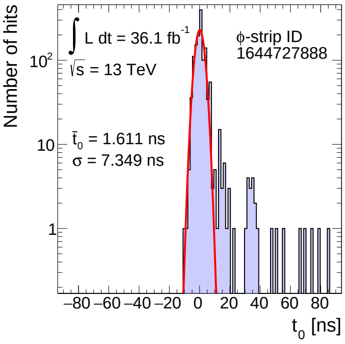

Figure 4.25: Timing distribution of an RPC ϕ strip with a tail towards large t_0.

- Fits were the mean is located outside the fitting range
- Fits with the character of a single spike in one timing bin
- Fits which are broader than $1.1 \cdot \sigma_{t_0}$ and thus underestimate the resolution of the strip

Failed fits are tried again in an enlarged fitting window of $6\sigma_{t_0}$. With this procedure 99.7% of the remaining η strips and 99.4% of ϕ strips are fitted successfully. For the strips with failed fits, the truncated mean and σ_{t_0} are taken as calibration constants. An example for a successfully fitted strip is shown in figure 4.26.

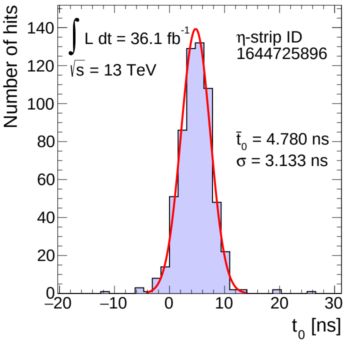

Figure 4.26: Timing distribution of an RPC ϕ strip with a Gaussian functional parameterisation.

Unfortunately some strips show peculiar multi-peak structures in their timing distributions. The affected strips have been studied care-fully. Since the online timing for the new chambers in the feet region of the detector was changed multiple times during the data-taking, it was first suggested that the multi-peaks originate from localised adjustments in the online calibration. However, strips with prominent double peaks were found throughout the detector. In addition, there is no time dependency discernable and all peaks grow in parallel over time. As an example, figure 4.27 shows the decomposition of a timing distribution as a function of time. Several peaks gather signal simultaneously which rules out an effect of changed online calibration. Instead, a likely explanation for the occurrence of the peaks is an effect in the readout. The signal from the same RPC strip is split and then sent to two or more different readout channels. If the path to the channel is not well synchronised it results in the observation of a double-peak [280]. Two examples of such problematic strips are given in figure 4.28. In both cases the additional peaks are shifted by multiples of the bunch spacing from the central peak. In case of the right-hand distribution the fitting procedure is able to pick the larger peak and correctly fit it, while the fit fails for the example on the left-hand side, which corresponds to the distribution of figure 4.27.

---

[10] Note that all plotted strips have at least one associated hit.

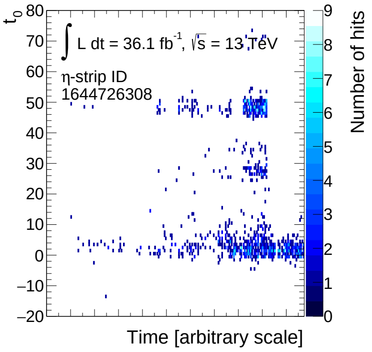

Figure 4.27: Decomposition of the t_0 distribution of the η strip shown on the left in figure 4.28 over time. All peaks are filled in parallel. It is not known why the additional peaks disappear at one point in time.

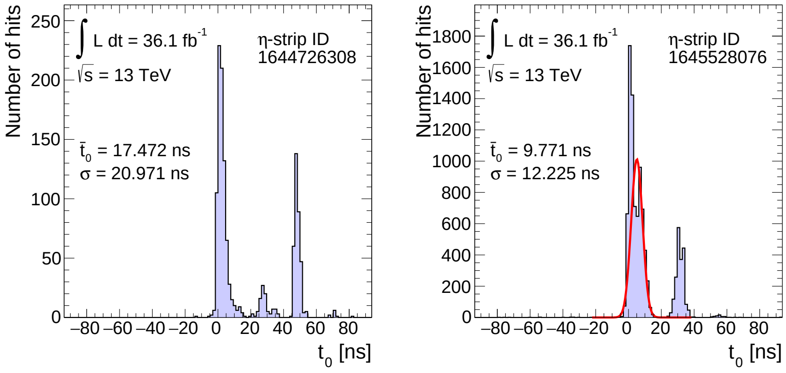

Figure 4.28: Examples of RPC strips with prominent multi-peak timing distributions. The right plot shows the calibration picking up the larger peak and fitting it, while the fit in the left plot failed. For β estimation such strips are rejected by a cut on the width of the distribution and by cuts on the consistency of a β measurement. In both cases the mean and width of the histogram (not the fit) are printed.

Obviously strips like the ones displayed in figure 4.28 are not usable for a β estimation. Their automated identification and rejection can however be tricky and two strategies are used. The first is a placement of a cut on the RMS of the timing distribution. Hits on strips with RMS$>$ 10.0 are rejected which results in the loss of $\approx 3.8\%$ of hits. The RMS distribution and the point of cutting are shown in figure 4.29. Since the magnitude of secondary peaks varies, this criterion alone is not enough and outliers like in figure 4.25 could still significantly bias the estimate. Consequently the second mechanism is a cut on the consistency of the β measurement: the weighted average $\bar{\beta}$ is calculated and the result taken as a seed value. Then the weighted average is repeated rejecting all measurements with $|\bar{\beta} - \beta_i|/\text{RMS} > 3.0$. This results in a further rejection of about 4.6% of the remaining hits.

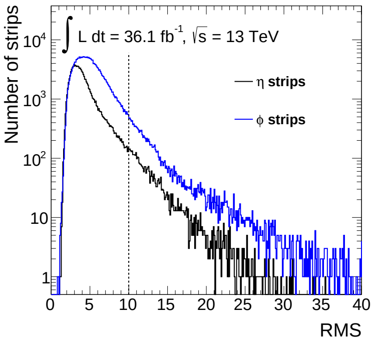

Figure 4.29: Distribution of the RMS for all RPC η and ϕ strips. The dashed line marks the cut.

Having so far dealt with bad resolution strips it is also illustrative to look at the strips with an unreasonably high resolution. Figure 4.30 shows the distribution of the uncertainties on the t_0 measure-

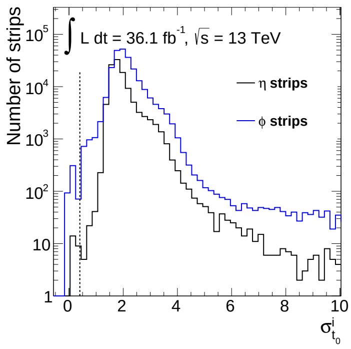

Figure 4.30: Resolution $\sigma^i_{t_0}$ of RPC readout strips.

ment coming from the Gaussian fit $\sigma^i_{t_0}$. The very small uncertainties might originate from strips where most of the data is contained in one or two bins, or where only a part of the distribution was fitted (e.g. a highly-populated bin in an otherwise wider distribution). Since such high resolution strips are not expected, but the associated measurement would dominate the weighted average, all strips with $\sigma^i_{t_0} < 0.4$ ns are rejected. This results in a loss of $< 0.05\%$ of hits. Further plots showing the uncertainty of the timing measurement as a function of t_0 and the ToF are given in figures B.9 and B.10 in appendix B.

The effect of the RMS and consistency cut can be seen in figure 4.31, where the strip-corrected t_0 distributions before and after are compared. It shows how the previously observable side-peaks are completely suppressed by the cuts. As to why the additional peak at -25 ns is only visible for ϕ strips can currently only be speculated about. The tail-suppressed distributions show minor discrepancies from a Gaussian shape in the tails, however, since they are three to four orders of magnitude smaller than the central value they can safely be disregarded. The distribution of calibration constants is shown in figure 4.32.

Figure 4.31: The strip-corrected t_0 distribution is drawn for η strips on the left and ϕ strips on the right. In both cases smaller side-peaks are observable. By cutting on the strip-timing RMS and rejecting β estimates which are inconsistent with the remaining measurements, it is possible to reduce the tails.

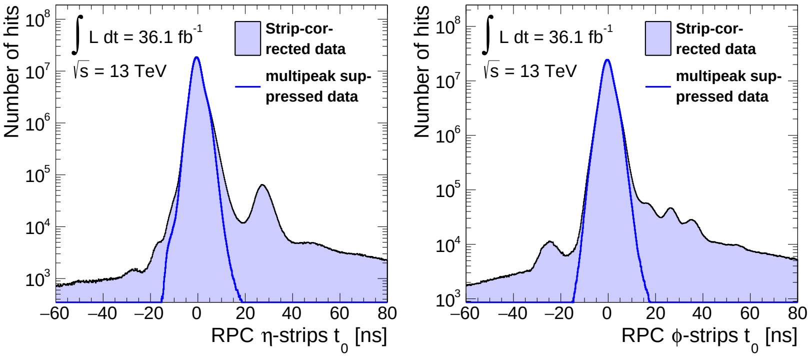

The improvements of the timing and β distributions through the strip calibration are shown in figure 4.33, where the uncalibrated data is compared to the data after online correction and strip calibration. As can be seen, the strip calibration restores the Gaussian shape of the timing distribution. While the width got only slightly smaller, the correct assignment of weights for the β calculation results in clear improvements in β resolution.

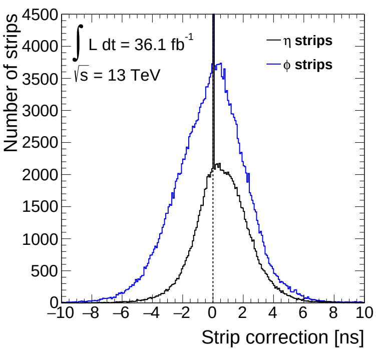

Figure 4.32: Distributions of calibration constants for η and ϕ strips. The spike at zero corresponds to all rejected strips that receive no correction.

4.5 Time-dependent phase-shift correction

All timing information evaluated here derives from the LHC bunch crossing clock. Its frequency varies around 40.08 MHz depending on beam parameters [281]. The timing signal is distributed to the experimental facilities along a complicated bunch-clock-distribution system [282] that involves several kilometres of optical fibres. The

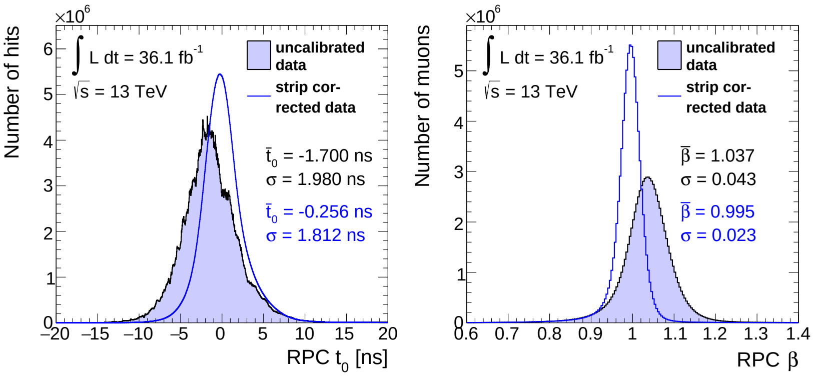

Figure 4.33: The uncalibrated RPC timing and β distributions are compared to the data after online correction and strip calibration. The Gaussian strip calibration restores the Gaussian shape of the RPC timing distribution. Further improvement to the β estimation results from the assignment of correct weights. Mean and width of all distributions are taken from a Gaussian fit.

system is thus vulnerable to changes of weather which can lead to phase shift variations of $\mathcal{O}(100 \text{ ps})$ [283]. As a result, a set of time-dependent phase shift correction factors is derived by looking at the arithmetic mean of timing distributions for individual periods of data-taking (runs). Since the phase-shift variations are overlaid by detector effects and shifts from online timing adjustments in individual parts of subdetectors, the time-dependent correction factors are derived for MDT and RPC η and ϕ strips separately. Figure 4.34 shows the timing corrections Δt_0^{run} for the MDT system.

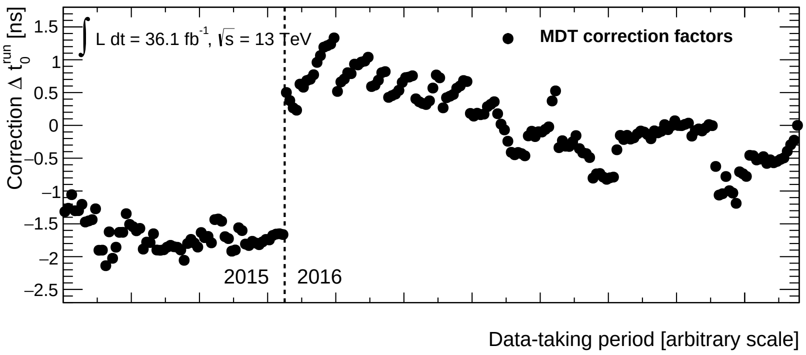

Figure 4.34: Phase-shift corrections Δt_0^{run} for the MDT system over all data-taking periods. The dashed line marks the transition from 2015 to 2016. The effects of online calibration changes are discernable as larger changes between two consecutive runs. During the first months of 2016 a desynchronisation effect can be observed, which is frequently corrected.

A change in the online timing calibration can be observed prominently at the change of years. In the following runs a continuous desynchronisation was observed, which resulted in drifting means of the timing distributions. The desynchronisation was corrected by realignment in short time intervals. Two consecutive runs can thus have widely different correction factors.

The timing corrections for the RPC system are plotted separately for η and ϕ strips in figure 4.35.

Since the global online timing changes have already been corrected the timing variation in between runs is much smaller for the RPC system than for the MDTs. The fluctuations are much larger during 2015 and early 2016 compared to the later part of 2016 data-taking. This is due to new RPC chambers that have been installed in the feet region of the detector[11] up until the end of 2015. The year 2015 and the first runs of 2016 were used for timing synchronisation

[11] The feet stations are located at $-2.0 < \phi < -1.0$.

Figure 4.35: Phase-shift corrections $\Delta t_0^{\mathrm{run}}$ for RPC η and ϕ strips over all data-taking periods. The dashed line marks the transition from 2015 to 2016. The effects of online calibration changes are discernable most prominently in early 2016. No large time-dependent effects are observed during 2016. η and ϕ strips receive similar corrections.

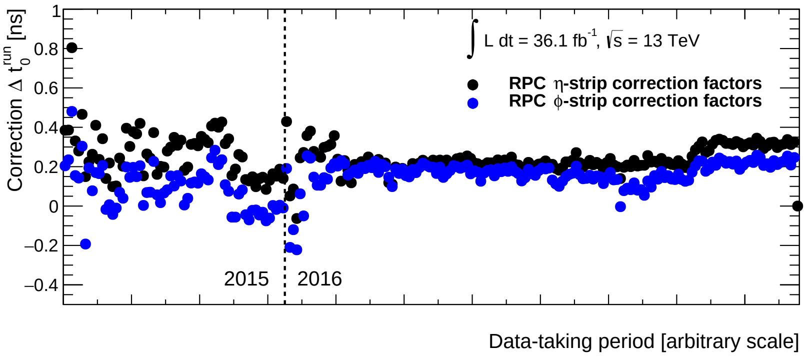

of the new chambers [284]. Later in 2016 the conditions are stable and variations are as expected $\mathcal{O}(100\ \mathrm{ps})$.

The effect of the run-dependent phase-shift correction (run correction) on the timing distributions is small and shown in figure B.11 in appendix B. A comparison between the MDT drift-tube corrected β distribution before and after run correction, as well as the RPC online and strip corrected t_0 distribution before and after run correction are shown in figure 4.36.

Figure 4.36: Effect of the phase-shift correction. The left plot compares the MDT drift-tube corrected β distribution before and after run correction. The right plot shows the RPC online and strip corrected β distribution before and after run correction. The mean and standard deviation of a Gaussian parameterisation to the data are given.

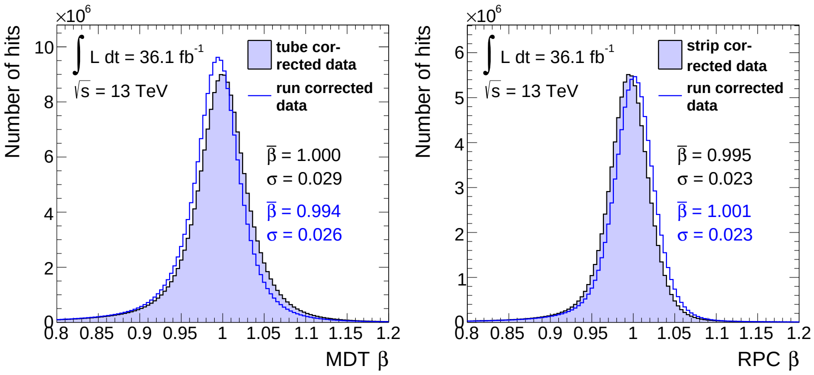

4.6 Order of calibrations

Since the different stages of calibration take the output of the previous stage as an input, the overall result depends on the order of calibrations. Therefore, the reverse order from what was presented in the previous chapter has also been tested. For MDTs the order of tube and phase-shift correction has been swapped. For RPCs on the other hand, the online calibration needs not be performed if the phase-shift correction is done before the strip correction as global calibration changes are accounted for in the phase-shift correction. A comparison between the β distributions resulting from both calibrations is given in figure 4.37.

It can be seen that both calibration yield very similar results. For MDTs the better result is achieved by first performing the tube correction, while for RPCs both methods perform equally well. The

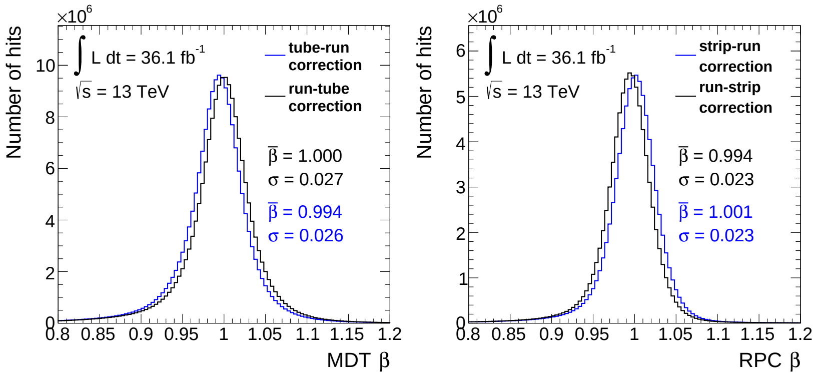

Figure 4.37: Comparison of different calibration orderings. For MDT the tube and phase-shift corrections have been reversed, for RPCs the online correction is necessarily the first correction and only strip and phase-shift correction have been reversed. Both strategies perform equally well and the order as presented in the previous chapters is adopted.

order of calibrations as presented here has thus been adopted for physics analysis.

4.7 Pull correction of σ_β

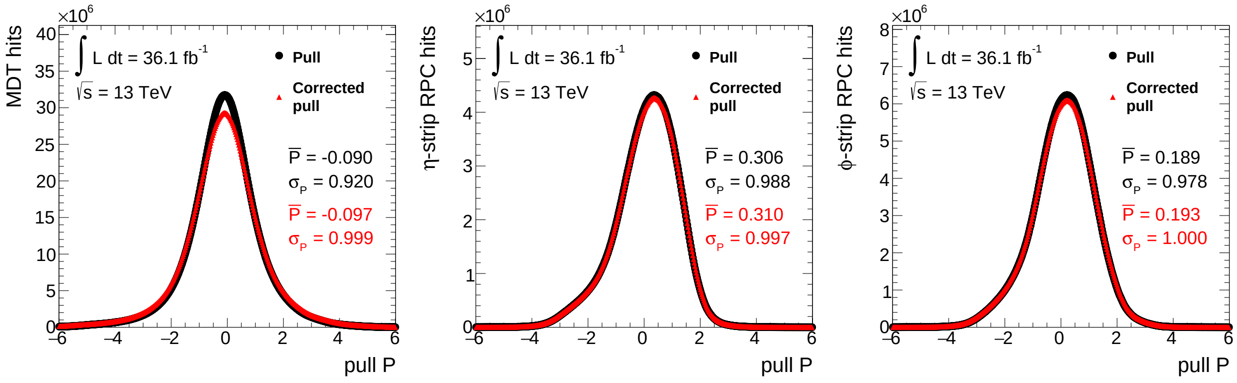

Figure 4.38: The pull $\frac{1-1/\beta_i}{\sigma(1/\beta_i)}$ is plotted for hits in MDT (left), RPC η strips (middle) and RPC ϕ strips (right). If the estimated individual uncertainties on β reflect the width of the β distribution over all muons, the distributions should have unity width. Correction factors on the hit uncertainty σ_{β_i} are derived.

After the combination of individual β measurements in a weighted average, the error on the weighted average σ_β should reflect the width of the β distribution over all muons. An accurate uncertainty is necessary for the combination of β measurements from different subsystems. In order to correct the uncertainty to the right values the pull values, i.e. $\frac{1-1/\beta_i}{\sigma(1/\beta_i)}$ are plotted. The distributions are expected to have Gaussian shape with mean zero and unity width, should the estimated individual uncertainties reflect the actual uncertainty of β correctly. Correction factors can thus be derived from the deviations of the widths from unity. Comparisons of the pull distributions before and after correction for MDTs and RPC η and ϕ strips separately are shown in figure 4.38.

The widths of the distributions are determined by fitting the peaks with a Gaussian function. The MDT distribution conforms to expectation, while in the RPC distributions a tail towards small pull values can be observed. The origins of these asymmetries are not well understood. However, since the widths of the pull distributions are very close to expectation and correction factors for σ_{β_i} therefore small, the errors caused by the asymmetries are marginal. Possible dependencies of the pull on η have been investigated and found to be negligible.

4.8 Combination of β estimates

This chapter serves to summarise the calibration of the MS by combining the β estimates from MDTs and RPCs in one weighted average. Figure 4.39 shows the final MDT β distribution and compares it to the uncalibrated data and all intermediate steps. During the analysis of the $\sqrt{s} = 8$ TeV data taken in 2012, an MDT resolution of $\sigma_\beta^{\mathrm{MDT,2012}} = 0.037$ was achieved [160]. Thus, the tube and phase shift corrected calibration presented here constitutes a significant improvement and yields the best MDT β resolution to date.

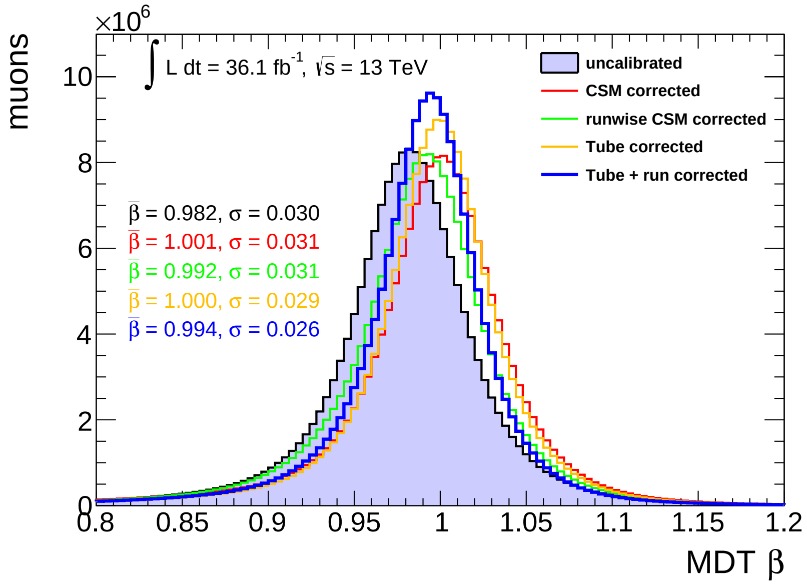

Figure 4.39: Summary of the MDT β calibration. Shown are the uncalibrated data along with the β distributions after each intermediate step. In the uncalibrated data the individual measurements β_i are combined with equal weight, while for all other calibrations the inverse of the standard deviation from a fit to the timing distribution is used as weight to perform a weighted average. The mean and width of the distributions are given. They are determined from a Gaussian fit to the data. The final tube and phase-shift corrected calibration yields the best MDT β resolution to date.

The RPC calibration is summarised in figure 4.40. The uncalibrated and intermediate β distributions are compared to the final pull corrected RPC distributions where measurements from η and ϕ strips are combined with the correct weights stemming from the uncertainty on the individual β estimate. The β resolution achieved through the calibrations described here can be compared to the resolution in the 2012 data, which was given by $\sigma_\beta^{\mathrm{RPC,2012}} = 0.024$. Just like for the MDT system, the newly developed calibration strategy yields a significant improvement in β resolution over previous results.

The corresponding summary plots showing the effects of the different calibration steps on the timing distributions are given in figures B.12 and B.13 in appendix B.

The inverse of the square of the uncertainty on the β estimate is used as a weight to combine the estimates from MDTs and RPCs. The distributions of the uncertainties is shown in figure 4.41. Both uncertainties are very similar in scale as expected from the compa-

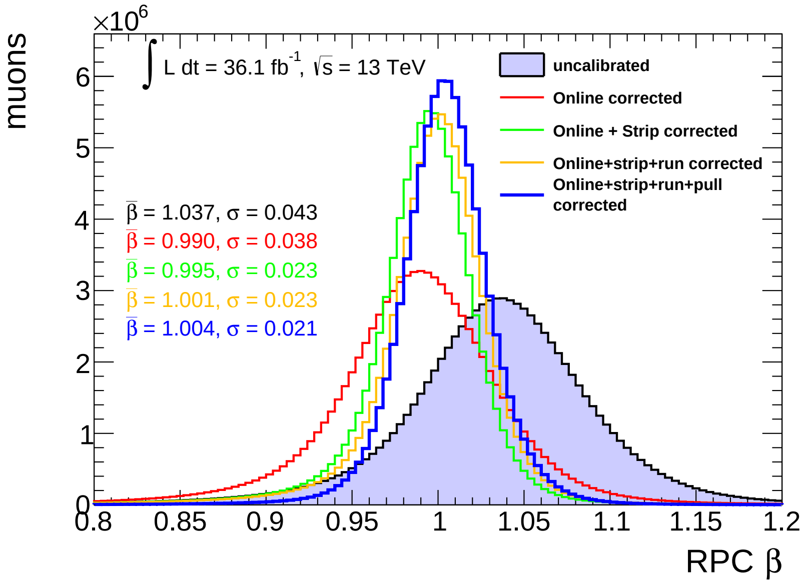

Figure 4.40: Summary of the RPC β calibration. Shown are the uncalibrated data along with the β distributions after each intermediate step. In the uncalibrated and online-corrected data the individual measurements β_i are combined with equal weight, while for all other calibrations the inverse of the standard deviation from a fit to the timing distribution is used as weight to perform a weighted average. The mean and width of the distributions are given. They are determined from a Gaussian fit to the data. For all distributions β estimates from η and ϕ strips were combined. The blue line shows the combination after pull correction.

rable β resolution in both systems. The long tails visible for both systems are many orders of magnitude smaller than the bulk of the distribution and have negligible effect.

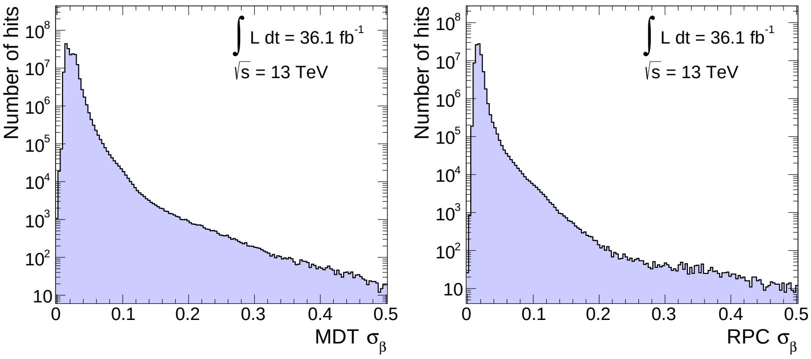

Figure 4.41: Uncertainties σ_β on the β estimate from MDTs (left) and RPCs (right). The magnitude of the uncertainties is very similar in both systems, as was expected from their similar resolution.

The dependence of the individual β estimates on the pseudorapidity has been investigated and found negligible for RPCs. For MDTs the expected β is slightly lower in the central region of the detector. As this is due to asymmetries in the timing distribution no correction has been performed. The dependence on η is plotted and shown in appendix B for MDTs in figure B.14, in figure B.15 for RPCs and in figure B.16 for the combined β. The dependence of σ_β on η is shown in figures B.17, B.18 and B.19 for MDTs, RPCs and combination, respectively.

Lastly the correlation between the MDT and RPC β estimate has been investigated. Figure 4.42 shows the two estimates plotted against each other. The correlation coefficient is found to be $\rho(\beta_{\mathrm{MDT}}, \beta_{\mathrm{RPC}}) =$ 12.7%. This is within the expectation of the β estimation, as the MDT and RPC system are not completely independent since the RPC delivers a β seed-value to the MDTs during reconstruction. The turns in the right plot of figure 4.42 can be attributed to the growing improbability of producing two outlier results in both systems.

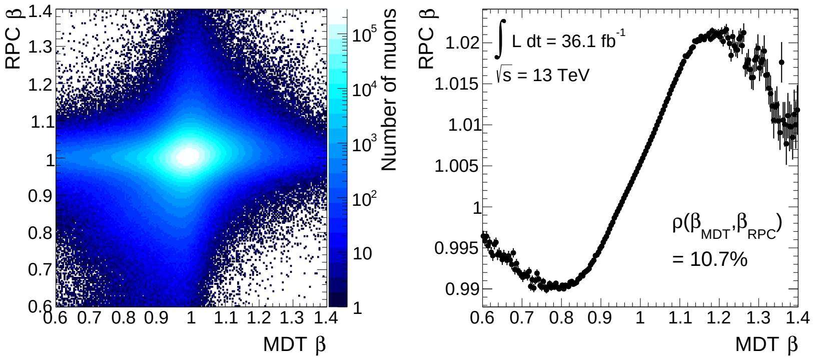

Figure 4.42: Correlation of the MDT and RPC β estimates. In the right-hand plot, the means of y-slices of the histogram on the left are plotted. A clear correlation can be seen for $\beta \approx 1$. The correlation strength is found to be 12.7%.

The combination of MDT and RPC β estimates is carried out and yields the final result of the calibration

$$\boxed{\text{MS } \beta\text{: } \bar{\beta} = 0.997, \quad \sigma_\beta^{\text{MS}} = 0.021} \tag{4.6}$$

The resolution of the combined MS β in the data taken in 2012 was given by $\sigma_\beta^{\text{MS,2012}} = 0.024$. Thus, the calibration presented here yields the best ATLAS Muon Spectrometer β resolution to date. The combined uncertainty on the β estimate is given in figure 4.43, the fully calibrated MS β distribution is plotted in figure 4.44.

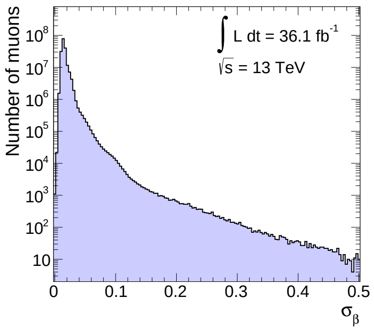

Figure 4.43: Uncertainty on the combined MDT and RPC β estimate.

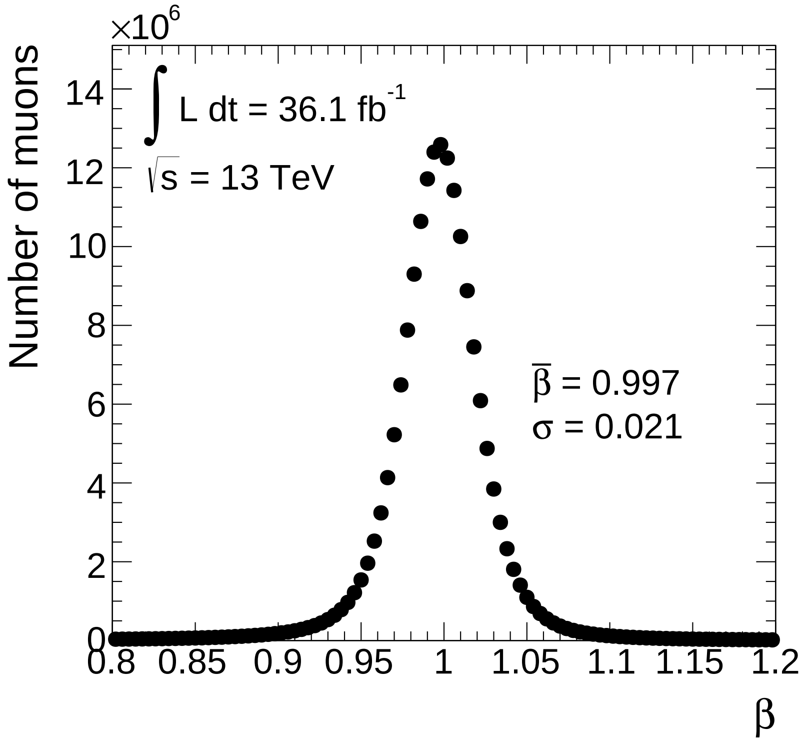

Figure 4.44: Fully calibrated Muon Spectrometer β distribution. The estimates from MDT and RPC have been combined in a weighted average with the weights derived from the uncertainty on the individual estimate. The mean and width of the distribution are given. They are determined to a Gaussian parameterisation of the data. The calibration presented here yields the best ATLAS MS β resolution to date.

4.9 MDT simulation timing smearing

The β resolution depends on many different detector effects and characteristics which are not expected to be well simulated in MC. Indeed, a comparison of the fully calibrated MDT β estimate with the untreated MDT β from simulation yields vastly different distributions, as can be seen in figure 4.45. A dataset of 20 million simulated $Z^0 \to \mu\mu$ decays is used for MC studies. All events have been generated using Powheg-Box v2 [285, 286] interfaced with Pythia8 [287] and EvtGen v1.2.0 [288] using the Cteq6L1 parameterisation of the parton distribution functions (pdfs) [289]. Photon radiation from charged leptons is provided by Photos [290]. All events are passed through the ATLAS detector simulation [291] that is implemented within the Geant4 framework [292].

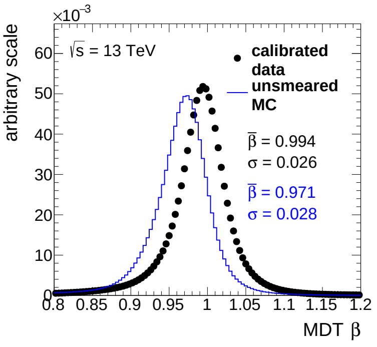

Figure 4.45: Comparison of the fully calibrated MDT β estimate with the untreated β from simulation. Mean and width are determined from Gaussian parameterisations of the data.

Because of the discrepancy between data and simulation it is necessary to develop a procedure to generate an accurate representation of timing information in simulation. In the past a successful strategy was the folding of the original timing distribution in simulation with a Gaussian distribution to smear simulation to match the resolution in data. Simulated hit times t_0^{MC} where treated according to

$$t_0^{\mathrm{smear}} = t_0^{\mathrm{MC}} - (\bar{t}_0^{\mathrm{MC}} - \bar{t}_0^{\mathrm{data}}) + R(0, \sigma_{\mathrm{smear}}) \quad , \tag{4.7}$$

where $\bar{t}_0^{\mathrm{MC}}$ and $\bar{t}_0^{\mathrm{data}}$ are the mean values of the timing distributions in MC and data respectively and R is a random number drawn from a Gaussian distribution with mean 0 and width σ_{smear}. The smearing width relates to the widths of the timing distributions in data σ_{data} and MC σ_{MC} through $\sigma_{\mathrm{smear}} = \sqrt{\sigma^2_{\mathrm{data}} - \sigma^2_{\mathrm{MC}}}$.

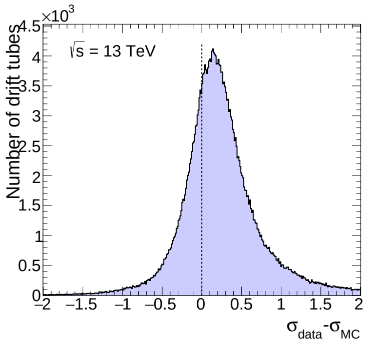

Figure 4.46: Differences in width of tube timing distributions in data and simulation. The dashed line represents equal width.

4.9.1 Underestimation of data resolution

The smearing procedure is only feasible if the simulated timing distribution overestimates the resolution of data. It is impossible to generate a sharper timing distribution through folding with a Gaussian function. The condition is tested by calculating $\sigma_{\mathrm{data}} - \sigma_{\mathrm{MC}}$ for every drift tube. The results are shown in figure 4.46. The dashed line marks equal width. Because the available statistics is much smaller in simulation than in data with only ≈ 750 hits per drift tube on average (figure 4.47), no fit is performed. Instead, timing information is truncated by discarding the largest and smallest 5% of associated t_0 values to remove the influence of individual outliers. The width is then calculated from the truncated distribution.

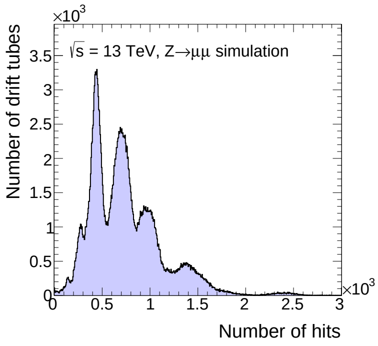

Figure 4.47: Number of hits per drift tube in simulation. On average about 750 hits are expected per drift tube.

It can be seen that 32.5% of all drift tubes have broader distributions in simulation than in data. Whether this is due to the unprecedented MDT timing resolution or a failure to keep simulation up-to-date with data is not clear. Several ideas have been tested to deal with such problematic strips. The tests were carried out on toy data, where one million pseudo-hits with Gaussian timing distribution have been produced.

Strategy 1: Reweighting A first approach is to reweight simulation to agree with data. This requires to first shift simulation to agree with the mean value in data[12]. To avoid the effects of statistical fluctuations, the distributions are fitted with a Gaussian function. Next, the ratio of the fits to data and MC is used to construct a reweighting function. The weights are then applied to individual hits during the calculation of the weighted β average. The left plot of figure 4.48 shows the reweighting strategy in the toy dataset which generates an excellent agreement between toy-data and toy-MC.

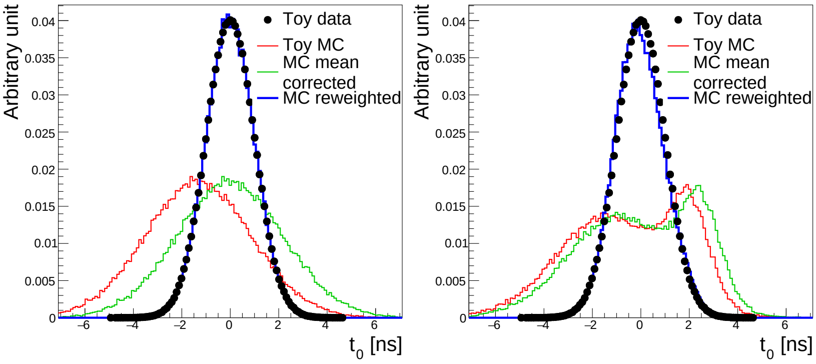

Figure 4.48: Toy study to investigate the possibility of reweighting as a solution to the underestimation of resolution in simulation. Left shows the reweighting of a perfectly Gaussian initial distribution. In the right plot a grave asymmetry has been introduced to investigate the stability of the strategy under distorted distributions.

However, in reality no distribution is a perfect Gaussian. Since potential asymmetries in the distribution influence the fit and therefore the efficiency of the procedure, the effects are investigated by introducing asymmetries to the toy distribution[13]. The right plot of figure 4.48 shows an extreme example. The method fares well even in such an extreme case and is therefore expected to be a viable option. No smearing as stated in equation 4.8 is required.

Strategy 2: Sharpening and smearing An alternative approach is the artificial enhancement of the timing distributions. Again a mean correction is performed as first step. Then the timing resolution is considered. Multiplying the t_0 values by a constant $s < 1.0$ will sharpen the timing distribution. Via s the magnitude of the sharpening can be chosen to create artificial resolutions which are better than what is observed in data. A smearing according to equation 4.8 can then be applied to generate agreement with data. Figure 4.49 shows the sharpening procedure acting on a perfectly Gaussian distribution and a distribution into which an extreme asymmetry has been introduced.

The sharpening procedure yields comparably good results to the reweighting approach and shows slight advantages in coping with asymmetries.

[12] Data has been calibrated to be centred around $t_0 = 0$. Since no large shifts have been simulated in MC, the mean correction should be small.

[13] The timing distributions in simulation are not asymmetric per se, however since many tubes have low statistics in simulation, grave statistical effects are expected that can influence the fit.

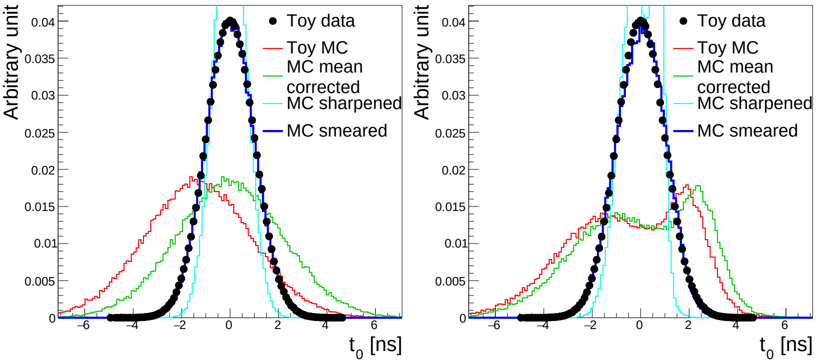

Figure 4.49: Toy study to investigate the possibility of sharpening and smearing as a solution to the underestimation of resolution in simulation. Left shows the sharpening of a perfectly Gaussian initial distribution with a subsequent smearing applied. In the right plot a grave asymmetry has been introduced to investigate the stability of the strategy under distorted distributions.

Strategy 3: Unfolding As a last strategy a singular value decomposition (SVD) is attempted. SVD methods have initially been developed to remove the effects of a particle detector to reveal the true nature of a distribution. Through careful studies on the method of measurement itself it is possible to construct a two-dimensional function parameterising the detector response to a given signal. The measured quantity can then be interpreted as the folding of the true distribution with the detector response. Turning this method around one can try to solve for the response function through the measured signal. This is called unfolding or unsmearing [293]. The result usually varies widely depending on small statistical effects [294]. To control these effects a smoothness condition[14] is imposed which is called regularisation.

If the true distribution is now taken to be the calibrated timing distribution in data and the "observed distribution" is taken to be simulation, then the inverse of the response function relates MC to data. A full SVD procedure is implemented in the TSVDUnfold package [295] for ROOT [296] and used on the toy data. Figure 4.50 shows the result of the unfolding technique on a Gaussian distribution and on a distribution with large asymmetries.

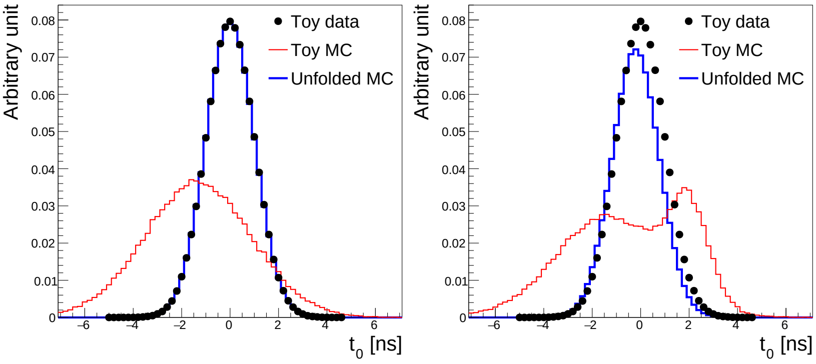

Figure 4.50: Toy study to investigate the possibility of an unfolding procedure as a solution to the underestimation of resolution in simulation. The unfolding was carried out using the TSVDUnfold software package. Left shows the unfolding of a perfectly Gaussian initial distribution. In the right plot a grave asymmetry has been introduced to investigate the stability of the strategy under distorted distributions.

As can be seen, the method yields perfect agreement between toy data and simulation in the Gaussian case but shows large discrepancies for asymmetric functions.

---

[14] Any requirement which restricts possible solutions helps, e.g. one could demand the solution to be strictly positive.

Choice of strategy All proposed strategies have been shown to work very well. While the unfolding strategy is unquestionably the most elegant solution, it also comes with some baggage. In order for it to be applicable in the analysis, two 2-dimensional histograms have to be stored for every distribution. Since 105 100[15] individual drift tubes need to be corrected, the resulting calibration files are large and difficult to handle. Furthermore, the low statistics for many tubes in MC renders the procedure very unstable and a successful and stable implementation was not possible. For these reasons the unfolding method was abandoned[16].

The reweighting and sharpening methods have also been tested with toy signal (see figure B.20 in appendix B). Both methods perform equally well. However, since the reweighting requires a fit to the timing distribution one again expects problems for the tubes with low statistics. Furthermore, the propagation of additional hit weights to the β calculation is not straight-forward. The sharpening method on the other hand is very robust as it relies solely on the mean of the distribution. It was therefore decided to use the sharpening method with a subsequent smearing for analysis.

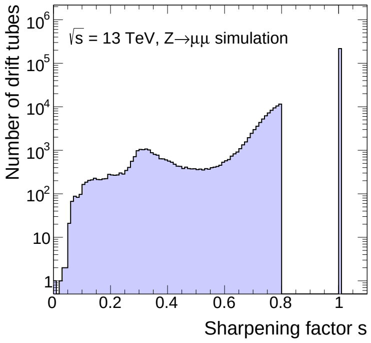

Figure 4.51: Sharpening factors derived from the widths of the tube timing distributions in data and MC. Tubes with $s = 1$ are already sharper than in data.

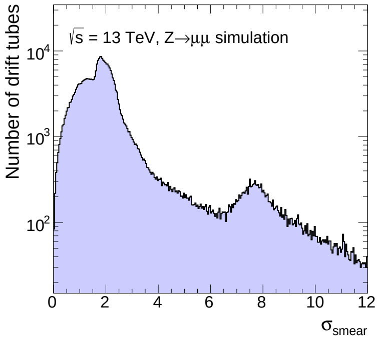

Figure 4.52: Smearing widths calculated from the width of the timing distributions in data and MC through $\sigma_{\text{smear}} = \sqrt{\sigma_{\text{data}}^2 - (\sigma_{\text{MC}}^{\text{sharp}})^2}$.

4.9.2 Drift-tube smearing

To generate agreement between data and MC the individual drift tubes are considered. The mean and width of tube-timing distributions are determined for simulation and fully calibrated data. To avoid a bias from outliers this is done for a truncated distribution in which the 5% largest and smallest values have been discarded. For tubes with broader distributions in MC the sharpening procedure is carried out. The sharpening factor $s = 0.8 \times \sigma_{\text{data}}/\sigma_{\text{MC}}$ is chosen, where the factor of 0.8 is introduced to allow a random component in the following smearing. The smearing width is then calculated from the sharpened MC width $\sigma_{\text{MC}}^{\text{sharp}}$ via $\sigma_{\text{smear}} = \sqrt{\sigma_{\text{data}}^2 - (\sigma_{\text{MC}}^{\text{sharp}})^2}$. Figure 4.51 shows the sharpening factors s for all tubes. The large spike at $s = 1$ corresponds to all tubes which already have a sharper timing distribution in MC than in data.

Figure 4.52 shows the values of σ_{smear}. The majority of tube timing distributions need only be convoluted with a Gaussian of small width. Two peaks in the distribution at $\sigma_{\text{smear}} = 2$ and $\sigma_{\text{smear}} = 7.5$ suggest that some systematic effect which causes tubes to have lower resolution was not correctly modelled in MC and thus affected tubes receive similar corrections.

For the calculation of the weighted β average the weights are taken directly from data.

The smearing is applied to $Z \to \mu\mu$ MC. The effect on the timing and β distribution can be seen in figure 4.53.

The timing distribution is much improved through the smearing with some discrepancies in the peak region. However, the β calcu-

---

[15] The number of drift tubes with broader distributions than measured in data. A total of 323 302 drift tubes have been seen in MC.

[16] In future iterations of this analysis, where more statistics is available, the method will be a feasible alternative and should be the preferred option.

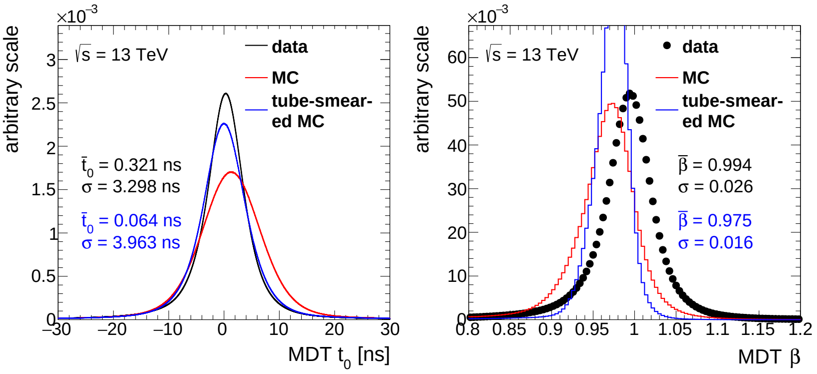

Figure 4.53: Effect of the drift-tube smearing on the simulated timing and β distribution. The t_0 clearly approximates the distribution in data much more through the smearing, however, the weighted β turns out much too sharp. The problem can be traced back to problems with statistics in simulation and an incorrect description of the tails of distributions.

lated from the smeared ToF turns out too precise. The reason for this has been investigated and two factors were identified: for many tubes the available statistics is too small for the smearing to be trustworthy and the non-Gaussian tails that are observed in data (e.g. figure 4.20) are not well represented in smeared MC. With the absence of tails in the timing distribution the β distribution necessarily overestimates the resolution. Both causes can be remedied by switching from a drift-tube based smearing to a chamber based one.

4.9.3 Chamber-based smearing

In the following individual MDT chambers instead of tubes are considered. To get an accurate description of the tails of the chamber timing distribution, a correct parameterisation has to be found. The central peak is well described by a Gaussian function, while the tails can be parameterised by a Breit-Wigner distribution. During fitting, the mean values of the Gauss and Breit-Wigner functions are treated as one parameter[17]. This can be seen exemplary for a random MDT chamber in figure 4.54.

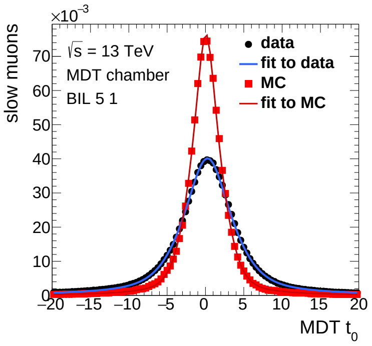

Figure 4.54: Data and simulated timing distribution for one MDT chamber fitted with a Gaussian plus Breit-Wigner function.

The problem of underestimated timing resolutions in simulation is also present on chamber level. It is therefore necessary to nevertheless apply the sharpening procedure. To not introduce any bias, a global sharpening value is chosen with which all drift tubes are treated. In order to minimise the effect of the procedure the highest possible value is chosen that still renders almost all chambers sharper than data. Figure 4.55 shows the percentage of chambers with broad distributions as a function of the sharpening value. The broadness has been determined from a fit to the timing distribution. It compares the width of the Gaussian and Breit-Wigner part of the fits individually. Since the fits have been optimised for large s, the fits fail for some chambers at low s values causing some irregularities. A value of $s = 0.7$ has been chosen.

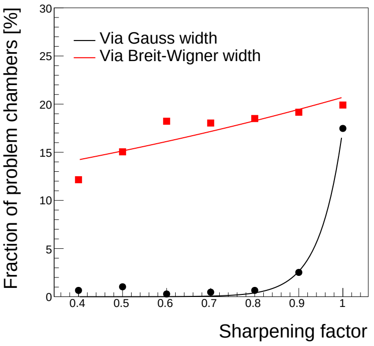

Figure 4.55: Fraction of chambers with timing distributions broader than data as function of the sharpening value. The fits were optimised for large sharpening values, thus at low values the data points become less trustworthy.

The smearing is realised by generating two random numbers G and B drawn from a Gaussian and a Breit-Wigner distribution and adding them to the sharpened t_0 measurement according to

---

[17] Different approaches like a double-Gaussian or Crystal Ball function have also been tested but did not yield a convincing result.

$$t_0^{\text{smear}} = t_0^{\text{MC}} - (\bar{t}_0^{\text{MC}} - \bar{t}_0^{\text{data}}) + G(0, \sigma_{\text{Gauss}}) + B(0, \sigma_{\text{BW}}) \quad . \tag{4.8}$$

Since there is no trivial way to calculate the smear widths σ_{Gauss} and σ_{BW} they are estimated through an iterative process. From the fit to data and MC toy distributions of 100 000 datapoints are created. The smearing procedure with different values for σ_{Gauss} and σ_{BW} is then applied to the toy data to limit the influence of statistical effects in data and a Kolmogorov-Smirnoff test performed for each hypothesis. The combination of smearing hypotheses which yield the highest Kolmogorov-Smirnoff probability are written into a calibration table. The successful smearing of the chamber from figure 4.54 can be seen in figure 4.56.

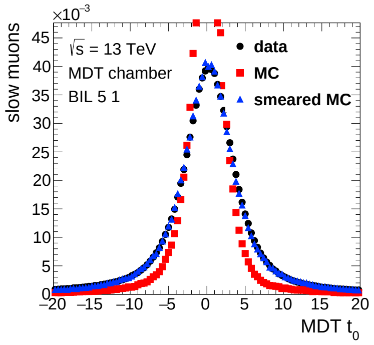

Figure 4.56: Smearing applied to one chamber.

Since the Breit-Wigner function has prominent long tails, it is likely that a timing value will receive a smearing correction where $B(0, \sigma_{\text{BW}})$ is many BCs large. To suppress too large corrections a cut off $\Lambda_{\text{BW}} = \lambda \cdot \sigma_{\text{BW}}$ is defined, where $\lambda > 0$. If a random number $B(0, \sigma_{\text{BW}}) > \Lambda_{\text{BW}}$ is drawn, another random number is chosen until the cut-off condition is passed. To find the optimal λ, the smearing is carried out with different cut-off parameters. The one yielding the largest agreement with data is chosen. The Kolmogorov-probability as a function of λ is shown in figure 4.57.

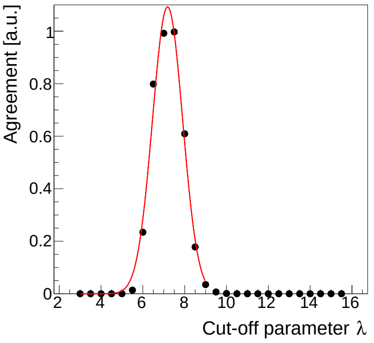

Figure 4.57: Agreement between data and smeared MC as function of different Breit-Wigner cutoff parameters λ. The uncertainties on the datapoint have been scaled to yield large Kolmogorov probabilities. A Gaussian fit is performed which yields the largest agreement for $\lambda \approx 7.2$.

The optimal λ is derived from the mean of a Gaussian fit to the data and $\lambda \approx 7.2$ is found.

A comparison of the simulated timing and β distributions after the chamber-based smearing with data are shown in figure 4.58. The t_0 values agree with the data except for small discrepancies in the peak region. The β distribution on the other hand agrees very well with the data. Discrepancies in the tails of the distribution play a limited role since the MC resolution is the crucial factor for analysis.

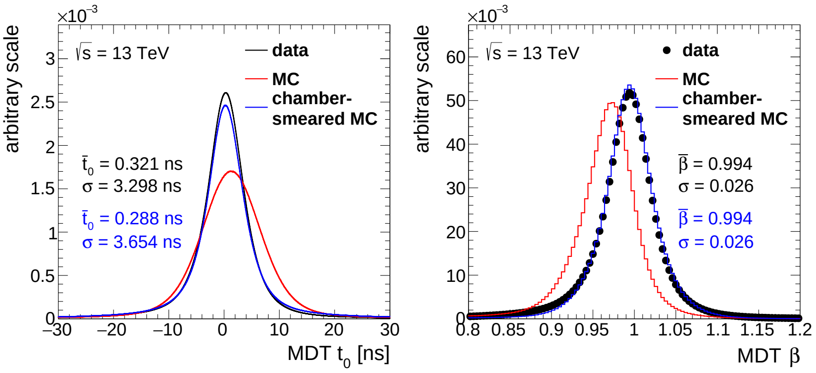

Figure 4.58: Effect of the chamber-based smearing on the simulated timing and β distributions. Some discrepancies on the peak of the t_0 distribution are observed. The β distributions on the other hand agree very well. Discrepancies here are confined to the tails and are of limited interest for analysis.

4.10 RPC simulation timing smearing

A comparison of the untreated RPC timing and corresponding β distributions produced from the sample of simulated $Z^0 \to \mu\mu$ events described in chapter 4.9 with fully calibrated RPC data is shown in figure 4.59.

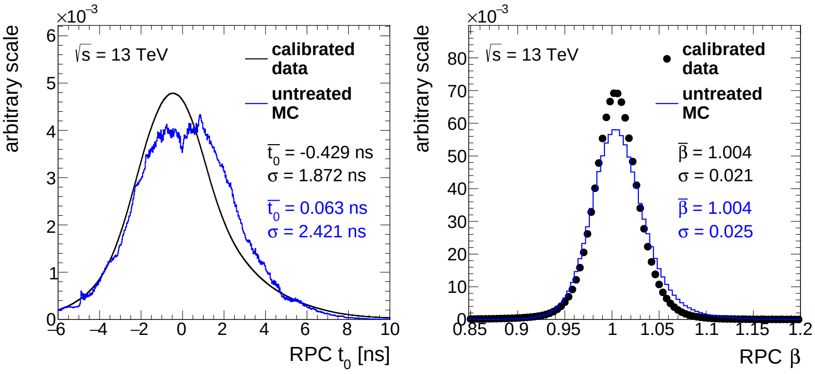

Figure 4.59: Comparison of unsmeared RPC timing and β distributions with fully calibrated RPC data. The MC t_0 distribution is very jagged and shows a dip in its central region resulting from the intrinsic detector timing granularity. Compared to MDTs the agreement of untreated MC with data is slightly better, a dedicated treatment procedure is nevertheless required.

Just like for the MDTs the untreated MC and data do not agree and a correction is therefore necessary. Contrary to data, the untreated MC t_0 distribution is far from smooth and shows a dip at the centre where $t_0 \approx 0$. As this seems unintuitive, a detailed study has been conducted to investigate the origin of this feature. The study is summarised in appendix C. In short, since the RPCs work with an internal 320 MHz clock the readout only happens in steps of 3.125 ns. Those ticks are then smeared out by the propagation time on the strip[18]. The position of the readout tick at $t_0 = \pm 1.5625$ ns results in a small dip in between the ticks at $t_0 = 0$.

The hit simulation is designed to reproduce the overall timing behaviour of the RPC system, but ignores individual differences between readout strips. Timing distributions are thus expected to be correctly calibrated and centred around $t_0 = 0$. However, this is not the case as can be seen from figure 4.60 where the means of strip-wise timing distributions are plotted. A significant fraction of strips has a mean that is clearly shifted away from zero towards larger values. Investigations have been conducted into the origin of those shifted values and it was found that more than 90% of the strips with shifted distributions are η strips located in the BMS stations. Other stations seem to be unaffected. Since this behaviour is neither expected nor explained yet, the dedicated experts have been made aware of the problem and they will carry on the investigation and develop a fix for future MC productions if needed.

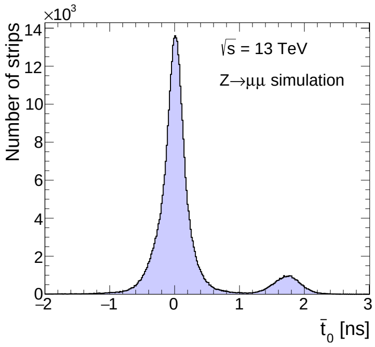

Figure 4.60: Means of the t_0 distributions for all RPC strips in simulated $Z \to \mu\mu$ events. While most strips have t_0 distributions centred around $t_0 = 0$, predominantly η strips in the BMS stations have shifted means.

The problem is easily corrected by applying a correction constant to all strips with $\bar{t}_0 > 1.0$ ns.

Similarly to the means of the strip timing distributions the widths are expected to be similar across all strips. The differences in widths of the strip timing distributions between data and simulation ($\sigma_{\text{data}} - \sigma_{\text{MC}}$) are plotted on the left of figure 4.61. Once again the result defies expectation. Instead of one Gaussian-like distribution, two separate distributions can be seen. The underlying cause is to be found in simulation as can be seen by plotting the differences in width as function of the width in MC as was done in the right plot of figure 4.61. Three distinct populations are visible. The main one is centred around $\sigma_{\text{data}} - \sigma_{\text{MC}} = 0$ and is found for small σ_{MC}. The second and third population have much larger simulated timing widths and are also the ones exhibiting the largest difference when compared to data.

---

[18] Depending on the hit position on the readout strip typical propagation times are < 4 ns for chambers which are broken up into two units of double gas gaps and < 5 ns for chambers with only a single unit of double gas gaps.

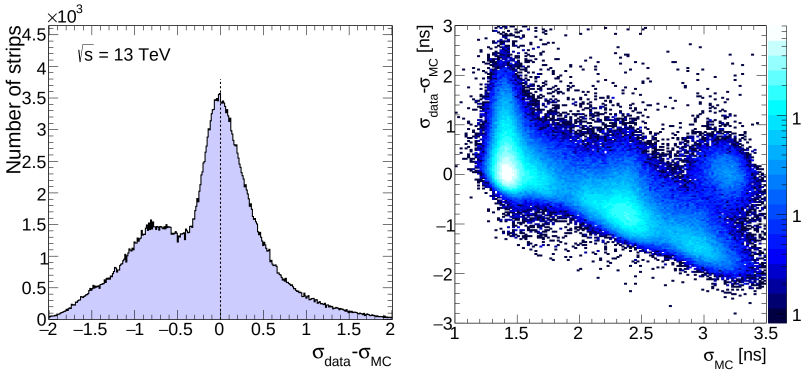

Figure 4.61: Left: Differences in width of strip timing distributions in data and simulation. The dashed line represents equal width. Right: The same quantity is plotted as a function of the width in MC. Three distinct populations are clearly discernible. The broader the timing distribution in MC, the larger also the discrepancy with data.

Some effort has been invested into pin-pointing the strips affected from this behaviour. It was found that once again the η strips in the BMS stations contribute, but also a large fraction of ϕ strips all throughout the detector. Plots and explanations summarising the investigations into the shifted means and wrongly simulated timing widths can be found in appendix D. Just as for the shifted means there is as of the moment of writing no explanation for this feature and RPC simulation experts have been notified.

The following strategy to treat too broad strips has been adopted: Strips in the main population with widths $\sigma_{\text{MC}} \leq 1.9$ receive no correction as their width seems to be in agreement with data[19]. The second population of strips with $1.9 < \sigma_{\text{MC}} \leq 2.7$ are artificially sharpened. Here it is important to respect the intrinsic timing granularity of the detector. Since the readout happens only every 3.125 ns, the sharpening can also only happen in multiples of this tick spacing. A sharpening factor of $s = 0.5$ is chosen, which is motivated retrospectively by the excellent results it yields. In essence this means a signal which arrives in the second tick after its supposed arrival calculated from truth, is shifted by 3.125 ns towards the intended arrival (see figure 4.62). Lastly, all strips with timing widths exceeding 2.7 are rejected from the β estimation. As a final step of the RPC MC treatment, a global overall shift of 120 ps is applied to simulation to produce an agreement of the mean value with data.

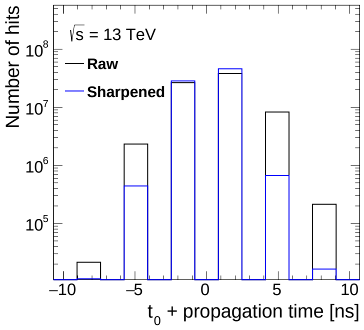

Figure 4.62: Plotted are the number of hits in the primary readout ticks for strips with $1.9 < \sigma_{\text{MC}} \leq 2.7$ prior to sharpening (black) and after tick-wise sharpening (blue). Signal arriving in the second tick from zero is shifted by one tick.

The procedure results in the overall RPC timing distribution shown on the left of figure 4.63. The effects of the sharpening result in less pronounced tails of the treated MC timing distribution and the shifted means in a generally smoother appearance. In the right plot of figure 4.63 the β distributions calculated from the treated timing distribution is compared to data. Here, an excellent agreement both in mean value and width is observed. The errors and therefore the weights for the weighted average calculation have been taken from data.

[19] i.e. the dashed line in the left plot of figure 4.61 is right at the centre of the main peak. Thus, too broad and too narrow distributions will compensate each other resulting in a good agreement with data.

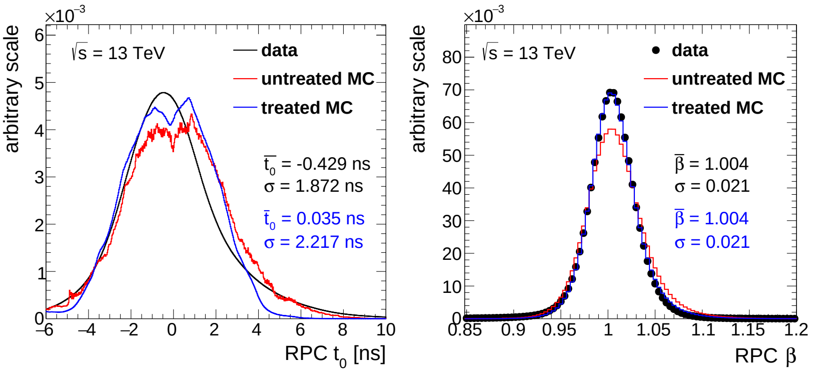

Figure 4.63: Comparison of data with the untreated and treated simulated RPC timing (left) and β (right) distributions. The effect of the sharpening for certain readout strips can be seen in the timing distribution where the tails have diminished through the treatment. Agreement with data is neither observed nor expected. The β distributions agree very well. Mean and width of Gaussian fits to the data are given.

It is now possible to combine the β measurements from the MDT and the RPC system and compare to the calibrated combined MS β in data. The result can be seen in figure 4.64. Once again the β estimates have been combined in a weighted average, where the weights are derived from the uncertainty on the individual estimate. Since the simulation treatment in the RPCs is not trying to precisely reproduce the timing distributions in data, the uncertainty on the β estimate has to be corrected for this. To that end, a pull correction like described in chapter 4.7 is performed for MC and uncertainties corrected accordingly. As was expected, a good agreement between data and MC can be observed. The combination serves as a good cross-check for the validity of the MC strategy applied here.

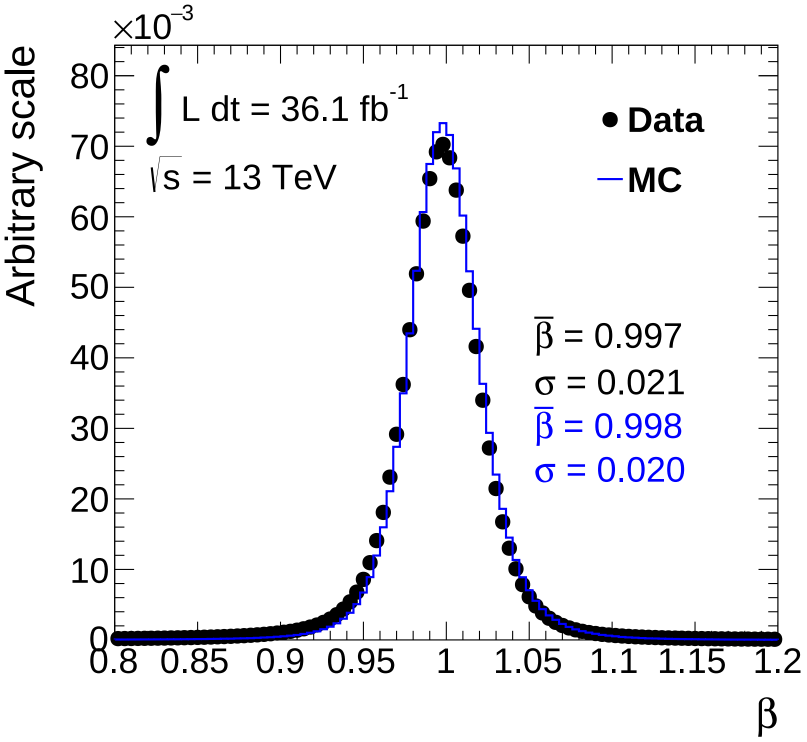

Figure 4.64: Comparison of the fully calibrated Muon Spectrometer β distribution with the treated MC β calculated from treated timing information. The estimates from MDT and RPC have been combined in a weighted average with the weights derived from the uncertainty on the tube or strip β estimate. The uncertainties on individual hits have been taken from data in either case and are pull corrected individually in data and simulation. The mean and width of the distributions are given. They are determined by a Gaussian parameterisation to the data. A good agreement between data and MC is observed.

4.11 Application to signal MC

The MC strategy developed in the previous two chapters is applied to signal MC for analysis. Since in signal particles are travelling with $\beta < 1.0$, the smearing and sharpening procedures are applied not to the t_0[20], but to the resolution of the tube or strip, which is defined as difference of the measured ToF and the ToF calculated under consideration of the correct β. In the following, signal MC is a dataset consisting of stable R-hadrons, charginos and staus with different masses. No discrimination between different types of signal or masses are attempted, the samples are only used as a source for $\beta < 1.0$ particles. The details of the signal samples used for the study are given in chapter 5.1.

A comparison of the MDT and RPC resolution for calibrated data and treated $Z \to \mu\mu$ and signal MC can be found in figure 4.65. The dip which was observed in the simulated timing distribution is not visible in signal since it is smeared out over different ticks because of the wide signal β distribution.

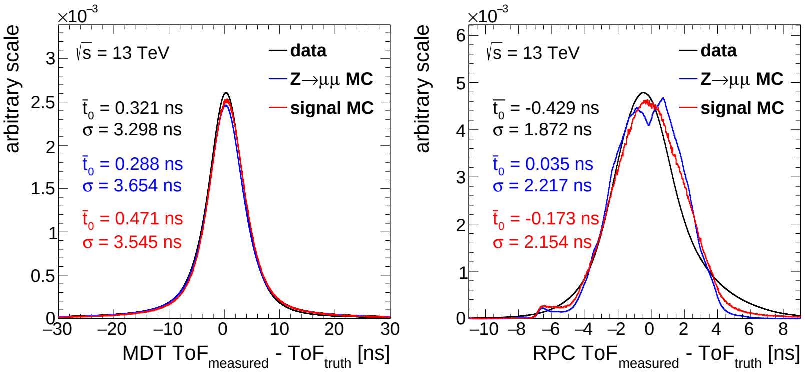

Figure 4.65: Comparison of the detector timing resolution of muons in calibrated data (black), muons from simulated $Z \to \mu\mu$ events (blue) and simulated slow particles (red). For MDTs (left) all three distributions are on top of each other. For RPCs this ideal case is not achieved, however, a generally similar behaviour is observed. Mean and widths of Gaussian parameterisations to the data are given. The general agreement between simulated $Z \to \mu\mu$ and signal validates the MC strategy developed here.

In the MDT system an excellent agreement between all three distributions is achieved. In the RPC system, where a precise agreement is not demanded, the general behaviour is recognisably the same. The agreement shows that the MC strategy developed for muons from simulated $Z \to \mu\mu$ events can be applied for simulated signal particles as well.

Figure 4.66 compares the β spectrum of signal MC samples before and after calibration.

The effect of the MC treatment on the signal β distribution is small but slightly more pronounced for the MDTs. In both cases the β distribution is corrected towards slightly larger values.

4.12 Summary

In this chapter a detailed description of the calibration of the MDT and RPC system for β measurement in data and simulation was given. High-p_T muons are used for the calibration as their veloc-

[20] Recall the definition of t_0 as the ToF of a speed-of-light particle subtracted from the measured ToF. For signal MC the t_0 is therefore a measure on the delay of the particles arrival with respect to the speed of light.

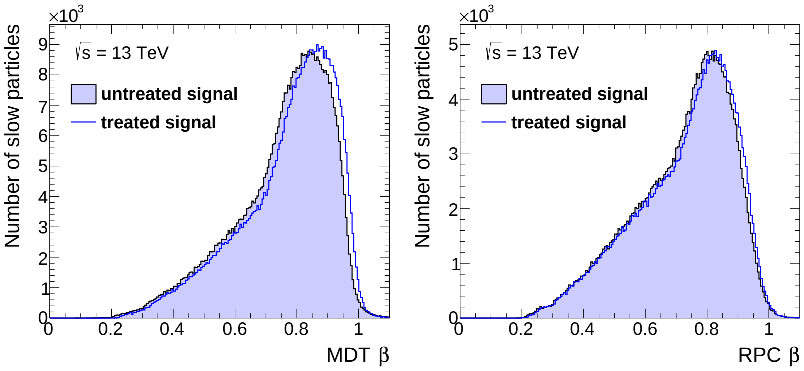

Figure 4.66: MDT (left) and RPC (right) β distributions for a combination of different hypothetical slow particles with different masses before and after application of the MC strategy. The effect of the calibration is small in both cases and corrects β towards slightly larger values.

ity is well known to be the speed of light. The uncalibrated data does not reproduce this result and a calibration is necessary. For the MDTs the calibration is done for every drift tube. 323 799 pairs of calibration constants are derived from Gaussian fits to the data. For the RPC system the first step is to counteract the effects of the online calibration that was changed several times during the taking of data. Afterwards, Gaussian fits are performed for all 362 262 readout strips from which calibration constants are derived. Many RPC strips with prominent multi-peak structures have been observed which requires strong hit selection cuts for their suppression. Both systems then undergo a time-dependent phase shift correction which corrects changes to the timing from environmental influences. Lastly, the uncertainties on the β estimate which were derived from the widths of the fitted Gaussian distributions are adjusted to be consistent with the width of the β distribution. The procedure yields not only the best combined MS β resolution to date, but also for both involved systems with a final resolution of $\sigma_\beta = 0.021$.

Since the timing distributions are not well modelled in simulation, it was necessary to develop a strategy for Monte Carlo treatment to reproduce the timing and β spectra observed in data. Simulated $Z \to \mu\mu$ events are used. It was found that a classical smearing could not be applied to the MDT system since simulated timing distributions underestimated the data resolution in many stations. A sharpening procedure was thus developed to artificially enhance the resolution in simulation and thus enable a subsequent smearing to work. Smearing constants have been derived for every chamber by fitting the timing distributions with the sum of a Gaussian and a Breit-Wigner function. The agreement of data and simulation for the RPC system has been better in general than for the MDTs. After artificial sharpening of a subset of readout strips with very wide timing distributions, the shape in data is well reproduced. The combination of systems yields a good agreement between data and Monte Carlo. Lastly, the application of the MC treatment has been demonstrated for signal MC and shown to produce the expected results.

CHAPTER 5

Search for Stable Massive Particles

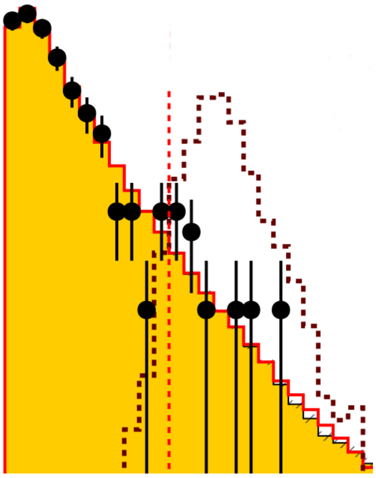

In the following a search for stable massive particles with the ATLAS detector is presented. The principle analysis strategy is similar for all sought-for particle hypotheses. Detector-stable gluinos from Split SUSY models, as well as bottom and top squarks hadronise into R-hadrons and are addressed in a full-detector and an MS-agnostic analysis, in which signals from the MS are ignored to account for charge-flip reactions, limited lifetimes and the lack of a comprehensive hadronic interaction model. Full-detector searches are performed for long-lived staus and charginos. The stau results are interpreted in the framework of GMSB models with the $\tilde{\tau}$ being the NLSP, while interpretations for minimal AMSB models are done for long-lived charginos.

The details of the dataset and simulated samples are given in chapter 5.1, followed by a descriptions of object definitions in chapter 5.2 and the main observables in chapter 5.3 and 5.4. The online selection of events and associated corrections are detailed in chapter 5.5. Chapter 5.6 lists the offline selection requirements and signal-region definitions. The procedure for a data-driven background estimation is given in chapter 5.7. An account of systematic uncertainties are listed in chapter 5.8. Lastly, the results of the searches are interpreted and discussed in chapter 5.9.

5.1 Data and Monte Carlo samples

The analysis is carried out using a data sample amounting to 36.1 fb^{-1} of proton–proton collisions at $\sqrt{s} = 13$ TeV collected in 2015 and 2016 with the ATLAS detector. A specific data format called the SUSY8 derivation, as defined in appendix A, is used for data and all simulated samples.

Simulated samples are treated equivalently to data. This means identical object definitions and the usage of the same reconstruction algorithms in data and simulation. All simulated events have to pass the full GEANT4 ATLAS detector simulation [291, 292]. Simulated $Z \to \mu\mu$ Monte Carlo events are used for the timing resolution stud-

	m [GeV]	σ [pb]	σ_σ [%]
$\tilde{g}$	400	9.82×10^{1}	14
$\tilde{g}$	600	9.22×10^{0}	14
$\tilde{g}$	800	1.49×10^{0}	15
$\tilde{g}$	1000	3.25×10^{-1}	17
$\tilde{g}$	1200	8.56×10^{-2}	18
$\tilde{g}$	1400	2.53×10^{-2}	21
$\tilde{g}$	1600	8.09×10^{-3}	24
$\tilde{g}$	1800	2.76×10^{-3}	28
$\tilde{g}$	2000	9.80×10^{-4}	32
$\tilde{g}$	2200	3.59×10^{-4}	36
$\tilde{g}$	2400	1.34×10^{-4}	41
$\tilde{g}$	2600	5.03×10^{-5}	46
$\tilde{g}$	2800	1.89×10^{-5}	51
$\tilde{g}$	3000	7.12×10^{-6}	57
$\tilde{b}$	600	1.75×10^{-1}	13
$\tilde{b}$	800	2.83×10^{-2}	14
$\tilde{b}$	1000	6.15×10^{-3}	16
$\tilde{b}$	1200	1.60×10^{-3}	19
$\tilde{b}$	1400	4.61×10^{-4}	23
$\tilde{t}$	600	1.75×10^{-1}	13
$\tilde{t}$	800	2.83×10^{-2}	14
$\tilde{t}$	1000	6.15×10^{-3}	16
$\tilde{t}$	1200	1.60×10^{-3}	19
$\tilde{t}$	1400	4.61×10^{-4}	23

Table 5.1: List of all R-hadron MC samples used for analysis. Given is the simulated SUSY constituent, its mass m, the production cross-section σ and the uncertainty on the production cross-section σ_σ. About 10 000 events have been generated per mass point.

ies described in chapter 4. The details of the sample are given in chapter 4.9.

For a meaningful physics interpretation it is necessary to know how a possible signal would turn up in the analysis and to optimise the selection for maximal signal significance. Thus, simulated signal MC samples are produced.

For stable R-hadron samples the pair production of gluinos, bottom and top squarks is simulated in PYTHIA6 V4.28.2 [297]. Specialised hadronisation routines [137, 298] are employed to ensure final states containing R-hadrons. Contributions from other SUSY particles to the pair production are minimised by setting their masses to very large values. The interactions of the R-hadrons in the detector are taken care of by dedicated GEANT4 algorithms that assume a generic interaction model for the gluino R-hadrons and a Triple-Regge model for the squark R-hadrons (see chapter 2.7.1). It is assumed that 10% of the produced gluinos form gluino balls [128]. Simulated gluino masses range from 400 GeV to 3000 GeV in steps of 200 GeV, bottom and top squarks were simulated with masses between 600 GeV and 1400 GeV with the same spacing. An overview of all stable R-hadron samples is given in table 5.1.

Simulations of mAMSB [299] events containing stable charginos are done using MG5_aMC@NLO v2.3.3 [300] which is interfaced with PYTHIA8.212 [287] for a correct modelling of parton showering and EVTGEN V1.2 [288] using the A14 generator tune [301] with the NNPDF23LO parton distribution function (pdf) set [302]. For all samples the model parameters were fixed to $m_0 = 5$ TeV and $\tan\beta = 5$, whereas the values of $m_{3/2}$ and $m_{\chi_1^\pm}$ were varied. Chargino masses between 200 GeV and 1500 GeV have been simulated in both a $\chi_1^\pm\chi_1^\pm$ and $\chi_1^\pm\chi_1^0$ production channel. The full list of samples with chargino masses, production cross-section and uncertainty on the cross section is given in table 5.2.

MC samples containing stable staus that are directly produced in pairs via Drell-Yan processes and originate from a GMSB scenario are generated using a similar setup to the chargino samples. MG5_aMC@NLO v2.3.3 is used for event generation. The correct modelling of parton showers, underlying event and hadronisation is done employing the A14 tune for PYTHIA8.212. The matrix element calculations are executed on tree-level and allows for the radiation of an additional parton. The model parameters are fixed to $m_{\text{Messenger}} = 500$ TeV, $\tan\beta = 10$ and $C_{\text{grav}} = 100000$, where the latter is a measure for the lifetime of the stau. The parameter λ is left floating to allow for different masses of the pair-produced stable staus in the range 287 GeV to 911 GeV. The full list of samples with stau masses, values of the model parameter λ, production cross-sections and uncertainty on the cross section is given in table 5.3.

An additional set of MC samples is required for the R-hadron search. The E_T^{miss}, which is also used for triggering, arises from the small energy deposits of R-hadrons in the calorimeters in combination with high-p_T jets originating from gluon or light quark radi-

	m [GeV]	σ [pb]	σ_σ [%]
$\tilde{\chi}_1^\pm\tilde{\chi}_1^\pm$	199.72	8.83×10^{-1}	7
$\tilde{\chi}_1^\pm\tilde{\chi}_1^\pm$	250.00	3.78×10^{-1}	6
$\tilde{\chi}_1^\pm\tilde{\chi}_1^\pm$	299.82	1.87×10^{-1}	6
$\tilde{\chi}_1^\pm\tilde{\chi}_1^\pm$	349.93	9.97×10^{-2}	6
$\tilde{\chi}_1^\pm\tilde{\chi}_1^\pm$	400.27	5.68×10^{-2}	6
$\tilde{\chi}_1^\pm\tilde{\chi}_1^\pm$	449.81	3.44×10^{-2}	6
$\tilde{\chi}_1^\pm\tilde{\chi}_1^\pm$	500.24	2.13×10^{-2}	7
$\tilde{\chi}_1^\pm\tilde{\chi}_1^\pm$	549.84	1.38×10^{-2}	7
$\tilde{\chi}_1^\pm\tilde{\chi}_1^\pm$	599.89	9.12×10^{-3}	7
$\tilde{\chi}_1^\pm\tilde{\chi}_1^\pm$	649.74	6.14×10^{-3}	7
$\tilde{\chi}_1^\pm\tilde{\chi}_1^\pm$	700.06	4.19×10^{-3}	7
$\tilde{\chi}_1^\pm\tilde{\chi}_1^\pm$	749.77	2.94×10^{-3}	7
$\tilde{\chi}_1^\pm\tilde{\chi}_1^\pm$	799.90	2.08×10^{-3}	8
$\tilde{\chi}_1^\pm\tilde{\chi}_1^\pm$	849.86	1.48×10^{-3}	8
$\tilde{\chi}_1^\pm\tilde{\chi}_1^\pm$	899.81	1.08×10^{-3}	9
$\tilde{\chi}_1^\pm\tilde{\chi}_1^\pm$	949.67	7.83×10^{-4}	8
$\tilde{\chi}_1^\pm\tilde{\chi}_1^\pm$	1000.05	5.73×10^{-4}	8
$\tilde{\chi}_1^\pm\tilde{\chi}_1^\pm$	1099.98	3.16×10^{-4}	9
$\tilde{\chi}_1^\pm\tilde{\chi}_1^\pm$	1200.01	1.79×10^{-4}	9
$\tilde{\chi}_1^\pm\tilde{\chi}_1^\pm$	1299.75	1.03×10^{-4}	9
$\tilde{\chi}_1^\pm\tilde{\chi}_1^\pm$	1400.10	5.99×10^{-5}	10
$\tilde{\chi}_1^\pm\tilde{\chi}_1^\pm$	1500.06	3.56×10^{-5}	10
$\tilde{\chi}_1^\pm\tilde{\chi}_1^0$	199.72	1.78×10^{0}	5
$\tilde{\chi}_1^\pm\tilde{\chi}_1^0$	250.00	7.69×10^{-1}	5
$\tilde{\chi}_1^\pm\tilde{\chi}_1^0$	299.82	3.81×10^{-1}	4
$\tilde{\chi}_1^\pm\tilde{\chi}_1^0$	349.93	2.06×10^{-1}	4
$\tilde{\chi}_1^\pm\tilde{\chi}_1^0$	400.27	1.18×10^{-1}	5
$\tilde{\chi}_1^\pm\tilde{\chi}_1^0$	449.81	7.18×10^{-2}	5
$\tilde{\chi}_1^\pm\tilde{\chi}_1^0$	500.24	4.47×10^{-2}	5
$\tilde{\chi}_1^\pm\tilde{\chi}_1^0$	549.84	2.92×10^{-2}	5
$\tilde{\chi}_1^\pm\tilde{\chi}_1^0$	599.89	1.94×10^{-2}	6
$\tilde{\chi}_1^\pm\tilde{\chi}_1^0$	649.74	1.31×10^{-2}	6
$\tilde{\chi}_1^\pm\tilde{\chi}_1^0$	700.06	9.02×10^{-3}	6
$\tilde{\chi}_1^\pm\tilde{\chi}_1^0$	749.77	6.35×10^{-3}	6
$\tilde{\chi}_1^\pm\tilde{\chi}_1^0$	799.90	4.50×10^{-3}	6
$\tilde{\chi}_1^\pm\tilde{\chi}_1^0$	849.86	3.22×10^{-3}	6
$\tilde{\chi}_1^\pm\tilde{\chi}_1^0$	899.81	2.34×10^{-3}	6
$\tilde{\chi}_1^\pm\tilde{\chi}_1^0$	949.67	1.70×10^{-3}	6
$\tilde{\chi}_1^\pm\tilde{\chi}_1^0$	1000.05	1.24×10^{-3}	7
$\tilde{\chi}_1^\pm\tilde{\chi}_1^0$	1099.98	6.82×10^{-4}	7
$\tilde{\chi}_1^\pm\tilde{\chi}_1^0$	1200.01	3.82×10^{-4}	7
$\tilde{\chi}_1^\pm\tilde{\chi}_1^0$	1299.75	2.17×10^{-4}	7
$\tilde{\chi}_1^\pm\tilde{\chi}_1^0$	1400.10	1.24×10^{-4}	7
$\tilde{\chi}_1^\pm\tilde{\chi}_1^0$	1500.06	7.26×10^{-5}	8

Table 5.2: List of all stable chargino MC samples used for analysis. Given is the simulated production channel, the mass m of the stable chargino, the production cross-section σ and the uncertainty on the production cross-section σ_σ. About 10 000 events have been generated per mass point.

ation. In order to achieve meaningful physical results it is crucial to have an accurate description of such initial-state radiation (ISR). Since MG5_aMC@NLO allows for the radiation of an additional jet in the calculation of the matrix element, it is expected to yield a more trustworthy ISR spectrum than Pythia6, which was used for the generation of samples, where additional jets are introduced only through showering. In the absence of a viable alternative to the event generation in Pythia6 and to nevertheless profit from the advantages of MG5_aMC@NLO, all events are reweighted to match the more accurate ISR spectrum in MadGraph. To that end, pair-produced gluino events are generated, where the gluino masses correspond exactly to the masses in table 5.1. Since only the information on truth-level is required, no detector simulation is necessary. Reweighting samples were produced with MG5_aMC@NLO v2.2.3 interfaced with Pythia8.186 and EvtGen v1.2 using the A14 tune and NNPDF23LO pdf set. Approximately 20 000 events were produced for every mass point.

λ [TeV]	m [GeV]	σ [pb]	σ_σ [%]
90	287	2.08×10^{-3}	6
100	318	1.37×10^{-3}	6
110	349	9.29×10^{-4}	7
120	380	6.46×10^{-4}	7
130	411	4.59×10^{-4}	7
140	442	3.32×10^{-4}	7
150	473	2.43×10^{-4}	7
160	504	1.80×10^{-4}	8
170	536	1.36×10^{-4}	8
180	567	1.04×10^{-4}	9
190	598	7.93×10^{-5}	8
200	629	6.13×10^{-5}	9
210	660	4.77×10^{-5}	9
220	692	3.75×10^{-5}	9
230	723	2.96×10^{-5}	9
240	754	2.35×10^{-5}	9
250	785	1.87×10^{-5}	10
260	817	1.50×10^{-5}	10
270	848	1.22×10^{-5}	10
280	879	9.81×10^{-6}	10
290	911	7.95×10^{-6}	10

Table 5.3: List of all stable stau MC samples used for analysis. Given is the mass m of the stable stau, the λ value of the model, the production cross-section σ and the uncertainty on the production cross-section σ_σ. About 10 000 events have been generated per mass point.

In order to derive reweighting factors, the pair of gluinos or quarks prior to hadronisation are identified on truth-level and their transverse momenta are added vectorially. This sum needs to be balanced by the recoil of an ISR jet. Comparing the spectra from both generators allows to derive bin-wise correction factors which are then applied as an additional event weight to the R-hadron event. To allow for an adequately fine binning with the limited statistics available in the samples, a smoothing function is applied to the calculated ratio[1]. An example reweighting function is depicted in figure 5.1.

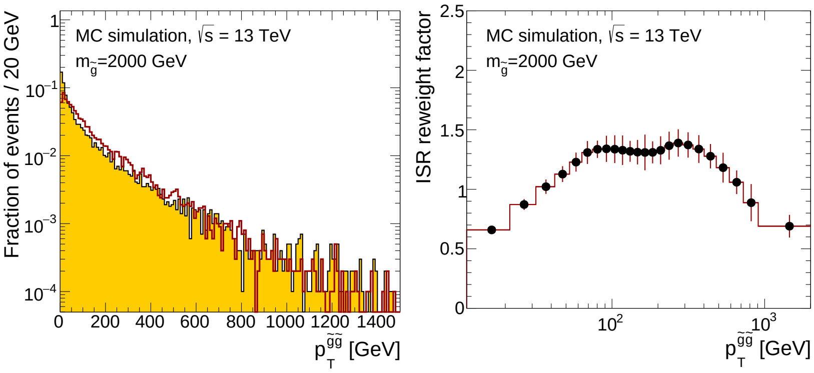

Figure 5.1: Illustration of the ISR reweighting for events with pair-produced gluinos with $m_{\tilde{g}} = 2000$ GeV. Left: comparison of the truth-level transverse momentum distributions for the gluino–gluino system in Pythia6 and MG5_aMC@NLO samples. Right: reweighting factors derived from the ratio of the p_T spectra after application of a smoothing function.

Reweighting files have only been produced for gluino-pairs, but it was shown that gluinos reproduce the ISR spectrum of bottom- and top-squark pairs (see for example figure 5.2). The bottom- and top-squark R-hadron samples are thus reweighted on the basis of the gluino–gluino transverse momentum spectrum. Stable stau and chargino samples do not require an ISR reweighting as they are already simulated in MadGraph. A systematic uncertainty on the ISR modelling is estimated in chapter 5.8.4.

[1] The smoothing function used is based on the 353QH algorithm. Its name suggests its functionality: it uses running medians in a sequence of three, followed by five and three again. The 'Q' indicates a quadratic interpolation and the 'H' refers to the running means ("Hanning"). For details see [303].

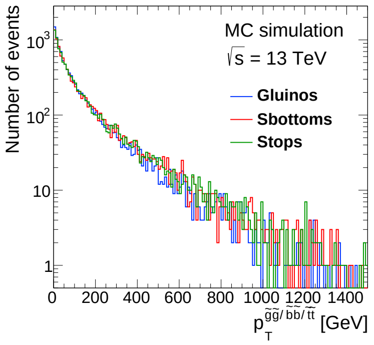

Figure 5.2: Comparison of the ISR spectrum of 1000 GeV gluinos, bottom and top squarks. Since the spectra agree within statistical uncertainties the bottom and top squark samples can be reweighted based on the gluino ISR spectrum.

5.2 Object reconstruction

Particle tracks in the ID are reconstructed by first forming clusters of hits in the Pixel and SCT detectors which then act as track seeds that are used by an iterative track-finding algorithm [304, 305]. Track finding is limited to $|\eta| < 2.5$ and $p_T > 400$ MeV. Furthermore, all tracks are required to possess at least 7 hits in the Pixel Detector and SCT.

Within ATLAS two different techniques for muon reconstruction are used. The first one constructs so-called standalone muons, i.e. tracklets in the MS, which are then extrapolated towards the IP and combined with nearby ID tracks [306]. The alternative is an inside-out approach in which ID tracks are extrapolated towards the MS and close-by hits are combined with the track measurement. After all hits have been identified, the track fit is repeated to improve the momentum measurement of the combined track [307]. In this analysis, full-detector tracks are reconstructed using the MuGirlStau algorithm which follows the inside-out approach and relies on signals coming from all MS technologies and the ID. Contrary to all other muon reconstruction algorithms, MuGirlStau does not assume particles to propagate with the speed of light [308]. Hence, it allows the reconstruction of charged SMPs besides regular muons. The algorithm reconstructs tracks in a window of $0.2 < \beta < 1.2$. As this track reconstruction is computationally expensive it is only executed for high-p_T tracks. During data-taking this cut was lowered from 60 GeV to 30 GeV[2].

5.3 Measurement of Pixel dE/dx

The specific ionisation is determined from cluster charge measurements in the Pixel Detector. It can be used to reconstruct the mass of a passing particle[3].

5.3.1 Pixel dE/dx measurement

The charge deposited in a pixel sensor is measured by recording the ToT as described in chapter 3.2.1 and expected to follow a Landau distribution with long tails. The detector was calibrated in order for a ToT of 30 BC (18 BC) to equate to the peak of the Landau distribution of a MIP crossing 250 μm of active material[4] in all pixel layers (in the first layer of the Pixel Detector (’B-layer’) during the 2016 data-taking period). The IBL has two kinds of sensors, planar and 3D, where the thresholds were tuned to correspond to 10 BC yielding an estimated 16 000 electron-hole pairs in 2015 and 8 BC in 2016.

Individual pixels are grouped into clusters and the cluster charge corrected for the path length within the sensor material is deter-

[2] See chapter 4.1 for more details on the transverse momentum cut

[3] For the dE/dx measurement the SMP search adapts the same procedure and method developed for the search of mSMPs which relied exclusively on Pixel Detector information to identify candidates. A more detailed description of the dE/dx determination can be found in the papers documenting the mSMP searches [167, 168, 309].

[4] This yields roughly 20,000 electron-hole pairs or 80 pairs per micrometer of sensor thickness.

mined. The dE/dx of a track is then calculated as the average of the cluster dE/dx measurements. Clusters at the module edges or in the ganged region[5] are rejected since the collected charge is biased for lower values. In order to reduce the long Landau tails, a truncated average is calculated by removing one or more clusters according to table 5.4.

Contrary to the rest of the Pixel Detector, the IBL offers a special readout bit indicating an overflow. If an IBL cluster is in overflow, the corresponding cluster is removed in any case. If another cluster with a charge larger than the one in overflow is present, it is removed as well provided more than three good clusters have been identified.

The measured Pixel dE/dx values are corrected for a slight η dependence and for changed threshold calibrations throughout data taking. Due to radiation damage the charge collection efficiency is notably reduced and scale factors are applied to correct the effect.

Good clusters	Removed cluster
1	None
2-4	Largest charge cluster
5+	Two largest charge clusters

Table 5.4: Pixel dE/dx values are determined by removing the up to two largest cluster charges as presented here.

5.3.2 $\beta\gamma$ and mass determination

For the mass estimation the most probable Pixel dE/dx value $\mathcal{M}_{dE/dx}$ is modelled as a function of $\beta\gamma$. To this end one considers minimum-bias collisions which contain high yields of pions, kaons and protons. The parameterisation is achieved in a stepwise fitting procedure[6]. First, the dE/dx distributions are fitted in momentum slices containing three asymmetric peaks from the three particle species. Second, the obtained pairs ($\mathcal{M}_{dE/dx}$,$\beta\gamma$) are fitted with one function $\mathcal{M}_{dE/dx}(\beta\gamma)$ that describes the dependency of the most probable value on $\beta\gamma$.

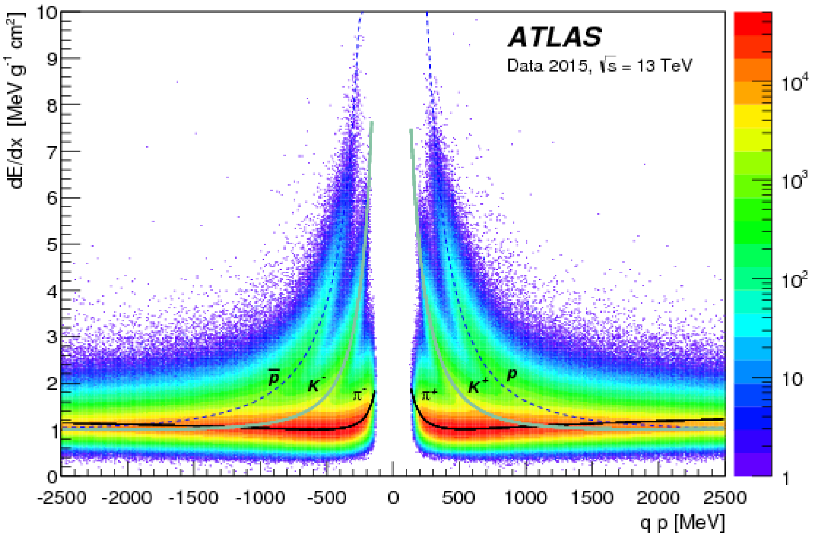

Figure 5.3: Measured dE/dx in minimum-bias collisions as a function of the particle momentum multiplied by its charge q. The fits for the most probable value according to equation 5.1 have been superimposed for pions, kaons and protons. The figure was taken from [167].

Figure 5.3 shows the dE/dx as a function of momentum multiplied by charge with parameterisations according to a Bethe-Bloch-function motivated empirical three-parameter function of the form

---

[5] Groups of pixels that share the same readout and can thus not be evaluated individually [235].

[6] The fitting is done independently for data and MC since simulation requires the scaling of measured dE/dx values for a systematic overestimation. It has also been verified with corrected MC that the parameterisation described here extends to large momenta and masses.

$$\mathcal{M}_{dE/dx}(\beta\gamma) = \frac{p_1}{(\beta\gamma)^{p_3}} + p_2 \tag{5.1}$$

superimposed for pions, kaons and protons.

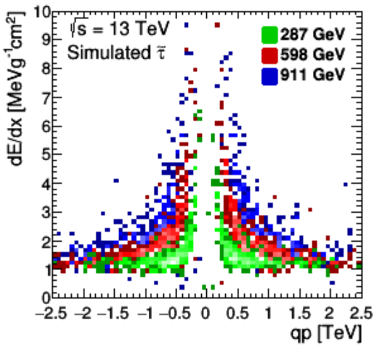

Figure 5.4: dE/dx as a function of momentum and charge for three stable stau mass points. Note the different scale on the x-axis when compared to figure 5.3.

By inversing the function $\mathcal{M}_{dE/dx}$ it is possible to derive $\beta\gamma$ for any measured dE/dx and momentum. The mass of the traversing particle is then determined via $m_{dE/dx} = p/\beta\gamma$.

The most important aspects of the pixel dE/dx and mass estimation are detailed in [237].

For comparison with figure 5.3, the dE/dx as function of momentum times electric charge is plotted in figure 5.4 for three different simulated stable $\tilde{\tau}$ masses.

A comparison of $\beta\gamma$ distributions for different masses and types of signal on truth level[7] is shown in figure 5.5. The $\beta\gamma$ for muons from simulated $Z \rightarrow \mu\mu$ decays is also drawn. However, the distribution peaks far outside the plotting range at values around $\beta\gamma \approx 630$.

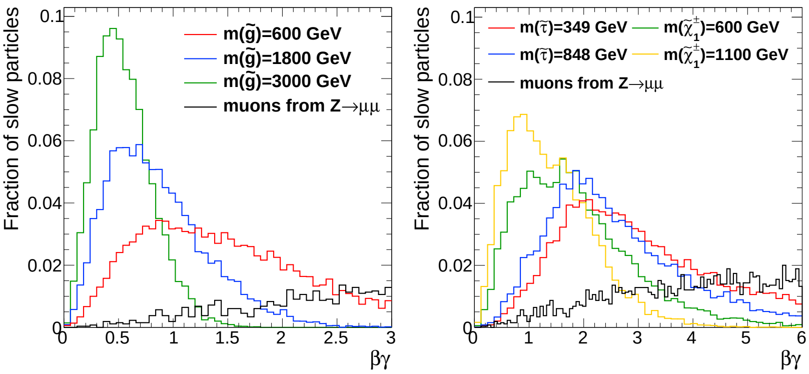

Figure 5.5: $\beta\gamma$ distributions taken from truth information for three gluino R-hadron masses (left) and two different stau and chargino masses (right). With increasing particle masses the propagation velocity decreases and the $\beta\gamma$ thus takes on small values. Note the different scales on the x-axis. The black line corresponds to muons of all momenta. The bulk is located far outside the plotting range. The distribution is normalised to the visible part.

5.4 Measurement of β via time-of-flight

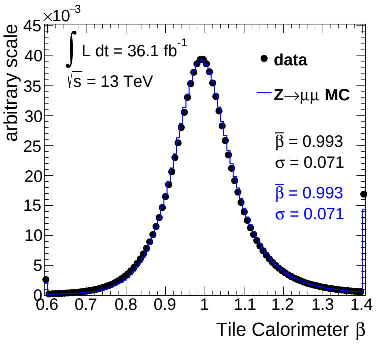

Figure 5.6: Comparison of the calibrated Tile Calorimeter β estimate with smeared $Z \rightarrow \mu\mu$ MC. Figure adapted from M. Adersberger.

An estimation of the propagation velocity β via time-of-flight measurements allows the reconstruction of the particle mass via $m_{\text{ToF}} = p/\beta\gamma$. The Tile Calorimeter as well as MDT and RPC chambers in the MS provide good enough sensitivity for an accurate measurement. The dedicated calibrations in the MS and resulting β resolution have been discussed in detail in chapter 4. The calibration process of the Tile Calorimeter is similar to the MS. The main features are detailed in [1, 2]. The calibration starts by correcting a bias introduced by the Optimal Filtering Algorithm [310] used in the readout and is followed by a geometry correction which accounts for the large cell sizes and a correction in bins of η. Since the timing depends on the deposited energy in the cell, an additional energy-dependent cell-timing correction is performed. A correction for run-dependent phase-shift variations, individual cell-by-cell differences and a pull correction of the uncertainties complete the Tile Calorimeter timing calibration. For simulation a dedicated smearing with subsequent

[7] Truth level refers to the true collision content before the detector response is simulated.

pull correction is applied. The calibrated Tile Calorimeter β distribution and smeared MC are drawn in figure 5.6.

The separate β measurements from the subsystems are combined in a weighted average according to the uncertainty σ_β on the individual measurement. The resulting combined β distribution for muons and combined uncertainty on the measurement are drawn in figure 5.7.

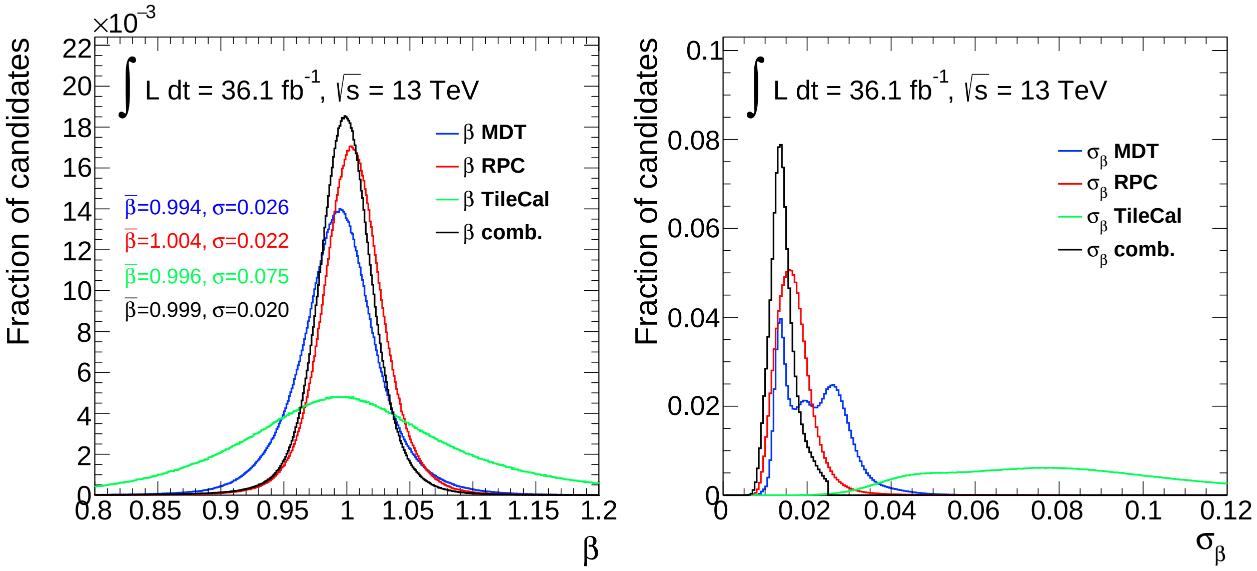

Figure 5.7: Combined β distribution and uncertainty σ_β alongside contributions from all subsystems. The combined β can be composed of only one, two or all three individual subsystem estimates. The structure in the Tile Calorimeter σ_β is a result of the number of cells used for the β estimation.

The direct comparison shows the advantages of the MS β-resolution over the Tile Calorimeter. The combined β and its uncertainty are dominated by the good RPC β resolution. Some structure can be observed in the σ_β distributions for MDTs and Tile Calorimeter. For MDTs it is due to the longer flight distances to the end-cap chambers resulting in better resolutions compared to the barrel, while for the Tile Calorimeter the resolution is driven by the number of cells used for the estimation.

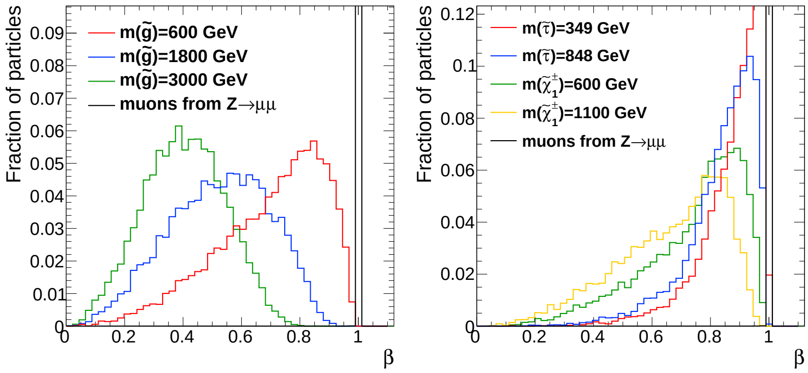

Figure 5.8: β distributions taken from truth information for three gluino R-hadron masses (left) and two different stau and chargino masses (right). With increasing particle masses the propagation velocity decreases and the β thus takes on small values. The black spike at $\beta = 1.0$ corresponds to the distribution for muons of all momenta.

In figure 5.8 the β distributions taken from truth information are plotted for different masses and types of signal. The distribution for muons of all momenta corresponds to a single spike at $\beta = 1$.

5.5 Online event selection

Events are selected online by requiring the event to be accepted by either a trigger on missing transverse energy or a single-muon trigger. For the MS-agnostic analysis the event selection relies exclusively on the E_T^{miss} trigger. During data-taking the trigger with the lowest threshold that was still running without a prescale (lowest unprescaled trigger) changed several times [311, 312]. Table 5.5 gives the thresholds of the lowest unprescaled triggers and the integrated luminosity of data collected with the trigger active.

In the following the triggers are discussed in more detail.

	$\mathcal{L}$ [fb^{-1}]	E_T^{miss} threshold [GeV]	Muon threshold [GeV]
A	3.2	70	20 L
B	0.5	90	24 L
C	5.6	90	24 M/VM
D	5.4	100	24 M/VM
E	1.1	100	26 M/VM
F	2.3	110	26 M/VM
G	18.0	110	26 VM

Table 5.5: Lowest unprescaled E_T^{miss} and single-muon trigger thresholds next to the amount of data for which the trigger chain has been active. To distinguish between time-intervals with different lowest unprescaled triggers, an arbitrary period number A-G is assigned. The supplemented letter to the single-muon trigger threshold indicates a loose (L), medium (M) or varmedium (VM) isolation definition of the trigger item.

5.5.1 Missing-transverse-energy trigger

With the exception of charginos that are produced in association with a neutralino, SMP events have no intrinsic missing energy. A momentum imbalance in the detector which can nevertheless give rise to reconstructed E_T^{miss} can originate from ISR, final-state radiation (FSR) and underlying event[8]. Underlying events cause soft uniform radiation with occasional upward fluctuations and are of negligible role for the trigger. FSR from the R-hadron, on the other hand, will not be confined to the cone around the direction of propagation as collinear FSR is suppressed [313] and will thus contribute to a momentum imbalance. However, at hadron colliders like LHC the expected ISR greatly surpasses FSR [128]. Thus, it has been concluded that in SMP events the E_T^{miss} trigger primarily relies on the presence of ISR. A generally low trigger efficiency can therefore be inferred for all particle hypotheses.

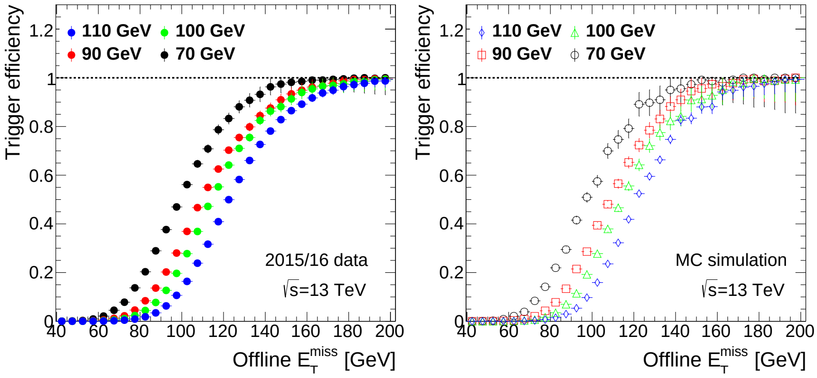

Figure 5.9: E_T^{miss} trigger onsets for all relevant triggers with different thresholds in data (left) and MC (right). The offline E_T^{miss} used here is based on calorimeter clusters without receiving corrections from the MS.

To cope with the rising instantaneous luminosities during data-taking, the threshold for the lowest unprescaled trigger was raised several times to keep the HLT trigger rate manageable. While the threshold stayed constant at 70 GeV throughout 2015, it was raised to a maximum of 110 GeV in 2016. The trigger is however not fully efficient above the designated threshold and instead exhibits a long

[8] Additionally detector effects like misreconstruction of the recoil jet play a minor role.

onset as function of the offline E_T^{miss}[9]. The onset behaviour of all relevant E_T^{miss} triggers in data and simulation is shown in figure 5.9.

The use of the E_T^{miss} trigger for R-hadron searches is primarily motivated by the lack of a feasible and better alternative. Though its efficiency is low, E_T^{miss} triggers still provide a better trigger efficiency for R-hadrons than the single-muon trigger in the full-detector event selection. Figure 5.10 shows the E_T^{miss} trigger efficiencies for all mass points of R-hadrons, charginos and staus.

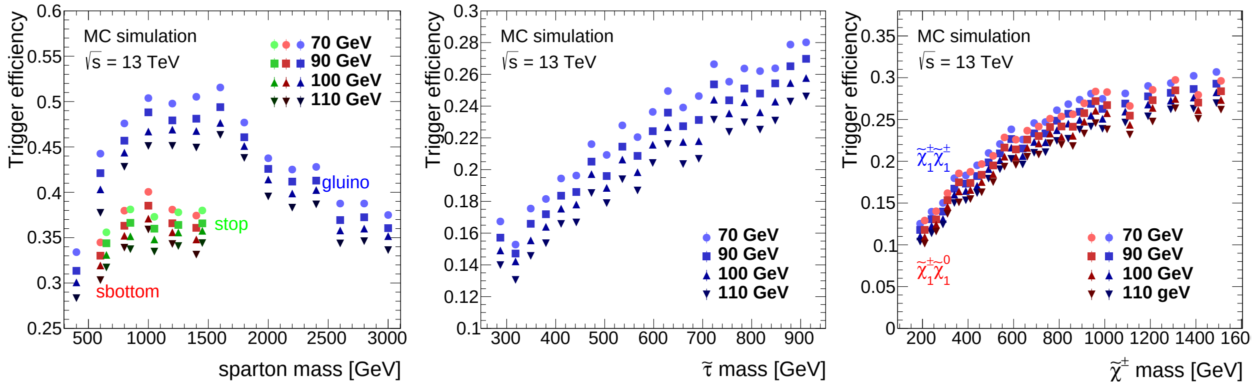

Figure 5.10: Efficiency of all E_T^{miss} triggers used in the analysis as function of the simulated R-hadron mass (left), stau mass (middle) and chargino mass (right). For better visibility the datapoints for the top squark have been shifted by 50 GeV on the mass axis, the datapoints for $\tilde{\chi}_1^{\pm}\tilde{\chi}_1^{\pm}$ have been shifted by 10 GeV to lower masses, $\tilde{\chi}_1^{\pm}\tilde{\chi}_1^{0}$ by 10 GeV towards larger masses.

A general feature is the rise in trigger efficiency for larger masses. This is due to the increased available energy which results in larger E_T^{miss} contributions from possible transverse-momentum imbalances through e.g. ISR. For R-hadrons, the increase in efficiency is followed by a rapid decrease since the dominant production channel changes from gluon–gluon fusion to quark–antiquark annihilation and reduces the ISR content for large masses.

5.5.2 Single-muon trigger

Single-muon triggers are only used in the full detector analysis. During the two years of data taking, the threshold has been raised several times ranging from 20 GeV to 26 GeV (table 5.5). Besides the threshold, an isolation requirement was used to control the trigger rate, where the working points have been chosen either loose (L), medium (M) or varmedium (VM)[10]. Since an offline cut on the muon momentum is applied during the analysis, the (anyway much sharper) trigger onset does not affect the signal efficiency like for the E_T^{miss} trigger. The trigger is only sensitive to muons arriving within the window of the collision bunch-crossing. Out-of-time muons arriving outside this trigger window will nevertheless fire the trigger, but will be attributed to the wrong BC. Since the ID has a readout window of only 1 BC, the ID information of the actual collision will be lost in such a case[11]. This has consequences for searches for slowly-propagating particles that arrive frequently too late in the trigger chambers and are thus lost. In MC, the L1 trigger electronics is simulated in detail and would reproduce the same trigger decisions as the hardware trigger, if the same signal is fed into the chain. However, in the

[9] Since the trigger decision needs to be fast, the calculation of the online E_T^{miss} is done only relying on calorimeter clusters. The offline E_T^{miss} receives corrections and can be very different from the online E_T^{miss}. Thus the broad onset functions.

[10] The isolation is computed using online reconstructed ID tracks within a cone of muon-p_T dependent size around the muon. E.g., the loose selection requires the scalar sum of transverse track momenta in a cone with $\Delta R = 0.2$ to be smaller than 12% of the muon p_T [314].

[11] Chapter 6 gives more information on this and introduces a novel trigger specialised on slow particles.

physical system the timing information is slightly distorted through cable delays which are approximately corrected for by application of electronic delays. While this compensation is working very well for muon physics, it is not accurate enough for SMP searches where timing is the key feature and the dedicated offline correction described in chapter 4 becomes necessary. However, the online trigger does not have access to the calibrated timing and the simulated timing does not reproduce data very well, as can be ascertained from figure 5.11. This causes a slight mismatch of trigger efficiency for slow particles. Since data does not provide any reasonable statistics to study the efficiency for late particles directly, the efficiency differences are assessed through a comparison of the absolute trigger times in data and MC.

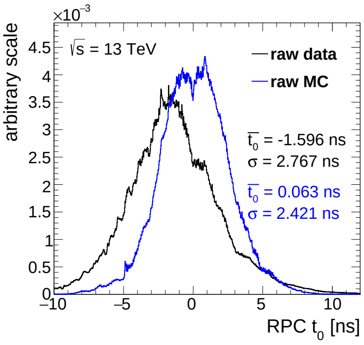

Figure 5.11: Uncalibrated RPC timing in data compared to untreated MC.

Figure 5.12 shows the result of a dedicated study carried out by the RPC trigger experts and shows the trigger times within the RPC L1 acceptance window ranging from 81.25 to 106.25 ns. Both the mean arrival time μ and the width of the timing distribution σ differ in data and MC.

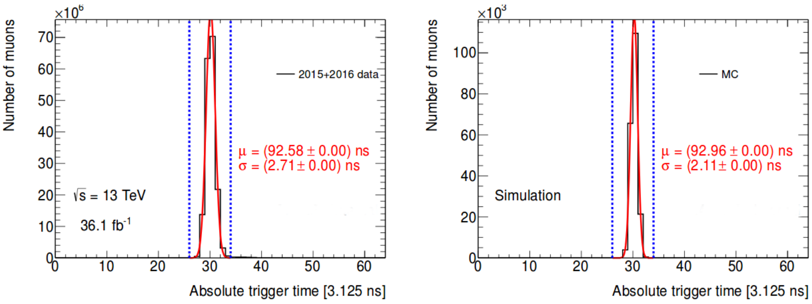

Figure 5.12: Arrival time of the trigger signal in the L1 RPC muon triggers in data (left) and MC (right). The x-axis denotes RPC readout ticks in the 8BC long readout window. An L1 Accept is issued if the trigger signal is located within the BC from tick 26 to 33, which is marked by dashed blue lines. Mean and width of the fitted timing distributions are printed, the associated uncertainties are small due to the large available statistics. The figure was taken from [315].

The parameters μ and σ being known, it is possible to calculate the trigger efficiency[12] as function of the particle β and η via

$$\varepsilon = \frac{1}{2}\left(1 - \operatorname{erf}\left(\frac{\frac{L}{\beta c} - \frac{L}{c} - t_{\text{end}} - \mu}{\sqrt{2}\sigma}\right)\right) \quad , \tag{5.2}$$

with $t_{\text{end}} = 106.25$ ns corresponding to the end of the trigger acceptance window, $L = r/\sin\theta$ and r the distance from the IP to the outermost RPC trigger chamber (i.e. $r = 10$ m). Plugging in the values for μ and σ from figure 5.12, one can derive scale factors to account for different trigger efficiencies. In events were exactly one candidate can be matched to a fired single-muon trigger in the barrel region with $|\eta| < 1.05$, scale factors ρ_1 are calculated via

$$\rho_1 = \frac{\varepsilon_{\text{data}}(\beta, \eta; \mu_{\text{data}}, \sigma_{\text{data}})}{\varepsilon_{\text{MC}}(\beta, \eta; \mu_{\text{MC}}, \sigma_{\text{MC}})} \quad . \tag{5.3}$$

Two examples of RPC trigger β onsets for data and MC are given in figure 5.13. In addition, the scaling factors ρ_1 are drawn. Since the efficiency functions assume very small values for small β, the resulting scaling factors can become very large. To prevent individual events from receiving too large weights a cut-off is introduced which restrains the scale factor to $\rho_1 < 5.0$.

---

[12] To be precise, ε is not the absolute trigger efficiency, but a scaled efficiency assuming a trigger which gets 100% efficient. This is not the case and to get the absolute trigger efficiency the calculated efficiency ε needs to be scaled to match the observed plateau efficiency in data. Since only the differences between data and MC are of concern at the moment, this scaling is neglected.

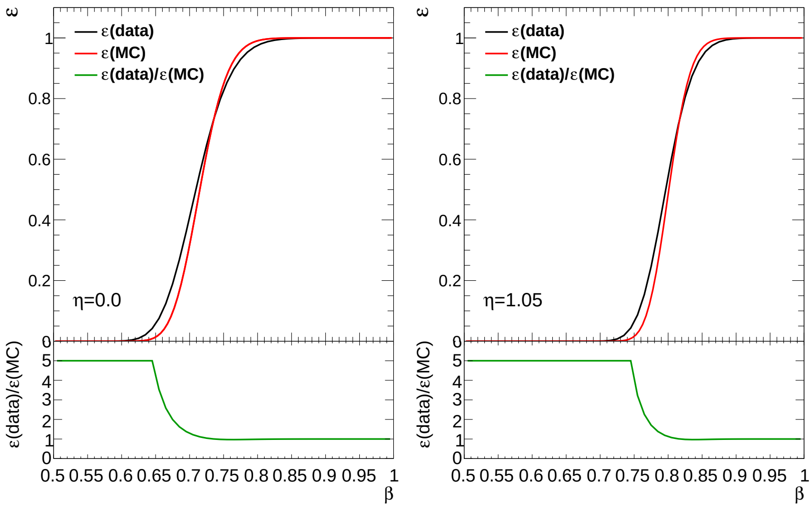

Figure 5.13: Comparison of trigger efficiencies in data (black) and MC (red) as function of β for particles passing in the centre of the barrel at $\eta = 0.0$ and particles at the edge of RPC acceptance at $|\eta| = 1.05$. The green function in the lower panel shows the scale factors ρ_1 which are given by the ratio of data and MC efficiency and a cutoff that prevents individual events from receiving too large weights.

In events where both SMP candidates can be matched to a fired single-muon trigger, the combined efficiency has to be considered. The scaling factors ρ_2 are calculated according to

$$\rho_2 = \frac{1 - (1 - \varepsilon^1_{\text{data}})(1 - \varepsilon^2_{\text{data}})}{1 - (1 - \varepsilon^1_{\text{MC}})(1 - \varepsilon^2_{\text{MC}})} \quad , \tag{5.4}$$

where the indices 1 and 2 denote the two candidates. A cutoff limiting $\rho_2 < 5.0$ is applied in this case as well. Thus, all events which were exclusively triggered through single-muon triggers receive a small correction to the event weight. The change in signal efficiency is $< 1\%$ for R-hadrons and $< 6\%$ for staus and charginos. As an example the scaled and unscaled combined β distributions of a stable stau sample with $m_{\tilde{\tau}} = 754$ GeV are plotted in figure 5.14.

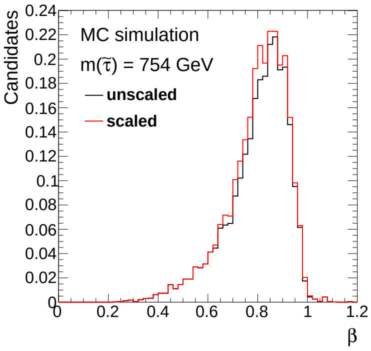

Figure 5.14: Combined β spectrum of a signal MC sample with 754 GeV staus before and after application of the single-muon trigger efficiency scaling.

The procedure is not an exact correction, since the absolute trigger time, i.e. the timing seen by the L1 muon trigger, is unknown on analysis level, and thus the β which needs to be used for equation 5.2 is merely an approximation. The uncalibrated reconstructed RPC beta is used as the best available estimator. To cross-check the results, the trigger efficiency is determined in signal MC where β is taken from the one RPC hit with the largest ToF. Figure 5.15 shows a comparison of the onset for different signal types and η regions.

The onsets thus determined compare well to the scaled generic onset determined from equation 5.2. Figure E.1 in Appendix E.1 shows a comparison between the onsets determined through both procedures in three η regions. There is good agreement between both methods. To account for possible systematic errors, a corresponding uncertainty is estimated in chapter 5.8.3.

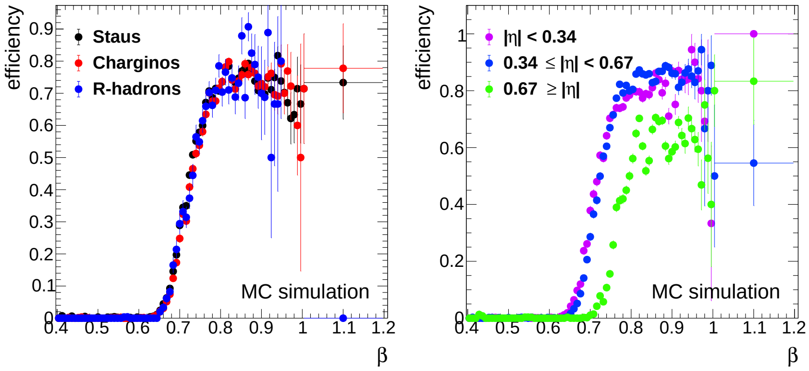

Figure 5.15: Left: onset function of the single-muon triggers for different signal types. As expected, the shape of the onset is reproduced regardless of the type of signal. Right: Combined signal MC onset for three different regions in η. For both plots β has been determined from the hit with the largest measured ToF in the RPC system.

The muon triggering in the end-caps of the detector is done using TGCs in which the simulation is based on detailed studies with test beams and ideal pulses [316, 317]. The electronic compensation of cable delays is working with greater accuracy than for the RPCs. No correction for the end-cap muon-trigger efficiency is necessary.

Figure 5.16 shows the single-muon trigger efficiency in all signal MC samples.

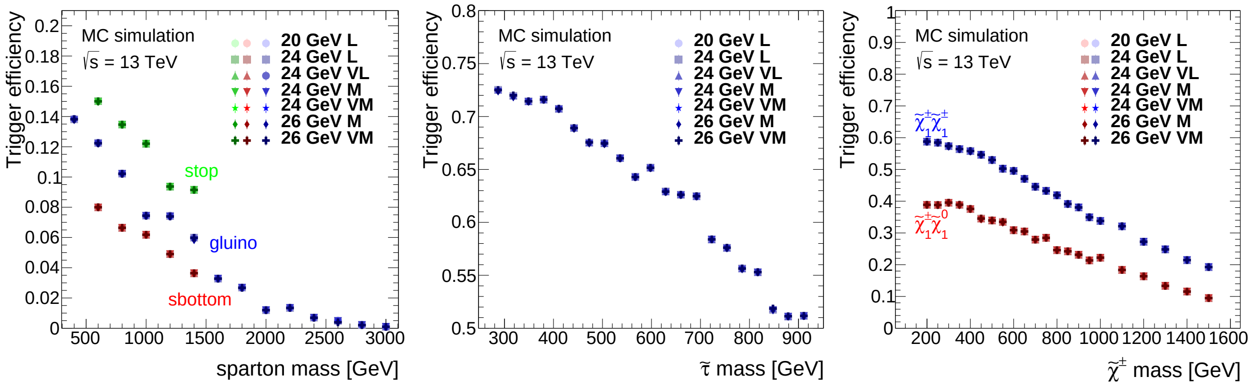

Figure 5.16: Efficiency of all single-muon triggers used in the analysis as function of the simulated R-hadron mass (left), stau mass (middle) and chargino mass (right).

Due to late arrival all signal types show similar behaviour of decreasing efficiency with increasing particle mass and thus smaller β. Consequently the largest efficiency can be observed for staus, where particle masses are smallest. Good efficiency is also seen for mAMSB scenarios with stable charginos. In R-hadron events the efficiency is generally small since a large fraction is produced electrically neutral and their propagation velocity is small.

Figure 5.17 gives the combined trigger efficiencies for E_T^{miss} and single-muon trigger in the periods A–G from table 5.5 for selected signal points.

5.6 Offline event selection

The offline event selection consists of a basic event and candidate selection which is referred to as pre-selection and a final signal selection based on momentum p and the main observables (and cor-

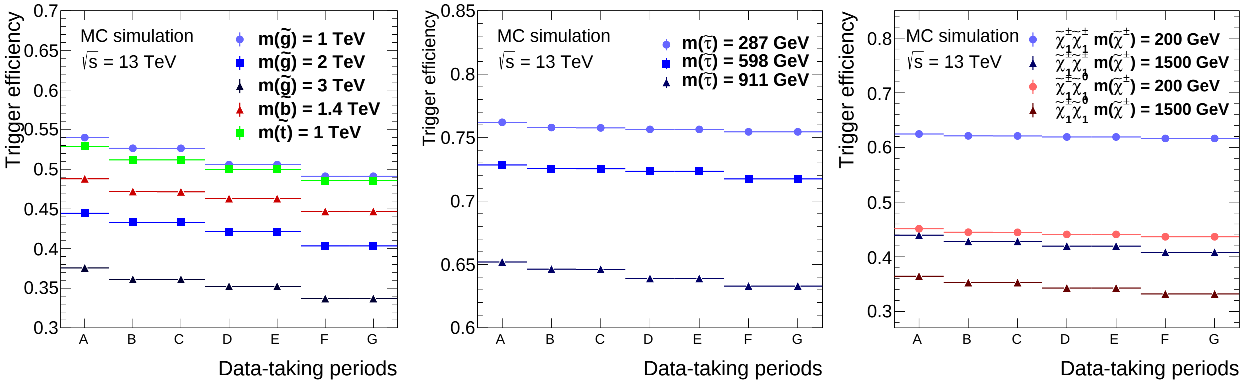

Figure 5.17: Efficiency of the trigger selection including both E_T^{miss} and single-muon triggers for different periods of data taking. Example mass points for R-hadrons (left), stable staus (middle) and charginos (right) have been selected.

responding calculated masses), β and $\beta\gamma$, where the latter is only used for the R-hadron searches. Candidates passing the pre-selection are later used to study the expected background distributions. Both steps of the offline selection are discussed in the following.

For the remainder of this chapter the following convention is used: the variable $\beta\gamma$ refers exclusively to the estimate derived from Pixel dE/dx used to calculate the mass $m_{dE/dx}$, while β is calculated from ToF measurements and used to determine m_{ToF}. In cases were the notation is unclear additional subscripts $\beta\gamma_{dE/dx}$ and β_{ToF} are used.

5.6.1 Pre-selection

All events are required to pass a quality selection to ensure all detector components operated within their regular parameters during data taking. This is done by rejection of whole luminosity blocks via the GRL and removal of individual events which either Tile Calorimeter, Liquid Argon or SCT have flagged as bad and thus indicate corruption. Events can be incomplete if the ATLAS TTC (timing, trigger and control) system was in recovery or restart mode during recording. Such events are rejected. To suppress events coming from non-collision backgrounds and ensure a good E_T^{miss} measurement the reconstructed jets of an event are evaluated and the event rejected if a bad jet is found. The procedure is described in [318], but needs to be customised for the non-standard event topology of an SMP search. If the long-lived particle decays within the calorimeter, it is possible that the jet fails some of the jet quality cuts[13]. Those cuts are therefore disabled. Further quality cuts require the reconstructed primary vertex (PV)[14] [319] to have at least two associated tracks with $p_T > 400$ MeV. Lastly, events are required to contain at least one SMP candidate particle. Candidates are either found from ID tracks for a selection based only on ID and calorimeters (ID+Calo selection), or from combined tracks reconstructed with MuGirlStau in the full-detector selection. The following basic quality cuts are common to all candidates:

- ID tracks[15] are required to originate from the PV. This is done by placing cuts on the transverse (d_0) and longitudinal (z_0) impact

[13] Mainly the EM fraction cut, i.e. the fraction of energy deposited in the EM calorimeters and a cut on the sum of associated track p_T divided by the jet p_T.

[14] The primary vertex is the vertex with the largest $\sum(p_T^i)^2$, where the sum runs over all i associated tracks.

[15] The superscript 'trk' is used to distinguish ID tracks from full-detector tracks

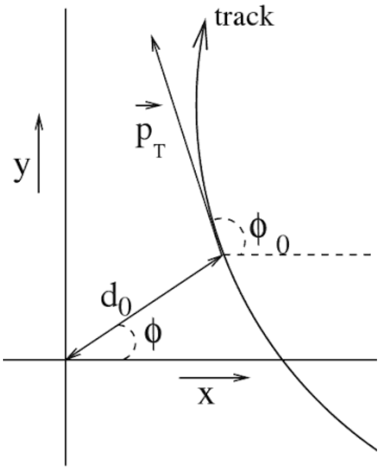

Figure 5.18: Illustration of the impact parameter of a track in the transverse plane. Figure taken from [320].

parameters of the track. They are defined as the displacement of the track's point of closest approach with respect to the beamline and accounts for the size of the beamspot. Figure 5.18 illustrates this for the transverse plane. The track is required to satisfy $|d_0| <$ 2 mm and $|\Delta z_0 \sin\theta| < 3$ mm, where Δz_0 is the impact parameter adjusted for the z position of the PV.

- All candidate ID tracks are required to have $p_T^{\text{trk}} > 50$ GeV and need to possess a physical momentum, i.e. $0 < p^{\text{trk}} < 6.5$ TeV.
- At least 7 hits in the Pixel Detector and SCT, where hits have been recorded in both the IBL and the next-to-innermost Pixel layer and no Pixel clusters or hits are shared with another track. The number of hits in the SCT plus the number of on-track dead sensors should at least be 3.
- Cuts are placed on the isolation of the candidate track. Candidates are rejected if the sum of transverse momenta of all tracks stemming from the PV with $p_T > 1.0$ GeV in a cone of $\Delta R = 0.2$ around the candidate track amounts to more than 5 GeV or if the candidate overlaps ($\Delta R < 0.05$) with a reconstructed jet with $p_T > 20$ GeV that is tagged as an electron jet ($>$ 95% of energy in the EM calorimeters) or hadron jet ($E/p > 1.0$).
- Candidates which are actually muons from $Z \to \mu\mu$ decays are suppressed by calculating the invariant mass of the candidate with the muon exhibiting the largest p_T in a cone of $\Delta R = 0.2$ around the candidate and rejecting the candidate should the invariant mass fall within 10 GeV of the mass of the Z boson. Fake candidates from cosmic showers are rejected by either looking for another track (if the candidate is an ID track) or muon (in case of a combined track), which lies within a cone of radius $\Delta R < 0.04$ around the candidate track extended beyond the PV to the opposite hemisphere of the detector and which has an opposite charge[16] than the candidate.

For the full-detector analysis two different cut-flows have been implemented. A LOOSE and a more restrictive TIGHT candidate selection. The LOOSE selection is executed after a candidate has failed the TIGHT selection. The following cuts are placed:

- A $p_T > 70$ GeV and a physical momentum of $0.0 < p < 6.5$ TeV for the combined track particle .
- The candidate must lie within $|\eta| < 2.0$[17]
- To ensure the quality of the MS β estimate all candidates are required to appear in at least two of the three MS super-layers, i.e. at least two different stations must have associated hits.
- The consistency of the combination of β_{ToF} estimates from Tile Calorimeter, MDTs and RPCs should be $\kappa > 0.00023$, where the consistency is defined in equation 4.5.

[16] Since the track reconstruction assumes particles originating from the collision point, the track leading towards the centre of the detector will be reconstructed with opposite sign.

[17] This cut is not motivated by detector acceptance, but rather through the method of the background estimate. As will be described in chapter 5.7, the background is sampled from a region with $p < 200$ GeV. Cuts on the p_T of a track therefore translate to an η-dependent momentum cut which completely eliminates events with $p < 200$ GeV beyond $\eta > 2.0$.

- Agreement between the combined β_{ToF} estimate and the $\beta\gamma_{dE/dx}$ measurement from the Pixel Detector is enforced by cutting on the consistency between the two estimates and requiring $\kappa > 0.00023$.
- A cut of $\sigma_\beta < 0.025$ on the combined β_{ToF} to guarantee a well-measured and trustworthy β, restricted to $0.2 < \beta_{\text{ToF}} < 2.0$.

In addition to these cuts, the TIGHT candidate selection requires furthermore

- a tighter pseudorapidity range of $|\eta| < 1.65$ for the candidate to be within acceptance of the Tile Calorimeter
- that at least two of the three systems (Tile Calorimeter, MDT, RPC) contributed to the β_{ToF} estimate, while one is enough for the LOOSE selection
- that the track exhibits large ionisation energy losses in the Pixel Detector with $1 < dE/dx < 20$ MeVg^{-1}cm^{-2}.

As an example, table 5.6 gives the TIGHT candidate selection cut-flow including event yields in data and stable staus at two different mass-points. The corresponding table for the LOOSE selection is given in table E.1 in Appendix E.1. For reference, the selection efficiencies for charginos in the LOOSE selection are plotted in figure 5.19, the efficiencies for staus in the TIGHT selection in figure 5.20.

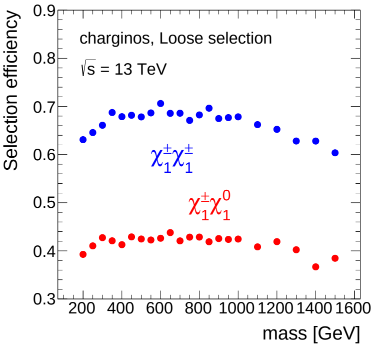

Figure 5.19: Selection efficiency of the LOOSE selection for all simulated chargino masses in the $\chi_1^\pm\chi_1^\mp$ production mode (blue) and $\chi_1^\pm\chi_1^0$ (red). The efficiencies are normalised to the number of events passing the trigger decision.

	data	411 GeV		629 GeV	
	observed	expected	eff.	expected	eff.
initial	6325439488	52.07		6.72	
trigger	926315840	42.26	0.81	5.18	0.77
data quality	897631104	42.26	0.81	5.18	0.77
PV with at least 2 tracks	897621248	42.26	0.81	5.18	0.77
candidate combined track	142200464	39.43	0.76	4.84	0.72
$p_T^{\text{cand}} > 70.0\ GeV$	15492583	39.42	0.76	4.84	0.72
$p_T^{\text{trk}} > 50.0\ GeV$	15477206	39.42	0.76	4.84	0.72
$0 < p^{\text{trk}} < 6.5\ TeV$	15464828	39.34	0.76	4.82	0.72
PV matched	15281664	39.31	0.75	4.81	0.72
$\text{N}_{\text{silicon}}^{\text{hits}} > 6$	15269703	39.31	0.75	4.81	0.72
$\text{N}_{\text{pix}}^{\text{shared}} + \text{N}_{\text{pix}}^{\text{split}} = 0$	14331513	39.19	0.75	4.79	0.71
$\text{N}_{\text{SCT}}^{\text{hits+dead}} > 2$	14331513	39.19	0.75	4.79	0.71
$p_T^{\text{iso}} < 5\ GeV$	11604712	39.12	0.75	4.78	0.71
hadron, electron veto	11555336	39.12	0.75	4.78	0.71
pix innermost	11387407	39.08	0.75	4.77	0.71
$0 < p^{\text{cand}} < 6.5\ TeV$	11386355	39.08	0.75	4.77	0.71
cosmics veto	11384572	38.96	0.75	4.75	0.71
Z veto	9342829	38.87	0.75	4.75	0.71
$\lvert\eta\rvert < 1.65$	6672813	32.08	0.62	4.19	0.62
two MS stations	6310966	31.61	0.61	4.13	0.61
β consistency	6068717	31.25	0.60	4.06	0.60
dE/dx–ToF consistency	6068525	31.25	0.60	4.06	0.60
$\sigma_\beta < 0.025$	5948443	29.35	0.56	3.87	0.57
$1 < dE/dx_{\text{pix}} < 20$ [MeVg^{-1}cm^2]	3541424	26.49	0.51	3.64	0.54
β quality	3500711	25.64	0.49	3.55	0.53
$0.2 < \beta < 2$	3500711	25.64	0.49	3.55	0.53

Table 5.6: Cut-flow of the TIGHT selection targeting the full-detector search. The number of events surviving a given cut is stated for data and as an example for stable staus with masses 411 GeV and 629 GeV. The efficiency of each cut is also given.

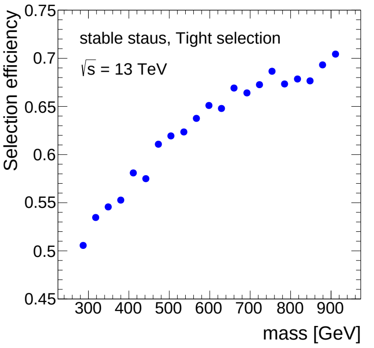

Figure 5.20: Selection efficiency of the TIGHT selection for all simulated stable stau masses. The efficiencies are normalised to the number of events passing the trigger decision. The rise in efficiency with increasing mass is mainly due to the signal being more central in the detector and thus less affected by the cut on $|\eta|$.

For the ID+CALO selection, which acts as a backup should a candidate fail the LOOSE selection in the full-detector search, the previously stated event-quality cuts are followed up by additional constraints on the quality of the main observables:

- The track is required to be located within the acceptance of the Tile Calorimeter with $|\eta| < 1.65$.
- To guarantee a good measurement of the Pixel dE/dx the candidate is demanded to possess at least two good clusters used for dE/dx measurement.
- Measured ionisation energy losses are rejected as unreasonable if not confined to the range $0 < dE/dx < 20\ \mathrm{MeVg^{-1}cm^{-2}}$.
- Analogously the allowed values for β_{ToF} and $\beta\gamma_{dE/dx}$ are restricted to the sensible ranges of $0.2 < \beta_{\mathrm{ToF}} < 2.0$ and $0.204 < \beta\gamma_{dE/dx} < 10.0$.
- The consistency of the Tile Calorimeter β estimate κ is required to be $\kappa > 0.0063$.

Table 5.7 gives the cut-flow of the MS-agnostic analysis stating the event yields in data after every cut and for gluino R-hadrons at two different mass points. The selection efficiencies for all R-hadron masses and types are plotted in figure 5.21.

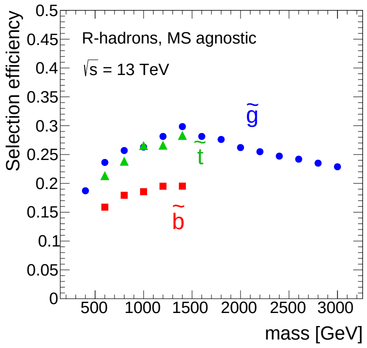

Figure 5.21: Selection efficiency of the MS-agnostic selection for all simulated gluino (blue), sbottom (red) and stop (green) R-hadron masses. The efficiencies are normalised to the number of events passing the trigger decision.

Table 5.7: Cut-flow of the ID+CALO selection in the MS-AGNOSTIC search. The number of events surviving a given cut is stated for data and as an example for gluino R-hadrons with masses 1600 GeV and 2000 GeV. The efficiency of each cut is also given.

	data	1600 GeV		2000 GeV	
	observed	expected	eff.	expected	eff.
initial	6325439488	291.84		35.35	
trigger	448411008	135.44	0.46	14.50	0.41
data quality	432608448	135.37	0.46	14.46	0.41
PV with at least 2 tracks	432598720	135.37	0.46	14.46	0.41
candidate ID track	52327680	100.73	0.35	10.65	0.30
$p_T^{\mathrm{trk}} > 50.0\ GeV$	35105560	81.43	0.28	8.72	0.25
$0 < p^{\mathrm{trk}} < 6.5\ TeV$	35066052	80.98	0.28	8.57	0.24
PV matched	32890668	80.87	0.28	8.55	0.24
$\mathrm{N}_{\mathrm{silicon}}^{\mathrm{hits}} > 6$	32881838	80.87	0.28	8.55	0.24
$\mathrm{N}_{\mathrm{pix}}^{\mathrm{shared}} + \mathrm{N}_{\mathrm{pix}}^{\mathrm{split}} = 0$	28111836	75.59	0.26	7.92	0.22
$\mathrm{N}_{\mathrm{SCT}}^{\mathrm{hits+dead}} > 2$	28111836	75.59	0.26	7.92	0.22
$p_T^{\mathrm{iso}} < 5\ GeV$	5365321	62.82	0.22	6.39	0.18
hadron, electron veto	4737133	62.75	0.21	6.38	0.18
pix innermost	4644899	61.28	0.21	6.26	0.18
cosmics veto	4628776	61.20	0.21	6.25	0.18
Z veto	4010437	59.50	0.20	6.09	0.17
$\lvert\eta\rvert < 1.65$	3994962	58.58	0.20	6.09	0.17
$\mathrm{N}_{\mathrm{good}\ dE/dx}^{\mathrm{hits}} > 1$	3702944	54.05	0.19	5.58	0.16
$0 < dE/dx_{\mathrm{pix}} < 20\ [\mathrm{MeVg^{-1}cm^{2}}]$	3702944	54.05	0.19	5.58	0.16
$0.2 < \beta\gamma < 10$	2730935	53.95	0.18	5.57	0.16
$0.2 < \beta < 2$	2720950	53.95	0.18	5.57	0.16
$\sigma_\beta < 0.06$	843877	53.28	0.18	5.51	0.16
$\kappa > 0.0063$	772827	51.65	0.18	5.12	0.14

An example for an ID+CALO cut-flow for the full-detector search is given in table E.2 in Appendix E.1.

5.6.2 Signal region definitions

To get an optimal sensitivity to all three investigated benchmark models of R-hadrons, staus and charginos, four different sets of signal regions are defined. Depending on the simulated particle masses, a final selection is applied on the mass m_{ToF} reconstructed through ToF measurements (and $m_{dE/dx}$ from the dE/dx measurement for the R-hadron searches). The lower mass thresholds of the signal regions are defined by taking the mean of the reconstructed simulated signal mass distribution and subtracting twice the resolution of the distribution at this mass point[18]. No upper boundaries are defined for any signal region. Since the mass resolution is dominated by the capability to accurately reconstruct the momentum, the signal regions are largely model independent.

R-hadron search Searches for R-hadrons are carried out in an MS-agnostic and a full-detector approach. The MS-agnostic analysis ignores all signals stemming from the MS including muon triggers. The search is thus less dependent on the precise mechanisms of R-hadron interaction with detector material, allows for charge-flip reactions where previously charged R-hadrons become neutral in the dense calorimeter materials and furthermore provide sensitivity to smaller lifetimes. Candidates are selected through triggers on E_T^{miss} and the ID+CALO selection. The final selection requires a minimal candidate momentum $p > 200$ GeV, $\beta_{\text{ToF}} < 0.75$ and $\beta\gamma_{dE/dx} < 1.00$. The corresponding signal regions are denoted `SR-RH-MA`. In the full-detector approach single-muon triggers are used in addition to E_T^{miss} triggers and β measurements from the MDTs and RPCs can be considered. Candidates have to pass the LOOSE selection. If no combined track candidate is found the ID+CALO selection is used as a fallback[19] resulting in an orthogonal selection. As in the MS-agnostic analysis a cut of $p > 200$ GeV is placed on the candidate, which is further required to possess $\beta_{\text{ToF}} < 0.75$ and $\beta\gamma_{dE/dx} < 1.30$. The designation `SR-RH-FD` is used to identify full-detector R-hadron signal regions. In rare cases two candidates are found in the same event and the one with the larger p_T is used while the other is dropped. The signal regions are defined in the two-dimensional mass space, where the final mass-dependent minimal requirements $m_{\text{ToF}}^{\text{min}}$ and $m_{dE/dx}^{\text{min}}$ are listed in table 5.8.

Table 5.8: Definitions of the two-dimensional signal regions for the R-hadron searches.

	`SR-RH-MA/SR-RH-FD`													
particle mass [GeV]	400	600	800	1000	1200	1400	1600	1800	2000	2200	2400	2600	2800	3000
$m_{\text{ToF}}^{\text{min}}$ [GeV]	350	450	550	650	700	750	800	850	850	850	850	850	850	850
$m_{dE/dx}^{\text{min}}$ [GeV]	300	400	450	550	600	650	700	700	750	750	750	750	750	750

Stable stau search Directly produced staus occur in pairs, which allows for the definition of two orthogonal signal regions depending on whether one or two candidates are found in an event. For the two-candidate region `SR-2C-FD` events have to pass the LOOSE selection. If only one candidate is identified it has to pass the stricter TIGHT selection and ends up in the region `SR-1C-FD`. Contrary to the R-hadron search the signal regions are one-dimensional and candidates are required to have $p > 200$ GeV and $\beta_{\text{ToF}} < 0.80$ ($p > 100$ GeV and $\beta_{\text{ToF}} < 0.95$) in the one candidate (two candidate) case. The mass-dependent minimal mass requirements $m_{\text{ToF}}^{\text{min}}$ are listed in table 5.9.

[18] Since statistics is low the lower mass limit derived from the fit can fluctuate. All mass requirements are taken in steps of 25 GeV for staus and charginos and 50 GeV for R-hadrons.

[19] Note that the full-detector ID+CALO and the MS-agnostic selection are identical with the exception of the trigger requirements since the full-detector approach allows for single-muon triggers.

Table 5.9: Definitions of the one- and two-candidate signal regions for the stable stau searches. Given are the lower-mass bounds $m_{\text{ToF}}^{\text{min}}$. No upper-mass boundaries exist.

	`SR-1C-FD/SR-2C-FD`										
particle mass [GeV]	287	318	349	380	411	442	473	504	536	567	598
$m_{\text{ToF}}^{\text{min}}$ [GeV] (`SR-1C-FD`)	250	275	300	325	350	375	400	425	450	475	500
$m_{\text{ToF}}^{\text{min}}$ [GeV] (`SR-2C-FD`)	225	250	275	300	325	350	375	400	425	425	450
particle mass [GeV]	629	660	692	723	754	785	817	848	879	911	
$m_{\text{ToF}}^{\text{min}}$ [GeV] (`SR-1C-FD`)	500	525	550	575	600	625	650	675	675	700	
$m_{\text{ToF}}^{\text{min}}$ [GeV] (`SR-2C-FD`)	475	500	525	550	575	600	600	625	650	675	

Chargino search The analysis strategy for charginos is identical to staus and requires either two candidates passing the LOOSE selection for signal regions `SR-2C-FD` with $p > 100$ GeV and $\beta_{\text{ToF}} < 0.95$, or one TIGHT candidate for the `SR-1C-FD` regions where the candidate is required to have $p > 200$ GeV and $\beta_{\text{ToF}} < 0.80$. The lower signal region boundaries are given in table 5.10.

Table 5.10: Definitions of the one- and two-candidate signal regions for the chargino searches. Given are the lower-mass borders $m_{\text{ToF}}^{\text{min}}$. No upper-mass boundaries exist.

	`SR-1C-FD/SR-2C-FD`										
particle mass [GeV]	200	250	300	340	400	450	500	550	600	650	700
$m_{\text{ToF}}^{\text{min}}$ [GeV] (`SR-1C-FD`)	175	225	250	300	350	375	425	450	500	525	550
$m_{\text{ToF}}^{\text{min}}$ [GeV] (`SR-2C-FD`)	150	200	225	275	325	350	400	425	450	500	525
particle mass [GeV]	750	800	850	899	950	1000	1100	1200	1300	1400	1500
$m_{\text{ToF}}^{\text{min}}$ [GeV] (`SR-1C-FD`)	600	625	675	700	725	750	825	875	925	975	1025
$m_{\text{ToF}}^{\text{min}}$ [GeV] (`SR-2C-FD`)	575	600	625	675	700	725	800	850	900	975	1025

A summary of the required cuts on the main observables momentum, β_{ToF} and $\beta\gamma_{dE/dx}$ for each of the four signal regions is given in table 5.11.

	[GeV]			
region	p^{min}	$\beta_{\text{ToF}}^{\text{max}}$	$\beta\gamma_{dE/dx}^{\text{max}}$	$\lvert\eta\rvert^{max}$
`SR-RH-MA`	200	0.75	1.00	1.65
`SR-RH-FD`	200	0.75	1.30	2.00
`SR-1C-FD`	200	0.80		1.65
`SR-2C-FD`	100	0.95		2.00

Table 5.11: Summary of momentum p, β_{ToF}, $\beta\gamma_{dE/dx}$ and $\lvert\eta\rvert$ requirements for each of the four signal regions.

5.7 Background estimate

The expected backgrounds for all signal regions are estimated entirely from data. Since masses are calculated via $m = p/\beta\gamma$, the key variables to consider for the background are momentum p, β_{ToF} and, for the R-hadron searches only, $\beta\gamma_{dE/dx}$. All candidates passing the respective pre-selections are evaluated to get probability density functions (PDFs) of the key variables. To prevent contamination of the estimate through possible signal, sideband-regions are used where possible.

The sidebands are the parameter space one gets by reversing the final selection cuts stated in table 5.11. For the R-hadron search, the momentum PDF is built from a set of events failing both the β_{ToF} and $\beta\gamma_{dE/dx}$ cuts, while the β_{ToF} and $\beta\gamma_{dE/dx}$ PDFs themselves require only reversion of the momentum cut. A minimum momentum of $p > 50$ GeV is required nonetheless. An overview of the sideband-region definitions is given in table 5.12. For the stau and chargino searches all p PDFs are evaluated by reversing the β_{ToF} cut. The reverse is however only possible in the one-candidate selections: The p_T cut of the MUGIRLSTAU algorithm constraints the minimal possible momentum as a function of $\lvert\eta\rvert$. As can be seen from figure 5.22, for $\lvert\eta\rvert > 1.8$ no tracks with $p < 200$ GeV are left. Since the TIGHT

region	PDF	cuts
`SR-RH-MA`	p	$\beta_{\text{ToF}} > 0.75$ $\beta\gamma_{dE/dx} > 1.00$
	β_{ToF}	$50 < p < 200$ GeV
	$\beta\gamma_{dE/dx}$	$50 < p < 200$ GeV
`SR-RH-FD`	p	$\beta_{\text{ToF}} > 0.75$ $\beta\gamma_{dE/dx} > 1.30$
	β_{ToF}	$50 < p < 200$ GeV
	$\beta\gamma_{dE/dx}$	$50 < p < 200$ GeV
`SR-1C-FD`	p	$\beta_{\text{ToF}} > 0.80$
	β_{ToF}	$70 < p < 200$ GeV
`SR-2C-FD`	p	$\beta_{\text{ToF}} > 0.95$
	β_{ToF}	70 GeV$< p$

Table 5.12: Definition of the sideband regions from which the corresponding PDFs are evaluated for all signal regions. If not stated in the last column, the cuts listed in table 5.11 remain active.

selection requires $|\eta| < 1.65$, it is not affected by this and the β_{ToF} PDF can be produced from the momentum sideband. The LOOSE selection, however, cuts on $|\eta| < 2.0$ and no sidebands can be used. A minimal momentum $p > 70$ GeV is required for the evaluation of all β_{ToF} PDFs for stau and chargino signal regions.

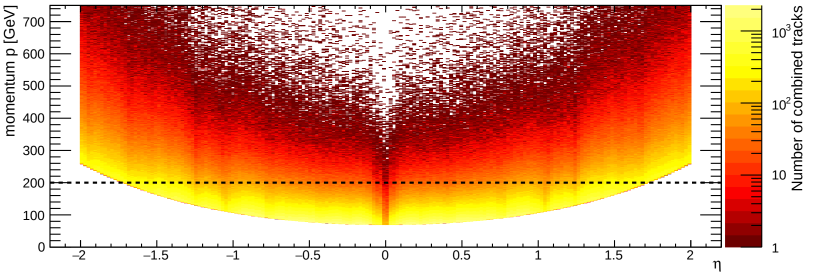

Figure 5.22: Measured momentum p of tracks reconstructed with the MuGirlStau algorithm. The internal p_T cut of the algorithm results in a dependency of the momentum on $|\eta|$. The dashed line indicates the offline momentum cut.

Since no known physical background exists for the SMP searches and consequently backgrounds arise predominantly through inaccurately measured particles, the PDFs can be sampled randomly to generate pseudo-data. Calculating the masses of the pseudo-candidate and sampling many times results in smoothly falling background mass distributions. The pseudo-data distributions are then normalised to the number of observed data events in the low-mass control regions (CRs) which are defined as $m_{\text{ToF}}^{\text{cand}} \leq m_{dE/dx}^{\text{cand}} < 300$ GeV for the R-hadron searches and $m_{\text{ToF}}^{\text{cand}} < 200$ GeV ($m_{\text{ToF}}^{\text{cand}} < 150$ GeV) for the signal region `SR-1C-FD` (`SR-2C-FD`).

The procedure is only viable if no correlations between the momentum and β distributions exist. While this is the case[20], an implicit correlation can be introduced via $|\eta|$. As described before and shown in figure 5.22, the track reconstruction p_T cut results in a dependency of p on η. Since the β resolution is not constant throughout the detector (e.g. there are no RPCs in the end-caps) it also results in a mild correlation with η. To minimise the effect of this correlation, the observable PDFs are estimated individually in five η bins for the R-hadron searches and `SR-1C-FD`, while `SR-2C-FD` incorporates a sixth bin due to its larger pseudorapidity range. In all cases the η is taken to be the reconstructed η of the candidate. The bins are not equidistant and are instead motivated by the detector layout seeking to align bin borders with subsystem edges (i.e. the crack regions in between subdetectors are roughly taken as borders between bins)[21].

As an example the β_{ToF} and p PDFs for the stau and chargino two-candidate signal regions are drawn in figure 5.23 for all six η slices.

For completeness, the $\beta\gamma_{dE/dx}$ PDF of the MS-agnostic search is drawn in figure 5.24. It becomes immediately apparent that the statistics is much lower, which is amongst other factors caused by the isolation requirement on the candidate, which rejects fractionally more events triggered by an E_T^{miss} trigger than muon triggers, and thus affects the MS-agnostic analysis to a greater extent.

[20] One has to bear in mind that this does not refer to a correlation between the physical momentum and β of a particle which unquestionably exists, but to a correlation of the mismeasured quantities. All known particles will have $\beta \approx 1$ at the minimal momenta required for track reconstruction in the detector. A correlation of mismeasurements is indeed not expected as the measurement of β and momentum rely on fundamentally different methods.

[21] The six η regions are:
1) $0.00 \leq |\eta| < 0.35$
2) $0.35 \leq |\eta| < 0.70$
3) $0.70 \leq |\eta| < 1.10$
4) $1.10 \leq |\eta| < 1.25$
5) $1.25 \leq |\eta| < 1.65$
6) $1.65 \leq |\eta| < 2.00$

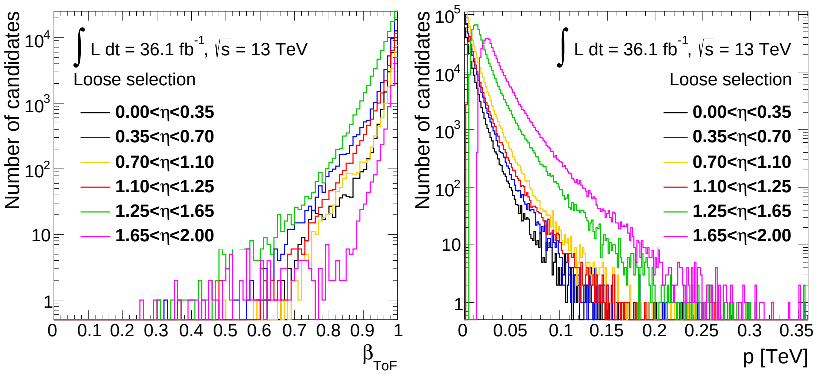

Figure 5.23: β_{ToF} and momentum PDF for the two-candidate stau and chargino signal regions. All candidates passing the LOOSE event selection are considered. The six η slices are not equidistant but instead seek to address regions of the detector with similar sensitivity.

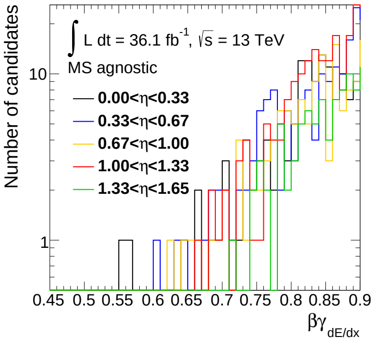

Figure 5.24: $\beta\gamma_{dE/dx}$ PDF in the MS-agnostic analysis. All five η slices are drawn. The statistics is much lower when compared to figure 5.23.

The statistical uncertainties on the background estimates are dominated by the uncertainties on the PDF templates. To correctly propagate those uncertainties through, 50 new sets of PDFs are created, where each time the content of each bin is varied randomly according to a Poisson distribution with its mean at the original content of the bin. The background estimation process is then carried out for all different PDFs. The final background estimate is given as the mean of all resulting bin-wise event yields, their variation determines the statistical uncertainty. The uncertainty due to the normalisation of the estimate is accounted for by taking the relative statistical uncertainty on the data yield in the CRs and propagating it to the uncertainty on the expected event yield in the signal regions. Examples of background estimates are drawn in figures 5.25–5.29 for different signal regions and mass points.

The background estimation procedure would be invalidated if a strong enough signal contamination is present in the original PDFs. The possible effect of such a contamination is investigated by infusing the event pool with simulated signal events at the extent of the current ATLAS exclusion limit at 20 fb for R-hadrons, 2.5 fb for staus and 5.0 fb for charginos [1, 160]. The PDFs are then built from this signal contaminated selection and a new background estimate is done. The contaminated background estimates are included in figures 5.25–5.29. The effect of signal contamination was found to be small for all signal regions and mass points.

The background estimates for the stable-stau searches are shown in figure 5.25 for the example of a stau with $m(\tilde{\tau}) = 629$ GeV in the one- and two-candidate selection.

The background estimates for the stable-chargino search regions are given in figure 5.26 and have been overlaid with data. The expected signal of a chargino with $m(\tilde{\chi}_1^{\pm}) = 1000$ GeV is also given.

For R-hadrons the signal regions are defined in two-dimensional m_{ToF}–$m_{dE/dx}$ space and consequently both background distributions need to be built independently. For the MS-agnostic analysis the individual background estimates for m_{ToF} and $m_{dE/dx}$ are shown in the upper two plots of figure 5.27 for the example of a gluino with

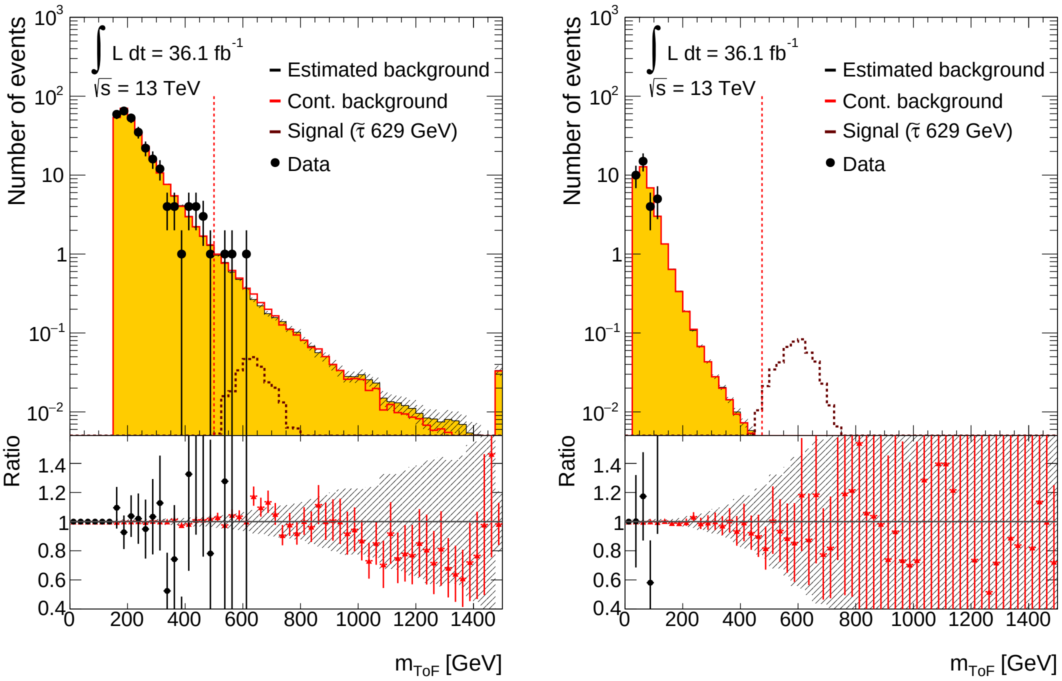

Figure 5.25: Background estimate for the stable stau signal regions `SR-1C-FD` (left) and `SR-2C-FD` (right). Black data markers have been drawn on top of the background estimate. As an example, the expected signal of a stau with $m(\tilde{\tau}) = 629$ GeV has been included in the figure as dashed brown line. The edge of the signal region is marked by the dashed red line. The last bin contains the overflow. As a cross-check, the background estimates resulting from PDFs that were deliberately contaminated with signal are drawn as solid red line. The lower panel gives the ratio of data and background (black markers) as well as the ratio of contaminated and nominal background estimate (red markers).

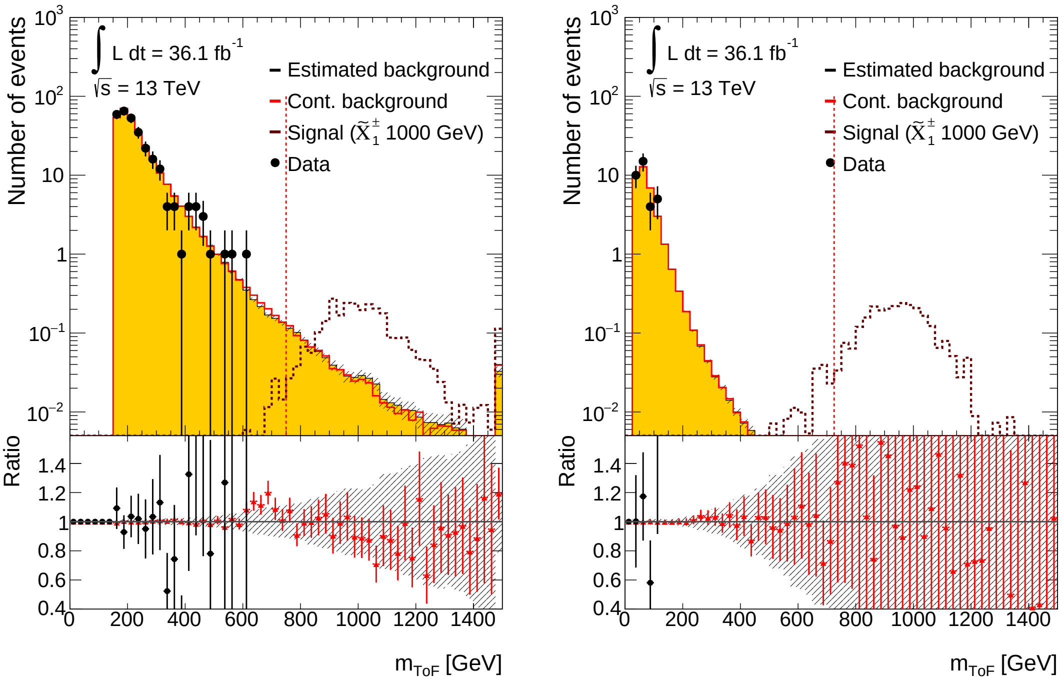

Figure 5.26: Background estimate for the stable chargino signal regions `SR-1C-FD` (left) and `SR-2C-FD` (right). Black data markers have been drawn on top of the background estimate. As an example, the expected signal of a chargino with $m(\tilde{\chi}_1^{\pm}) = 1000$ GeV has been included in the figure as dashed brown line. The edge of the signal region is marked by the dashed red line. The last bin contains the overflow. As a cross-check, the background estimates resulting from PDFs that were deliberately contaminated with signal are drawn as solid red line. The lower panel gives the ratio of data and background (black markers) as well as the ratio of contaminated and nominal background estimate (red markers).

$m(\tilde{g}) = 2200$ GeV. Note that no signal region can be shown as the plots are merely the projections of the event counts onto the mass-axes and a high-m_{ToF} candidate (high-$m_{dE/dx}$ candidate) might still fail the $m_{dE/dx}$ (m_{ToF}) requirement. The actual two-dimensional signal region is shown in the lower plot of figure 5.27 and is marked by dashed lines. Two events appear in the signal region.

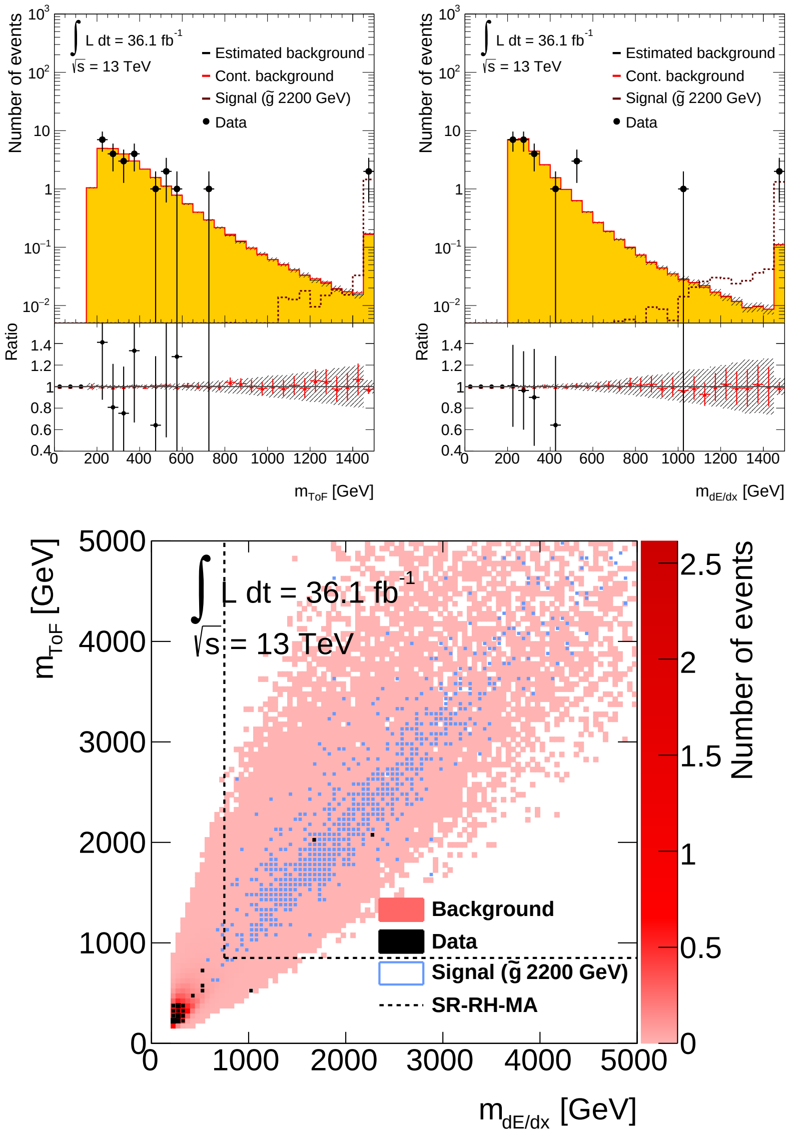

Figure 5.27: Background estimates in the m_{ToF} (top left) and $m_{dE/dx}$ (top right) distribution for the MS-agnostic gluino R-hadron search. A potential signal distribution for gluinos with $m(\tilde{g}) = 2200$ GeV is given. The last bin contains the histogram overflow. The estimated background produced from data with an infused signal contamination at the current ATLAS exclusion limit of 20 fb is drawn in red and is consistent with the nominal estimate. The data are superimposed on the background estimates and shows good agreement with expectation in the low-mass regions. Since the signal region is defined in two-dimensional m_{ToF}–$m_{dE/dx}$ space, no signal region can be drawn in the projection plots. Instead, the region is shown in the bottom plot where the expected background is drawn in red, simulated signal in blue and the measured data in black, where the size of the data marker corresponds to the number of events in the bin. The figure is meant to give a qualitative impression of the distributions, precise event counts will be given in table 5.24 in chapter 5.9.

Lastly, the full-detector R-hadron search requires background estimations for m_{ToF} and $m_{dE/dx}$ in the LOOSE and ID+CALO selection. Figure 5.28 shows the background estimate for the LOOSE selection alongside the potential signal from a 1000 GeV bottom squark, figure 5.29 gives the estimate for the ID+CALO selection with the potential signal from a 1000 GeV top squark overlaid. Once again, the signal regions are drawn below the projections of the background estimates.

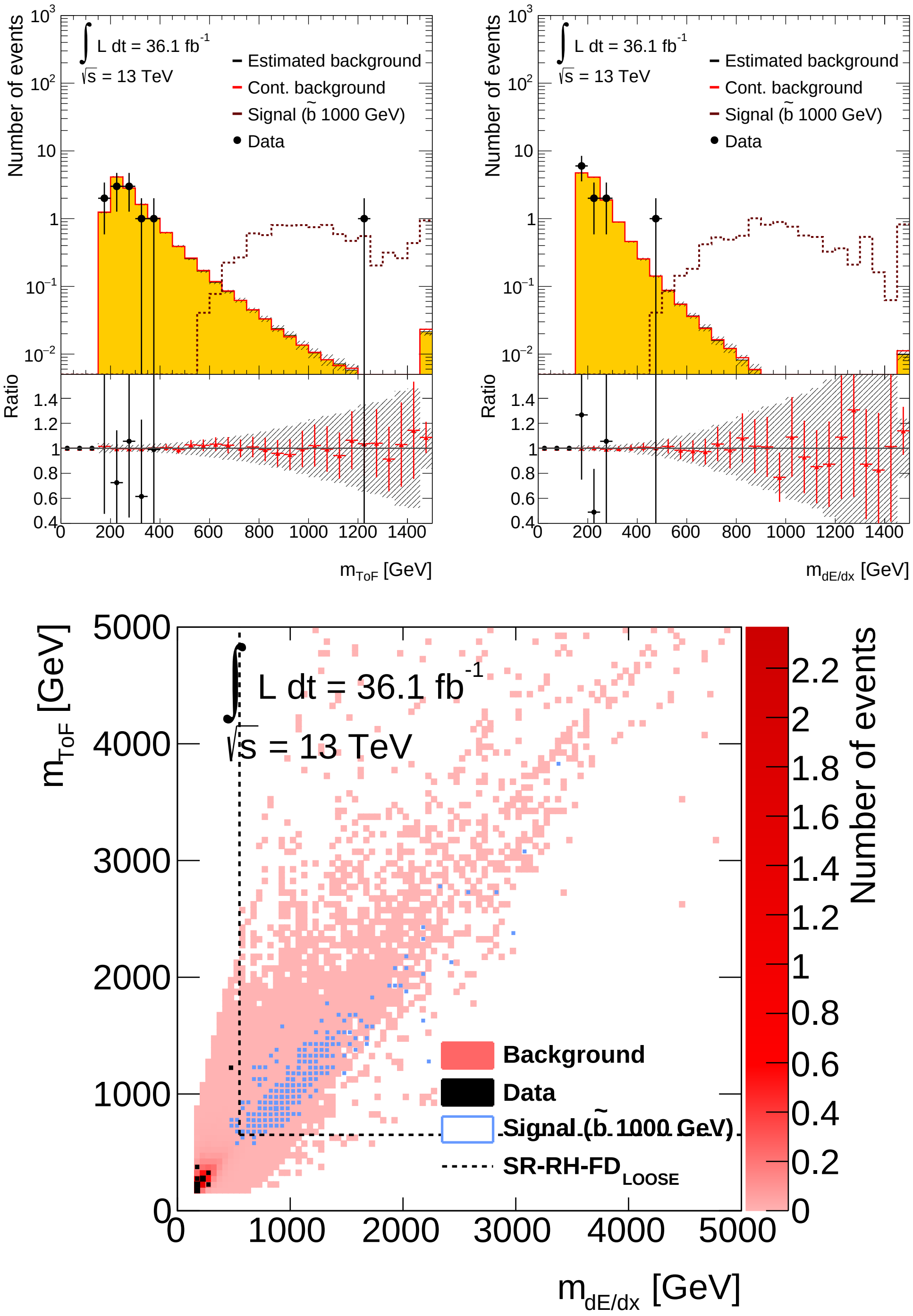

Figure 5.28: Background estimates in the m_{ToF} (top left) and $m_{dE/dx}$ (top right) distribution for the full-detector R-hadron search in the LOOSE selection. A potential signal distribution for bottom squarks with $m(\tilde{b}) = 1000$ GeV is given. The last bin contains the histogram overflow. The estimated background produced from data with an infused signal contamination at the current ATLAS exclusion limit of 20 fb is drawn in red and is consistent with the nominal estimate. The data are superimposed on the background estimates and shows good agreement with expectation in the low-mass regions. Since the signal region is defined in two-dimensional m_{ToF}–$m_{dE/dx}$ space, no signal region can be drawn in the projection plots. Instead, the region is shown in the bottom plot where the expected background is drawn in red, simulated signal in blue and the measured data in black, where the size of the data marker corresponds to the number of events in the bin. The figure is meant to give a qualitative impression of the distributions, precise event counts will be given in table 5.25 in chapter 5.9.

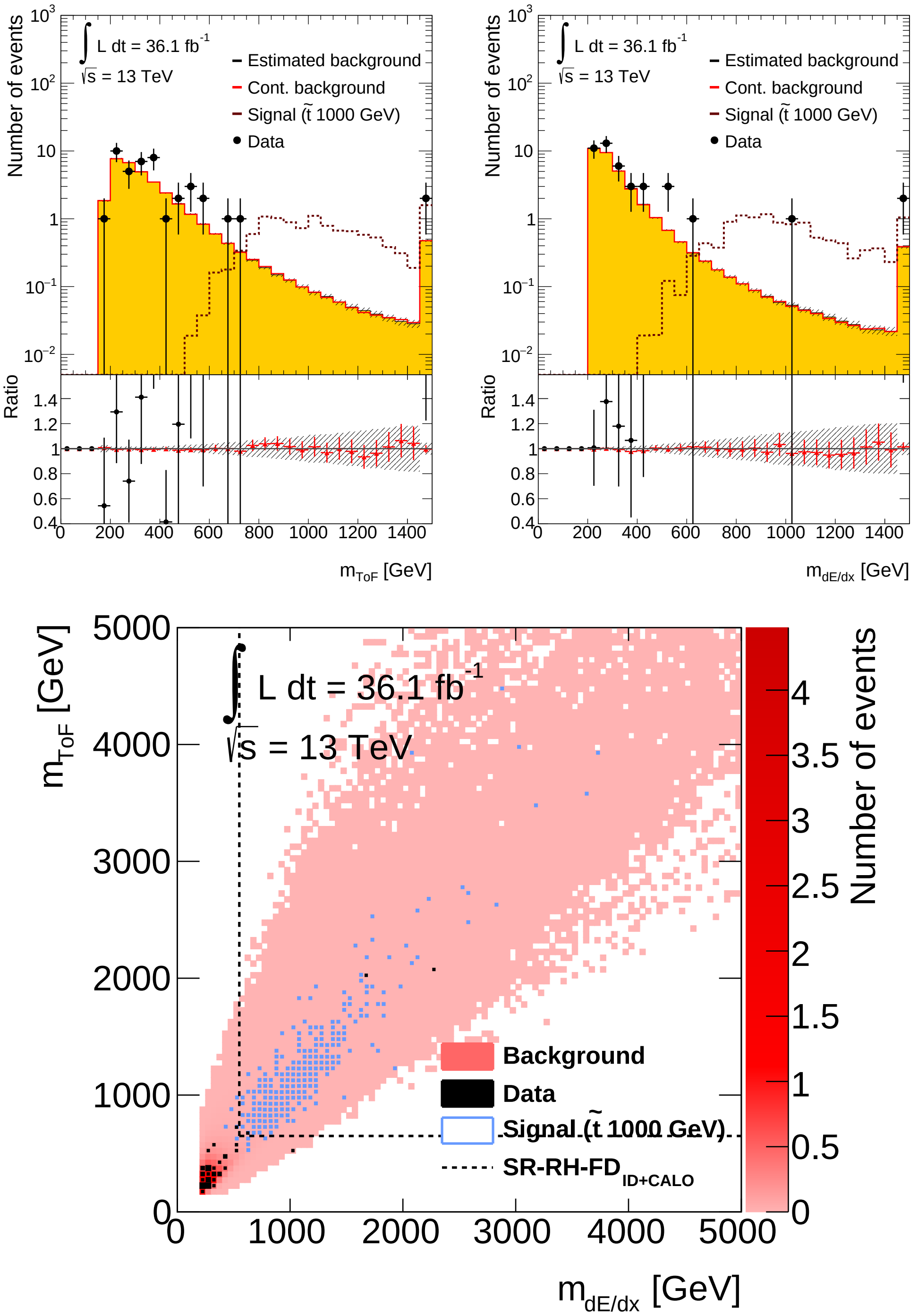

Figure 5.29: Background estimates in the m_{ToF} (top left) and $m_{dE/dx}$ (top right) distribution for the full-detector R-hadron search in the ID+Calo selection. A potential signal distribution for top squarks with $m(\tilde{t}) = 1000$ GeV is given. The last bin contains the histogram overflow. The estimated background produced from data with an infused signal contamination at the current ATLAS exclusion limit of 20 fb is drawn in red and is consistent with the nominal estimate. The data are superimposed on the background estimates and shows good agreement with expectation in the low-mass regions. Since the signal region is defined in two-dimensional m_{ToF}–$m_{dE/dx}$ space, no signal region can be drawn in the projection plots. Instead, the region is shown in the bottom plot where the expected background is drawn in red, simulated signal in blue and the measured data in black, where the size of the data marker corresponds to the number of events in the bin. The figure is meant to give a qualitative impression of the distributions, precise event counts will be given in table 5.25 in chapter 5.9.

5.8 Systematic Uncertainties

The following chapter gives a summary of the estimation of systematic uncertainties affecting theoretical predictions, expected signal yield and background estimation.

5.8.1 Theoretical cross sections

The cross sections of the R-hadron simulated samples are calculated at NLO+NLL level, i.e. at next-to-leading order in the strong coupling constant α_S and soft gluon emissions are resummed at next-to-leading-logarithmic accuracy [321–323]. The procedure to estimate the uncertainty is described in [324]. It results from a comparison of different cross-section predictions obtained by using various sets of parton distribution functions following the 68% confidence limit ranges of the MSTW2008 [325] and CTEQ6.6 [326] pdf sets and incorporating different factorisation and renormalisation scales. The resulting uncertainties are listed next to the calculated cross sections in table 5.1. For gluinos they range from 14% at $m(\tilde{g}) = 400$ GeV to 57% at $m(\tilde{g}) = 3000$ GeV and for squarks from 13% at $m(\tilde{b}/\tilde{t}) = 600$ GeV to 23% for $m(\tilde{b}/\tilde{t}) = 1400$ GeV.

For stau and chargino samples the cross sections are calculated at NLO in α_S. Uncertainties are obtained by evaluation of the 68% confidence level (CL) ranges of the underlying pdfs and variation of the factorisation and renormalisation scales by factors 0.5 and 2.0. Following the recommendations in [327], the quoted cross sections are taken as the central value of the enveloping functions, the uncertainty is taken as half the spread. The assigned uncertainties are listed in table 5.3 (table 5.2) for stau (chargino) samples and range from 6% at $m(\tilde{\tau}) = 287$ GeV to 10% at $m(\tilde{\tau}) = 911$ GeV (6% at $m(\tilde{\chi}_1^{\pm}) = 250$ GeV to 10% at $m(\tilde{\chi}_1^{\pm}) = 1500$ GeV for the $\tilde{\chi}_1^{\pm}\tilde{\chi}_1^{\pm}$ production channel and 4% at $m(\tilde{\chi}_1^{\pm}) = 300$ GeV to 8% at $m(\tilde{\chi}_1^{\pm}) = 1500$ GeV for $\tilde{\chi}_1^{\pm}\tilde{\chi}_1^{0}$).

A summary of systematic uncertainties due to theoretical cross-section predictions can be found in table 5.13.

particle	sys. unc.
Gluinos	14%–57%
Sbottom	13%–23%
Stops	13%–23%
Staus	6%–10%
Charginos $\tilde{\chi}_1^{\pm}\tilde{\chi}_1^{\pm}$	6%–10%
Charginos $\tilde{\chi}_1^{\pm}\tilde{\chi}_1^{0}$	4%–8%

Table 5.13: List of systematic uncertainties assigned to all particle types due to the uncertainty on the theoretical cross-section prediction.

5.8.2 E_T^{miss} trigger efficiency

The missing transverse energy which the E_T^{miss} triggers are sensitive to is calculated exclusively from clusters of deposited energy in the calorimeters. Since muons do not cause extensive showering in the calorimeters the E_T^{miss} trigger is blind to them and muons thus provide a possibility to access systematic uncertainties regarding the trigger efficiency.

Events are selected via the lowest unprescaled single-muon trigger and undergo a basic $Z \to \mu\mu$ selection[22]. The E_T^{miss} trigger onset is

[22] This includes event quality conditions and exactly two muons with tracks in the ID and the MS with $p_T > 10$ GeV that have opposite charge and combine to an invariant mass within 10 GeV of the Z-boson mass

studied in data and simulated $Z \rightarrow \mu\mu$ events. An error function of the form

$$\varepsilon(E_T^{\text{miss}}) = \frac{A}{2}\left[1 + \text{erf}\left(\frac{E_T^{\text{miss}} - B}{\sqrt{2}C}\right)\right] \tag{5.5}$$

can be used to fit the trigger onset, where the parameter A describes the maximal trigger efficiency and is fixed to 1.0, parameter B corresponds to the E_T^{miss} value at 50% efficiency and thus constitutes an effective threshold and parameter C, which represents the resolution as the width of a Gaussian that cumulatively models the slope of the fit. Figure 5.30 shows the fitted trigger efficiency onset as function of the reconstructed offline E_T^{miss} for two exemplary triggers.

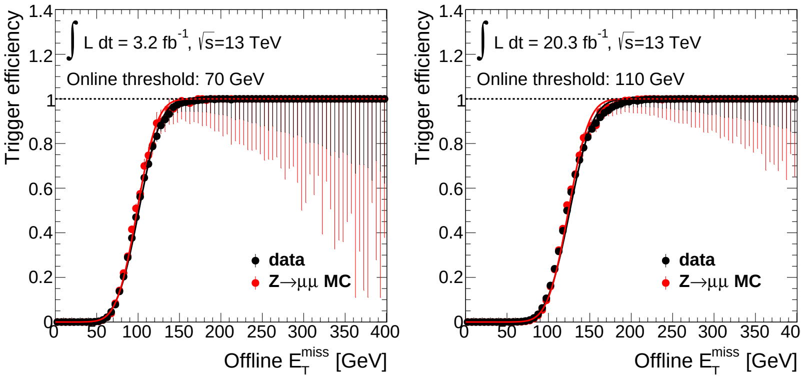

Figure 5.30: E_T^{miss} trigger onsets in data and MC with an applied $Z \rightarrow \mu\mu$ selection for the employed triggers with the lowest (70 GeV) and the largest (110 GeV) trigger threshold. Fitted error functions to the onset are drawn as solid lines. The corresponding plots for the remaining two E_T^{miss} triggers with thresholds of 90 GeV and 100 GeV are given in figure E.2 in Appendix E.1. The offline E_T^{miss} used here is based on calorimeter clusters without receiving corrections from the MS.

The effect of the trigger efficiency on the signal yield can be quantified via a bin-by-bin multiplication of the E_T^{miss} spectrum in signal MC with the fitted trigger onset. Since the same detector response models have been used for signal MC and $Z \rightarrow \mu\mu$ MC, the onset derived from the latter is also valid in signal MC[23]. Four individual components are considered to contribute to the total associated uncertainty:

- the relative difference between the signal yields derived by folding the signal MC E_T^{miss} distributions with the onsets from data and MC,
- the relative effect of a 10% variation in scale of the signal MC E_T^{miss},
- the relative signal yield differences from independent $\pm 1.0\sigma$ variations of the fit parameters B and C in the fit on data, and
- the same variations for the fit on MC.

As an example, the relative changes in signal yield through variation of fit parameters are given in table 5.14 for the fit in data and table 5.15 for the fit in MC. In both cases a 2000 GeV gluino R-hadron sample and an E_T^{miss} trigger with an online threshold of 110 GeV has been considered. The largest individual relative change is taken as the contribution from the parameter variation.

[%]	$C-1\sigma$	C	$C+1\sigma$
$B-1\sigma$	0.3352	0.3565	0.3775
B	0.0217	0.0000	0.0216
$B+1\sigma$	0.3780	0.3557	0.3336

Table 5.14: Given is the relative change in signal yield for a 2000 GeV gluino R-hadron sample with respect to the central fit values under independent 1σ variations of the fit parameters B and C of the fit in data for an E_T^{miss} trigger with a threshold of 110 GeV.

---

[23] In fact, $Z \rightarrow \mu\mu$ MC is only used to characterise the behaviour of the trigger onset in simulation and assess the difference from data.

The absolute uncertainty for each trigger and signal mass point is calculated by adding all four contributions in quadrature. This procedure has been applied to all signal MC samples and all E_T^{miss} triggers. Estimates from the different triggers are combined by weighting the estimate according to the fraction of integrated luminosity during which the trigger was actively used. As an example, figure 5.31 shows the individual uncertainties for all trigger and signal mass points of gluino R-hadrons and stable staus, as well as the luminosity weighted average. A full overview over all signal samples is given in figure E.3 in Appendix E.1.

[%]	$C - 1\sigma$	C	$C + 1\sigma$
$B - 1\sigma$	0.3947	0.4161	0.4374
B	0.0222	0.0000	0.0220
$B + 1\sigma$	0.4379	0.4151	0.3924

Table 5.15: Given is the relative change in signal yield for a 2000 GeV gluino R-hadron sample with respect to the central fit values under independent 1σ variations of the fit parameters B and C of the fit in MC for an E_T^{miss} trigger with a threshold of 110 GeV.

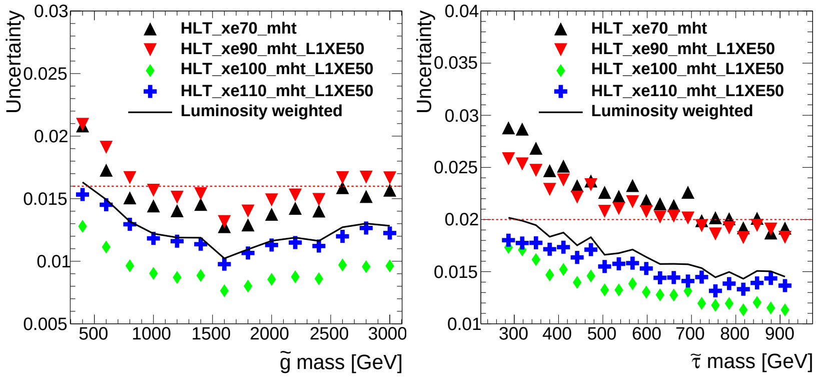

Figure 5.31: Estimated systematic uncertainties of the E_T^{miss} trigger efficiency evaluated for gluino R-hadrons and stable staus. The uncertainties derived from the onset for individual triggers are shown with coloured markers, while the solid black line indicates the luminosity-weighted average of all triggers. The variation in scale between samples is generally small and the approach of a flat uncertainty indicated by the dashed red line is well justified.

For simplicity and since the variation in between samples is small, a flat systematic uncertainty is assigned to each particle hypothesis. The resulting uncertainties are listed in table 5.16.

particle	sys. unc.
Gluinos	1.7%
Sbottoms	1.5%
Stops	1.5%
Staus	2.0%
Charginos	2.4%

Table 5.16: List of systematic uncertainties assigned to all particle types due to E_T^{miss} trigger efficiency.

5.8.3 Single-muon trigger efficiency

In chapter 5.5.2 it was described how the mismodelled trigger timing in simulation was corrected for by applying an additional weight to signal MC. These weights depend on the pseudorapidity of the candidate and its propagation velocity. Since we do not have access to the precise hit time (and thus β) seen by the L1 muon trigger, the uncalibrated RPC β measurement, which gives a good estimate, is used. To account for possible systematic errors made in this reweighting process, the trigger efficiency of all employed triggers is evaluated for all signal types and mass points with and without the efficiency scaling. The assigned systematic uncertainty is taken as half the difference in signal trigger efficiency between scaled and unscaled signal yield. Figure 5.32 gives the estimated systematic uncertainties for R-hadrons, staus and charginos separately. The effect of the cutoff parameter which restrains the scale factors to values $\rho_{1/2} < 5.0$ has been evaluated by performing a 50% variation on the value of the cutoff. The effects on the systematic uncertainty were found to be small and covered by the conservative estimate. Since the single-muon trigger efficiency for R-hadrons is low, the resulting uncertainties are also smaller compared to staus and charginos. A

particle	sys. unc.
Gluinos	1.0%
Sbottoms	1.0%
Stops	1.0%
Staus	4.0%
Charginos	3.0%

Table 5.17: List of systematic uncertainties assigned to all particle types due to the single-muon trigger efficiency.

flat uncertainty of 1% is assigned to R-hadrons, 3% to charginos and 4% to staus as listed in table 5.17 for convenience.

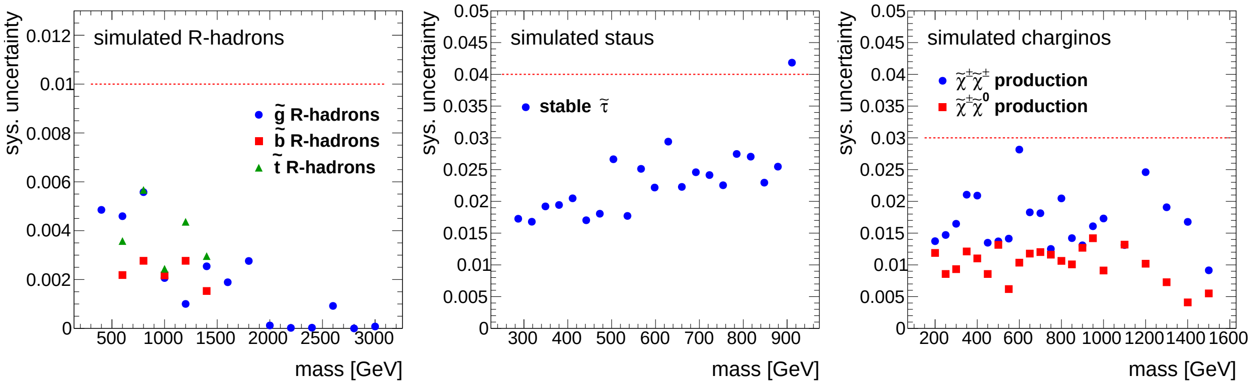

Figure 5.32: Systematic uncertainties on the single-muon trigger efficiency for R-hadrons (left), staus (middle) and charginos (right). The uncertainty is taken as half the difference in trigger efficiency between unscaled and scaled event weights. A flat systematic uncertainty visualised by the red dashed line is assigned.

5.8.4 Initial-state radiation

The E_T^{miss} trigger relies primarily on an energy imbalance which originates from ISR. With the effects of underlying event and FSR negligible, the ISR modelling can have a strong impact on the efficiency of the E_T^{miss} trigger and thus the signal yield. It is therefore necessary to estimate a systematic uncertainty on the ISR description in simulation.

In chapter 5.1 it was described how R-hadron samples generated in Pythia are reweighted to match the ISR spectrum in MadGraph. A systematic uncertainty on this procedure is obtained by comparing the signal yield after trigger selection with the reweighting applied and turned off. The uncertainty is taken as half the difference and is estimated individually for every mass point in the MS-agnostic and full-detector selection. The relative systematic uncertainties are given in figure 5.33.

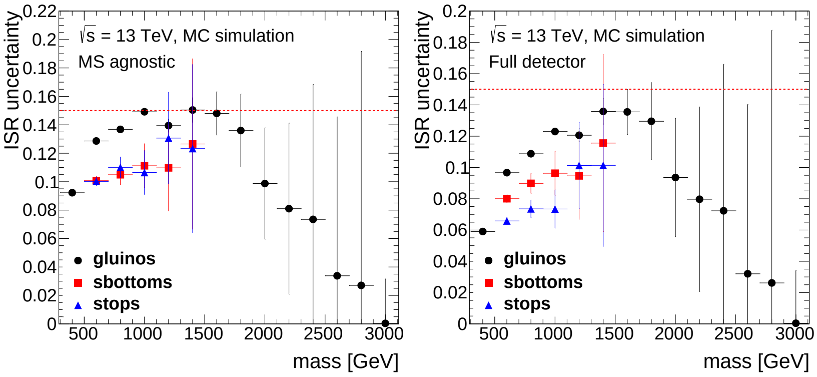

Figure 5.33: Relative systematic uncertainty on the modelling of ISR for all R-hadron mass points. The left plot shows the uncertainty in the MS-agnostic trigger selection, the right plot for the full-detector selection where uncertainties tend to be slightly lower due to the additional single-muon trigger. A flat systematic uncertainty visualised by the red dashed line is assigned.

A mass dependency of the uncertainty is clearly visible[24]. A conservative approach is chosen which assigns a systematic uncertainty of 15% to all masses and particle types. Since large contributions from the gluon–gluon fusion production channel are absent for bottom and top squarks, the probability for additional radiation in

---

[24] The initial rise is due to the larger amount of available energy, while the subsequent falloff is caused by the change in dominant production channel from gluon–gluon fusion to quark–antiquark production and thus reduced ISR emission

MadGraph is smaller and thus the uncertainty estimated from the difference results in smaller uncertainties for squarks.

Stau and chargino sample are already produced in MadGraph and no reweighting is needed. The uncertainty on the ISR modelling can be estimated by varying different generator parameters independently of each other. The first variation scales the chosen renormalisation/factorisation parameter downwards by a factor of 0.5 (QCDW) and upwards by 2.0 (QCUP). The uncertainty due to the CKKW-L[25] merging scale is similarly evaluated by applying variations of 0.5 (SCDW) and 2.0 (SCUP). Lastly, the effects of systematic variations of the parton shower tuning are estimated. In [301] groups of independent parameters have been combined to form five separate variations which are labelled VAR1 to VAR3C. Of these five only VAR3C, which corresponds to a downwards (PY3CDW) and upwards (PY3CUP) variation of the α_S value, was found to have a non-negligible influence. The overall systematic uncertainty is now taken as the maximal deviations from nominal values for each variation individually and adding them, in quadrature. Since this requires the production of six additional MC samples for every signal sample, only three mass points, chosen to cover all of the relevant mass spectrum, have been considered for each signal model. The uncertainties are taken to be flat over the full mass range but are estimated individually for $\tilde{\chi}_1^{\pm}\tilde{\chi}_1^{\pm}$, $\tilde{\chi}_1^{\pm}\tilde{\chi}_1^{0}$ and $\tilde{\tau}$. The adopted systematic uncertainties are listed in table 5.18. Figure 5.34 shows the final uncertainty and deviations from the nominal MC yields through all six variations.

particle	sys. unc.
Gluinos	15%
Sbottoms	15%
Stops	15%
Staus	4%
Charginos $\tilde{\chi}_1^{\pm}\tilde{\chi}_1^{\pm}$	5%
Charginos $\tilde{\chi}_1^{\pm}\tilde{\chi}_1^{0}$	7%

Table 5.18: List of systematic uncertainties assigned to all particle types due to ISR modelling.

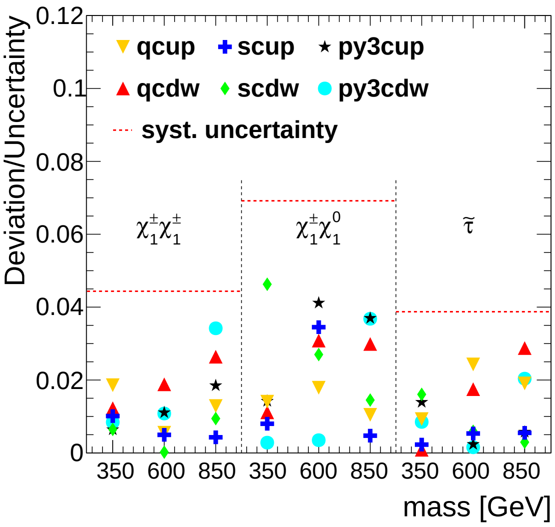

Figure 5.34: Relative deviations from nominal MC yields through variations of generator parameters in MadGraph. See text for explanations on the nature of variations. The systematic uncertainties due to the ISR modelling are taken to be flat over all mass points and are calculated by adding the largest deviations from each of the three up-down variations in quadrature individually for $\tilde{\chi}_1^{\pm}\tilde{\chi}_1^{\pm}$ (left segment), $\tilde{\chi}_1^{\pm}\tilde{\chi}_1^{0}$ (middle segment) and $\tilde{\tau}$ (right segment). The final values are indicated by the dashed red horizontal lines. Only three mass points have been simulated for all scenarios.

As a cross-check for the uncertainty on *R*-hadrons, the same variations of the MadGraph generator parameters have also been applied to a range of di-gluino samples. The deviations from nominal MC have been evaluated as described above and were found to be of similar size as the uncertainty derived from the efficiency difference between Pythia and MadGraph. Plots showing the deviations caused by individual parameter variations are given in figure E.4 in appendix E.1.

---

[25] An algorithm which addresses the merging of tree-level matrix elements and parton showers. For more details see [328] and references therein.

5.8.5 Measurement of Pixel dE/dx

The most probable values for the Pixel dE/dx distribution differ slightly in data and simulation. This is accounted for by the application of correction factors. A systematic uncertainty on the dE/dx modelling will be estimated by varying the correction factors by $\pm 1\sigma$ and treating the difference to the nominal value as uncertainty.

Since the detector conditions change over time due to radiation damage[26], the measured ionisation varies as well. A run-by-run correction of the measured dE/dx is performed accordingly, which derives scale factors to create a constant ionisation measurements throughout data taking. Small changes of condition within a run are taken care of by a 2% smearing of the dE/dx signal[27].

Lastly, the dE/dx estimation in simulation contains an η correction. A systematic uncertainty on this correction will be estimated by comparing the proton, pion and kaon mass peaks at a fixed low-momentum value as a function of η after the correction has been applied.

The combined systematic uncertainty on the Pixel dE/dx measurement is expected to be small[28].

5.8.6 β estimation in signal MC

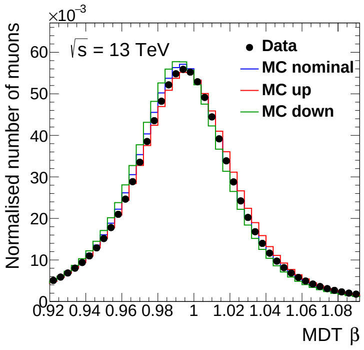

Figure 5.35: MDT β distribution for muons from data and simulated $Z \to \mu\mu$ decays for nominal and scaled MC, in which the smearing has been increased and decreased by 5%. The scaled MC distributions bracket the data distribution as intended.

Simulated timing undergoes dedicated treatments to generate an agreement with the data distribution. For MDTs this is done by smearing the hit times as described in chapter 4.9. To estimate the influence of a systematic error within the procedure, the derived smearing constants are varied by 10% up and down to create two new β distributions which encapsulate the data distribution. The event and candidate selections are then repeated with the altered β values and the effect on the signal yield within the signal regions are evaluated. The largest deviation from the nominal yield is taken as systematic uncertainty. Figure 5.35 shows the nominal, up- and down-scaled β distributions for muons from simulated $Z \to \mu\mu$ decays compared to muons from data. A summary of the thus derived systematic uncertainties are included in table 5.19.

	sys. unc. [%]		
particle	MDT	RPC Corr.	RPC thres.
Gluinos	0.0–0.7	0.1–2.0	0.0–0.6
Sbottoms	0.1–0.8	0.3–1.6	0.2–1.3
Stops	0.2–0.9	0.3–1.9	0.1–0.7
Staus	0.2–2.2	0.9–3.1	0.1–1.0
Charginos	0.1–2.5	0.3–2.7	0.1–0.7

Table 5.19: List of systematic uncertainties assigned to all particle types due to the MS β estimation.

No smearing is performed for RPCs. Instead some strips with wrongly modelled timing behaviour are corrected as was detailed in chapter 4.10. Two sources of systematic errors are investigated. First, the RPC β is re-evaluated without the correction and the relative difference in signal yield with respect to the correctly treated RPC β is taken as systematic uncertainty. The second effect is the choice of threshold values for the corrections to become active. Recall that only a subset of strips was affected by the mismodelling and that only those strips with resolution $\sigma_{t_0} > 2.1$ ns and mean $\bar{t}_0 > 1.0$ ns are corrected. The choice of these threshold parameters were taken as the local minima in the corresponding distributions (see figures 4.60

---

[26] this is especially relevant for the IBL which only started data-taking in 2015 and effects of radiation damage to the detector are clearly discernible.

[27] The 2% are chosen since it reflects the maximal difference in scale factors of two consecutive runs.

[28] For comparison, the uncertainty derived for the MS-agnostic analysis performed with the 2015 data was $<$ 3% [1].

and 4.61) but remain somewhat arbitrary. To consider the effect of the threshold choices the treatment is repeated with changed thresholds $\sigma_{t_0} > 1.8$ and $\bar{t}_0 > 0.8$ (MC down) and $\sigma_{t_0} > 2.4$ and $\bar{t}_0 > 1.2$ (MC up). The effect of all variations on the RPC β distribution can be seen from figure 5.36. The uncertainties for all particle types are listed in table 5.19.

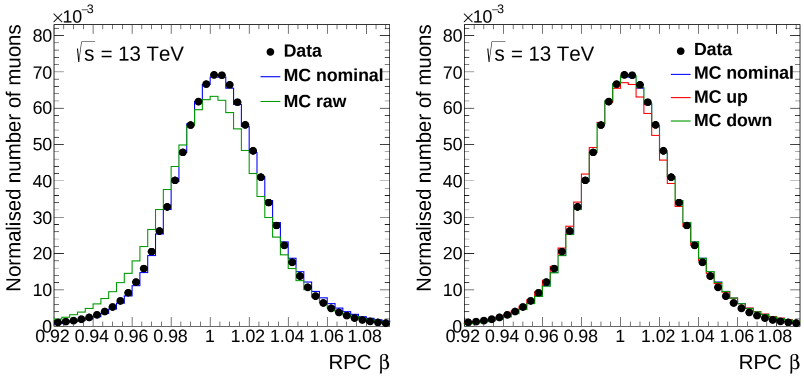

Figure 5.36: RPC β distributions for muons from data and simulated $Z \to \mu\mu$ decays to estimate systematic uncertainties. The left plot compares the fully treated β distribution with the distribution for which no strip correction was performed. In the right plot the threshold values for the correction to become active have been altered to generate two distributions roughly bracketing the data distribution. The final systematic uncertainty is estimated as the largest relative change in signal yield with respect to nominal MC.

Since the Tile Calorimeter MC treatment also involves the smearing of simulated timing information, a systematic uncertainty is estimated analogously to the MDTs through a 5% up and down scaling of the smearing. The final uncertainties are given in table 5.20.

particle	TileCal β] sys. unc. [%] MS agnostic	full detector
Gluinos	0.4–3.2	0.5–4.5
Sbottoms	0.5–1.0	1.0–1.4
Stops	0.4–1.4	1.2–2.3
Staus		0.1–0.6
Charginos		0.1–1.5

Table 5.20: List of systematic uncertainties assigned to all particle types due to the TileCal β estimation.

5.8.7 MuGirlStau reconstruction efficiency

To assess whether the reconstruction efficiency of the MuGirlStau algorithm is the same in data and simulation, $Z \to \mu\mu$ decays are evaluated in data using a standard muon reconstruction algorithm[29]. The estimation thus rests on two basic assumptions: the reconstruction efficiency of MuGirlStau is the same for muons and slow particles and the MuGirlStau efficiency for particles reconstructed with the standard reconstruction algorithm is the same as the true MuGirlStau reconstruction efficiency. Both assumptions have been tested and were found to be fulfilled.

A data sample consisting of $Z \to \mu\mu$ decays is selected using the standard reconstruction algorithm. The efficiency of MuGirlStau is evaluated in this sample and compared to simulation. Figure 5.37 shows a comparison of the efficiencies as function of η. The discrepancies peak at about $15 - 20\%$ in the region $1.2 < |\eta| < 1.6$ where simulation underestimates the efficiency in data. The difference is taken to be 10%, which results in systematic uncertainties ranging from 0.2% to 5.8% on the signal yield.

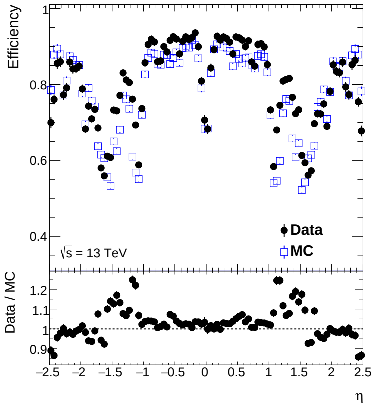

Figure 5.37: Reconstruction efficiency of the MuGirlStau algorithm in data and MC as a function of η. The efficiencies have been measured in $Z \to \mu\mu$ events with respect to tracks identified by the standard reconstruction algorithm. Figure adapted from M. Habedank.

5.8.8 Pileup

All simulated samples have been reweighted to get agreement with the pileup profile in data. This includes a scale factor of $1/1.09$

[29] The reconstruction efficiency of this standard algorithm is the same in data and MC as simulation was tuned for this algorithm.

on simulated events which was determined by a dedicated ATLAS study group[30]. To estimate the influence of the pileup modelling on the signal yield, the scale factor is varied up and down to values 1 and 1/1.18. The change with respect to nominal is taken as a systematic uncertainty and ranges from 0.1% to 5.5% (0.2% to 3.8%) for the full-detector (MS-agnostic) analysis.

5.8.9 Luminosity

The uncertainty on the quoted integrated luminosity of the full dataset is estimated through the van der Meer method[31] [329] similar to the procedure detailed in [330]. A final uncertainty of 2.1% is obtained.

5.8.10 Background estimate

Two factors could potentially cause a systematic error on the background estimation: the choice and number of η bins for the creation of the PDFs and the definitions of the sidebands from which the PDFs are created.

To test the influence of the first, the number of η bins is varied to 3 and 6 for all selections with a nominal of 5 η bins and to 4 and 9 for `SR-2C-FD` where the nominal is 6 η bins. For each variation the background is estimated according to the description in chapter 5.7 and the number of events in the signal regions evaluated. Half the maximal discrepancy in event yield with respect to nominal is taken as a systematic uncertainty.

The influence of the definition of sidebands are evaluated by defining two new sets of sidebands with medium (MED.) and tight (TIG.) cuts as specified in table 5.21 from which the PDFs are created. Analogue to the previous procedure, half of the maximal difference with respect to nominal event yield in the signal region is assigned as uncertainty.

An uncertainty caused through the normalisation of the background estimate in the CR is asserted by propagating the relative statistical uncertainty on the data event count in the CR N_{data}, given by $\sqrt{N_{\text{data}}}$, to the estimated number of background events in the signal region.

For final systematic uncertainty on the background estimate both components are added in quadrature. Table 5.22 gives a full list of the associated systematic uncertainties for all signal regions.

PDF	obs.	X	
p	$\beta_{\text{ToF}} < X$	1.0	NOM.
		0.98	MED.
		0.96	TIG.
p	$\beta\gamma_{dE/dx} < X$	2.5	NOM.
		2.45	MED.
		2.4	TIG.
β_{ToF} & $\beta\gamma_{dE/dx}$	$p < X$	200	NOM.
		190	MED.
		180	TIG.

Table 5.21: Definitions of alternative sidebands for PDF creation. A medium (MED.) and tight (TIG.) sideband is added in addition to the nominal (NOM.) definition. The maximal $p/\beta/\beta\gamma$ cuts as defined in table 5.12 remain in place for all three definitions.

	region	sys. uncer.
$\tilde{g}$	`SR-RH-MA`	33 – 34%
$\tilde{b}$		34%
$\tilde{t}$		34%
$\tilde{g}$	`SR-RH-FD`	27 – 53%
$\tilde{b}$		27 – 47%
$\tilde{t}$		27 – 47%
$\tilde{\tau}$	`SR-1C-FD`	9 – 11%
$\tilde{\tau}$	`SR-2C-FD`	18 – 31%
$\tilde{\chi}_1^{\pm}$	`SR-1C-FD`	18 – 34%
$\tilde{\chi}_1^{\pm}$	`SR-2C-FD`	9 – 19%

Table 5.22: Overview of the systematic uncertainties on the background estimate for all signal regions and particle types.

5.8.11 Summary of systematic uncertainties

A list of all investigated systematics and their relative magnitudes on searches for R-hadrons, staus and charginos is given in table 5.23.

---

[30] The purpose of the scale factor is to account for the incorrect total scattering cross-section which was assumed in simulation.

[31] Dedicated runs are necessary in which the beams are swept across each other and the relative interaction rate is measured.

	Relative uncertainties [%]			
Systematic	MS agnostic R-hadrons	full detector R-hadrons	staus	charginos
Theoretical cross sections	13–57	13–57	6–10	4–10
E_T^{miss}-trigger efficiency	1.7	1.7	2.0	2.4
Single-muon trigger		1.0	4.0	3.0
Initial-state radiation	15.0	15.0	4.0	7.0
Pixel dE/dx	–	–	–	–
TileCal β estimation	< 4	< 5	< 1	< 2
MDT β estimation		< 1	< 3	< 3
RPC β estimation		< 2	< 4	< 3
MuGirlStau reco. efficiency		1.7–5.8	0.2–5.8	0.8–5.8
Pileup	0.2–3.8	0.3–5.5	0.1–3.1	0.2–4.4
Luminosity	2.1	2.1	2.1	2.1
Background estimate	33–34	27–53	9–31	9–34

Table 5.23: Summary of all investigated systematic uncertainties and their relative effect on R-hadron, stau and chargino searches. The items are split into four groups through horizontal lines: theoretical cross section, signal efficiency, luminosity and background estimate.

Additionally, a series of cross-checks has been performed to validate the SMP search which are briefly summarised in appendix E.2.

5.9 Results

The results of the MS-agnostic R-hadron search are summarised in table 5.24 where the event yields of expected signal, estimated background, corresponding uncertainties and observation are listed for all signal regions and particle types.

			`SR-RH-MA`		
	mass [GeV]	N_{exp}	Efficiency	N_{est}	N_{obs}
$\tilde{g}$	400	160000 ± 10000	0.045 ± 0.003	8.0 ± 3.0	8
$\tilde{g}$	600	28000 ± 1000	0.085 ± 0.004	3.0 ± 1.0	7
$\tilde{g}$	800	5700 ± 200	0.106 ± 0.005	1.8 ± 0.6	4
$\tilde{g}$	1000	1350 ± 60	0.116 ± 0.005	1.0 ± 0.3	2
$\tilde{g}$	1200	400 ± 20	0.128 ± 0.006	0.7 ± 0.3	2
$\tilde{g}$	1400	135 ± 7	0.148 ± 0.007	0.6 ± 0.2	2
$\tilde{g}$	1600	42 ± 2	0.144 ± 0.007	0.5 ± 0.2	2
$\tilde{g}$	1800	13.6 ± 0.8	0.137 ± 0.007	0.4 ± 0.1	2
$\tilde{g}$	2000	4.4 ± 0.3	0.124 ± 0.005	0.4 ± 0.1	2
$\tilde{g}$	2200	1.5 ± 0.2	0.113 ± 0.004	0.4 ± 0.1	2
$\tilde{g}$	2400	0.5 ± 0.2	0.107 ± 0.004	0.4 ± 0.1	2
$\tilde{g}$	2600	0.2 ± 0.2	0.101 ± 0.004	0.4 ± 0.1	2
$\tilde{g}$	2800	0.1 ± 0.2	0.092 ± 0.004	0.4 ± 0.1	2
$\tilde{g}$	3000	0.0 ± 0.2	0.088 ± 0.004	0.4 ± 0.1	2
$\tilde{b}$	600	320 ± 20	0.051 ± 0.003	3 ± 1	7
$\tilde{b}$	800	66 ± 3	0.065 ± 0.003	1.8 ± 0.6	4
$\tilde{b}$	1000	15.2 ± 0.7	0.069 ± 0.003	1.0 ± 0.3	2
$\tilde{b}$	1200	4.3 ± 0.2	0.074 ± 0.003	0.7 ± 0.3	2
$\tilde{b}$	1400	1.1 ± 0.2	0.068 ± 0.003	0.6 ± 0.2	2
$\tilde{t}$	600	470 ± 20	0.074 ± 0.004	3 ± 1	7
$\tilde{t}$	800	93 ± 4	0.091 ± 0.004	1.8 ± 0.6	4
$\tilde{t}$	1000	22.1 ± 0.8	0.099 ± 0.004	1.0 ± 0.3	2
$\tilde{t}$	1200	5.9 ± 0.3	0.103 ± 0.004	0.7 ± 0.3	2
$\tilde{t}$	1400	1.8 ± 0.2	0.110 ± 0.004	0.6 ± 0.2	2

Table 5.24: Final event yields for the MS-agnostic R-hadron searches. Given are the number of expected signal events N_{exp}, the selection efficiency, number of estimated background events N_{est} and the number of observed events N_{obs}. No significant excess of events above expectation is observed with the largest deviations occurring for the high-mass gluino R-hadrons regions where 2 events are observed with an expected background of 0.4 ± 0.1.

The largest deviation occurs in the high-mass gluino R-hadron search where 2 events are observed while a background of 0.4 ± 0.1 events is expected. Thus no significant excess of events above expectation was observed in any signal region. As a result, the data is used to derive 95% CL upper limits on the production cross-sections of all particle types as shown in figure 5.38. The limits are obtained by considering the estimated background and expected signal following the CL_s technique [331]. Knowledge of the theoretical cross sections allows the translation of these limits into lower-mass limits, resulting in observed 95% CL mass limits of $m(\tilde{g}) > 1950$ GeV, $m(\tilde{b}) > 1170$ GeV and $m(\tilde{t}) > 1220$ GeV. The expected limits of $m(\tilde{g}) > 2060$ GeV, $m(\tilde{b}) > 1230$ GeV and $m(\tilde{t}) > 1300$ GeV are not reached due to the slight surplus of events in the high-mass signal regions.

Figure 5.38: 95% CL upper cross-section limits for gluino (left), sbottom (middle) and stop (right) R-hadrons in the MS-agnostic analysis are shown. The expected limit is drawn as dashed black line, the solid red line illustrates the observed limit. The theoretical prediction is drawn as solid black line including the $\pm\sigma$ uncertainty band.

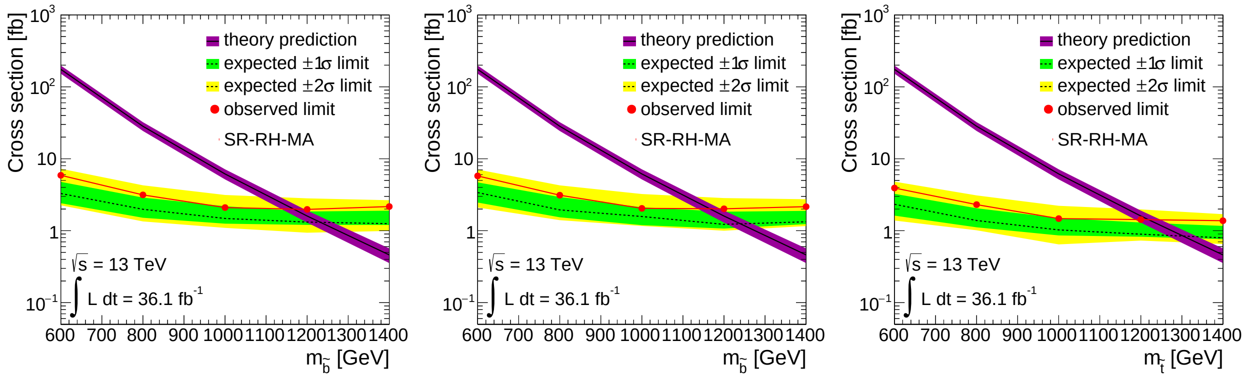

The event yields of the full-detector R-hadron search are shown in table 5.25 separately for the ID+Calo and Loose selection. No deviations from expectation are observed in any of the signal regions. The event yields are generally lower in the loose selection as the additional measurement of momentum and β in the MS suppresses mismeasurements more efficiently. Upper limits on the production cross section are derived as shown in figure 5.39. Just as for the MS agnostic analysis limits on the heavy R-hadron constituents mass are derived, resulting in lower limits of $m(\tilde{g}) > 2015$ GeV, $m(\tilde{b}) > 1240$ GeV and $m(\tilde{t}) > 1325$ GeV, whereas lower-mass limits of $m(\tilde{g}) > 2070$ GeV, $m(\tilde{b}) > 1255$ GeV and $m(\tilde{t}) > 1340$ GeV were expected. Once again the expected limits are not matched as a slight surplus of events is observed. As expected, the full-detector analysis places more stringent limits on all particle masses when compared to the MS-agnostic approach.

Figure 5.39: 95% CL upper cross-section limits for gluino (left), sbottom (middle) and stop (right) R-hadrons in the full-detector analysis are shown. The expected limit is drawn as dashed black line, the solid red line illustrates the observed limit. The theoretical prediction is drawn as solid black line including the $\pm\sigma$ uncertainty band.

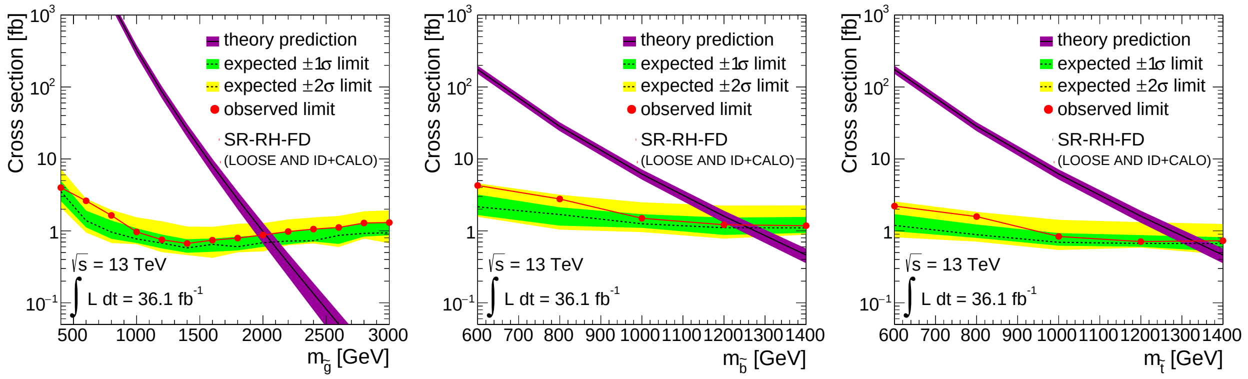

		SR-RH-FD (ID+Calo)				SR-RH-FD (Loose)			
	mass [GeV]	N_{exp}	Efficiency	N_{est}	N_{obs}	N_{exp}	Efficiency	N_{est}	N_{obs}
$\tilde{g}$	400	132000 ± 10000	0.037 ± 0.003	9 ± 2	13	93000 ± 7000	0.026 ± 0.002	1.5 ± 0.5	1
$\tilde{g}$	600	20000 ± 1000	0.059 ± 0.004	4 ± 1	9	17000 ± 1000	0.051 ± 0.003	0.5 ± 0.2	1
$\tilde{g}$	800	3800 ± 200	0.072 ± 0.004	2.5 ± 0.7	5	3300 ± 200	0.062 ± 0.004	0.3 ± 0.1	1
$\tilde{g}$	1000	940 ± 60	0.080 ± 0.005	1.6 ± 0.4	3	710 ± 40	0.061 ± 0.003	0.14 ± 0.05	0
$\tilde{g}$	1200	260 ± 20	0.083 ± 0.005	1.3 ± 0.4	2	220 ± 10	0.071 ± 0.005	0.10 ± 0.04	0
$\tilde{g}$	1400	81 ± 5	0.089 ± 0.006	1.1 ± 0.3	2	77 ± 6	0.084 ± 0.006	0.07 ± 0.03	0
$\tilde{g}$	1600	26 ± 2	0.088 ± 0.006	1.0 ± 0.3	2	23 ± 1	0.077 ± 0.005	0.06 ± 0.03	0
$\tilde{g}$	1800	8.3 ± 0.6	0.083 ± 0.005	0.9 ± 0.3	2	7.2 ± 0.5	0.072 ± 0.005	0.05 ± 0.03	0
$\tilde{g}$	2000	2.5 ± 0.2	0.071 ± 0.004	0.9 ± 0.2	2	2.4 ± 0.2	0.067 ± 0.004	0.05 ± 0.02	0
$\tilde{g}$	2200	0.9 ± 0.2	0.067 ± 0.003	0.9 ± 0.2	2	0.8 ± 0.2	0.061 ± 0.003	0.05 ± 0.02	0
$\tilde{g}$	2400	0.3 ± 0.2	0.066 ± 0.004	0.9 ± 0.2	2	0.3 ± 0.2	0.052 ± 0.003	0.05 ± 0.02	0
$\tilde{g}$	2600	0.1 ± 0.2	0.063 ± 0.003	0.9 ± 0.2	2	0.1 ± 0.2	0.050 ± 0.003	0.05 ± 0.02	0
$\tilde{g}$	2800	0.0 ± 0.2	0.061 ± 0.003	0.9 ± 0.2	2	0.0 ± 0.2	0.040 ± 0.002	0.05 ± 0.02	0
$\tilde{g}$	3000	0.0 ± 0.2	0.055 ± 0.003	0.9 ± 0.2	2	0.0 ± 0.2	0.042 ± 0.002	0.05 ± 0.02	0
$\tilde{b}$	600	210 ± 10	0.033 ± 0.002	4 ± 1	9	200 ± 10	0.032 ± 0.002	0.5 ± 0.2	1
$\tilde{b}$	800	42 ± 2	0.041 ± 0.002	2.5 ± 0.7	5	40 ± 3	0.039 ± 0.002	0.3 ± 0.1	1
$\tilde{b}$	1000	9.7 ± 0.5	0.044 ± 0.002	1.6 ± 0.4	3	9.3 ± 0.5	0.042 ± 0.002	0.14 ± 0.05	0
$\tilde{b}$	1200	2.7 ± 0.2	0.046 ± 0.002	1.3 ± 0.4	2	2.6 ± 0.2	0.045 ± 0.003	0.10 ± 0.04	0
$\tilde{b}$	1400	0.7 ± 0.2	0.045 ± 0.002	1.1 ± 0.3	2	0.7 ± 0.2	0.043 ± 0.003	0.07 ± 0.03	0
$\tilde{t}$	600	230 ± 20	0.037 ± 0.003	4 ± 1	9	420 ± 20	0.067 ± 0.003	0.5 ± 0.2	1
$\tilde{t}$	800	51 ± 3	0.050 ± 0.003	2.5 ± 0.7	5	78 ± 3	0.077 ± 0.003	0.3 ± 0.1	1
$\tilde{t}$	1000	11.6 ± 0.6	0.052 ± 0.002	1.6 ± 0.4	3	19.4 ± 0.8	0.088 ± 0.004	0.14 ± 0.05	0
$\tilde{t}$	1200	3.1 ± 0.2	0.053 ± 0.003	1.3 ± 0.4	2	5.0 ± 0.2	0.086 ± 0.003	0.10 ± 0.04	0
$\tilde{t}$	1400	0.9 ± 0.2	0.056 ± 0.003	1.1 ± 0.3	2	1.5 ± 0.2	0.093 ± 0.004	0.07 ± 0.03	0

Table 5.25: Final event yields for the full-detector R-hadron searches. Given are the number of expected signal events N_{exp}, the selection efficiency, number of estimated background events N_{est} and the number of observed events N_{obs}. No significant excess of events above expectation is observed.

Table 5.26 gives the event yields for the stau search separately for `SR-1C-FD` and `SR-2C-FD`. As can be seen, no event appears in any of the `SR-2C-FD` signal regions consistent with the background where a maximum number of 0.33 ± 0.06 events is expected. The one-candidate region also offers reasonable agreement between background and observation. Figure 5.40 shows the derived 95% CL limits. A lower-mass limit of $m(\tilde{\tau}) > 420$ GeV can be placed, slightly exceeding the expected limit of $m(\tilde{\tau}) > 410$ GeV.

	SR-2C-FD				SR-1C-FD			
mass [GeV]	N_{exp}	Efficiency	N_{est}	N_{obs}	N_{exp}	Efficiency	N_{est}	N_{obs}
287	11.2 ± 0.4	0.148 ± 0.004	0.33 ± 0.06	0	5.6 ± 0.3	0.075 ± 0.003	80 ± 7	74
318	8.0 ± 0.4	0.162 ± 0.007	0.22 ± 0.04	0	4.2 ± 0.3	0.084 ± 0.005	56 ± 5	52
349	5.5 ± 0.2	0.163 ± 0.005	0.15 ± 0.03	0	2.8 ± 0.2	0.084 ± 0.003	41 ± 4	36
380	3.9 ± 0.2	0.166 ± 0.006	0.11 ± 0.02	0	2.3 ± 0.2	0.101 ± 0.005	30 ± 3	24
411	2.9 ± 0.2	0.174 ± 0.005	0.08 ± 0.02	0	1.6 ± 0.2	0.098 ± 0.004	23 ± 2	20
442	2.2 ± 0.2	0.181 ± 0.007	0.06 ± 0.01	0	1.2 ± 0.2	0.103 ± 0.006	17 ± 2	16
473	1.6 ± 0.2	0.185 ± 0.005	0.045 ± 0.009	0	1.0 ± 0.2	0.115 ± 0.004	13 ± 1	15
504	1.2 ± 0.2	0.191 ± 0.005	0.035 ± 0.007	0	0.8 ± 0.2	0.116 ± 0.004	10 ± 1	11
536	1.0 ± 0.2	0.194 ± 0.005	0.027 ± 0.006	0	0.6 ± 0.2	0.118 ± 0.004	7.9 ± 0.8	7
567	0.8 ± 0.2	0.207 ± 0.005	0.027 ± 0.006	0	0.5 ± 0.2	0.125 ± 0.004	6.3 ± 0.6	4
598	0.6 ± 0.2	0.212 ± 0.005	0.022 ± 0.005	0	0.4 ± 0.2	0.125 ± 0.004	5.0 ± 0.5	3
629	0.5 ± 0.2	0.214 ± 0.006	0.017 ± 0.004	0	0.3 ± 0.2	0.131 ± 0.004	5.0 ± 0.5	3
660	0.4 ± 0.2	0.215 ± 0.005	0.014 ± 0.003	0	0.2 ± 0.2	0.134 ± 0.005	4.0 ± 0.4	3
692	0.3 ± 0.2	0.209 ± 0.007	0.011 ± 0.003	0	0.2 ± 0.2	0.134 ± 0.005	3.2 ± 0.3	2
723	0.2 ± 0.2	0.213 ± 0.007	0.009 ± 0.002	0	0.1 ± 0.2	0.136 ± 0.005	2.7 ± 0.3	1
754	0.2 ± 0.2	0.218 ± 0.006	0.008 ± 0.002	0	0.1 ± 0.2	0.141 ± 0.004	2.2 ± 0.2	1
785	0.1 ± 0.2	0.216 ± 0.006	0.007 ± 0.002	0	0.1 ± 0.2	0.142 ± 0.005	1.8 ± 0.2	0
817	0.1 ± 0.2	0.216 ± 0.006	0.007 ± 0.002	0	0.1 ± 0.2	0.141 ± 0.004	1.5 ± 0.1	0
848	0.1 ± 0.2	0.212 ± 0.005	0.006 ± 0.001	0	0.1 ± 0.2	0.141 ± 0.004	1.3 ± 0.1	0
879	0.1 ± 0.2	0.215 ± 0.005	0.005 ± 0.001	0	0.1 ± 0.2	0.155 ± 0.005	1.3 ± 0.1	0
911	0.1 ± 0.2	0.222 ± 0.005	0.004 ± 0.001	0	0.0 ± 0.2	0.153 ± 0.005	1.1 ± 0.1	0

Table 5.26: Final event yields for the stable stau searches. Given are the number of expected signal events N_{exp}, the selection efficiency, number of estimated background events N_{est} and the number of observed events N_{obs}.

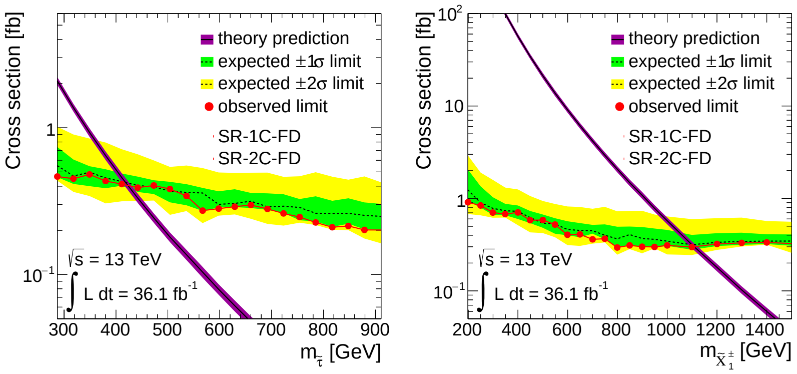

Figure 5.40: 95% CL upper cross-section limits for staus (left) and charginos (right). The expected limit is drawn as dashed black line, the solid red line illustrates the observed limit. The theoretical prediction is drawn as solid black line including the $\pm\sigma$ uncertainty band.

Lastly, the event yields for the stable-chargino searches are shown in table 5.27 for both the one-candidate and two-candidate selection. Once again, no events are observed in any of the two-candidate signal regions with a maximal expected background of 1.5 ± 0.3 events, while the two-candidate region shows a good agreement of estimated background and number of observed events. 95% CL limits are derived according to figure 5.40, which allows the exclusion of stable charginos with masses $m(\tilde{\chi}_1^{\pm}) < 1100$ GeV matching the expected limit of $m(\tilde{\chi}_1^{\pm}) < 1095$ GeV. This constitutes a significant improvement with respect to the previous ATLAS limit at $\sqrt{s} = 8$ TeV which was given by $m(\tilde{\chi}_1^{\pm}) < 620$ GeV. For the limit setting currently only the $\tilde{\chi}_1^{\pm}\tilde{\chi}_1^{\pm}$ samples are used. It is however planned to expand this with the $\tilde{\chi}_1^{\pm}\tilde{\chi}_1^{0}$ samples in the future.

	SR-2C-FD				SR-1C-FD			
mass [GeV]	N_{exp}	Efficiency	N_{est}	N_{obs}	N_{exp}	Efficiency	N_{est}	N_{obs}
200	2600.0 ± 100.0	0.082 ± 0.003	1.5 ± 0.3	0	1260 ± 70	0.039 ± 0.002	240 ± 20	227
250	1250.0 ± 50.0	0.092 ± 0.004	0.51 ± 0.09	0	930 ± 40	0.068 ± 0.003	120 ± 10	109
300	690.0 ± 20.0	0.102 ± 0.004	0.32 ± 0.06	0	530 ± 20	0.079 ± 0.004	81 ± 8	74
350	370.0 ± 10.0	0.104 ± 0.004	0.15 ± 0.03	0	310 ± 10	0.087 ± 0.003	41 ± 4	36
400	212.0 ± 7.0	0.104 ± 0.004	0.08 ± 0.01	0	214 ± 8	0.104 ± 0.004	23 ± 2	20
450	141.0 ± 5.0	0.113 ± 0.004	0.06 ± 0.01	0	140 ± 5	0.113 ± 0.004	17 ± 2	16
500	91.0 ± 3.0	0.119 ± 0.004	0.033 ± 0.007	0	88 ± 3	0.115 ± 0.004	10 ± 1	11
550	62.0 ± 2.0	0.124 ± 0.004	0.026 ± 0.005	0	59 ± 2	0.119 ± 0.004	8.2 ± 0.9	7
600	43.0 ± 1.0	0.130 ± 0.004	0.021 ± 0.004	0	43 ± 1	0.131 ± 0.004	5.2 ± 0.5	3
650	28.8 ± 0.9	0.130 ± 0.004	0.013 ± 0.003	0	26.6 ± 0.9	0.120 ± 0.004	4.2 ± 0.4	3
700	19.9 ± 0.7	0.132 ± 0.005	0.011 ± 0.002	0	19.3 ± 0.6	0.128 ± 0.004	3.4 ± 0.3	2
750	12.7 ± 0.4	0.120 ± 0.004	0.007 ± 0.002	0	14.3 ± 0.5	0.135 ± 0.004	2.2 ± 0.2	1
800	9.9 ± 0.4	0.132 ± 0.004	0.006 ± 0.002	0	10.0 ± 0.4	0.133 ± 0.004	1.9 ± 0.2	0
850	6.3 ± 0.3	0.118 ± 0.004	0.005 ± 0.002	0	6.9 ± 0.3	0.129 ± 0.005	1.3 ± 0.2	0
900	4.7 ± 0.2	0.121 ± 0.004	0.004 ± 0.001	0	5.3 ± 0.2	0.136 ± 0.004	1.1 ± 0.1	0
950	3.5 ± 0.2	0.124 ± 0.004	0.003 ± 0.001	0	3.8 ± 0.2	0.133 ± 0.004	1.0 ± 0.1	0
1000	2.6 ± 0.2	0.124 ± 0.005	0.003 ± 0.001	0	2.8 ± 0.2	0.136 ± 0.006	0.80 ± 0.09	0
1100	1.4 ± 0.2	0.121 ± 0.004	0.0017 ± 0.0009	0	1.7 ± 0.2	0.145 ± 0.005	0.48 ± 0.07	0
1200	0.7 ± 0.2	0.109 ± 0.004	0.0013 ± 0.0008	0	0.9 ± 0.2	0.136 ± 0.004	0.33 ± 0.07	0
1300	0.4 ± 0.2	0.106 ± 0.004	0.0011 ± 0.0006	0	0.5 ± 0.2	0.131 ± 0.004	0.24 ± 0.07	0
1400	0.2 ± 0.2	0.105 ± 0.004	0.0008 ± 0.0006	0	0.3 ± 0.2	0.130 ± 0.004	0.19 ± 0.06	0
1500	0.1 ± 0.2	0.096 ± 0.004	0.0006 ± 0.0005	0	0.2 ± 0.2	0.133 ± 0.004	0.14 ± 0.05	0

Table 5.27: Final event yields for the stable chargino searches. Given are the number of expected signal events N_{exp}, the selection efficiency, number of estimated background events N_{est} and the number of observed events N_{obs}. No significant excess of events above expectation is observed.

The final 95% CL limits for all hypothesised particles and signal regions are summarised in table 5.28 alongside previous results.

	95% CL mass limits				
	Full detector		MS agnostic		
Particle	2012	2015 + 2016	2012	2015	2015 + 2016
$\tilde{g}$	1270 GeV	2015 GeV	1260 GeV	1580 GeV	1950 GeV
$\tilde{b}$	845 GeV	1240 GeV	835 GeV	805 GeV	1170 GeV
$\tilde{t}$	900 GeV	1325 GeV	870 GeV	890 GeV	1220 GeV
$\tilde{\tau}$	(440 GeV)	420 GeV			
$\tilde{\chi}_1^{\pm}$	620 GeV	1100 GeV			

Table 5.28: Summary of 95% CL lower-mass limits from three ATLAS SMP searches: (1) based on the dataset from 2012 at $\sqrt{s} = 8$ TeV corresponding to 19.1 fb^{-1} [160], (2) based on the 2015 dataset at $\sqrt{s} = 13$ TeV corresponding to 3.2 fb^{-1} [1], (3) the present study based on 2015 and 2016 data. For stable staus the chosen GMSB parameters varied between 2012 and the search presented here. Thus, a direct comparison of limits is not practicable.

5.10 Summary

In this chapter a detailed description of the analysis strategy and results of a search for stable massive particles was given. All data collected in 2015 and 2016 is used to search for R-hadrons containing gluinos, bottom or top squarks, staus from GMSB models and charginos stemming from mAMSB scenarios. The amount of initial-state radiation in an event is a crucial quantity for the analysis. Since it is not well modelled for R-hadron samples a reweighting of events is required on the basis of the MadGraph generator. Stable massive particles are identified in the detector based on their large anomalous ionisation energy losses and their reduced velocity. The ionisation energy losses are measured in the Pixel Detector as a truncated mean of several cluster charges, while the propagation velocity is determined in time-of-flight measurements in the Tile Calorimeter and Muon Spectrometer. Both observables possess a good discrimination power between signal and background. The online selection of events is based on either a trigger on missing transverse energy or a single-muon trigger. Timing plays an important role for the single-muon trigger as slow particles might arrive out of time and thus influence the efficiency negatively. This effect is not well reflected in simulation and an efficiency scaling is therefore necessary. The search for R-hadrons follows two different approaches: a full-detector search and a Muon-Spectrometer-agnostic version in which all information from the muon system including triggers is ignored. Stau and chargino searches employ the full detector and are split up in a two-candidate and one-candidate search. Candidates are found from either Inner Detector tracks or full-detector tracks, depending on the analysis. All candidates are required to pass certain event and candidate quality criteria to ensure physically sensible main observables. Candidates are further restricted in pseudorapidity and required to have a large momentum. Signal regions are defined based on the masses determined from the main observables. Since the background originates predominantly from mismeasurements, it is sampled from probability density functions generated from all particles in dedicated control regions. A detailed account of possible systematic errors and additional uncertainties on the calculated cross sections, signal efficiency and background estimate was given. No statistically significant excess of events was observed in any of the signal regions and mass-exclusion limits have been set on all hypothesised particles which are the most stringent limits to-date.

CHAPTER 6

Late-muon trigger for slow-particle searches

In chapter 5.5.2 it was shown that single-muon triggers are inefficient for slow particles that arrive with a delay at the trigger chambers. The mitigation strategy currently used relies on triggers on missing transverse energy, but results in large sensitivity losses for SMPs with large masses. This chapter introduces a conceptually new trigger that is dedicated to retain efficiency for late-arriving particles.

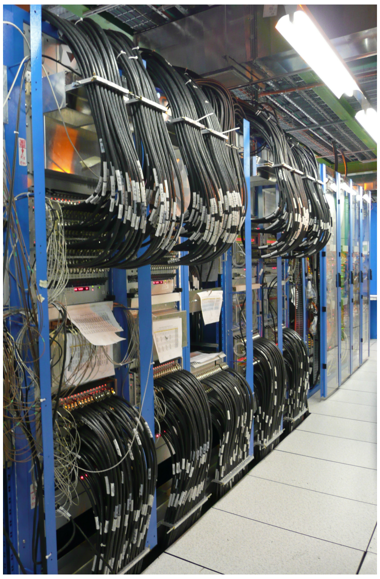

ATLAS L1 trigger racks in the service cavern next to the detector. Figure taken from [332]

6.1 Concept of the late-muon trigger

The muon trigger chambers are calibrated to centre the arrival time of particles travelling with the speed of light in the 25 ns long window that consitutes the trigger BC (BC0). Particles arriving outside this acceptance window will be registered in a BC other than BC0, but get rejected by the HLT since the reconstruction of a muon-like particle fails with the ID information from the wrong BC. This is the case for all particles with $\beta < 0.65$, as can be seen in figure 6.1. A late-muon trigger is therefore required to consider information from at least two consecutive BCs. The easiest way to do this is to combine two L1 objects: A frequent trigger object (TOB)[1] like a soft jet or missing energy in BC0, and a muon as the candidate for the late particle in one of the following BCs. By adjusting the allowed range of the late muon (BC+1, BC+2, etc), one is able to construct an efficient trigger in a wide β range. However, the concept has limitations: L1 items can only be combined after an 'L1 accept' (L1A) has been issued, i.e. after a potential prescale has been evaluated. To get maximum efficiency it is therefore necessary to use the lowest-unprescaled L1 items. In case of E_T^{miss} this has been a trigger with threshold 50 GeV. Since all E_T^{miss} triggers used in the analysis were based on this L1 item anyway, the maximally possible signal efficiency increase through the new trigger is given by those events, which are accepted on L1 but rejected on HLT. In essence, the expected signal gain is small.

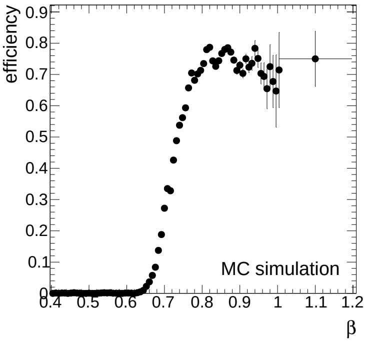

Figure 6.1: Single-muon trigger efficiency as function of the particles β evaluated from simulated long-lived massive particles.

The comissioning of the topological processor (L1Topo) [333] during 2016 allows for a more efficient approach in the future. L1Topo receives information from L1Calo and L1Muon and can run complex algorithms like the calculation of angular separation, invariant mass or hardness of different TOBs, and then deliver the result to the

---

[1] TOBs on L1 could be electrons, muons, jets, photons, taus and E_T^{miss}

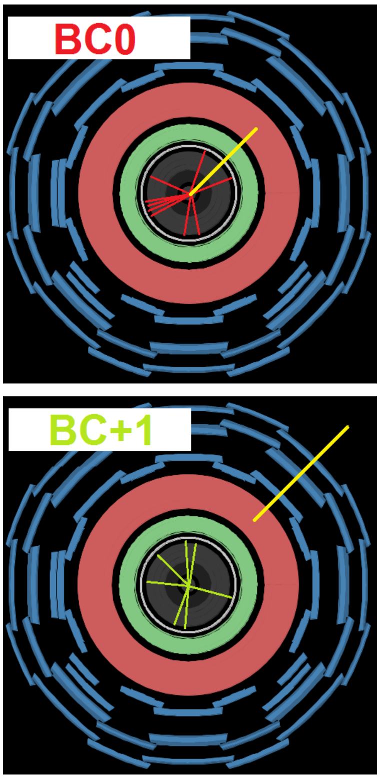

Figure 6.2: The event topology of the late-muon trigger. The first collision produces a slow particle (yellow) in association with a jet or E_T^{miss}. The arrival of the slow particle at the trigger chambers in the MS is delayed until the following BC. The detector cross-section was extracted from the HYPATIA event visualisation software [334].

CTP where the trigger decision is made. L1Topo therefore allows the combination of TOBs before application of prescales, thus avoiding the restriction imposed by the previous approach. However, there is also a drawback to this method. The late-muon information can only be supplied while L1Topo is processing and before delivering the signal to the CTP. This limits the late muon to BC+1. Even larger delays will not be registered in time. Nevertheless, the usage of low E_T^{miss} or jet thresholds is very attractive to SMP searches even if the window of β efficiency is limited.

Figure 6.2 shows the event topology the late-muon trigger is sensitive to. ID information is shown for two consecutive BCs, while the slow particle arrives late in the muon system.

On HLT level the trigger runs an algorithm similar to the offline reconstruction of slow particles with MuGirlStau and seeks to reconstruct the full-detector track of the particle allowing for $\beta < 1$.

6.2 Trigger thresholds

Two thresholds have to be defined for the late-muon trigger: the amount of missing energy or jet p_T and the p_T associated with the late muon. In the following only the version of the trigger that is based on E_T^{miss} is discussed, however, the reasoning also applies to the jet-based trigger. From an analysers point of view it would be desirable to have the thresholds as low as possible. Especially the missing-energy threshold is required to be low, since in most signal models no intrinsic E_T^{miss} is expected. Limitations come from readout bandwidth and computing capabilities on the HLT farm, since the track reconstruction with variable β is a complex and computing intensive process.

To evaluate the trigger efficiency a gluino R-hadron sample with $m_{\tilde{g}} = 2000$ GeV has been considered. The trigger simulation was executed with different threshold values. For the late-muon threshold it has to be taken into account that the Muon-to-Central-Trigger-Processor Interface (MuCTPI) [335] sends only limited muon information to L1Topo. Therefore only three low-p_T thresholds for the late muon are available: 4 GeV, 6 GeV and 10 GeV. Figure 6.3 gives the trigger efficiencies for all simulated thresholds.

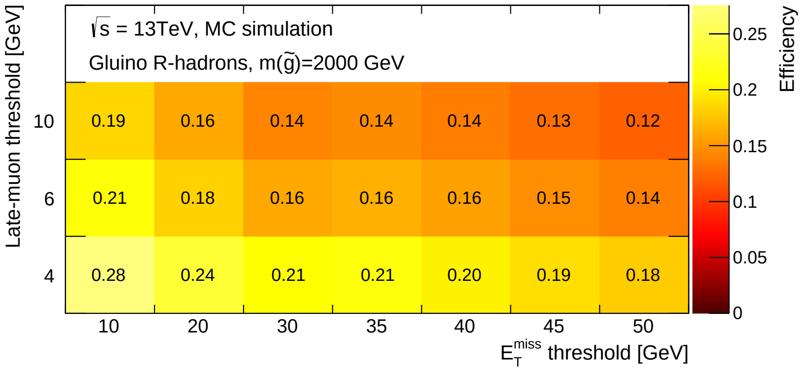

Figure 6.3: Efficiency of the late-muon trigger in a gluino R-hadron sample with $m(\tilde{g}) = 2000$ GeV for different simulated L1 E_T^{miss} and late-muon thresholds. Only three possible muon thresholds are available for L1Topo. The E_T^{miss} triggers in the analysis were seeded by a 50 GeV L1 item. Samples with larger thresholds than 50 GeV were therefore not simulated as they would not yield an increase in signal efficiency.

The efficiency clearly depends on both thresholds. In order to select the lowest possible thresholds which are still manageable by readout and computing, it is necessary to have an estimate of the expected rate of the trigger.

6.3 L1 rate estimation

To calculate the rate of a specific trigger in a data-driven manner[2], one needs to consider a dataset that does not contain any trigger bias. This can for example be achieved by using only random triggers. However, since the cross-section of physically interesting event topologies is many orders of magnitude smaller than the total cross-section, an unreasonably large dataset would be required. To prevent this, an enhanced bias dataset is taken, in which the number of physically relevant topologies[3] are overrepresented. Events are selected using L1 triggers of different signatures and thresholds and are stored without running any HLT algorithms[4]. The trigger menu for enhanced bias datasets is designed to allow to derive event-weights, which restore the desired zero-bias spectrum for rate predictions [336]. The specific beam parameters of the collider (like optics or pileup) are reflected in the enhanced-bias data and a new dataset has to be recorded should the parameters change.

Three types of weights need to be considered for every event: a weight w_{EB} which corrects the effect of the trigger selection on the dataset and restores the zero bias spectrum, a weight w_C that accounts for the trigger chain and includes possible prescale corrections and lastly a weight $w_{\mathcal{L}}$, which is a weight to extrapolate the event rate from the instantaneous luminosity at recording of the data to a desired reference luminosity. The rate R of a specific trigger can now be estimated through

$$R = \frac{\sum_{e=1}^{N} w_{EB}(e) w_C(e) w_{\mathcal{L}}(e)}{\Delta t} \quad , \tag{6.1}$$

where the sum runs over all N recorded events e, and Δt is the length of data collection.

Undergoing this calculation one arrives at an expected rate of the L1 muon trigger with threshold $p_T = 10$ GeV of (224.6 ± 1.3) kHz and at a rate of (8.38 ± 0.04) kHz for a trigger on $E_T^{\text{miss}} > 50$ GeV for luminosity $\mathcal{L} = 2.0 \times 10^{34}$ cm^{-2}s^{-1}[5]. In a first step the expected rate of the late-muon trigger is estimated by neglecting the late component and the muon is treated as being in-time. The combined rate, which could be seen as an upper bound, is calculated as random coincidence between both components according to

$$R_{\text{comb.}} = \frac{p_{\text{muon}} \cdot p_{E_T^{\text{miss}}} \cdot b}{T} \quad , \tag{6.2}$$

---

[2] Since the simulation of the trigger was not yet working at the time it was not possible to do the rate estimation from MC.

[3] For example the number of events containing one or more high-p_T leptons.

[4] The enhanced-bias data taking is based on five trigger chains that are seeded by 10–30 L1 items, including one random chain that selects events at random. The collection of enhanced-bias data is done while regular physics data is taken, which means L1 prescales have to be taken into account. Enhanced-bias data is collected at a rate of $\approx$ 300 Hz and one collection run lasts approximately one hour. Thus, about 1 million events are recorded to base rate estimations on.

[5] The quoted rates are based on enhanced-bias data taken in September 2016 with 2208 colliding bunches in the machine. 1.5 million events were recorded.

where p_{muon} and $p_{E_T^{\text{miss}}}$ are the probability of the muon or E_T^{miss} trigger firing in an event, b is the number of bunches in the machine and $T = 88.924\ \mu$s the revolution time of a proton bunch around the accelerator ring. Assuming a full ring, one arrives at a combined rate of

$$R_{\text{comb.}} = (96.4 \pm 0.7)\ \text{Hz} \tag{6.3}$$

hinting at a very low rate when considering the total L1 bandwidth of 100 kHz[6].

The effect of the delayed muon on the trigger rate cannot be assessed directly from data because of the dead time after any L1A was issued. Instead, the bunch structure within the collider can be exploited. Recall the LHC filling scheme described in chapter 3.1.2. In between the proton bunch trains there are empty buckets for which no collisions occur within ATLAS. Neglecting the influence of possible signal[7] the trigger only fires if a muon is wrongly attributed to the following BC. To estimate how frequent this happens, those BCs which immediately follow the end of a bunch train, i.e. the first empty buckets, are considered. A special trigger menu is used to record events from empty BCs. One long 2016 data run corresponding to 277 pb^{-1} of integrated luminosity is considered here for a rough estimate. The filling scheme delivers 46 empty buckets following a filled one. An empty BC trigger with a muon threshold of 4 GeV is used[8]. With the total time of data recording known (27556 s), one can estimate the rate of a trigger with > 50 GeV E_T^{miss} in the first BC and a delayed muon with $p_T > 4$ GeV in the following BC to be

$$R_{\text{comb.,delayed}} = 120.03\ \text{Hz} \tag{6.4}$$

confirming the low expected rate from the previous estimate.

Three incarnations of the late-muon trigger have been activated in mid-2017 for data-taking. A 10 GeV delayed muon is combined with either a 50 GeV jet or with E_T^{miss} of either 40 or 50 GeV. The actual rate of the late-muon trigger in configuration as for the rate estimate above was measured in October 2017 to be

$$R_{\text{truth}} = 44.39\ \text{Hz} \tag{6.5}$$

and is therefore in good agreement with the derived upper rate limits.

6.4 Expected efficiency

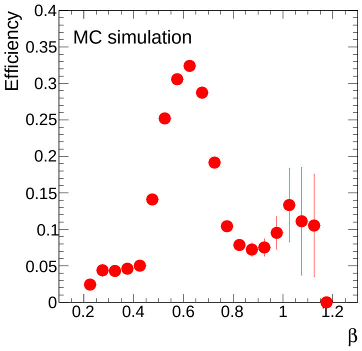

Figure 6.4: Efficiency of the L1 late-muon triggers as function of the particle β.

The expected efficiency has been estimated for gluino R-hadron samples. Figure 6.4 shows the efficiency of the L1 late-muon trigger as function of β of the particle firing the trigger. The efficiency is highest in the region $0.5 < \beta < 0.7$, which corresponds exactly to the region for which the single-muon triggers are not efficient anymore (compare to figure 6.1). The loss of efficiency for particles with $\beta < 0.5$ is due to arrivals at the MS trigger stations with delays larger than 1 BC. Figure 6.5 shows the efficiency of the jet-based late-muon trigger and the lower-threshold E_T^{miss}-based trigger as function of the simulated gluino masses. The efficiency is dictated by the underlying β spectrum. The increase in signal efficiency is ranging from 4% at $m_{\tilde{g}} = 1200$ GeV to 2% at $m_{\tilde{g}} = 3000$ GeV. For stau and chargino samples the efficiency is expected to be much higher since no neutral particles are produced (except for $\tilde{\chi}_1^{\pm}\tilde{\chi}_1^0$ production) and because a larger portion of the β spectrum is located inside the region of maximal efficiency of the late-muon trigger since the possible expected signal masses are smaller.

---

[6] The main limitation for the late-muon trigger is unfortunately not the L1 bandwidth, but the computing power needed for the track fit done on HLT level. A low L1 rate can thus nevertheless cause problems later on if the CPU costs for the HLT are too high.

[7] which would be small in any case and can therefore safely be ignored.

[8] The implemented variety of trigger thresholds is limited. The motivation is to estimate upper bounds to the rate of the late-muon trigger by choosing a trigger with a low threshold.

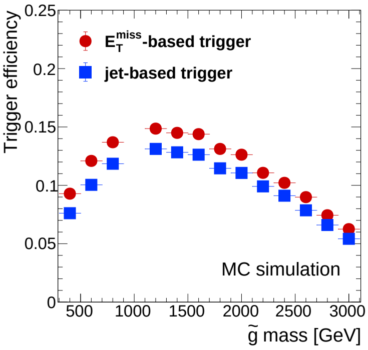

Figure 6.5: Efficiency of the L1 late-muon triggers as function of the simulated gluino mass.

6.5 Summary

Single-muon triggers are inefficient for slow particles since arrival delays cause the trigger signal to be shifted to one of the following bunch crossings. The late-muon trigger is a fundamentally new trigger that aims to recover efficiency for slow particles by considering two consecutive events. The target signature expects a soft jet with 50 GeV transverse momentum or missing-transverse energy of 40 GeV in the first bunch crossing and a muon in the immediately following one. The muon acts as the slow-particle candidate that arrives with delay at the trigger chambers in the Muon Spectrometer.

The trigger thresholds were chosen to allow for a largest possible signal efficiency while still retaining a manageable data-taking rate. To this end the signal efficiency for various thresholds has been evaluated. The expected trigger rate was estimated in enhanced-bias data assuming random coincidence between trigger elements while for the late component the first empty bucket after a filled bunch train in the collider was used. The late-muon trigger performs within expectation and extends the coverage of muon triggers to $\beta > 0.5$.

CHAPTER 7

Conclusion and Outlook

$\beta = 0.55 \pm 0.09$
$m = 2123 \pm 517$ GeV
$p_T = 472$ GeV
$m = \frac{p}{\beta\gamma}$

This thesis presented a series of searches for charged stable massive particles with the ATLAS detector in 36.1 fb^{-1} of proton–proton collisions at $\sqrt{s} = 13$ TeV. In order to exploit the SMP signature of slow propagation speeds by performing time-of-flight measurements in the ATLAS Muon Spectrometer, extensive timing calibrations of the MDTs and RPCs were necessary. Gaussian parameterisations have been used to derive pairs of calibration constants for every individual drift tube or readout strip. Time dependent variations were accounted for by dedicated run-wise calibration steps. The successful calibration results in an MDT β resolution of $\sigma_{\beta}^{MDT} = 0.026$, which constitutes a 40% improvement compared with previous calibration efforts during LHC's first operational run. For the RPC system a resolution of $\sigma_{\beta}^{MDT} = 0.021$ is achieved, which marks a 14% improvement. In order for simulation to reflect the better sensitivity two different treatments were devised to accommodate both systems which generated a good agreement between data and MC timing. The calibrated β, and for R-hadron searches the anomalous ionisation energy losses measured in the Pixel Detector, were used to identify SMPs and furthermore allow for a calculation of the particle mass. The background is estimated in a purely data-driven manner. Signal regions were defined via the estimated masses. To account for shorter lifetimes, model independence and possible charge-flip reactions the R-hadron searches are done, in addition to the full-detector analysis, in an MS agnostic version, where all signals from the MS are ignored. Stau and Chargino searches comprise two orthogonal signal regions depending on whether one or two SMP candidates are found in an event. No statistically significant excess of events was observed in any signal region and lower limits on the particle mass at 95% CL have been placed. Long-lived gluinos from Split SUSY models, where long lifetimes originate from a decoupling of the sfermion and sboson sectors, were excluded up to masses of $m(\tilde{g}) = 2015$ GeV. Long-liced bottom and top squarks could be excluded to $m(\tilde{b}) = 1240$ GeV and $m(\tilde{t}) = 1325$ GeV. Directly produced long-lived staus from GMSB models, where the long lifetimes result from the weak coupling of the LSP, are excluded to masses up to $m(\tilde{\tau}) = 420$ GeV. Detector-stable charginos originating from mAMSB models with nearly mass-degenerated states of neutralinos and charginos can be ruled out up to masses of $m(\tilde{\chi}_1^{\pm}) = 1100$ GeV. All limits are the most stringent limits on stable SUSY particles to date and are a significant improvement over previously reported ATLAS and CMS results. The largest departure from expectation occurs for the MS agnostic gluino R-hadron search, where 2 events are observed over an expected background of 0.4 ± 0.1, marking a $< 2\sigma$ deviation. The expected signal yield for gluinos with $m(\tilde{g}) = 2200$ GeV in the corresponding signal region is given by 1.5 ± 0.2, consistent with the measurement. More data is needed to extent sensitivity into the relevant mass range.

These results put severe pressure on Split SUSY models containing long-lived gluinos. Following the reasoning of [337], one can determine the mean lifetime of the gluino according to

$$\tau(\tilde{g}) = 4\ \mathrm{s} \left(\frac{1\ \mathrm{TeV}}{m(\tilde{g})}\right)^5 \cdot \left(\frac{m_S}{10^9\ \mathrm{GeV}}\right)^4 , \tag{7.1}$$

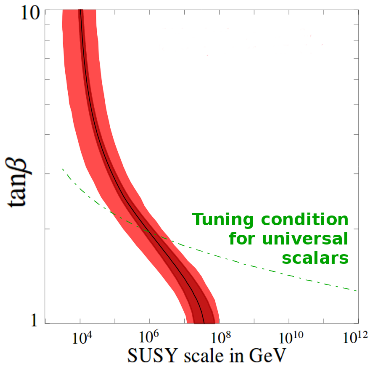

Figure 7.1: Combinations of Split SUSY $\tan\beta$ and m_S values which reproduce the Higgs mass marked as a solid black line. The dark red shaded band corresponds to a $\pm 1\sigma$ variation of the top mass, the light shaded band indicates a variation in the scalar mass parameters. Gaugino and higgsino masses were set to 1 TeV. The green line marks the EW tuning condition resulting in universal scalar masses at the GUT scale. The figure was adapted from [338].

which depends only on the mass of the gluino and the scale of SUSY breaking m_S. Consider figure 7.1, where pairs of $\tan\beta$ and m_S reproducing the measured Higgs-boson mass are marked as solid black line. Assuming $\tan\beta \approx 2$, the breaking scale is fixed to $m_S \approx 1000$ TeV. Using equation 7.1, one can calculate an expected gluino lifetime of $\tau(\tilde{g}) \approx 0.03$ ps for $m(\tilde{g}) = 2000$ GeV, which corresponds to a mean decay length of $< 100\ \mu$m. This is obviously far too short-lived for the SMP analysis. Lifetimes which allow for detector stability are still possible if $\tan\beta$ approaches 1, however, this might lead to EW vacuum instability [338].

The results of the present and future analyses have to be interpreted in terms of simplified models where the gluino lifetime is long for whatever reason, just like it was done for the long-lived bottom and top squark search. Since the analysis does not depend on the decay signature and is to a large degree model independent, such simplified models will continue to be of relevance in future searches.

The pressure on long-lived particles from GMSB and mAMSB models is less severe. In GMSB the lifetime of the NLSP is dictated by its mass and the mass of the gravitino [109]. Heavier and heavier staus can still possess longevity, provided the mass of the gravitino increases accordingly. In mAMSB, where the long lifetimes follow from the small mass difference between neutralino and chargino, a similar argument holds.

LHC will continue to provide proton–proton collision data until the end of 2018 resulting in more than 100 fb^{-1} of data[1]. This increase in data will expand sensitivity to larger SMP masses and probe further in the available parameter space. However, the new data also provides additional challenges. The beam conditions during 2017 resulted in very large pileup with up to 70 simultaneous interactions. This will have consequences for the dE/dx estimation in the Pixel Detector, where especially the IBL will suffer from radiation damages, and the Tile Calorimeter, where the higher multiplicities of jets and soft radiation cause a more challenging environment for timing measurements. The high-density hit environment

[1] This marks the end of run 2. It is followed by a 2-year maintenance break. LHC and its high-luminosity upgrade are expected to keep delivering collision data well beyond 2030.

in the Inner Detector is also challenging for tracking and requires time and computing efficient algorithms. The MuGirlStau reconstruction algorithm as used in this analysis was decommissioned for the 2017 data-taking and replaced by a new more efficient version that was re-written from the ground up. It is expected to yield a better tracking efficiency for slow particles than the algorithm used in the present study. The principle steps and procedure of the calibration as presented here are easily transferable to any new dataset and thus remain of relevance for future SMP searches. The MC treatments, especially the unfolding technique presented in chapter 4.9.1 will also be important in the future. The larger amount of available data will increase the quality of the calibration as the individual fits to drift-tube and readout-strip timing will suffer less from statistics-caused inaccuracies. It might even be possible to account for slight asymmetries and tails in the tube and strip timing distributions. A possibility for improvement of the calibration itself is given for the run calibrations. With the length of many runs exceeding 20 hours, it is worth investigating in-run timing changes. These could be of the order 100 ps.

As has been shown, the single-muon trigger becomes increasingly inefficient for slow particles with larger masses due to late arrival. The late-muon trigger was introduced as a new concept for online event selection. It became active in the second half of 2017 and is expected to run unprescaled during the remainder of LHC run 2. While the sensitivity gain for gluino R-hadrons will be small, the largest increase is expected for the stable stau search, where the mass limits are weakest.

One motivation for the MS-agnostic R-hadron search are possible charge-flip reactions in which charged R-hadrons undergo a parton exchange and end up being neutral and therefore invisible to the MS. It is possible to imagine an SMP search considering the reverse scenario: a neutral R-hadron becomes charged in the calorimeters. Its track would thus show up only in the MS. While this analysis would suffer from larger uncertainties on the momentum measurement, it would profit from the good timing resolution in the MDTs and RPCs and an independent β determination in the Tile Calorimeter. The list of observables could be expanded by performing ionisation energy loss measurements in the MDT chambers similar to [339].

In addition to MDT dE/dx, one could imagine a dE/dx estimation in the TRT[2], and a time-of-flight measurement in the LAr calorimeter. While the sensitivity of these systems will not be able to rival the measurements which are currently performed[3], they could be used in a multi-variate analysis for background suppression.

So far no search for supersymmetric particles has resulted in a discovery. With ever-tightening exclusion limits and shrinking of parameter spaces, the long-lived sector still delivers some of the weakest exclusion limits and therefore remains a promising candidate for the appearance of the first hints on particles beyond the Standard Model.

[2] In fact, the TRT dE/dx is used in [339] just like the MDT dE/dx.

[3] The LAr calorimeter has a very good timing resolution, however since the system is much closer to the IP the β resolution will not be competetive with the Tile Calorimeter and the MS.

APPENDICES

APPENDIX A

Definition of an SMP specific derivation

All recorded data and all simulated MC events are ultimately processed into the analysable xAOD format. Since the xAODs contain all reconstructed physical objects, the required amount of disk space is enormous. A single event of a simulated gluino R-hadron sample averages at 326 kB per event. Most of the information contained in the xAOD, however, is irrelevant for the present study. The event data model as described in chapter 3.3 suggests the production of a derived format which is specific for a group of related analyses. The size of a single derivation (DxAOD) should be $\ll 1\%$ of the whole xAOD. This can be achieved through three mechanisms which are also schematically shown in figure A.1:

- *Skimming*: Events are rejected if they do not fulfill certain selection criteria. In the simple most case this is achieved via a trigger selection, but object requirements or topological considerations are possible as well.
- *Slimming*: Individual variables or collections of variables are removed from the output if they are superfluous.
- *Thinning*: Removal of individual objects from collections in the data file. This could for example be the rejection of all muons which do not fulfill a certain momentum cut.

In addition to the procedures leading to a reduction of disk space, a derivation can also be subject to a fourth treatment which leads to an addition of information

- *Augmentation*: Additional information is appended to an object which was previously not available for a specific object.

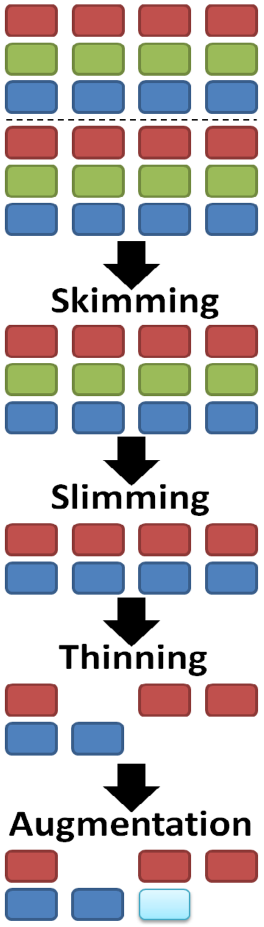

Figure A.1: Schematic representation of how the size of an xAOD can be reduced. Here, two input events are taken of which one is skimmed away. The remaining event is slimmed and thinned to reduce its disk size. In a last augmentation step, new information is added to a collection.

Since the search for SMPs is unlike most ATLAS searches, the DxAOD used was solely produced for the present analysis and carries the name SUSY8 derivation. Events which have not fired either a single-muon, di-muon, E_T^{miss} or jet+E_T^{miss} trigger are skimmed away. Since the analysis relies heavily on ID tracks and muon-like objects, all variables are kept for the associated objects. Further, SUSY8 contains all available E_T^{miss} information. Even though collections like photons or electrons are not needed for analysis, a rudimentary selection of associated variables is kept to ensure the reconstructability of the event topology and the functionality of software tools supplied by dedicated ATLAS performance study groups. Lastly, since the biggest contributor to the derivation size are tracks ("‘track particles"’), a mild thinning is applied and tracks are rejected if they posess no hits in the Pixel Detector, $p_T^{\text{track}} < 10$ GeV or longitudinal impact parameter $|z_0| > 10$ mm. However, tracks which are associated to muons, electrons, jets or taus, are kept regardless of their properties.

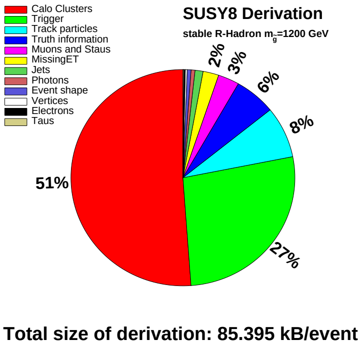

Figure A.2: Content of the SUSY8 derivation upon first creation. The disk size is dominated by the stored calorimeter cell information.

In order to perform time-of-flight measurements in the calorimeters it is necessary to have access to the hit information of all relevant cells. Upon first creation of the SUSY8 derivation all calorimeter cells have been stored which led to very large derivations with ≈ 85 kB per event.

To reduce the size, a tool has been written, which picks out the calorimeter cells associated to an ID track with $p_T^{\text{track}} > 30$ GeV ($p_T^{\text{track}} > 50$ GeV throughout 2015 and early 2016) and augments the track with the necessary information. This way, considerably less calorimeter cell information has to be stored. This becomes apparent in the left panel of figure A.3, where the composition of the SUSY8 derivation in late 2015 has been plotted.

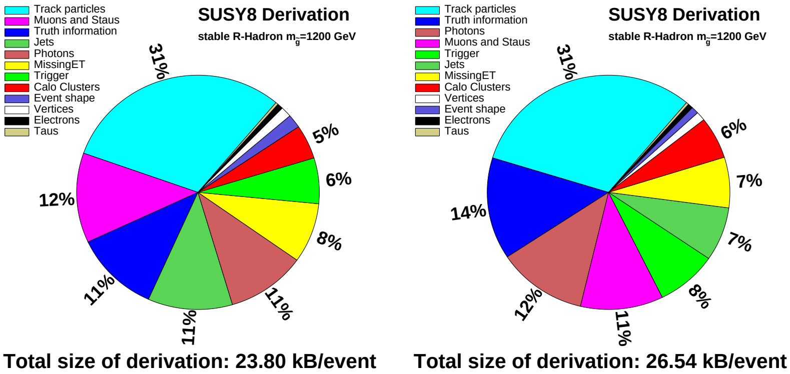

Figure A.3: Composition of the SUSY8 derivation in late 2015 (left) and 2017 (right). Changes to the derivation were made due to new requirements for common software tools and updated trigger specifications resulting in a slight increase of the derivation size per event.

The right panel of figure A.3 shows the SUSY8 composition in 2017. The composition has changed slightly due to updated requirements for common software tools. Since the trigger menu was changed in between data-taking in 2015 and 2016, the changes in the derivation reflect the updated trigger selection and associated trigger elements. Lastly, a few variables which were found to be beneficial during analysis have been added to the derivation.

APPENDIX B

Further Muon Spectrometer Calibration Plots

Projections for drift tubes with resolution $\sigma_{t_0} < 7.5$ are shown in figure B.1 in the z–y projection and in figure B.2 in the x–y projection.

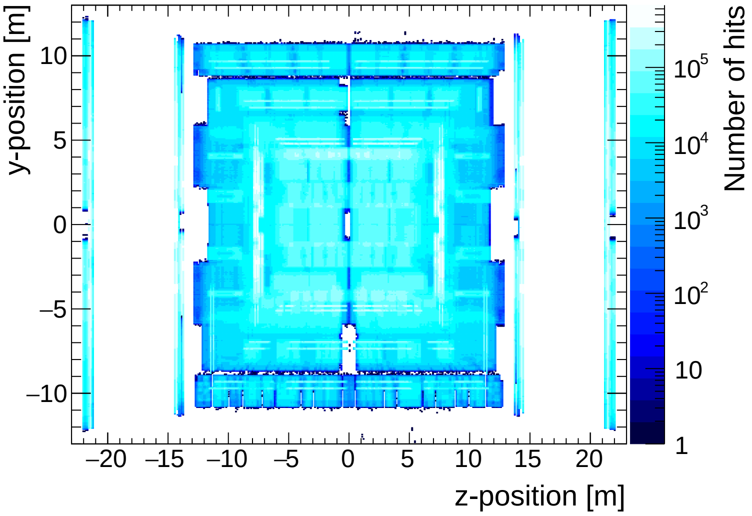

Figure B.1: The number of hits in drift tubes with a resolution $\sigma_{t_0} < 7.5$ is shown in a projection into the z–y plane of the detector.

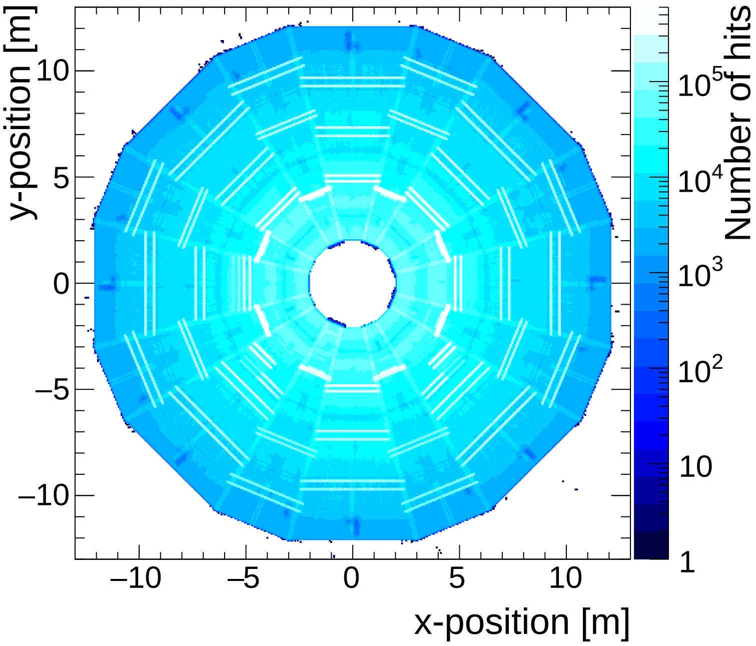

Figure B.2: The number of hits in drift tubes with a resolution $\sigma_{t_0} < 7.5$ is shown in a projection into the x–y plane of the detector.

The corresponding plots for drift tubes with $\sigma_{t_0} > 7.5$ are given in figure B.3 in the z–y projection and in figure B.4 in the x–y projection. From the comparison of plots one can see that "bad" drift tubes are not distributed randomly throughout the detector.

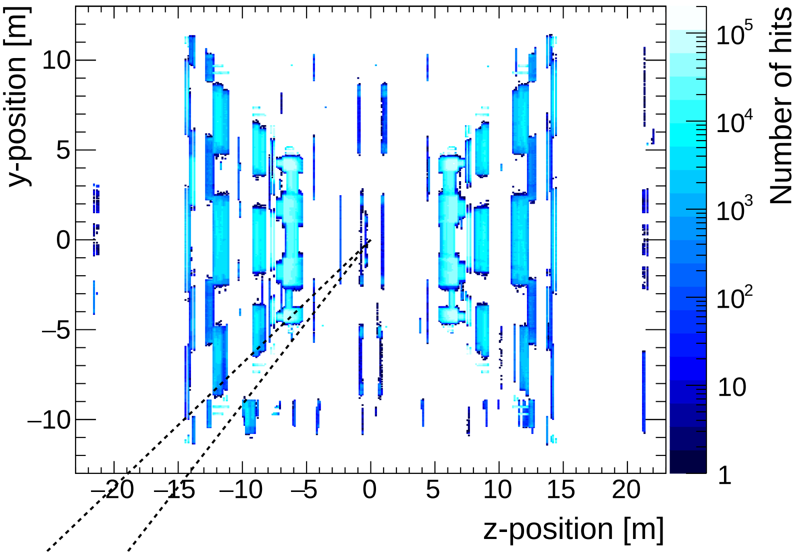

Figure B.3: The number of hits in drift tubes with a resolution $\sigma_{t_0} > 7.5$ is shown in a projection into the z–y plane of the detector. The transition region between the barrel and the end-caps is marked by dashed lines in the lower left-hand sector

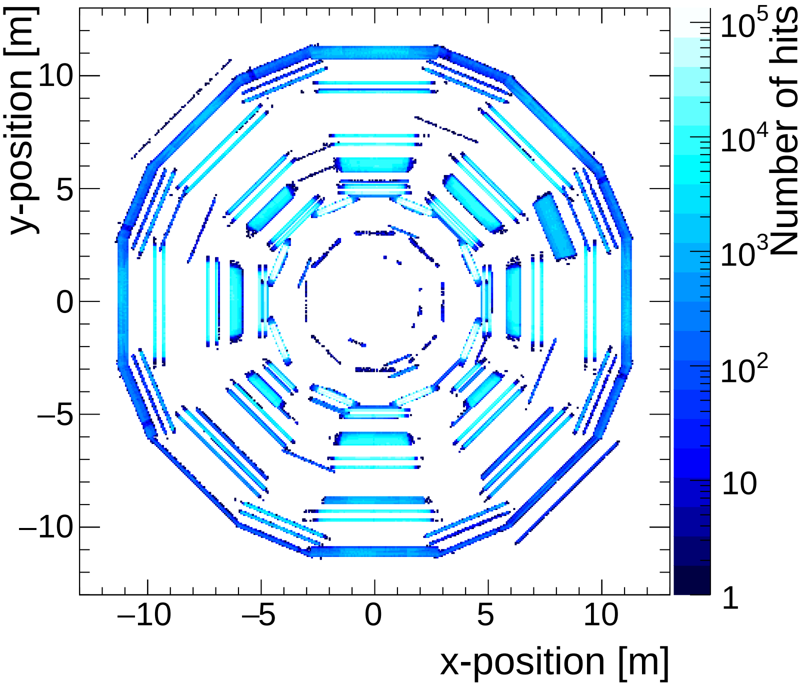

Figure B.4: The number of hits in drift tubes with a resolution $\sigma_{t_0} > 7.5$ is shown in a projection into the x–y plane of the detector.

It was observed that about 2.3% of RPC η and 3.4% of RPC ϕ strips have < 40 associated hits. The number of such low-statistics strips is much larger than what could have been expected. It is surmised that some hits are wrongfully associated to dead strips. In order to reject such strips one has to make sure to not introduce any bias. Low-statistics strips should therefore be distributed randomly throughout the detector. Figure B.5 shows the distribution in the x–y projection, while the z–y projection is given in figure B.6. It can be clearly seen that the low-statistics strips are distributed randomly throughout the detector and that a rejection therefore does not introduce any analysis bias.

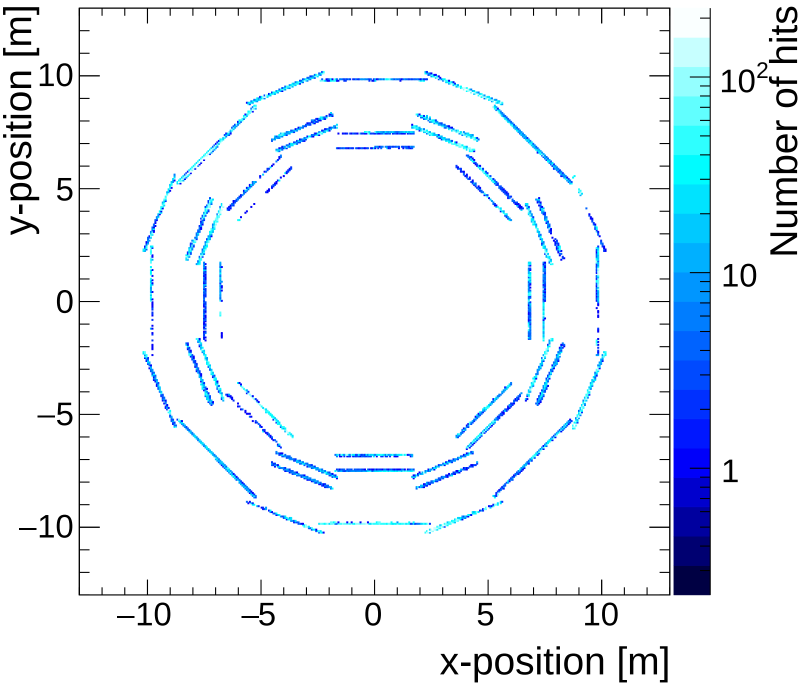

Figure B.5: Distribution of hits that were associated to an RPC readout strip with < 40 hits shown on the projection into the x–y plane of the detector.

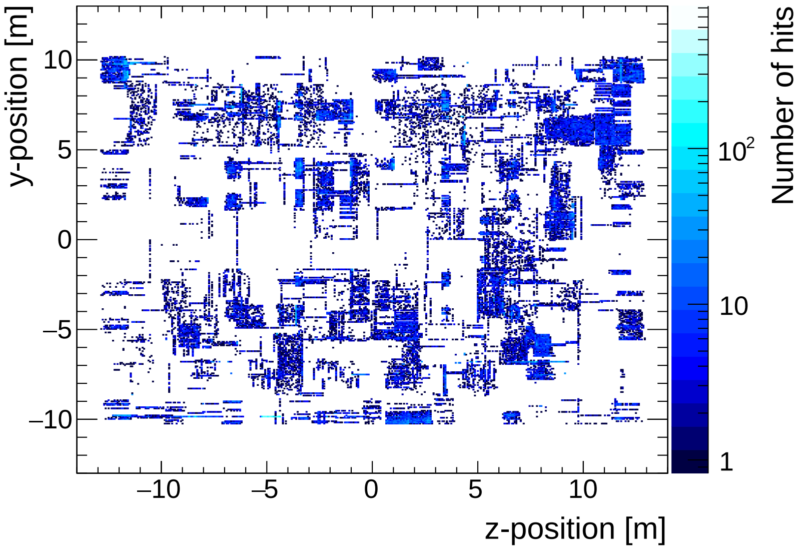

Figure B.6: Distribution of hits that were associated to an RPC readout strip with < 40 hits shown on the projection into the z–y plane of the detector.

For comparison, the high-statistics strips with ≥ 40 hits are shown in figure B.7 in the x–y projection and in figure B.8 in the z–y projection.

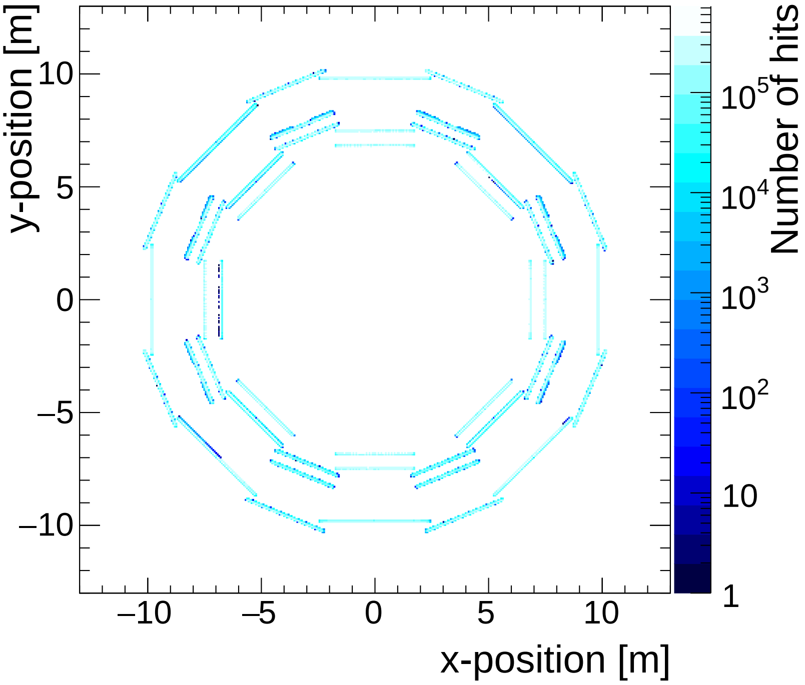

Figure B.7: Distribution of hits that were associated to an RPC readout strip with ≥ 40 hits shown on the projection into the x–y plane of the detector.

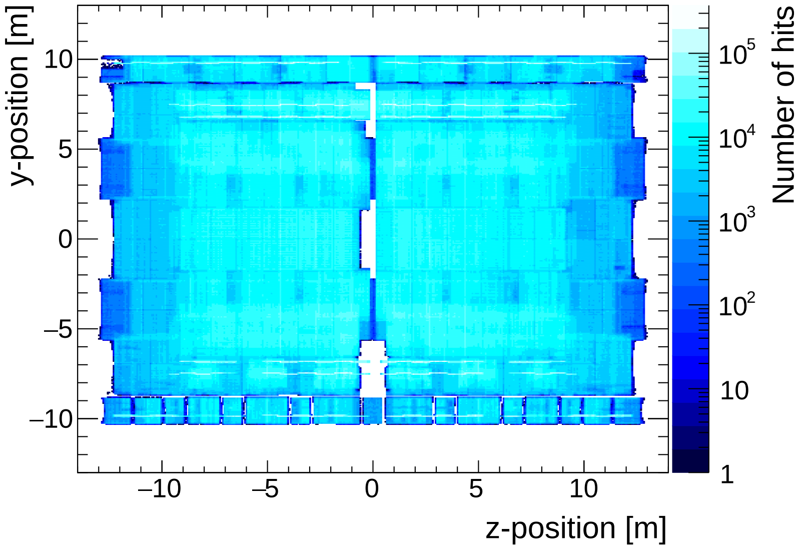

Figure B.8: Distribution of hits that were associated to an RPC readout strip with ≥ 40 hits shown on the projection into the z–y plane of the detector.

All RPC readout strips are fitted with Gaussian functions. The mean of the fit is used as a calibration constant for all associated hits, while the inverse of the standard deviation $\sigma^i_{t_0}$ of the fit is used as a weight to calculate a weighted β average. Figure B.9 shows $\sigma^i_{t_0}$ as function of the fully calibrated (i.e. after online correction, strip calibration and run correction) t_0. Figure B.10 shows the same as function of the fully calibrated time-of-flight. Both plots show accumulations of hits with very small $\sigma^i_{t_0}$ that could potentially bias a weighted average. Therefore all strips with $\sigma^i_{t_0} < 0.4$ ns are rejected. A noteworthy feature in figure B.9 are columns observable in the lower part of the plot. The spacing in between them is 3.125 ns. They originate from hits in the wrong readout tick.

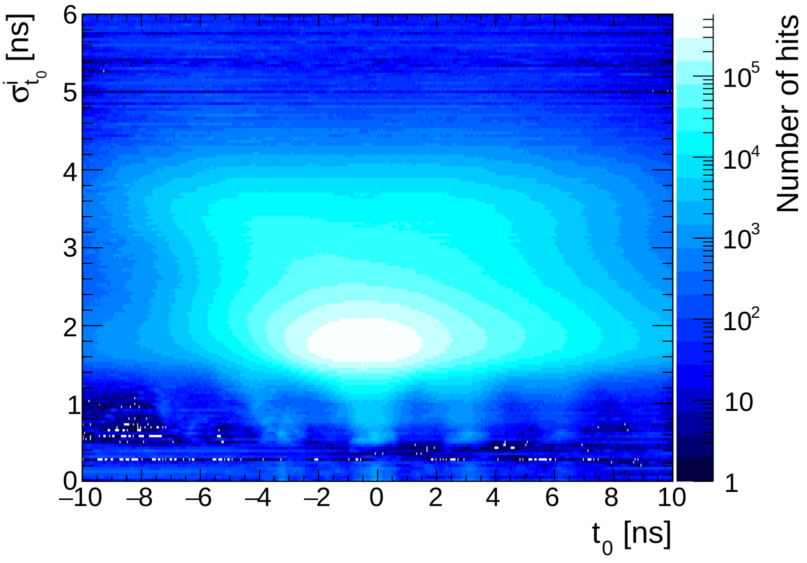

Figure B.9: Uncertainty on the timing measurement $\sigma^i_{t_0}$ derived from the standard deviation of a Gaussian fit to the timing distribution of the readout strip as a function of the measured t_0 of a hit. The "columns" in the lower part of the plot originate from high-resolution RPC strips that were presumably shifted by one or more readout ticks during data-taking. Strips with resolution $\sigma^i_{t_0} <$ 0.4 ns are rejected from β estimation.

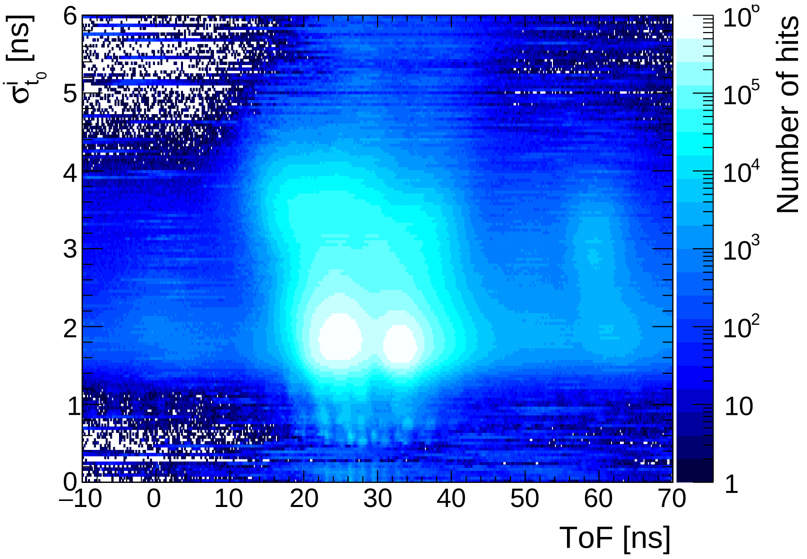

Figure B.10: Uncertainty on the timing measurement $\sigma^i_{t_0}$ derived from the standard deviation of a Gaussian fit to the timing distribution of the readout strip as a function of the measured time-of-flight of a hit. Strips with resolution $\sigma^i_{t_0} <$ 0.4 ns are rejected from β estimation. The two distinct accumulations of hits come from different layers in the RPC system. The outer-most layer naturally has a larger time-of-flight.

Figure B.11 shows the effects of the phase-shift correction on the already drift-tube corrected MDT t_0 distribution and online and strip corrected RPC t_0 distribution.

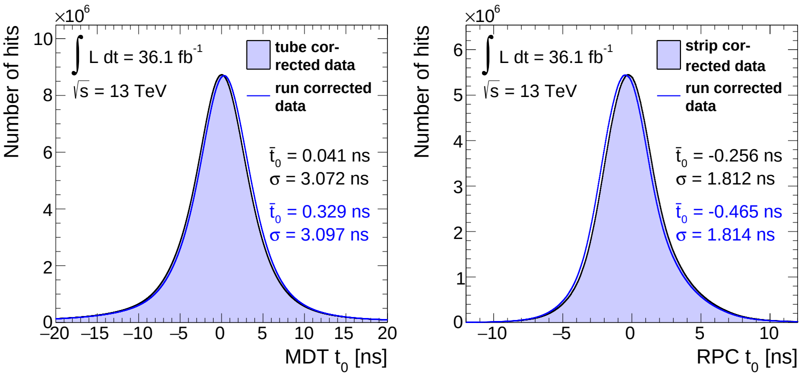

Figure B.11: Effect of the phase-shift correction. The left plot compares the MDT drift-tube corrected t_0 distribution before and after run correction. The right plot shows the RPC online and strip corrected t_0 distribution before and after run correction. The mean and standard deviation of a Gaussian parameterisation to the data are given.

A summary of the effects of the different steps of calibration are given in figures B.12 for MDTs and B.13 for RPCs where the uncalibrated timing is compared to the timing distribution of all intermediate calibration steps.

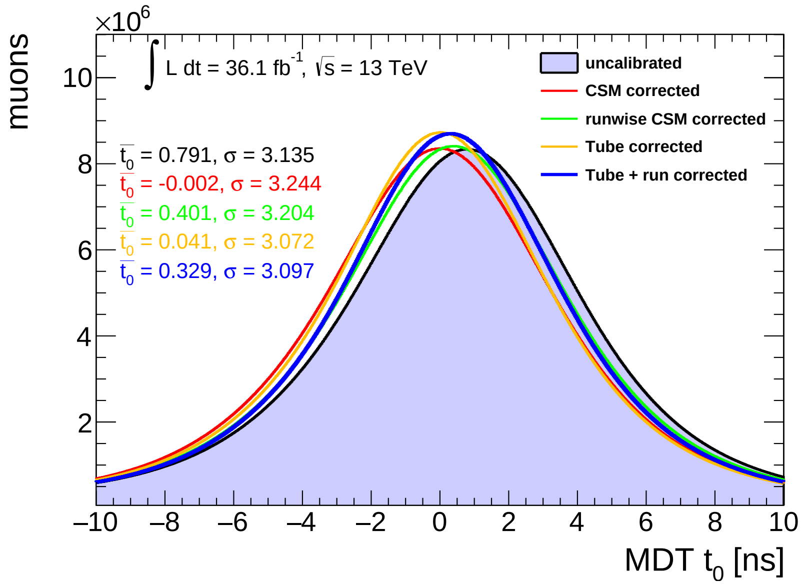

Figure B.12: Summary of the effects of the MDT β calibration on the timing distribution. Shown is the uncalibrated data along with the t_0 distributions after each intermediate step. The mean and width of the distributions are given. They are determined from a Gaussian fit to the data.

To investigate the stability of the fully calibrated β estimates in pseudorapidity, the two quantities are plotted against each other. Figure B.14 shows this for MDTs with the contour of the histogram, i.e. the arithmetic mean in y-slices of the histogram, added. A slight discrepancy from the expected value of $\beta = 1$ can be seen in the central region of the detector. This is due to asymmetries in the timing distributions that are treated correctly while fitting and correcting the drift tubes, but result in too low values in the arithmetic means shown here. No correction is therefore performed.

The corresponding plot for the RPC β is given in figure B.15. An excellent stability of the β estimate over the full η range is oserved.

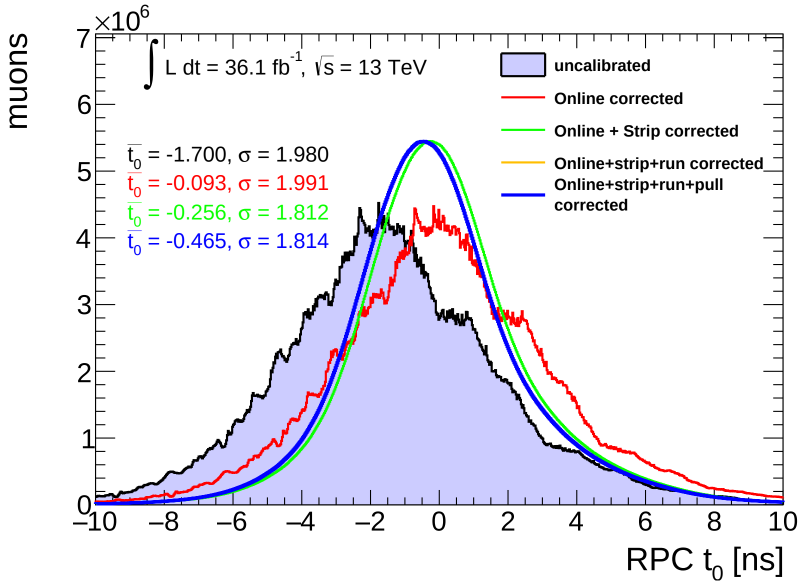

Figure B.13: Summary of the effects of the RPC β calibration on the timing distribution. Shown is the uncalibrated data along with the t_0 distributions after each intermediate step. The mean and width of the distributions are given. They are determined from a Gaussian fit to the data.

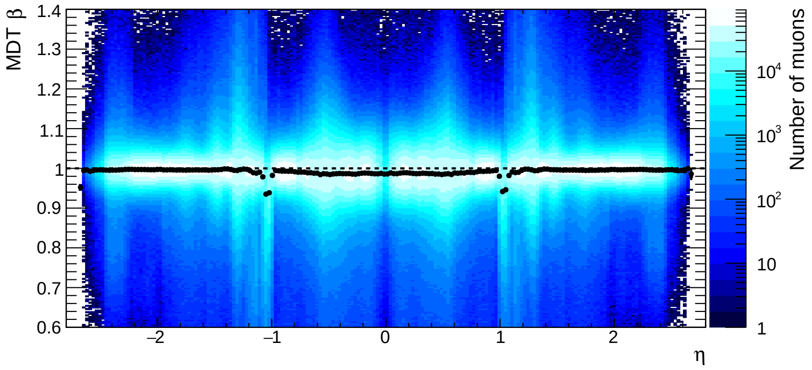

Figure B.14: MDT β as function of the pseudorapidity η. The black data points mark the means in y-slices of the histogram. A slight discrepancy to the expected value of $\beta = 1$ can be seen in the central detector region. These have been traced back to asymmetries in the timing distributions. The transition region between barrel and end-cap of the MS at $|\eta| = 1.05$ can be seen systematically producing too low β values.

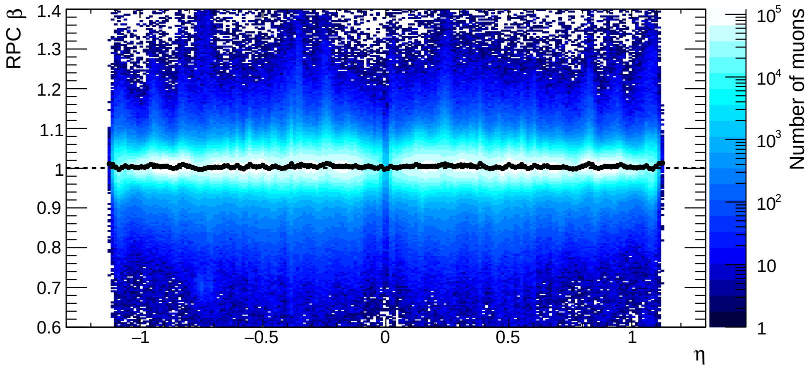

Figure B.15: RPC β as function of the pseudorapidity η. The black data points mark the means in y-slices of the histogram. A very nice stability of β over the full η range is observed.

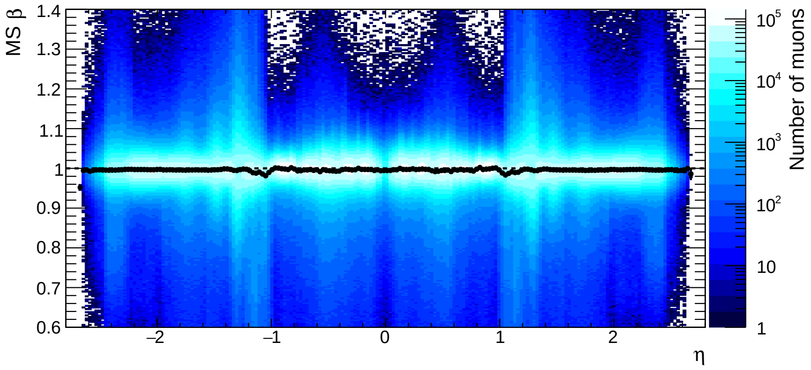

Figure B.16: Combined β calculated as a weighted average of the MDT and RPC β estimates as function of the pseudorapidity η. The black data points mark the means in y-slices of the histogram. Slight discrepancies in the central region of the detector are stemming from the MDT β.

After the β estimates from MDT and RPC have been combined in a weighted average the values over η are plotted again and shown in figure B.16. The same slight discrepancy in the central detector region stemming from the MDTs is observed.

Analogously the uncertainty on the β estimate can be plotted as a function of η. This is done for MDTs in figure B.17, for RPCs in figure B.18 and for the combined MS β in figure B.19.

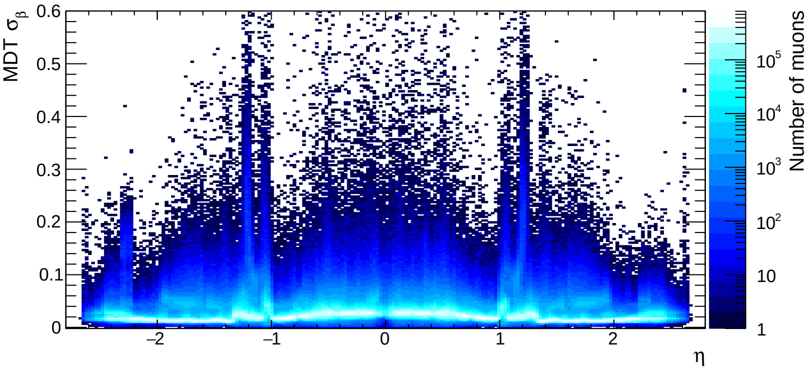

Figure B.17: MDT σ_β as function of the pseudorapidity η. The transition region between the MS barrel and endcaps can be seen as producing β estimates with large uncertainties. The uncertainty is lower at large $|\eta|$ since the distance and therefore the ToF is larger, and the relative measurement uncertainty smaller.

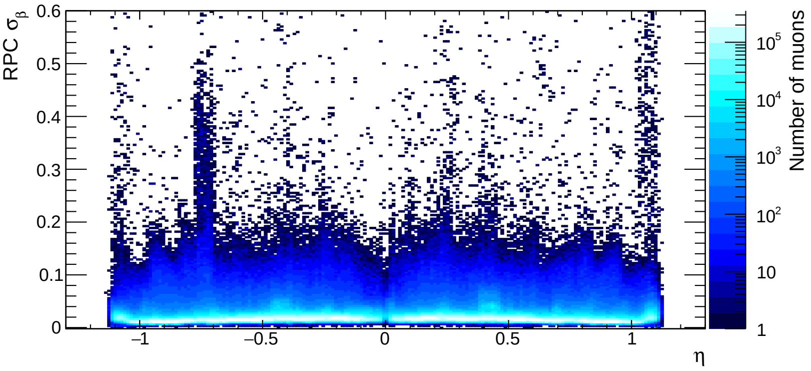

Figure B.18: RPC σ_β as function of the pseudorapidity η. The uncertainty is flat over the full η range of the RPC system. The larger asymmetries at $\eta \approx -0.75$ are attributed to some dead channels in this region [340].

Several methods have been evaluated in trying to cope with simulated MDT timing distributions that underestimate the resolution in data. In the process of evaluating the usability of different methods it was also tested whether or not the method works with signal

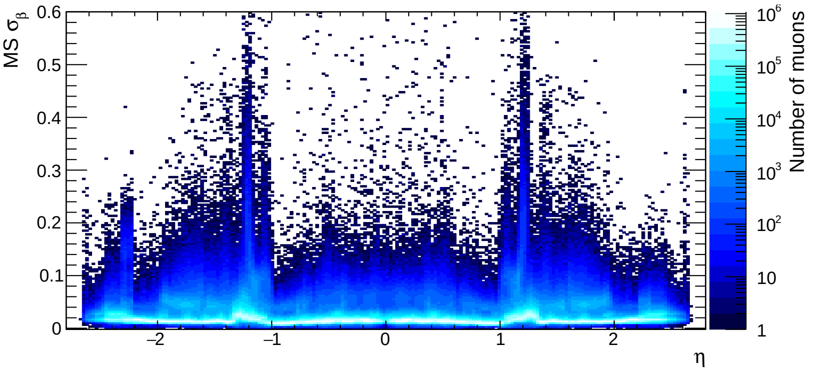

Figure B.19: Uncertainty σ_β on the combined β calculated as a weighted average of the MDT and RPC β estimates, as function of the pseudorapidity η. The transition region between the MS barrel and end-caps can be seen as producing β estimates with large uncertainties. The uncertainty is nearly stable over the full η range. The larger uncertainties in the barrel region which were observed in the MDTs are compensated by the additional RPC measurement.

simulation. For this, a toy signal has been introduced which should result in a second peak in the t_0 distribution at $t_0 = 5.0$. Both methods need to preserve the position of the additional peak with respect to the main peak. Note, that both methods act on the resolution $\mathrm{ToF}_{\mathrm{reco}} - \mathrm{ToF}_{\mathrm{truth}}$ rather than the plain t_0 distribution, thereby treating background and signal on the same footing. Figure B.20 shows the two methods acting on the toy signal. As can be seen, the exact position of the signal is preserved after the procedure.

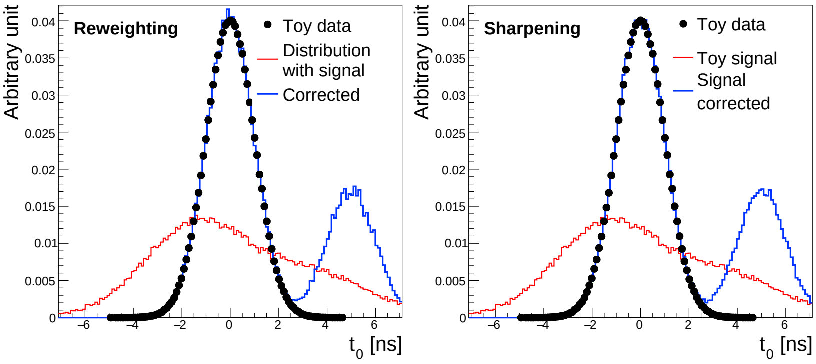

Figure B.20: Toy signal has been simulated. The t_0 distributions possess an additional peak at $t_0 > 0$. After both procedures act on the resolution $t_0^{\mathrm{reco}} - t_0^{\mathrm{truth}}$ the position of the peak needs to be preserved. In both the reweighting (left) and the sharpening procedure (right) this is the case.

APPENDIX C

Decomposition of the simulated RPC timing distributions

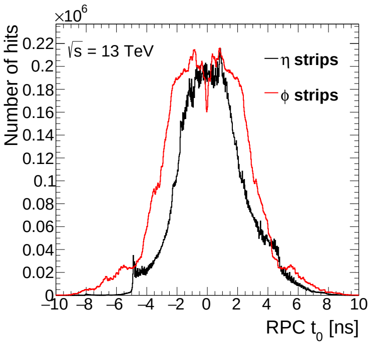

Figure C.1: Untreated RPC t_0 distributions separately for η and ϕ strips.

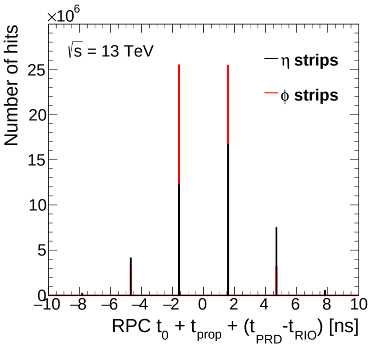

Figure C.2: By adding the propagation time and the difference between the RIO and PRD time to the observed RPC t_0, the granularity of the detector can be made visible.

The feature-rich t_0 distributions depicted in figure C.1 have been observed in simulated RPC timing. Here and in the following the η and ϕ strips are plotted separately to rule out any overlay effects between the orthogonal strips. While both distributions show a very jagged shape the most curious feature is the dip for the ϕ strips at $t_0 \approx 0$.

In the RPCs the signal from a passing particle first has to propagate along the strip to the readout element. The time it takes to reach the readout is called the propagation time t_{prop}. As the strip is read out, the precise position of the hit along the strip is unknown. As a first approximation it is therefore assumed the hit occurred right at the centre of the strip. The calculated hit time on the basis of the incorrect position is internally called the Prep-Raw-Data (PRD) time t_{PRD}. The position of the hit on the strip can be determined more accurately after the track or segment fit and a new more refined time is calculated. The position-corrected time is stored as the reconstruction-input-object-on-Track (RIO) time t_{RIO}. The xAOD data files supply not only the time-of-flight information but also a pseudo-propagation time consisting of the actual propagation time and the difference of RIO and PRD time. This includes not only the propagation time difference, but also the difference in ToF due to the hit position on the strip. Adding the pseudo-propagation time $(t_{\mathrm{prop}} + (t_{\mathrm{PRD}} - t_{\mathrm{RIO}}))$ to the t_0 reveals the timing granularity of the detector by visualising its individual readout ticks with a spacing of 3.125 ns, as can be seen in figure C.2.

It is now possible to decompose figure C.1 by looking at the individual contributions from the dominant ticks after getting smeared out by the propagation time. This can be seen in figure C.3 for η and ϕ strips individually. The origin of the central dip in the ϕ distributions becomes now evident. Contrary to η strips, the central tick is missing in ϕ distributions and results in the two neighbouring ticks forming a valley in between them. However, in both η and ϕ distributions still a vast amount of structure remains. Since all hits throughout the detector are considered in these distributions it seems likely to have some effects from many different strips overlay-

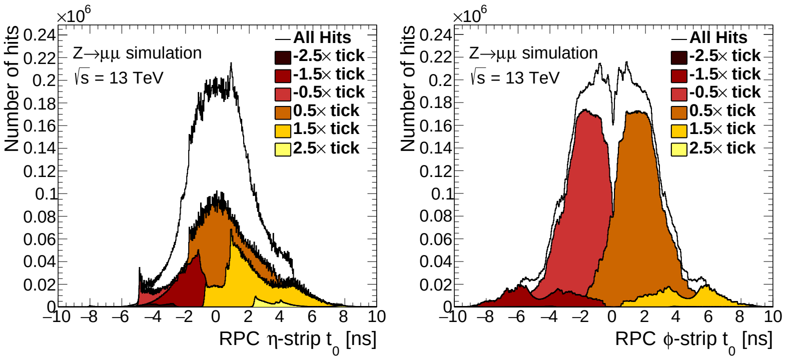

Figure C.3: Decomposition of the RPC simulated timing distributions into individual contributions from the dominant readout ticks. The figures show η strips on the left and ϕ strips on the right.

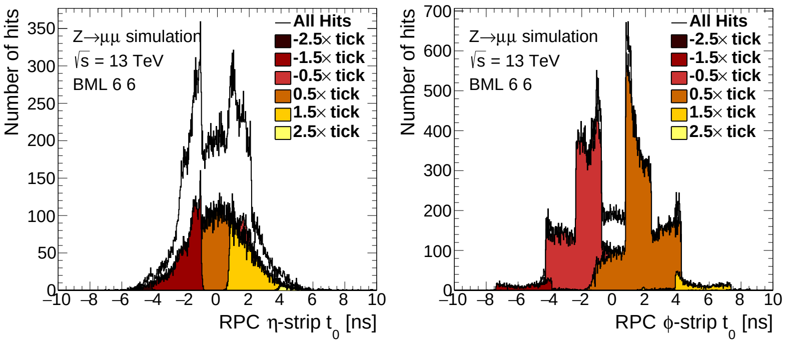

Figure C.4: Decomposition of the RPC simulated timing distributions into individual contributions from the dominant readout ticks of one RPC chamber. The figures show η strips on the left and ϕ strips on the right.

ing each other. To gain further insights one specific chamber within the detector is studied. One two-module chamber mounted on the underside of the sixth long middle-layer barrel station (BML station) from the detector middle in sector 6 (see e.g. appendix F) has been chosen. One one layer of the double gas-gap is considered. The station is at an angle of 45° relative to the accelerator plane. The correct association of readout strips to these gas gaps has been verified by plotting the hit positions. Looking at the decomposition of the timing distributions for this chamber results in figure C.4.

Several curious features still remain. Predominantly the jumps in the ϕ strip distribution. To trace their origin the pseudo-propagation time as stored in the xAODs is plotted in figure C.5 for η and in figure C.6 for ϕ strips of the chamber. Since all strips within a chamber have the same length and the propagation speed on the strip should be the same for all strips (about 4 ns/m), the expected distributions should be close to uniform. This is clearly not the case for the ϕ strips where two different values of the pseudo-propagation time seem to overlay each other. To investigate the origin, the pseudo-propagation time is plotted as a function of the three spatial coordinates x, y and z and as a function of the radial distance in the transverse plane. The resulting plots are shown in figure C.7

The pseudo-propagation time distribution on the η strips looks exactly as expected. The chamber is made of two units with two gas gaps each that overlap slightly in the central region. The centre of each gas gap is defined as zero propagation time. From the shape in the x and y plots one can correctly deduce that both units have their readout electronics at opposite ends of the readout strips. Plotting as

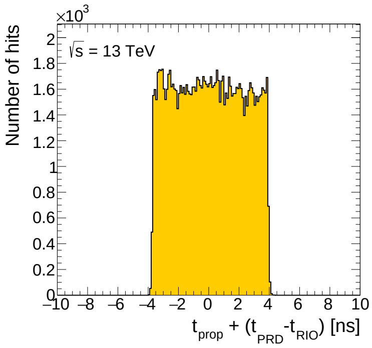

Figure C.5: RPC η strip pseudo-propagation time. The distribution is uniform which is expected since each part of the readout strip has in good approximation the same probability of being hit by a passing muon.

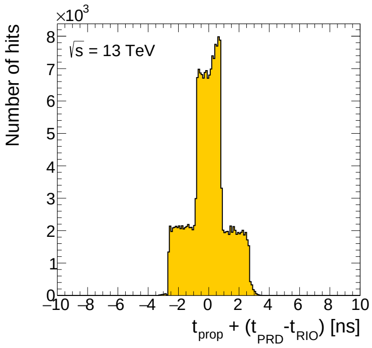

Figure C.6: RPC ϕ strip pseudo-propagation time. Instead of a uniform distribution as for the η strips, two different populations can be observed.

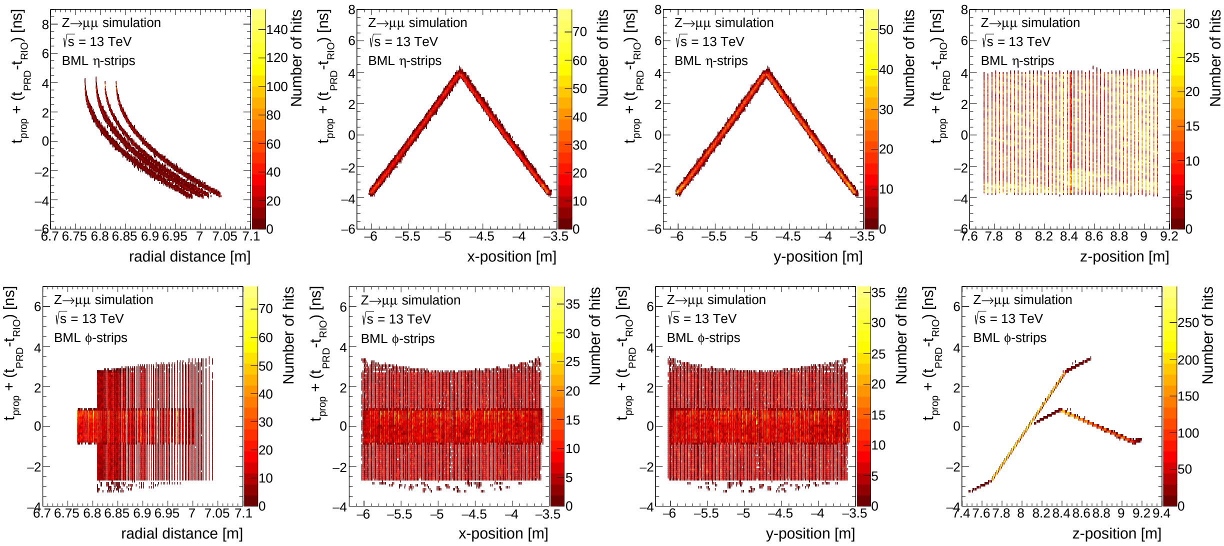

Figure C.7: Pseudo-propagation time as a function of the radial distance and spatial coordinates x, y and z for η strips in the top row and ϕ strips in the bottom row. The BML chamber chosen here is composed of two double-layers of gas gaps with read-outs at opposing ends of the strips which accounts for the triangular shapes in the x plots. For ϕ strips the two different scales of pseudo-propagation times can be seen. Especially the bottom right-hand plot needs further evaluation.

function of the z position illustrates the structure of parallel readout strips next to each other. For η strips the hit is always assumed to be in the centre of the strip in z direction. Lastly, plotting the pseudo-propagation time as a function of the radial distance further reveals the four separate gas gaps in the chamber. The distributions for the η strips are thus very well understood.

Once again it is the ϕ strips which reveal some curious features. The first observation is the presence of hits seemingly outside the chamber itself (lower right-hand plot in figure C.7). These are due to consecutive strips being put into a logical 'OR' either by wiring in the same chamber or during the readout in neighbouring chambers. The track reconstruction then only knows that one of the strips has fired and tries to identify the correct one. At the edge of a strip this might fail resulting in the tails observed in the plot. The second feature responsible for the two different scales of pseudo-propagation times is best visible in the z plot. The two units of the chamber seem to have different propagation speeds. However, this is clearly not physical. Instead there are two effects to consider: The true propagation time on the strip and the intrinsic spread of the ToF. Since the chamber is located at large η, the first unit (left part in the bottom-right-hand plot of Figure C.7) is further away from the IP than the other unit and thus has longer ToF. Consider Figure C.8 where a rough schematic of a two-unit chamber is given. The readout electronics are mounted mirror-symmetrically on the two units. Thus, the spread of the ToF causes a counteracting of the propagation time in unit 2 and an amplification in unit 1. This gives rise to the curious shapes observed in Figure C.7. Since the effect depends on the relative ToF differences between the units, the effect should be larger in chambers at high η compared to central chambers. Figure C.9 shows the pseudo-propagation time as a function of z for a 'column' of RPC chambers (ϕ sector 6, all RPC chambers η -7 to 7).

One can clearly see the chambers which are manufactured from

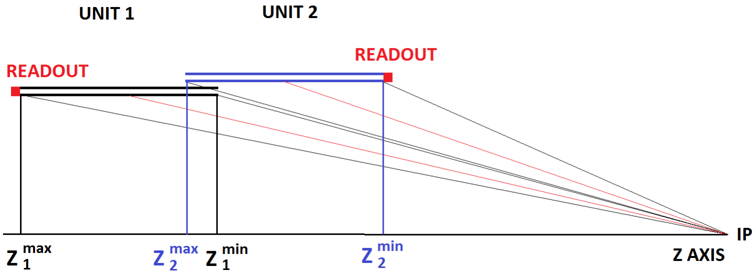

Figure C.8: Schematic view of a two-unit RPC chamber with a double gas-gap in each unit. The readout electronics sit at opposite ends of the units thus the intrinsic spread of the ToF amplifies or compensates the propagation time.

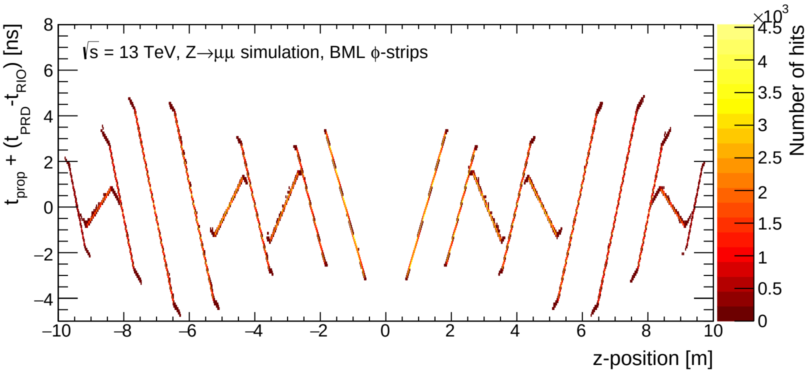

Figure C.9: Pseudo-propagation time as a function of the z coordinate along a sequence of BML chambers. The chambers with two units are discernible by their subdivided structure. The tilt (and thus the pseudo propagation velocity) of the separate components decreases to large $|\eta|$.

two separate units. Studying closely the tilt of the two bands in two-unit chambers one can see it decrease towards large $|z|$ and with that large $|\eta|$. The tilt is a measure for the perceived propagation velocity. The expected amplification of the effect can be clearly observed.

As a result of the investigation the compositions of the RPC timing distributions have been understood and it can be concluded that the initially observed distribution is expected.

APPENDIX D

Shifted means and large widths in RPC MC timing

While looking at the timing distributions in RPC readout strips for muons coming from simulated $Z \to \mu\mu$ decays it has been noted that some have mean values which are considerably shifted from $\bar{t}_0 = 0$ (see figure 4.60). This observation was not expected since all RPC strips are assumed to be treated identically in simulation. An example of a strip with an incorrect mean is given in figure D.1, where the (pseudo-)propagation time has been added to the t_0 to reveal the readout ticks. The plot does not give a good hint upon the source of the shifts. The investigation is continued isolating the affected strips from the correct ones by cutting the $\bar{t}_0$ distribution in two and defining good strips as strips with $\bar{t}_0 < 1.0$, and as bad strips otherwise (see figure 4.60). Then the position of the good and bad strips are plotted. This was done in figure D.2.

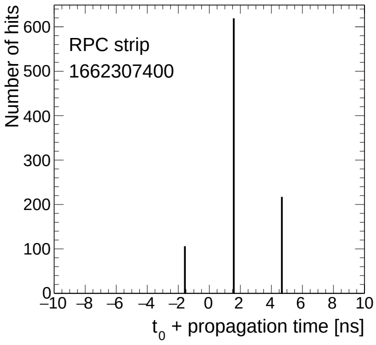

Figure D.1: One RPC strip has been picked randomly to give an example of a shifted distribution. The propagation time was added to the t_0 which reveals the readout ticks corresponding to the actual measurement of the detector. Besides the shift the plot reveals no further irregularities or hints on the origin of the shift.

The top row shows the $x - y$ projection of the detector, the bottom row the $z - y$ projection. The position of hits on good strips are plotted jointly for η and ϕ strips in (a) and (d). They give a good orientation on where the different detector elements are found. For the bad strips the plots are done separately for η and ϕ strips. Plots (b) and (e) clearly show that the bad η strips are not distributed randomly throughout the detector, but are instead found exclusively in the BMS stations. It is further possible to see that more than 90% of the bad strips are in fact BMS η strips. The much lower number of bad ϕ strips are also found dominantly in the small sectors of the detector, but at large z values. Their location is given in figures (c) and (f).

The precise origin of these features is not yet understood. The findings have been reported to dedicated experts who will continue the investigation and provide a fix for future MC productions if needed.

A further irregularity which has emerged while reviewing the simulated RPC timing distributions is a number of RPC strips that show much wider timing distributions when compared to both data and other *MC* distributions (figure 4.61). Analogously to the investigation for the shifed means, the RPC strips are split up into ’good’ and ’bad’ strips. The separation in this case is done at $\sigma_{\mathrm{MC}} = 1.9$. Once again the positions of hits on good and bad strips are plotted separately to localise the faulty strips. This has been done in

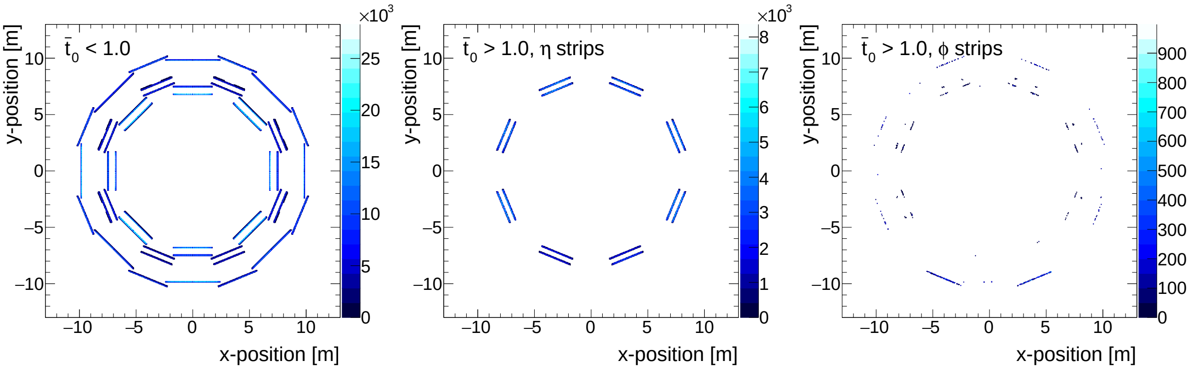

(a) All good strips $x-y$ projection (b) Bad η strips in $x-y$ projection (c) Bad ϕ strips in $x-y$ projection

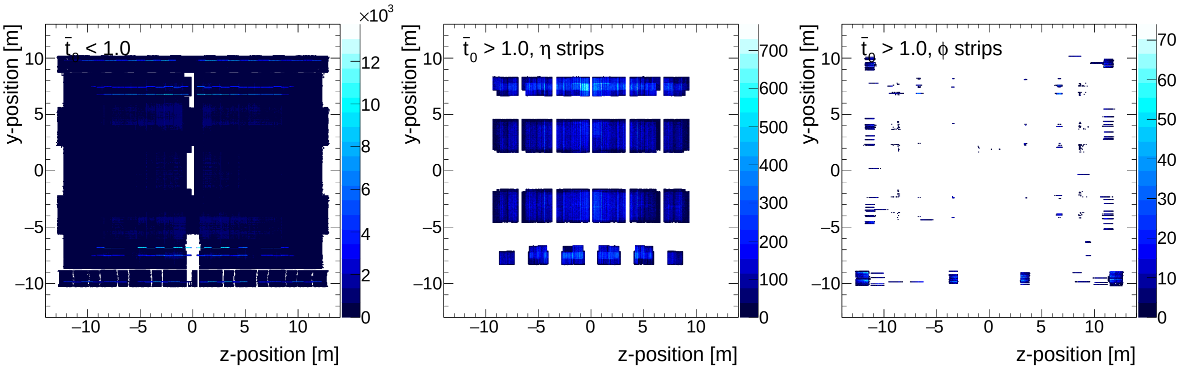

(d) All good strips $z-y$ projection (e) Bad η strips $z-y$ projection (f) Bad ϕ strips $z-y$ projection

Figure D.2: Distribution of hits on RPC readout strips with regular and shifted means throughout the detector. The left column contains the good RPC strips, while the middle (right) column shows the position of bad η strips (ϕ strips).

figure D.3.

Similarly to before, the problematic η strips are found almost exclusively in the BMS stations with some additional contributions from outer stations in the foot region of the detector. Whether the shifted means and the broad distributions in those stations are connected is in the absence of an explanation difficult to judge, however a coincidence is highly unlikely. For the ϕ strips the situation is more complicated. From figures (c) and (f) it can be seen that broader distributions are found for strips in all stations. Nevertheless a pattern emerges and the affected strips are not distributed randomly. In fact, for those chambers which are composed of two units, the broad strips are found exclusively in the unit which is closer to the IP in z direction. In the remaining unit all strips are fine. This observation is presumably closely linked to the findings reported in Appendix C. The (pseudo-)propagation time is larger for the units close to the IP (compare to the scan of propagation times along the z axis in figure C.9), which results in a larger spread of the underlying ticks and thus a broader timing distribution. It is therefore believed that the broad distributions for ϕ strips are an artefact of the handling of propagation time, PRD and RIO time within the resonstruction algorithm. However, as of the time of writing no explanation can be offered for the broad distributions in η strips.

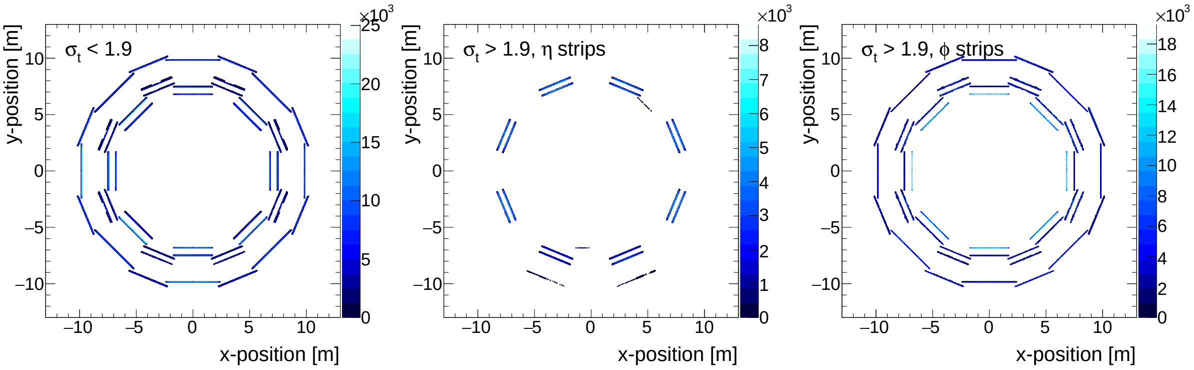

(a) All good strips $x - y$ projection (b) Bad η strips in $x - y$ projection (c) Bad ϕ strips in $x - y$ projection

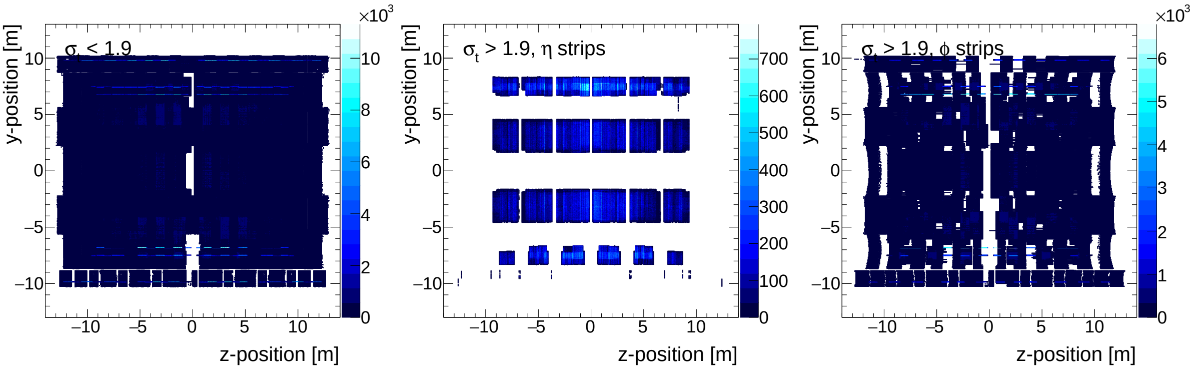

(d) All good strips $z - y$ projection (e) Bad η strips $z - y$ projection (f) Bad ϕ strips $z - y$ projection

Figure D.3: Distribution of hits on RPC readout strips with regular and broad timing distributions throughout the detector. The left column contains the good RPC strips, while the middle (right) column shows the position of bad η strips (ϕ strips).

APPENDIX E

Supplementary material for SMP searches

E.1 Further plots and tables

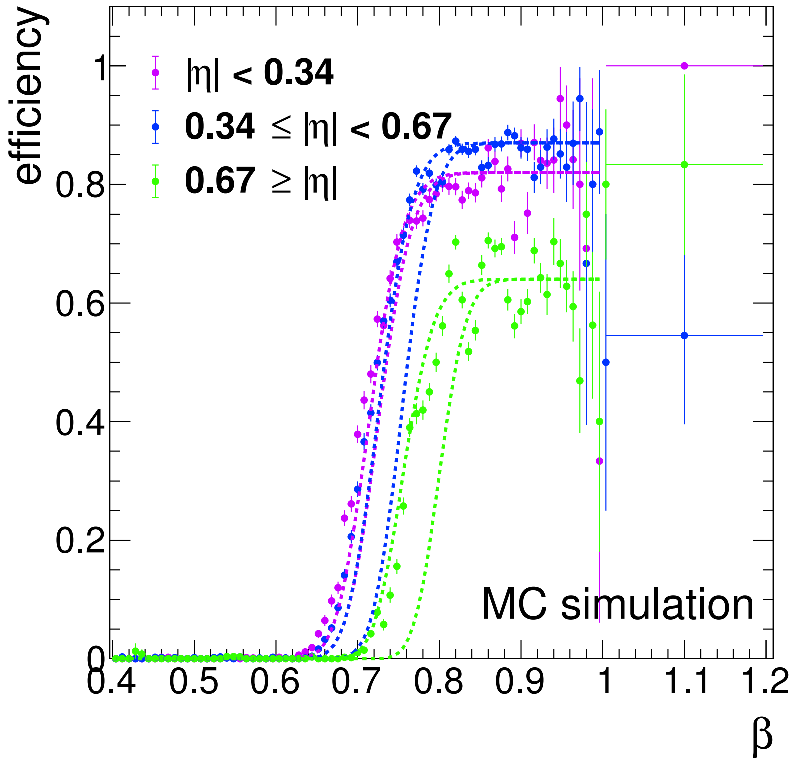

Figure E.1: The markers give the single-muon trigger onsets determined by looking at signal MC and taking the β from the hit with the largest measured ToF in three η regions of the detector. The dashed lines correspond to the onset determined from equation 5.2 where the edges of the η windows were taken. Furthermore, the generic efficiency has been scaled to match the plateau efficiency in signal MC. The principal features of the onsets like threshold value and onset shape are well matched between both procedures.

Chapter 5.6 gives a detailed account of the candidate selection. An example cut-flow of the MS-agnostic analysis was already given in table 5.7. In the full-detector analysis several cut-flows are implemented. An exemplary table of the TIGHT selection cut-flow was given in table 5.6. A cut-flows for the LOOSE selection is given in table E.1. Finally, table E.2 states the cut-flow for the ID+CALO selection.

Table E.1: Cut-flow of the LOOSE selection targeting the full-detector search. The number of events surviving a given cut is stated for data and as an example for gluino R-hadrons with masses 1600 GeV and 2000 GeV. The efficiency of each cut is also given.

	data	1600 GeV		2000 GeV	
	observed	expected	eff.	expected	eff.
initial	6325439488	291.84		35.35	
trigger	926315840	141.09	0.48	14.82	0.42
data quality	897631104	141.02	0.48	14.78	0.42
PV with at least 2 tracks	897621248	141.02	0.48	14.78	0.42
candidate combined track	142200464	45.02	0.15	4.57	0.13
$p_T^{\text{cand}} > 70.0\ GeV$	15492583	44.80	0.15	4.47	0.13
$p_T^{\text{trk}} > 50.0\ GeV$	15477206	44.80	0.15	4.47	0.13
$0 < p^{\text{trk}} < 6.5\ TeV$	15464828	43.45	0.15	4.28	0.12
PV matched	15281664	43.32	0.15	4.26	0.12
$\text{N}_{\text{silicon}}^{\text{hits}} > 6$	15269703	43.32	0.15	4.26	0.12
$\text{N}_{\text{pix}}^{\text{shared}} + \text{N}_{\text{pix}}^{\text{split}} = 0$	14331513	43.01	0.15	4.24	0.12
$\text{N}_{\text{SCT}}^{\text{hits+dead}} > 2$	14331513	43.01	0.15	4.24	0.12
$p_T^{\text{iso}} < 5\ GeV$	11604712	42.29	0.14	4.18	0.12
hadron, electron veto	11555336	42.29	0.14	4.18	0.12
pix innermost	11387407	41.54	0.14	4.07	0.12
$0 < p^{\text{cand}} < 6.5\ TeV$	11386355	39.13	0.13	3.87	0.11
cosmics veto	11384572	39.09	0.13	3.87	0.11
Z veto	9342829	38.51	0.13	3.78	0.11
$\|\eta\| < 2$	7860437	35.46	0.12	3.61	0.10
two MS stations	7417328	31.02	0.11	3.06	0.09
β consistency	6959917	27.83	0.10	2.81	0.08
dE/dx–ToF consistency	6959649	27.83	0.10	2.81	0.08
$\sigma_\beta < 0.025$	6833380	27.79	0.10	2.81	0.08
β quality	6833288	27.57	0.09	2.79	0.08
$0.2 < \beta < 2$	6833288	27.57	0.09	2.79	0.08

Table E.2: Cut-flow of the ID+CALO selection targeting the full-detector search. The number of events surviving a given cut is stated for data and as an example for stable staus with masses 411 GeV and 629 GeV. The efficiency of each cut is also given.

	data	411 GeV		629 GeV	
	observed	expected	eff.	expected	eff.
initial	6325439488	52.07		6.72	
trigger	926315840	42.26	0.81	5.18	0.77
data quality	897631104	42.26	0.81	5.18	0.77
PV with at least 2 tracks	897621248	42.26	0.81	5.18	0.77
candidate ID track	188613888	37.33	0.72	4.81	0.72
$p_T^{\text{trk}} > 50.0\ GeV$	65976344	36.93	0.71	4.78	0.71
$0 < p^{\text{trk}} < 6.5\ TeV$	65918760	36.91	0.71	4.77	0.71
PV matched	63148044	36.89	0.71	4.77	0.71
$\text{N}_{\text{silicon}}^{\text{hits}} > 6$	63134604	36.89	0.71	4.77	0.71
$\text{N}_{\text{pix}}^{\text{shared}} + \text{N}_{\text{pix}}^{\text{split}} = 0$	57846400	36.74	0.71	4.75	0.71
$\text{N}_{\text{SCT}}^{\text{hits+dead}} > 2$	57846400	36.74	0.71	4.75	0.71
$p_T^{\text{iso}} < 5\ GeV$	33016852	36.54	0.70	4.72	0.70
hadron, electron veto	32237924	36.53	0.70	4.72	0.70
pix innermost	31720652	36.49	0.70	4.71	0.70
cosmics veto	31663028	36.37	0.70	4.68	0.70
Z veto	25173912	36.32	0.70	4.68	0.70
$\|\eta\| < 1.65$	25067764	36.29	0.70	4.68	0.70
$\text{N}_{\text{good}\ dE/dx}^{\text{hits}} > 1$	23295944	35.64	0.68	4.58	0.68
$0 < dE/dx_{\text{pix}} < 20\ [\text{MeVg}^{-1}\text{cm}^2]$	23295944	35.64	0.68	4.58	0.68
$0.2 < \beta\gamma < 10$	17185952	34.24	0.66	4.49	0.67
$0.2 < \beta < 2$	17120692	34.22	0.66	4.49	0.67
$\sigma_\beta < 0.06$	5133322	17.92	0.34	2.67	0.40
$\kappa > 0.0063$	4631851	17.05	0.33	2.57	0.38

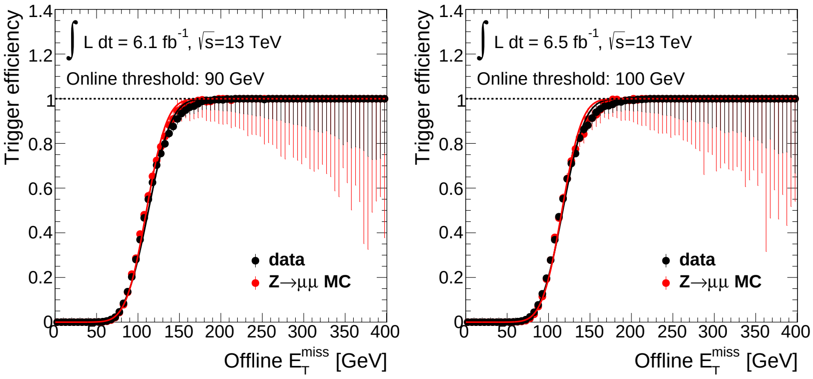

Figure E.2: E_T^{miss} trigger onsets in data and MC with an applied $Z \to \mu\mu$ selection for the employed triggers with online threshold 90 GeV and 100 GeV. Fitted error functions according to equation 5.5 to the onset are drawn as solid lines. The corresponding plots for the other two E_T^{miss} triggers with thresholds 70 GeV and 110 GeV were given in figure 5.30 in Chapter 5.8.2.

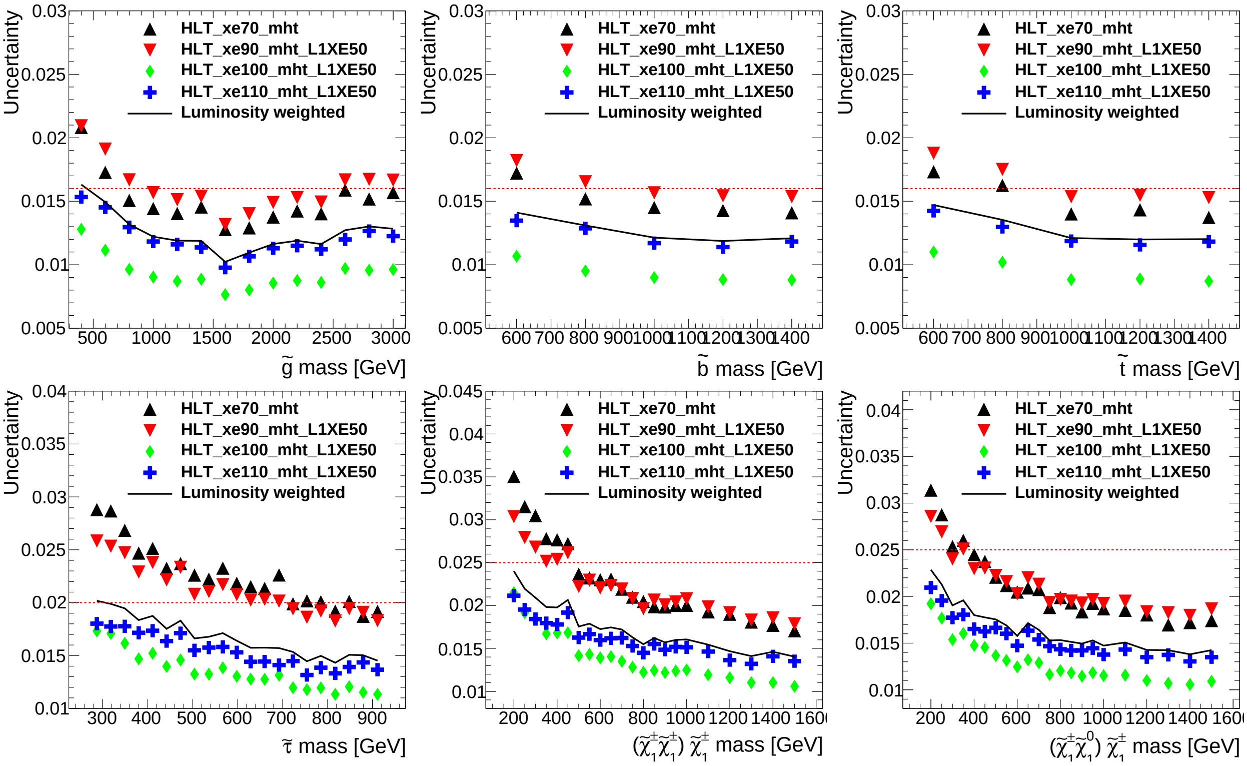

Figure E.3: Estimated systematic uncertainties of the E_T^{miss} trigger efficiency evaluated for all available signal MC samples. The uncertainties derived from the onset for individual triggers are shown with coloured markers, while the solid black line indicates the according to luminosity weighted average of all triggers. The variation in scale between samples is gernerally small and the approach of a flat uncertainty indicated by the dashed red line is well justified.

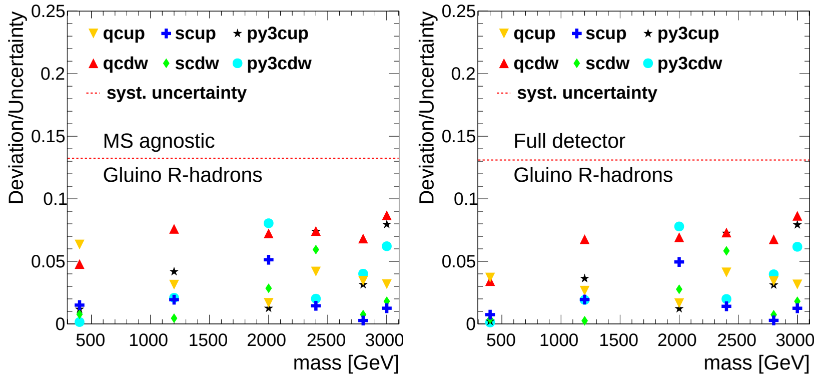

Figure E.4: Relative deviations from nominal MC by variations of generator parameters in MadGraph for gluino R-hadrons in the MS agnostic (left) and full-detector (right) selection. The combined systematic uncertainty is taken to be flat over all mass points and is calculated by adding the largest deviations of each up-down variation in quadrature. The value is marked with a dashed red line and is similar in size the the uncertainty estimated from the efficiency differences between Pythia and MadGraph.

E.2 Validation plots

In order to validate the SMP search a number of cross-checks have been performed. Tests to check whether no events are missed in either data or MC during the analysis or whether any events are processed more than once are performed. No missing or duplicated events have been found.

The stability of the signal selection efficiency of the pre-selection over the full pileup range is demonstrated in figure E.5 for all different selections and concerned MC signals. The efficiencies have been normalised with respect to all reconstructed candidates that were successfully matched to truth signal thus resulting in large signal efficiencies. No major dependency of the selection efficiency on pileup outside the statistical fluctuations is discernible.

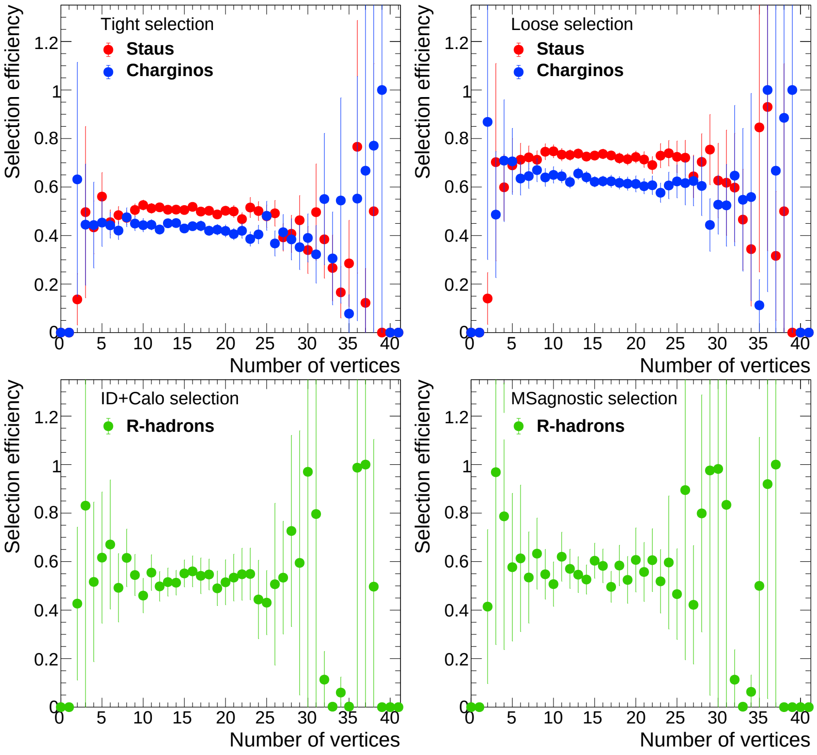

Figure E.5: The signal pre-selection efficiency is drawn as function of the number of reconstructed vertices in simulated collision events for all types of selections. The efficiencies are drawn for staus and charginos of all masses for the TIGHT (top left) and LOOSE (top right) selection and for *R*-hadrons of all masses and regardless of the type of heavy constituent for the ID+CALO selection (bottom left) and MS agnostic analysis (bottom right). The selection efficiencies are found to be insensitive to pileup.

During MC sample production events are overlaid by minimum-bias collisions to mimic the effects of pileup. However, the overall pileup distribution will not be identical to data. A dedicated pileup-reweighting (PRW) tool is used which reweights simulated events according to the number of pileup collisions to generate agreement of the pileup profiles. In order to check the functionality of the tool, the average number of simultaneous interactions before and after application of the PRW tool are plotted as done in figure E.6. The expected effect on the simulated distributions is clearly observed. Note that no agreement with data is expected. While this may seem unintuitive, one needs to realise that the average number of interactions is a quantity calculated purely through the current instantaneous luminosity of the collider and the total pp scattering cross-section. The number of actually reconstructed vertices needs to be taken into account as well.

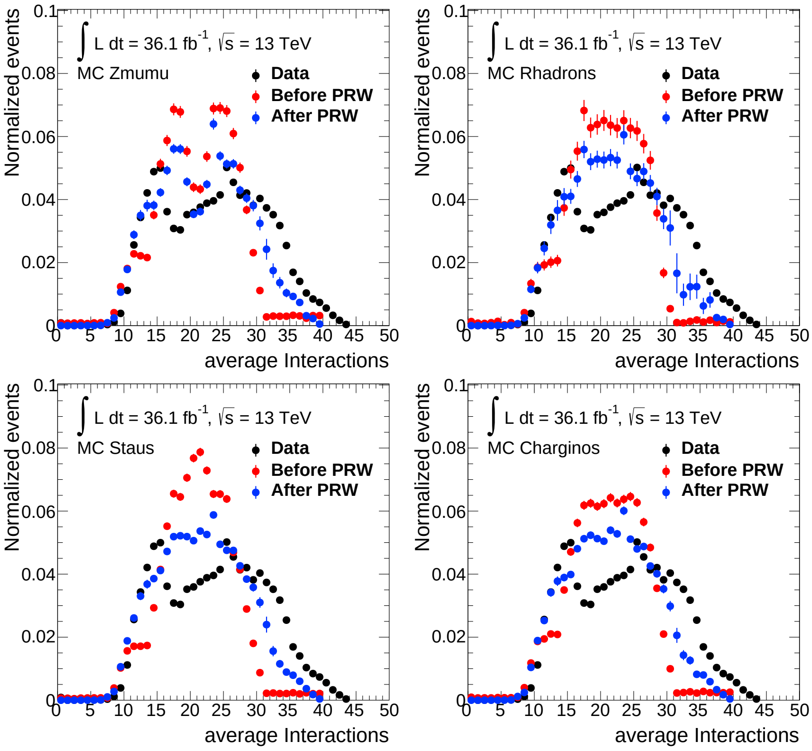

Figure E.6: Average number of simultaneous interactions of data and simulation before and after application of the PRW tool. It can be clearly seen that the distribution is closer to data after application of the tool. However, no agreement is expected since the PRW tool needs to take both the average number of simultaneous interactions and the number of reconstructed vertices into account. The PRW tool acts as expected for all types of MC: Simulated $Z \to \mu\mu$ decays (top left), R-hadrons of all types and masses (top right), staus (bottom left) and charginos (bottom right).

Lastly, time-dependent effects are ruled out by a comparison of the expected and observed event yields, where the expected is derived from the integrated luminosity of each data run. The expected event yields are calculated individually for all periods with constant trigger conditions. As expected, the ratio of observed and expected events is close to 1.0 throughout the data for all selections. The corresponding plots can be found in figure E.7.

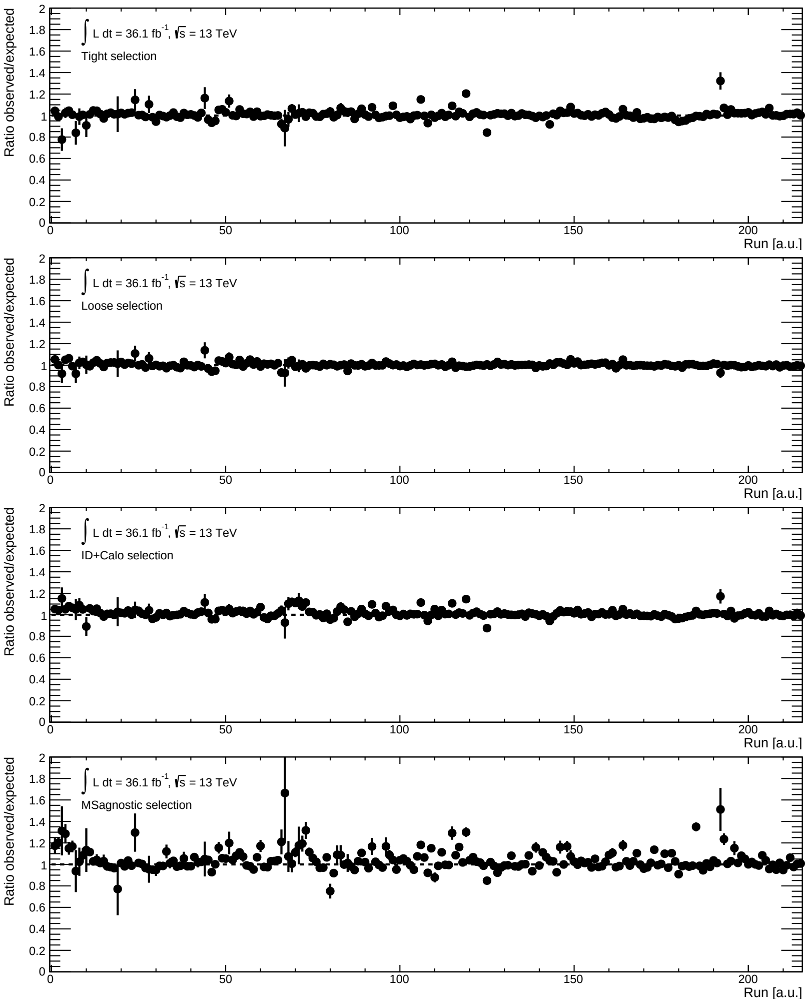

Figure E.7: Ratio of expected and observed event yields for all selection cutflows over all runs of the 2015 and 2016 data-taking. Top to bottom: TIGHT, LOOSE, ID+CALO and MS agnostic selection. The ratio is found to be in good agreement with 1.0.

APPENDIX F

Layout of the Muon Spectrometer

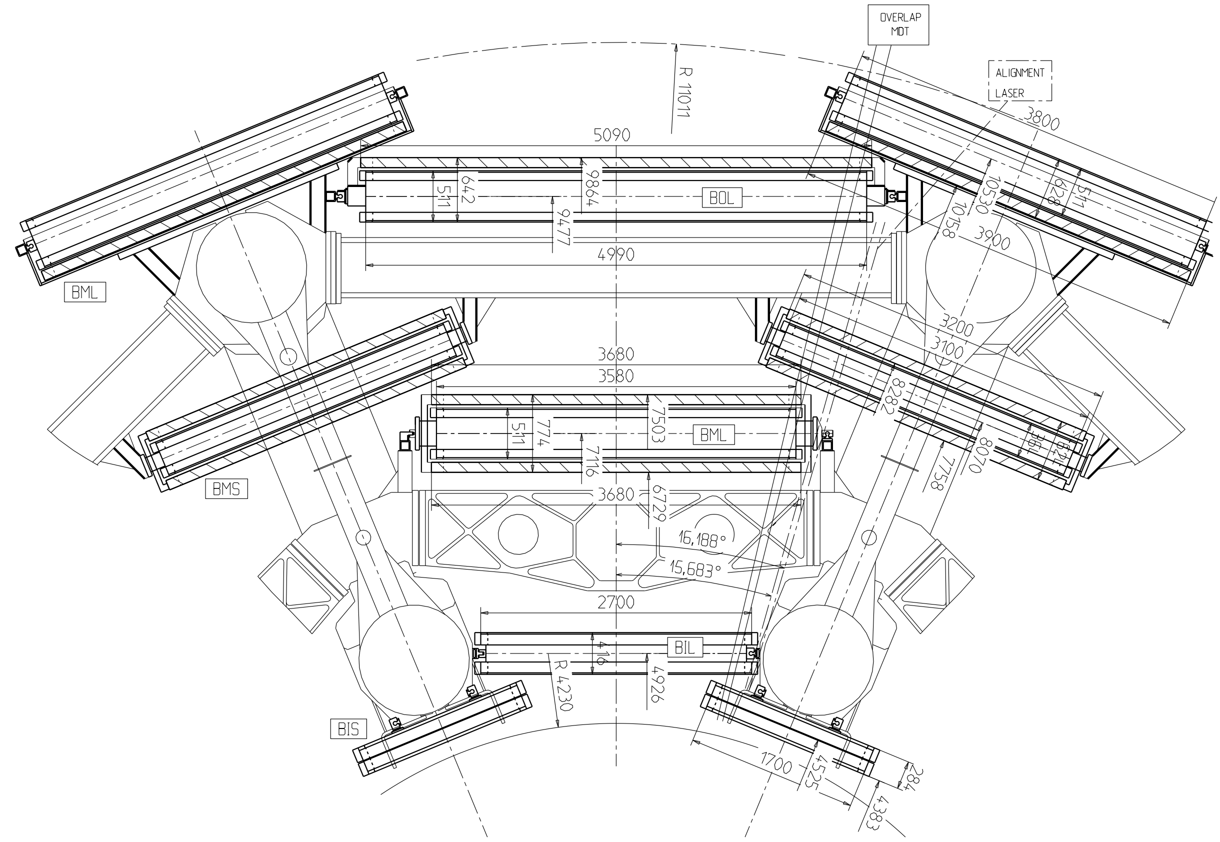
OVERLAP MDT
ALIGNMENT LASER
R 11011
5090
3800
642
511
9864
BOL
9477
4990
10530
10158
628
511
3900
BML
3200
3100
3680
3580
774
511
7503
BML
8282
7116
361
624
8070
7758
BMS
3680
6729
16,188°
15,683°
2700
BIL
416
R 4230
4926
BIS
1700
4525
284
4383

Figure F.1: View of one sector of the barrel MS with chamber naming and dimensions. Figure taken from [252]. Note: The designation of the outer-most station on the left-hand side is incorrectly stated as 'BML'. Located in a small sector the correct name is 'BOS'.

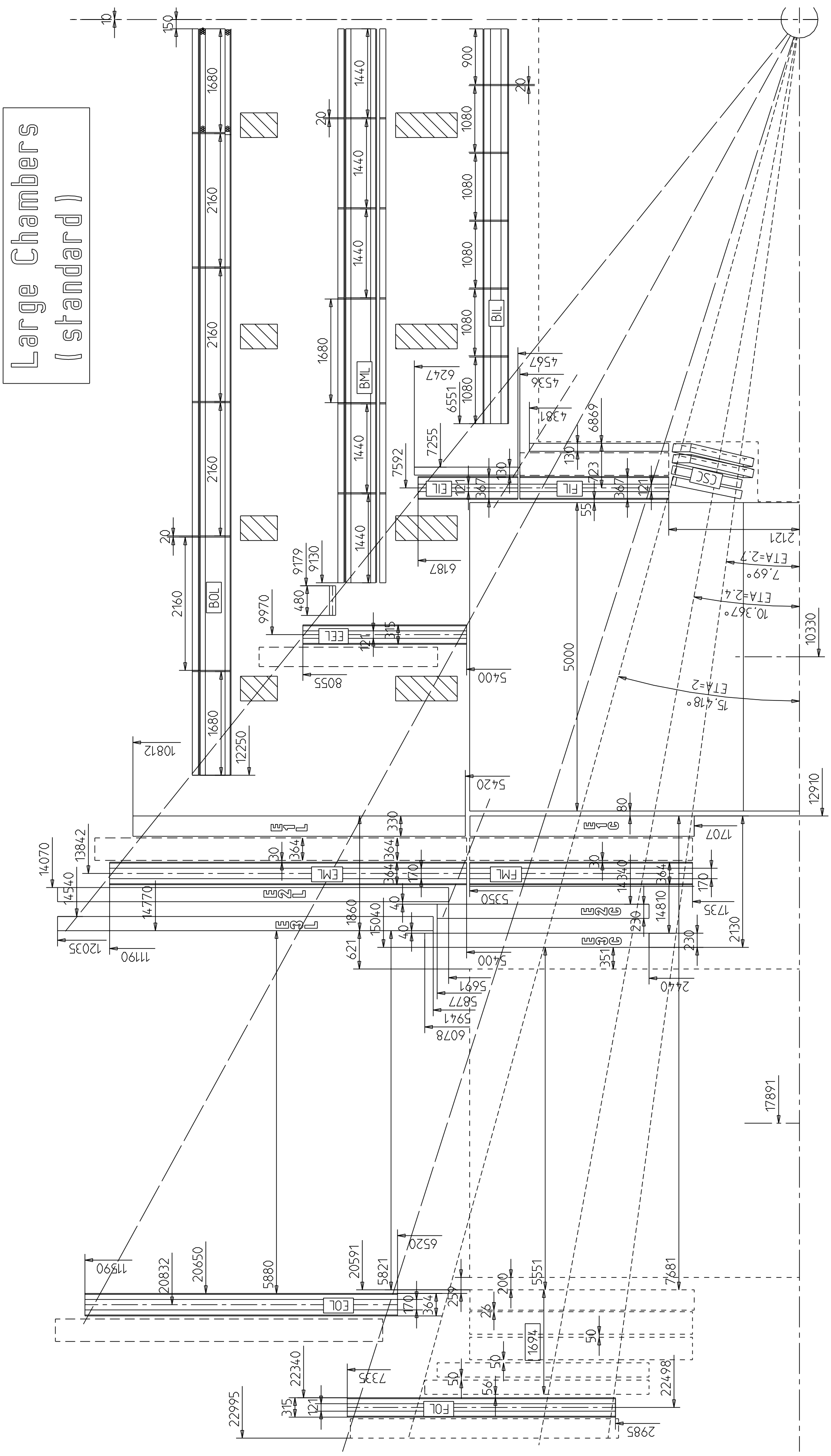
Large Chambers
(standard)
BOL
BML
BIL
EIL
FIL
CSC
EEL
EML
EOL
FOL
E1L
E2L
E3L
E1G
E2G
E3G
ETA=2.7
ETA=2.4
ETA=2
7.69°
10.367°
15.418°
10
150
1680
2160
2160
2160
2160
1680
20
1440
1440
1440
1680
1440
1440
900
1080
1080
1080
1080
1080
20
4567
4536
4381
6247
6551
6869
7255
7592
130
130
30
121
367
123
367
121
55
2121
6187
9179
9130
9970
480
315
121
8055
5400
5000
10330
12250
10812
5420
80
330
364
364
30
13842
14070
14540
14770
1707
12910
170
364
5350
14340
14810
1735
1860
15040
40
40
40
621
230
351
230
2130
11190
12035
5400
5691
5877
5941
6078
2440
17891
6520
11590
20832
20650
5880
20591
5821
200
5551
7681
170
364
250
26
1694
50
50
50
56
50
22340
7335
22498
22995
315
121
2985

Figure F.2: Cut through the MS showing the z–y plane for a quarter of the detector. The layout of a large sector is given. The IP is drawn in the bottom right-hand corner. Figure taken from [252].

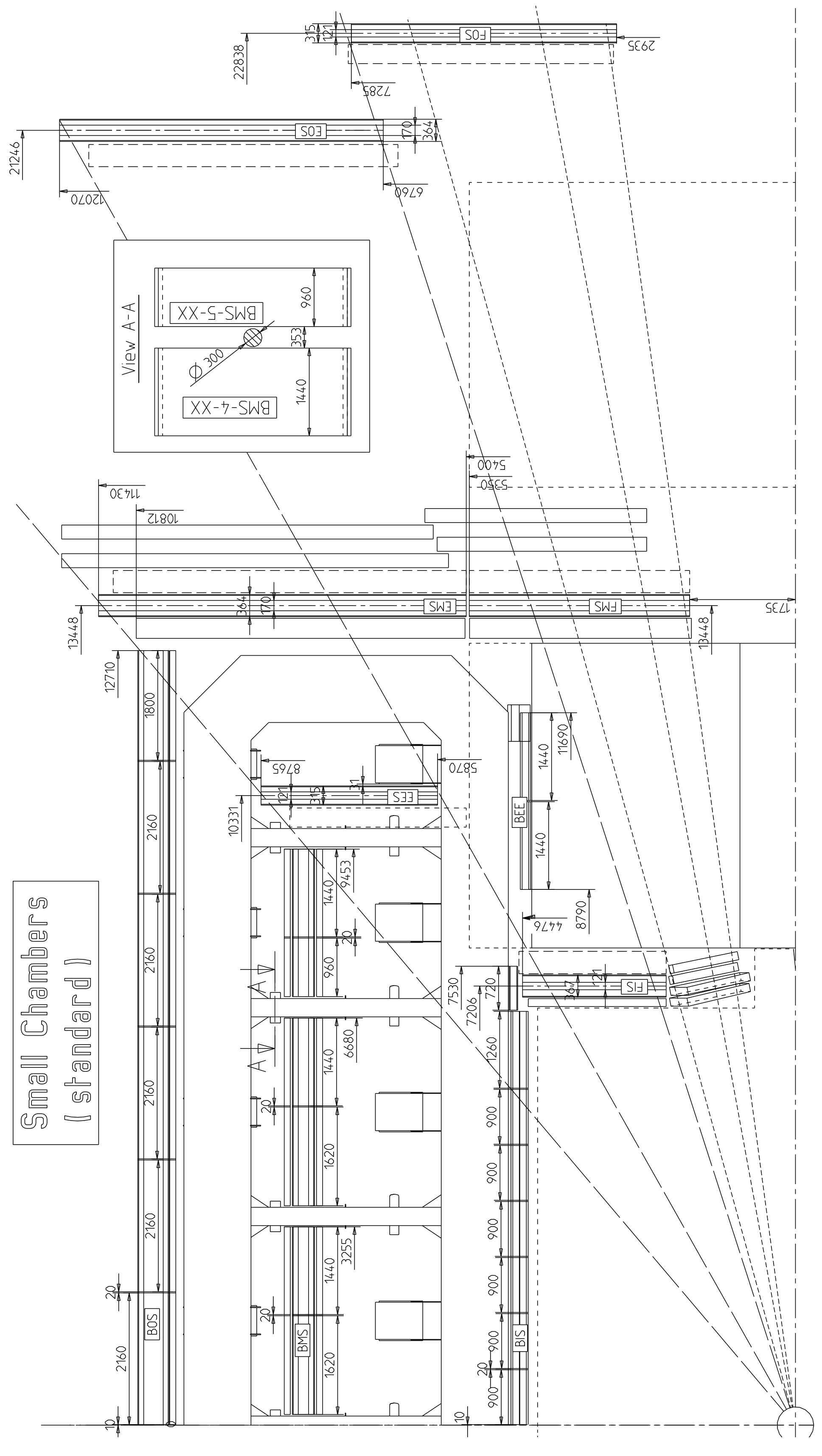
Small Chambers
(standard)
View A-A
BMS-5-XX
BMS-4-XX
Ø 300
FOS
EOS
EMS
EES
BEE
FIS
BOS
BMS
BIS
A
22838
315
121
2935
7285
21246
170
364
12070
6760
960
353
1440
5400
5350
11430
10812
13448
1735
12710
1800
2160
8765
5870
31
10331
11690
9453
8790
4476
20
7530
7206
720
367
6680
1260
900
1620
3255
10

Figure F.3: Cut through the MS showing the plane of a barrel magnet coil for a quarter of the detector. The layout of a small sector is given. The IP is drawn in the bottom left-hand corner. Figure taken from [252].

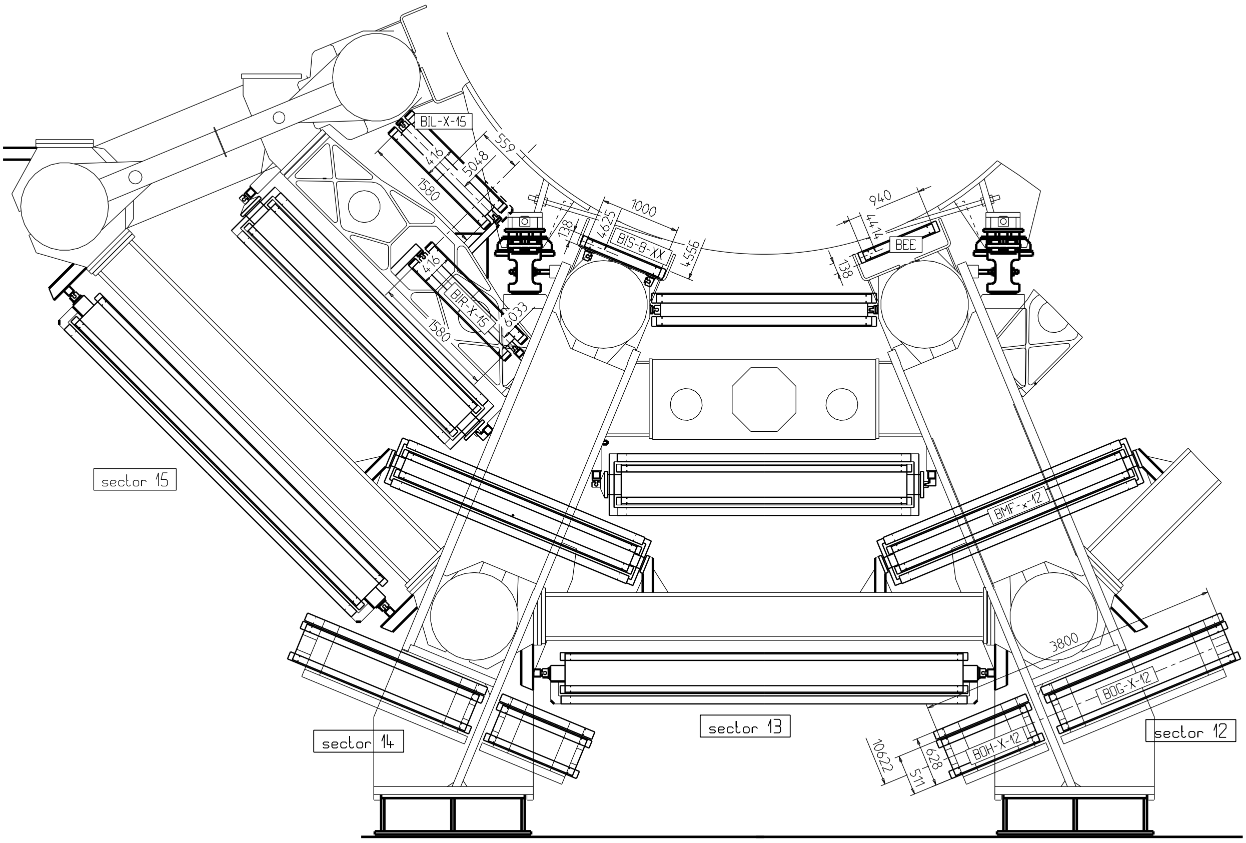
BIL-X-15
559
416
5048
1580
BIR-X-15
416
1580
6033
138
4625
1000
BIS-8-XX
4556
940
4414
BEE
138
sector 15
BMF-x-12
3800
BOG-X-12
sector 14
sector 13
10622
628
511
BOH-X-12
sector 12

Figure F.4: Layout of the detector in the feet region. Figure taken from [252].

List of Figures

1.1 Schematic of a displaced vertex 1

2.1 Overview of all Standard Model particles 4
2.2 Electromagnetic interaction vertex 5
2.3 Weak interaction vertices 5
2.4 Strong interaction vertices 6
2.5 Colour confinement in QCD 7
2.6 Muon decay 7
2.7 Known SM long-lived particles 8
2.8 Content of the Universe 9
2.9 Neutrino oscillation 9
2.10 Quantum corrections to the physical Higgs mass 10
2.11 Hypothetical heavy scalar to Higgs coupling 11
2.12 Gauge coupling unification 11
2.13 Hidden sector in SUSY models 12
2.14 Total SUSY production cross sections 14
2.15 SUSY decay vertices 14
2.16 Split SUSY gluino decay 15
2.17 SUSY breaking scale as function of Higgs mass 15
2.18 Kaluza-Klein additional dimension 16
2.19 Lifetime of the $\tilde{\tau}_1$ in CMSSM 17
2.20 Stopping power as function of $\beta\gamma$ 17
2.21 R-hadron elastic scattering 18
2.22 Conversion of R-meson to R-baryon 18
2.23 R-hadron inelastic scattering with charge flip 19
2.24 R-hadron cross section in generic and Triple-Regge model 19
2.25 Formation of an R-hadron resonance 20

3.1 Cross section of an LHC dipole magnet 26
3.2 Colliding proton bunches 26
3.3 Instantaneous luminosities in ATLAS during 2016 pp data-taking 27
3.4 Integrated luminosity in ATLAS during 2016 pp data-taking 27
3.5 Pileup profile in 2015 and 2016 27
3.6 The LHC acceleration chain 28
3.7 Schematic representation of the LHC filling scheme 28
3.8 The ATLAS detector 29
3.9 Working principle of the ATLAS detector 30
3.10 The ATLAS magnet system 31
3.11 Positioning of the coordinate system in ATLAS 31
3.12 Pseudorapidity and its relation to θ 31

3.13 Schematic of the ATLAS Pixel Detector 32
3.14 Installation of the Insertable B-Layer 32
3.15 Schematic view of a barrel segment of the ID 33
3.16 Schematic view of the calorimeter system 33
3.17 Development of an electromagnetic shower 34
3.18 Section of the LAr electromagnetic calorimeter 34
3.19 Schematic of a scintillating tile 34
3.20 Schematic of the Muon Spectrometer in x–y projection 35
3.21 Schematic view of the Muon Spectrometer 35
3.22 r–z projection of the Muon Spectrometer 36
3.23 Cross section of a drift tube 36
3.24 MDT chamber 37
3.25 MDT readout schematic 37
3.26 Cross section through a barrel sector of the ATLAS detector 37
3.27 Overlap region of two RPC units 38
3.28 Illustration of the ATLAS trigger system 38
3.29 Event data model in ATLAS 39

4.1 Muon-p_T distribution 42
4.2 Uncalibrated ToF for MDT and RPC 42
4.3 Uncalibrated t_0 for MDT and RPC 43
4.4 Uncalibrated t_0 for RPC η and ϕ strips 43
4.5 Uncalibrated β for MDT and RPC 44
4.6 RPC t_0 distribution with timing bug 44
4.7 RPC t_0 with timing bug as function of z 45
4.8 RPC t_0 before and after online-timing correction 45
4.9 RPC t_0 for six periods 46
4.10 RPC β before and after online-timing correction 46
4.11 t_0 distribution of MDT CSM 18 47
4.12 Overview of MDT CSM calibration constants 47
4.13 MDT t_0 and β before and after chamber calibration 47
4.14 Entries in run-wise chamber calibration 48
4.15 Δt_0 in run-wise chamber calibration 48
4.16 MDT t_0 and β before and after run-wise chamber calibration 48
4.17 Hits per drift tube 49
4.18 Distribution of tube t_0 corrections 49
4.19 Distribution of drift tube timing resolutions 49
4.20 t_0 distributions for two drift tubes 50
4.21 Bad resolution MDT hits in z–y projection 50
4.22 Internal MDT consistency before and after truncation 51
4.23 MDT t_0 and β before and after drift-tube calibration 51
4.24 Number of hits on RPC η and ϕ strips 52
4.25 RPC ϕ strip t_0 distribution with tail 52
4.26 Fitted t_0 distribution of an RPC ϕ strip 52
4.27 t_0 multi-peak distribution over time 53
4.28 Multi-peak RPC timing distributions 53
4.29 Distribution of the RMS for all strips 53
4.30 Resolution $\sigma^i_{t_0}$ of RPC readout strips 54

4.31 RPC t_0 before and after tail suppression 54
4.32 Distributions of calibration constants for η and ϕ strips 54
4.33 RPC t_0 and β before and after strip calibration 55
4.34 MDT phase-shift corrections 55
4.35 RPC phase-shift corrections 56
4.36 β distributions before and after run correction 56
4.37 Comparison of calibration orderings 57
4.38 Pull distributions for MDT and RPC hits 57
4.39 Summary of MDT β calibration 58
4.40 Summary of RPC β calibration 59
4.41 Uncertainties on β estimate in MDT and RPC 59
4.42 Correlation of the MDT and RPC β estimates 60
4.43 Uncertainty on combined β estimate 60
4.44 Fully calibrated Muon Spectrometer β distribution 60
4.45 Comparison of calibrated MDT β with untreated simulation 61
4.46 Differences in tube t_0 widths in data and MC 61
4.47 Number of hits per drift tube in simulation 61
4.48 Reweighting too broad MC distributions 62
4.49 Sharpening too broad MC distributions 63
4.50 Unfolding too broad MC distributions 63
4.51 Sharpening factors for drift tubes 64
4.52 Smearing widths for drift tubes 64
4.53 t_0 and β distributions after drift-tube smearing 65
4.54 Fit of data and MC t_0 distribution of one chamber 65
4.55 Too broad MDT chambers as function of the sharpening factor 65
4.56 Smearing applied to one chamber 66
4.57 Data-MC agreement as function of λ 66
4.58 t_0 and β distributions after chamber smearing 66
4.59 Comparison of calibrated RPC t_0 and β with untreated MC 67
4.60 Means of t_0 distributions for all RPC strips 67
4.61 Difference of RPC strip timing widths in data and MC 68
4.62 RPC tick sharpening 68
4.63 Treated RPC t_0 and β distributions 69
4.64 Comparison of calibrated MS β with treated MC 69
4.65 Comparison of detector resolution in data, $Z \to \mu\mu$ MC and signal MC 70
4.66 Comparison of untreated and treated signal MC β 71

5.1 ISR reweighting for sample with $m_{\tilde{g}} = 2000$ GeV 75
5.2 Comparison of the ISR spectrum of 1000 GeV gluinos, bottom and top squarks 76
5.3 dE/dx as function of momentum with superimposed fits 77
5.4 dE/dx as function of momentum for three stau mass points 78
5.5 $\beta\gamma$ distributions for muons and different signals on truth 78
5.6 Comparison of calibrated Tile Calorimeter β and smeared MC 78
5.7 Combined β distribution and uncertainty σ_β 79
5.8 β distributions for muons and different signals on truth 79
5.9 E_T^{miss} trigger onsets for data and MC 80
5.10 Efficiency of all employed E_T^{miss} triggers in signal MC 81
5.11 Uncalibrated RPC timing in data compared to untreated MC 82

5.12 Absolute RPC trigger times in data and simulation 82
5.13 Trigger efficiencies as function of β in data and MC and scale factors 83
5.14 β spectrum before and after single-muon trigger efficiency scaling 83
5.15 Trigger onsets from MC for all signal types and three η regions 84
5.16 Efficiency of all employed single-muon triggers in signal MC 84
5.17 Efficiency of the trigger selection in signal MC for all periods 85
5.18 Illustration of the transverse impact parameter 86
5.19 Selection efficiency of the LOOSE selection for all chargino masses 87
5.20 Selection efficiency of the TIGHT selection for all stau masses 87
5.21 Selection efficiency of the MS-agnostic selection for all R-hadron masses 88
5.22 Measured momentum of tracks reconstructed with MuGirlStau 91
5.23 β_{ToF} and momentum PDF for the two-candidate stau and chargino signal regions 92
5.24 $\beta\gamma_{dE/dx}$ PDF in the MS-agnostic analysis 92
5.25 Background estimate for stable stau signal regions 93
5.26 Background estimate for chargino signal regions 93
5.27 Background estimate for MS-agnostic gluino R-hadron searches 94
5.28 Background estimate for full-detector R-hadron search in the LOOSE selection 95
5.29 Background estimate for full-detector R-hadron search in the ID+Calo selection 96
5.30 Fitted E_T^{miss} trigger onsets for two exemplary triggers 98
5.31 Systematic E_T^{miss} trigger efficiency uncertainties for gluinos and staus 99
5.32 Systematic uncertainties on the single-muon trigger efficiency 100
5.33 Systematic uncertainties on the ISR modelling for R-hadrons 100
5.34 Deviations from nominal MC by MadGraph parameter variations for charginos and staus 101
5.35 MDT β distributions with scaled MC for systematics estimation 102
5.36 RPC β distributions with uncorrected and scaled MC for systematics estimation 103
5.37 Reconstruction efficiency of the MuGirlStau algorithm in data and MC 103
5.38 95% CL upper cross-section limits for R-hadrons in the MS-agnostic analysis 106
5.39 95% CL upper cross-section limits for R-hadrons in the full-detector analysis 106
5.40 95% CL upper cross-section limits for stable staus and charginos 108

6.1 Single-muon trigger efficiency as function of the particles β 111
6.2 Event topology of the late-muon trigger 112
6.3 Late-muon trigger efficiency for different trigger thresholds 112
6.4 L1 late-muon trigger efficiency as function of β 114
6.5 L1 late-muon trigger efficiency as function of gluino mass 115

7.1 Split SUSY $\tan\beta$ and m_S values consistent with the Higgs mass 118

A.1 Size reduction in derivations 123
A.2 Original composition of SUSY8 124
A.3 Composition of SUSY8 during 2015/2016 124

B.1 Good resolution MDT hits in z–y projection 125
B.2 Good resolution MDT hits in x–y projection 125
B.3 Bad resolution MDT hits in z–y projection 126
B.4 Bad resolution MDT hits in x–y projection 126
B.5 Low-statistics RPC strips in x–y projection 127
B.6 Low-statistics RPC strips in z–y projection 127

B.7 High-statistics RPC strips in x–y projection 128
B.8 High-statistics RPC strips in z–y projection 128
B.9 Timing uncertainty $\sigma_{t_0}^i$ as function of t_0 129
B.10 Timing uncertainty $\sigma_{t_0}^i$ as function of the ToF 129
B.11 t_0 distributions before and after run correction 130
B.12 Summary of MDT t_0 distributions 130
B.13 Summary of RPC t_0 distributions 131
B.14 MDT β as function of the pseudorapidity η 131
B.15 RPC β as function of the pseudorapidity η 131
B.16 MS β as function of the pseudorapidity η 132
B.17 MDT σ_β as function of the pseudorapidity η 132
B.18 RPC σ_β as function of the pseudorapidity η 132
B.19 MS σ_β as function of the pseudorapidity η 133
B.20 Reweighting and sharpening for toy signal 133

C.1 Untreated RPC t_0 for η and ϕ strips 135
C.2 RPC timing detector granularity 135
C.3 Decomposition of RPC simulated t_0 distributions 136
C.4 Decomposition of RPC simulated t_0 distribution in one chamber 136
C.5 RPC η strip pseudo-propagation time 136
C.6 RPC ϕ strip pseudo-propagation time 136
C.7 Propagation time as function of r, x, y and z 137
C.8 Schematic view of a two-unit RPC chamber 138
C.9 Propagation time as function of z along a sequence of BML chambers 138

D.1 Readout ticks for strip with shifted mean 139
D.2 Position of strips with shifted means 140
D.3 Position of strips with large widths 141

E.1 Comparison of muon trigger onsets determined by two methods 143
E.2 Fitted E_T^{miss} trigger onsets for remaining two triggers 145
E.3 Systematic E_T^{miss} trigger efficiency uncertainties for all samples 145
E.4 Deviations from nominal MC by MadGraph parameter variations for R-hadrons 145
E.5 Signal selection efficiency dependency on pileup 146
E.6 Average number of interactions before and after application of the PRW tool 147
E.7 Ratio of expected and observed event yields for all selections and runs 148

F.1 One barrel MS sector with chamber naming and dimensions 149
F.2 Cut through the MS showing layout in a large sector 150
F.3 Cut through the MS showing the layout in a small sector 151
F.4 Layout of the detector in the feet region 152

List of Tables

2.1 Fundamental forces of nature with range and strength 3
2.2 The free parameters of the SM 10
2.3 Overview of SUSY particles 13
2.4 Summary of lower slepton mass limits 21
2.5 Summary of lower squark mass limits 22
2.6 Summary of lower gluino mass limits 22
2.7 Summary of lower chargino mass limits 23

3.1 LHC beam energies since begin of physics operation 25
3.2 Summary of the basic characteristics of the LHC 29
3.3 Overview of the naming of stations in the MS 36

4.1 RPC online-timing calibration constants 45

5.1 Summary of all R-hadron MC samples 73
5.2 Summary of all stable chargino MC samples 74
5.3 Summary of all stable stau MC samples 75
5.4 Modus of removal of clusters for Pixel dE/dx calculation 77
5.5 Lowest unprescaled E_T^{miss} and single-muon trigger thresholds 80
5.6 Cut-flow of the TIGHT selection in the full-detector search 87
5.7 Cut-flow for the MS-agnostic analysis 88
5.8 Signal regions of the R-hadrons searches 89
5.9 Signal regions of the stable stau searches 90
5.10 Signal regions of the chargino searches 90
5.11 Summary of p, β_{ToF}, $\beta\gamma_{dE/dx}$ and $|\eta|$ cuts for all signal regions 90
5.12 Definition of the sideband regions for PDF evaluation in all signal regions 90
5.13 List of systematic uncertainties on signal cross section predictions 97
5.14 Relative change through 1σ E_T^{miss} onset fit parameter variations in data 98
5.15 Relative change through 1σ E_T^{miss} onset fit parameter variations in MC 99
5.16 List of systematic E_T^{miss} trigger uncertainties for all particles 99
5.17 List of systematic single-muon trigger uncertainties for all particles 99
5.18 List of systematic uncertainties due to ISR modelling 101
5.19 List of systematic uncertainties due to the MS β estimation 102
5.20 List of systematic uncertainties due to the TileCal β estimation 103
5.21 Definitions of alternative sidebands for PDF creation 104
5.22 Overview of the systematic uncertainties on the background estimate 104
5.23 Summary of all systematic uncertainties 105
5.24 Final event yields for the MS-agnostic R-hadron searches 105
5.25 Final event yields for the full-detector R-hadron searches 107
5.26 Final event yields for the stable stau searches 107
5.27 Final event yields for the stable chargino searches 108

5.28 Summary of 95% CL lower-mass limits of the last three ATLAS SMP searches 109

E.1 Cut-flow of the LOOSE selection in the full-detector search 144
E.2 Cut-flow of the ID+CALO selection in the full-detector search 144

List of Abbreviations

ALICE	A large ion collider experiment
AMSB	Anomaly-mediated supersymmetry breaking
AOD	Analysis object data
ATLAS	A toroidal Large Hadron Collider apparatus
BC	Bunch crossing
CERN	European organization for nuclear research
CL	Confidence limit
CM	Coincidence matrix
CMB	Cosmic microwave background
CMS	Compact muon solenoid
CMSSM	Constrained minimal supersymmetric Standard Model
CP	Charge-parity
CR	Control region
CSC	Cathode strip chamber
CTP	Central trigger processor
DxAOD	Derived analysis object data
EF	Event filter
EM	Electromagnetic
EWT	Electroweak theory
FCal	Forward calorimeter
FSR	Final-state radiation
GMSB	Gauge-mediated supersymmetry breaking
GRL	Good-runs list
GUT	Grand unified theory
HIP	Highly ionizing particle
HLT	High level trigger
IBL	Insertable B-layer
ID	Inner Detector
IP	Interaction point
ISR	Initial-state radiation
KK	Kaluza-Klein
L1	Level-1 trigger
L1A	Level-1 trigger accept
LEP	Large electron-positron collider

LHC	Large Hadron Collider
LHCb	Large Hadron Collider beauty
LHCf	Large Hadron Collider forward
LINAC	Linear accelerator
LLP	Long-lived particle
LSP	Lightest supersymmetric particle
MDT	Monitored drift tubes
MIP	Minimum ionizing particle
MoEDAL	Monopole and exotics detector at the Large Hadron Collider
MS	Muon spectrometer
mSMP	Metastable massive particle
MSSM	Minimal supersymmetric Standard Model
mSUGRA	minimal supergravity
MuCTPI	Muon-to-Central-Trigger-Processor Interface
NLL	Next-to-leading logarithmic (accuracy)
NLO	Next-to-leading order
NLSP	Next-to-lightest supersymmetric particle
PDF	Probability density function
pdf	parton distribution function
PRW	Pileup reweighting
PS	Proton Synchrotron
PSB	Proton Synchrotron Booster
PV	Primary vertex
QCD	Quantum Chromodynamics
QED	Quantum electrodynamics
qSMP	Quasi-stable massive particle
RF	Radiofrequency
RMS	Root mean square
RoI	Region of interest
RPC	Resistive plate chambers
SCT	Semiconductor tracker
SM	Standard Model (of particle physics)
SMP	Stable massive particle
SPS	Super Proton Synchrotron
SR	Signal region
SSUSY	Split SUSY
SUSY	Supersymmetry
SVD	Singular value decomposition

TGC	Thin gap chambers
TOB	Trigger object
ToF	Time of flight
ToT	Time over threshold
TOTEM	Total elastic and diffractive cross section measurement
TRT	Transition radiation tracker
UED	Universal extra dimensions
WIMP	Weakly interacting massive particle
xAOD	Analysis object data

Bibliography

[1] **ATLAS** Collaboration M. Aaboud *et. al.* *"Search for heavy long-lived charged R-hadrons with the ATLAS detector in 3.2 fb*$^{-1}$ *of proton–proton collision data at* $\sqrt{s} = 13$ *TeV"*, *Phys. Lett.* **B760** (2016) 647–665 `arXiv:1606.05129 [hep-ex]`.

[2] **ATLAS** Collaboration *"Search for heavy long-lived charged particles with the ATLAS detector in 36.1 fb*$^{-1}$ *of proton–proton collision data at* $\sqrt{s} = 13$ *TeV", forthcoming, 2018.*

[3] J. J. Heinrich *"Search for stable massive SUSY particles with the ATLAS detector"*, SUSY 2016, Melbourne, Australia, ATL-PHYS-SLIDE-2016-595, Sep, 2016.

[4] ATLAS Stand-Alone Event Displays `https://twiki.cern.ch/twiki/bin/view/AtlasPublic/EventDisplayStandAlone`, retrieved: July 26, 2017.

[5] D. Geerts *The single top t-channel fiducial cross section at 8 TeV measured with the ATLAS detector.* PhD thesis University of Amsterdam 2015.

[6] `https://i.ytimg.com/vi/2bwiO-Beuwo/maxresdefault.jpg`, retrieved: July 10, 2017.

[7] A. Trevillion and G. Priddle, *Salters Horners Advanced Physics A2.* Heinemann Educational Publishers 2001.

[8] S. L. Glashow *"Partial-Symmetries of Weak Interactions"*, *Nucl. Phys.* **22** (1961) 579-588.

[9] F. Englert and R. Brout, *"Broken Symmetry and the Mass of Gauge Vector Mesons"*, *Phys. Rev. Lett.* **13** (1964) 321–323.

[10] P. W. Higgs *"Broken symmetries, massless particles and gauge fields"*, *Phys. Lett.* **12** (1964) 132–133.

[11] P. W. Higgs *"Broken Symmetries and the Masses of Gauge Bosons"*, *Phys. Rev. Lett.* **13** (1964) 508–509.

[12] G. S. Guralnik, C. R. Hagen and T. W. B. Kibble, *"Global Conservation Laws and Massless Particles"*, *Phys. Rev. Lett.* **13** (1964) 585–587.

[13] S. Weinberg *"A Model of Leptons"*, *Phys. Rev. Lett.* **19** (1967) 1264-1266.

[14] A. Salam *"Weak and Electromagnetic Interactions"*, *Conf.Proc.* **C680519** (1968) 367–377.

[15] **ATLAS** Collaboration *"Observation of a New Particle in the Search for the Standard Model Higgs Boson with the ATLAS Detector at the LHC"*, *Phys. Lett.* **B 716** (2012) 1-29, `arXiv:1207.7214 [hep-ex]`.

[16] **CMS** Collaboration *"Observation of a New boson at a mass of* 125 *GeV with the CMS experiment at the LHC"*, *Phys. Lett.* **B 716** (2012) 30, `arXiv:1207.7235 [hep-ex]`.

[17] The NIST Reference on Constants, Units and Uncertainty `http://physics.nist.gov/cgi-bin/cuu/Value?e`, retrieved: July 08, 2017.

[18] M. Gonzalez-Garcia and Y. Nir, *"Neutrino Masses and Mixing: Evidence and Implications"*, *Rev. Mod. Phys.* **75** (2003) 345–402 `arXiv:hep-ph/0202058 [hep-ph]`.

[19] O. Eberhardt, G. Herbert, H. Lacker *et. al.* *"Impact of a Higgs boson at a mass of 126 GeV on the standard model with three and four fermion generations"*, *Phys. Rev. Lett.* **109** (2012) 241802, `arXiv:1209.1101 [hep-ph]`.

[20] Standard Model of particle physics Wikipedia `https://en.wikipedia.org/wiki/Standard_Model`, retrieved: July 08, 2017.

[21] D. J. Griffiths *Introduction to elementary particles; 2nd rev. version.* Physics textbook. Wiley New York, NY 2008.

[22] A. Pich *"The Standard Model of Electroweak Interactions"*, `arXiv:0502010v1 [hep-ph]`.

[23] F. Halzen and A. D. Martin, *Quarks and Leptons: An Introductory Course in Modern Particle Physics*. John Wiley and sons 1984. first edition.

[24] F. Wilczek *"QCD Made Simple"*, *Physics Today* (2000) S-0031-9228-0008-010-8 22–28.

[25] H. Fritzsch *"QCD: 20 years later"*, in *QCD 20 Years Later: Proceedings, Workshop, Aachen, Germany, June 9-13, 1992* pp. 827–852 1992.

[26] V. Martin *"Particle Physics"*, Lecture slides 2013 `http://www2.ph.ed.ac.uk/~vjm/Lectures/SH_IM_Particle_Physics_2013_files/Jets-Lecture10.pdf`.

[27] K. Olive *et. al. Chin. Phys.* **C38** (2014) 090001. Particle Data Group.

[28] J. Beringer *et. al. Phys. Rev.* **D86** (2012) 010001. Particle Data Group.

[29] **Particle Data Group** Collaboration C. Patrignani, K. Agashe, G. Aielli *et. al. "Review of Particle Physics, 2016-2017"*, *Chin. Phys. C* **40** (2016) 10 100001. 1808 p.

[30] T. Aoyama, M. Hayakawa, T. Kinoshita and M. Nio, *"Tenth-Order QED Contribution to the Electron g-2 and an Improved Value of the Fine Structure Constant"*, *Phys. Rev. Lett.* **109** (2012) 111807 `arXiv:1205.5368 [hep-ph]`.

[31] D. Hanneke, S. Fogwell and G. Gabrielse, *"New Measurement of the Electron Magnetic Moment and the Fine Structure Constant"*, *Phys. Rev. Lett.* **100** (Mar, 2008) 120801.

[32] D. Hanneke, S. Fogwell Hoogerheide and G. Gabrielse, *"Cavity control of a single-electron quantum cyclotron: Measuring the electron magnetic moment"*, *Phys. Rev. A* **83** (May, 2011) 052122.

[33] **UA1** Collaboration *"Experimental observation of isolated large transverse energy electrons with associated missing energy at $\sqrt{s} = 540$ GeV"*, *Physics Letters B* **122** (1983) 1 103 – 116.

[34] **UA2** Collaboration *"Observation of single isolated electrons of high transverse momentum in events with missing transverse energy at the CERN pp collider"*, *Physics Letters B* **122** (1983) 5-6 476 – 485.

[35] **UA1** Collaboration *"Experimental observation of lepton pairs of invariant mass around 95 GeV/c2 at the CERN SPS collider"*, *Physics Letters B* **126** (1983) 5 398 – 410.

[36] **UA2** Collaboration *"Evidence for $Z^0 \to e^+e^-$ at the CERN $\bar{p}p$ collider"*, *Physics Letters B* **129** (1983) 1-2 130 – 140.

[37] **CDF** Collaboration *"Observation of Top Quark Production in Pbar-P Collisions"*, *Phys. Rev. Lett.* **74** (1995) 2626–2631 `arXiv:hep-ex/9503002 [hep-ex]`.

[38] **DØ** Collaboration *"Observation of the Top Quark"*, *Phys. Rev. Lett.* **74** (1995) 2632–2637 `arXiv:hep-ex/9503003 [hep-ex]`.

[39] **ATLAS** Collaboration *"Observation of an Excess of Events in the Search for the Standard Model Higgs boson with the ATLAS detector at the LHC"*, Tech. Rep. ATLAS-CONF-2012-093 CERN Geneva Jul, 2012.

[40] **CMS** Collaboration *"Observation of a new boson with a mass near 125 GeV"*, Tech. Rep. CMS-PAS-HIG-12-020 CERN Geneva 2012.

[41] A. O. Sushkov, W. J. Kim, D. A. R. Dalvit and S. K. Lamoreaux, *"New Experimental Limits on Non-Newtonian Forces in the Micrometer Range"*, *Phys. Rev. Lett.* **107** (Oct, 2011) 171101.

[42] B. Schulz *"Review on the quantization of gravity"*, `arXiv:1409.7977 [gr-qc]`.

[43] R. P. Woodard *"How far are we from the quantum theory of gravity?"*, *Reports on Progress in Physics* **72** (2009) 12 126002.

[44] **ATLAS** Collaboration *"A Search for High Mass Diphoton Resonances in the Context of the Randall-Sundrum Model in $\sqrt{s} = 7$ TeV pp Collisions"*, Tech. Rep. ATLAS-CONF-2011-044 CERN Geneva Mar, 2011.

[45] **CMS** Collaboration *"Search for high-mass diphoton resonances in protonŰproton collisions at 13 TeV and combination with 8 TeV search"*, *Phys. Lett.* **B767** (2017) 147–170 `arXiv:1609.02507 [hep-ex]`.

[46] European Space Agency ESA `http://www.esa.int/spaceinimages/Images/2013/03/Planck_cosmic_recipe`, retrieved: July 09, 2017.

[47] E. Corbelli and P. Salucci, *"The Extended Rotation Curve and the Dark Matter Halo of M33"*, *Mon. Not. Roy. Astron. Soc.* **311** (2000) 441–447 `arXiv:astro-ph/9909252 [astro-ph]`.

[48] S. M. Faber and R. E. Jackson, *"Velocity dispersions and mass to light ratios for elliptical galaxies"*, *Astrophys. J.* **204** (1976) 668.

[49] X.-P. Wu, T. Chiueh, L.-Z. Fang and Y.-J. Xue, *"A comparison of different cluster mass estimates: consistency or discrepancy ?"*, *Mon. Not. Roy. Astron. Soc.* **301** (1998) 861 `arXiv:astro-ph/9808179 [astro-ph]`.

[50] **Planck** Collaboration P. A. R. Ade *et. al.* *"Planck 2013 results. I. Overview of products and scientific results"*, *Astron. Astrophys.* **571** (2014) A1 `arXiv:1303.5062 [astro-ph.CO]`.

[51] L. Bergström *"Nonbaryonic dark matter: Observational evidence and detection methods"*, *Rept. Prog. Phys.* **63** (2000) 793 `arXiv:hep-ph/0002126 [hep-ph]`.

[52] **WMAP** Collaboration E. Komatsu *et. al.* *"Five-Year Wilkinson Microwave Anisotropy Probe (WMAP) Observations: Cosmological Interpretation"*, *Astrophys. J. Suppl.* **180** (2009) 330–376 `arXiv:0803.0547 [astro-ph]`.

[53] The Spectrum of Riemannium `https://thespectrumofriemannium.files.wordpress.com/2013/07/neutrinos.jpg`, retrieved: July 10, 2017.

[54] **Super-Kamiokande** Collaboration Y. Ashie *et. al.* *"Evidence for an oscillatory signature in atmospheric neutrino oscillation"*, *Phys. Rev. Lett.* **93** (2004) 101801 `arXiv:hep-ex/0404034 [hep-ex]`.

[55] A. D. Sakharov *"Violation of CP Invariance, c Asymmetry, and Baryon Asymmetry of the Universe"*, *Pisma Zh. Eksp. Teor. Fiz.* **5** (1967) 32–35.

[56] M. B. Gavela, P. Hernandez, J. Orloff and O. Pene, *"Standard model CP violation and baryon asymmetry"*, *Mod. Phys. Lett.* **A9** (1994) 795–810 `arXiv:hep-ph/9312215 [hep-ph]`.

[57] M. B. Gavela, P. Hernandez, J. Orloff, O. Pene and C. Quimbay, *"Standard model CP violation and baryon asymmetry. Part 2: Finite temperature"*, *Nucl. Phys.* **B430** (1994) 382–426 `arXiv:hep-ph/9406289 [hep-ph]`.

[58] P. Huet and E. Sather, *"Electroweak baryogenesis and standard model CP violation"*, *Phys. Rev.* **D51** (1995) 379–394 `arXiv:hep-ph/9404302 [hep-ph]`.

[59] K. G. Wilson *"The Renormalization Group and Strong Interactions"*, *Phys. Rev.* **D3** (1971) 1818.

[60] M. Dine *"Naturalness Under Stress"*, *Ann. Rev. Nucl. Part. Sci.* **65** (2015) 43–62 `arXiv:1501.01035 [hep-ph]`.

[61] G. 't Hooft, C. Itzykson, A. Jaffe, H. Lehmann, P. K. Mitter, I. M. Singer and R. Stora, *"Recent Developments in Gauge Theories. Proceedings, Nato Advanced Study Institute, Cargese, France, August 26 - September 8, 1979"*, *NATO Sci. Ser. B* **59** (1980) pp.1–438.

[62] L. Susskind *"Dynamics of Spontaneous Symmetry Breaking in the Weinberg-Salam Theory"*, *Phys. Rev.* **D20** (1979) 2619–2625.

[63] C. Giganti, S. Lavignac and M. Zito, *"Neutrino oscillations: the rise of the PMNS paradigm"*, *Prog. Part. Nucl. Phys.* **98** (2018) 1–54 `arXiv:1710.00715 [hep-ex]`.

[64] R. K. Kaul and P. Majumdar, *"Cancellation of Quadratically Divergent Mass Corrections in Globally Supersymmetric Spontaneously Broken Gauge Theories"*, *Nucl. Phys.* **B199** (1982) 36.

[65] Yu. A. Golfand and E. P. Likhtman, *"Extension of the Algebra of Poincare Group Generators and Violation of p Invariance"*, *JETP Lett.* **13** (1971) 323–326. [Pisma Zh. Eksp. Teor. Fiz.13,452(1971)].

[66] D. V. Volkov and V. P. Akulov, *"Is the Neutrino a Goldstone Particle?"*, *Phys. Lett.* **46B** (1973) 109–110.

[67] J. Wess and B. Zumino, *"Supergauge Transformations in Four-Dimensions"*, *Nucl. Phys.* **B70** (1974) 39–50.

[68] J. Wess *"Supergauge invariant extension of quantum electrodynamics"*, *Nucl. Phys.* **B78** (1974) 1–13.

[69] S. Ferrara and B. Zumino, *"Supergauge Invariant Yang-Mills Theories"*, *Nucl. Phys.* **B79** (1974) 413.

[70] A. Salam and J. A. Strathdee, *"Supersymmetry and Nonabelian Gauges"*, *Phys. Lett.* **51B** (1974) 353–355.

[71] R. Haag, J. T. Lopuszánski and M. F. Sohnius, *"All possible generators of supersymmetries of the S-matrix"*, *Nucl. Phys. B* **88** (Nov, 1974) 257–74. 45 p.

[72] H. P. Nilles *"Supersymmetry, Supergravity and Particle Physics"*, *Phys. Rept.* **110** (1984) 1–162.

[73] P. Binetruy *Supersymmetry.* Oxford University Press 2006.

[74] S. P. Martin *"A Supersymmetry primer"*, `arXiv:hep-ph/9709356 [hep-ph]`. [Adv. Ser. Direct. High Energy Phys.18,1(1998)].

[75] M. Drees *"An Introduction to supersymmetry"*, in *Current topics in physics. Proceedings, Inauguration Conference of the Asia-Pacific Center for Theoretical Physics (APCTP), Seoul, Korea, June 4-10, 1996. Vol. 1, 2* 1996. `arXiv:hep-ph/9611409 [hep-ph]`.

[76] S. Dimopoulos, S. Raby and F. Wilczek, *"Supersymmetry and the Scale of Unification"*, *Phys. Rev.* **D24** (1981) 1681–1683.

[77] L. E. Ibanez and G. G. Ross, *"Low-Energy Predictions in Supersymmetric Grand Unified Theories"*, *Phys. Lett.* **105B** (1981) 439–442.

[78] W. J. Marciano and G. Senjanovic, *"Predictions of Supersymmetric Grand Unified Theories"*, *Phys. Rev.* **D25** (1982) 3092.

[79] V. Barger, J. Jiang, P. Langacker and T. Li, *"Gauge coupling unification in the standard model"*, *Phys. Lett.* **B624** (2005) 233–238 `arXiv:hep-ph/0503226 [hep-ph]`.

[80] `https://i.stack.imgur.com/3gARs.png`, retrieved: July 31, 2017.

[81] L. Girardello and M. T. Grisaru, *"Soft Breaking of Supersymmetry"*, *Nucl. Phys.* **B194** (1982) 65.

[82] D. J. H. Chung, L. L. Everett, G. L. Kane, S. F. King, J. D. Lykken and L.-T. Wang, *"The Soft supersymmetry breaking Lagrangian: Theory and applications"*, *Phys. Rept.* **407** (2005) 1–203 `arXiv:hep-ph/0312378 [hep-ph]`.

[83] L. Randall and R. Sundrum, *"A Large mass hierarchy from a small extra dimension"*, *Phys. Rev. Lett.* **83** (1999) 3370–3373 `arXiv:hep-ph/9905221 [hep-ph]`.

[84] L. Randall and R. Sundrum, *"An Alternative to compactification"*, *Phys. Rev. Lett.* **83** (1999) 4690–4693 `arXiv:hep-th/9906064 [hep-th]`.

[85] G. R. Farrar and P. Fayet, *"Phenomenology of the Production, Decay, and Detection of New Hadronic States Associated with Supersymmetry"*, *Phys. Lett.* **76B** (1978) 575–579.

[86] M. Lisanti *"Lectures on Dark Matter Physics"*, in *Proceedings, Theoretical Advanced Study Institute in Elementary Particle Physics: New Frontiers in Fields and Strings (TASI 2015): Boulder, CO, USA, June 1-26, 2015* pp. 399–446 2017. `arXiv:1603.03797 [hep-ph]`.

[87] S. P. Ahlen, F. T. Avignone, R. L. Brodzinski, A. K. Drukier, G. Gelmini and D. N. Spergel, *"Limits on Cold Dark Matter Candidates from an Ultralow Background Germanium Spectrometer"*, *Phys. Lett.* **B195** (1987) 603–608.

[88] D. O. Caldwell, R. M. Eisberg, D. M. Grumm, M. S. Witherell, B. Sadoulet, F. S. Goulding and A. R. Smith, *"Laboratory Limits on Galactic Cold Dark Matter"*, *Phys. Rev. Lett.* **61** (1988) 510.

[89] S. Weinberg *"Supersymmetry at Ordinary Energies. 1. Masses and Conservation Laws"*, *Phys. Rev.* **D26** (1982) 287.

[90] N. Sakai and T. Yanagida, *"Proton Decay in a Class of Supersymmetric Grand Unified Models"*, *Nucl. Phys.* **B197** (1982) 533.

[91] L. E. Ibáñez and G. G. Ross, *"Discrete gauge symmetries and the origin of baryon and lepton number conservation in supersymmetric versions of the standard model"*, *Nucl. Phys. B* **368** (1992) CERN-TH-6111-91 3–37.

[92] H. Baer and X. Tata, *Weak scale supersymmetry: From superfields to scattering events.* Cambridge University Press 2006.

[93] B. Dumont *Higgs, Supersymmetry and Dark Matter After Run I of the LHC.* Springer Theses 2017.

[94] H. A. Weber *Search for Supersymmetry in Hadronic Final States.* PhD thesis ETH Zurich 2015.

[95] N. Okada and H. M. Tran, *"125 GeV Higgs boson mass and muon $g-2$ in 5D MSSM"*, *Phys. Rev.* **D94** (2016) 7, 075016 `arXiv:1606.05329 [hep-ph]`.

[96] W. Beenakker, R. Hopker, M. Spira and P. Zerwas, *"Squark and gluino production at hadron colliders"*, *Nucl. Phys.* **B492** (1997) 51–103 `arXiv:hep-ph/9610490 [hep-ph]`.

[97] C. Borschensky, M. Krämer *et. al.* *"Squark and gluino production cross sections in pp collisions at $\sqrt{s}$ = 13, 14, 33 and 100 TeV"*, *Eur. Phys. J. C* **74** (Jul, 2014) 3174. 22 p.

[98] W. Beenakker, R. Hopker and P. M. Zerwas, *"SUSY QCD decays of squarks and gluinos"*, *Phys. Lett.* **B378** (1996) 159–166 `arXiv:hep-ph/9602378 [hep-ph]`.

[99] W. Beenakker, M. Klasen, M. Kramer, T. Plehn, M. Spira and P. M. Zerwas, *"The Production of charginos / neutralinos and sleptons at hadron colliders"*, *Phys. Rev. Lett.* **83** (1999) 3780–3783 `arXiv:hep-ph/9906298 [hep-ph]`. [Erratum: Phys. Rev. Lett.100,029901(2008)].

[100] J. A. Conley, J. S. Gainer, J. L. Hewett, M. P. Le and T. G. Rizzo, *"Supersymmetry Without Prejudice at the LHC"*, *Eur. Phys. J.* **C71** (2011) 1697 `arXiv:1009.2539 [hep-ph]`.

[101] G. F. Giudice and A. Romanino, *"Split supersymmetry"*, *Nucl. Phys.* **B699** (2004) 65–89 `arXiv:hep-ph/0406088 [hep-ph]`. [Erratum: Nucl. Phys.B706,487(2005)].

[102] N. Arkani-Hamed and S. Dimopoulos, *"Supersymmetric unification without low energy supersymmetry and signatures for fine-tuning at the LHC"*, *JHEP* **06** (2005) 073 `arXiv:hep-th/0405159 [hep-th]`.

[103] B. Carter *"Large number coincidences and the anthropic principle in cosmology"*, *IAU Symp.* **63** (1974) 291.

[104] S. Weinberg *"Anthropic Bound on the Cosmological Constant"*, *Phys. Rev. Lett.* **59** (Nov, 1987) 2607–2610.

[105] J. L. Hewett, B. Lillie, M. Masip and T. G. Rizzo, *"Signatures of long-lived gluinos in split supersymmetry"*, *JHEP* **09** (2004) 070 `arXiv:hep-ph/0408248 [hep-ph]`.

[106] G. F. Giudice and A. Strumia, *"Probing High-Scale and Split Supersymmetry with Higgs Mass Measurements"*, *Nucl. Phys.* **B858** (2012) 63–83 `arXiv:1108.6077 [hep-ph]`.

[107] C. F. Kolda *"Gauge mediated supersymmetry breaking: Introduction, review and update"*, *Nucl. Phys. Proc. Suppl.* **62** (1998) 266–275 `arXiv:hep-ph/9707450 [hep-ph]`.

[108] P. G. Mercadante, J. K. Mizukoshi and H. Yamamoto, *"Analysis of longlived slepton NLSP in GMSB model at linear collider"*, *Phys. Rev.* **D64** (2001) 015005 `arXiv:hep-ph/0010067 [hep-ph]`.

[109] G. F. Giudice and R. Rattazzi, *"Theories with gauge mediated supersymmetry breaking"*, *Phys. Rept.* **322** (1999) 419–499 `arXiv:hep-ph/9801271 [hep-ph]`.

[110] H. Dorn *"Conformal invariance in quantum field theory"*, Lecture slides 2014 `http://qft.physik.hu-berlin.de/˜dorn/cft-review.pdf`.

[111] L. Randall and R. Sundrum, *"Out of this world supersymmetry breaking"*, *Nucl. Phys.* **B557** (1999) 79–118 `arXiv:hep-th/9810155 [hep-th]`.

[112] G. F. Giudice, M. A. Luty, H. Murayama and R. Rattazzi, *"Gaugino mass without singlets"*, *JHEP* **12** (1998) 027 `arXiv:hep-ph/9810442 [hep-ph]`.

[113] A. Pomarol and R. Rattazzi, *"Sparticle masses from the superconformal anomaly"*, *JHEP* **05** (1999) 013 `arXiv:hep-ph/9903448 [hep-ph]`.

[114] F. E. Paige and J. D. Wells, *"Anomaly mediated SUSY breaking at the LHC"*, in *1st Les Houches Workshop on Physics at TeV Colliders (PhysTeV 1999) Les Houches, France, June 7-18* 1999. `arXiv:hep-ph/0001249 [hep-ph]`.

[115] S. Roy *"Linear collider signals of anomaly mediated supersymmetry breaking"*, in *Supersymmetry and unification of fundamental interactions. Proceedings, 9th International Conference, SUSY'01, Dubna, Russia, June 11-17, 2001* pp. 221–223 2001. `arXiv:hep-ph/0110330 [hep-ph]`.

[116] T. Appelquist, H.-C. Cheng and B. A. Dobrescu, *"Bounds on universal extra dimensions"*, *Phys. Rev.* **D64** (2001) 035002 `arXiv:hep-ph/0012100 [hep-ph]`.

[117] G. Servant and T. M. P. Tait, *"Is the lightest Kaluza-Klein particle a viable dark matter candidate?"*, *Nucl. Phys.* **B650** (2003) 391–419 `arXiv:hep-ph/0206071 [hep-ph]`.

[118] K. R. Dienes, E. Dudas and T. Gherghetta, *"Extra space-time dimensions and unification"*, *Phys. Lett.* **B436** (1998) 55–65 `arXiv:hep-ph/9803466 [hep-ph]`.

[119] I. Antoniadis *"A possible new dimension at a few TeV"*, *Phys. Lett. B* **246** (Jun, 1990) 377–384. 14 p.

[120] N. Arkani-Hamed and M. Schmaltz, *"Hierarchies without symmetries from extra dimensions"*, *Phys. Rev.* **D61** (2000) 033005 `arXiv:hep-ph/9903417 [hep-ph]`.

[121] Wikipedia: Kaluza-Klein theory
`https://en.wikipedia.org/wiki/Kaluza%E2%80%93Klein_theory`, retrieved: July 15, 2017.

[122] G. Bhattacharyya, A. Datta, S. K. Majee and A. Raychaudhuri, *"Exploring the Universal Extra Dimension at the LHC"*, *Nucl. Phys.* **B821** (2009) 48–64 `arXiv:0904.0937 [hep-ph]`.

[123] D. Hooper and S. Profumo, *"Dark matter and collider phenomenology of universal extra dimensions"*, *Phys. Rept.* **453** (2007) 29–115 `arXiv:hep-ph/0701197 [hep-ph]`.

[124] M. Citron, J. Ellis, F. Luo, J. Marrouche, K. Olive and K. de Vries, *"End of the CMSSM coannihilation strip is nigh"*, *Phys. Rev. D* **87** (Dec, 2012) 036012. 18 p. Comments: 33 pages, 19 pdf figures.

[125] E. L. Berger and Z. Sullivan, *"Lower limits on R parity violating couplings in supersymmetry"*, *Phys. Rev. Lett.* **92** (2004) 201801 `arXiv:hep-ph/0310001 [hep-ph]`.

[126] R. Barbier *et. al.* *"R-parity violating supersymmetry"*, *Phys. Rept.* **420** (2005) 1–202 `arXiv:hep-ph/0406039 [hep-ph]`.

[127] H. K. Dreiner *"An Introduction to explicit R-parity violation"*, `arXiv:hep-ph/9707435 [hep-ph]`. [Adv. Ser. Direct. High Energy Phys.21,565(2010)].

[128] M. Fairbairn, A. C. Kraan, D. A. Milstead, T. Sjostrand, P. Z. Skands and T. Sloan, *"Stable massive particles at colliders"*, *Phys. Rept.* **438** (2007) 1–63 `arXiv:hep-ph/0611040 [hep-ph]`.

[129] H. Baer, K.-m. Cheung and J. F. Gunion, *"A Heavy gluino as the lightest supersymmetric particle"*, *Phys. Rev.* **D59** (1999) 075002 `arXiv:hep-ph/9806361 [hep-ph]`.

[130] S. J. Gates, Jr. and O. Lebedev, *"Searching for supersymmetry in hadrons"*, *Phys. Lett.* **B477** (2000) 216–222 `arXiv:hep-ph/9912362 [hep-ph]`.

[131] N. Arkani-Hamed, S. Dimopoulos, G. F. Giudice and A. Romanino, *"Aspects of split supersymmetry"*, *Nucl. Phys.* **B709** (2005) 3–46 `arXiv:hep-ph/0409232 [hep-ph]`.

[132] A. Kusenko and M. E. Shaposhnikov, *"Supersymmetric Q balls as dark matter"*, *Phys. Lett.* **B418** (1998) 46–54 `arXiv:hep-ph/9709492 [hep-ph]`.

[133] D. Bazeia, M. A. Marques and R. Menezes, *"Exact solutions, energy and charge of stable Q-balls"*, *Eur. Phys. J.* **C76** (2016) 5, 241 `arXiv:1512.04279 [hep-th]`.

[134] J. Schwinger *"Magnetic Charge and Quantum Field Theory"*, *Phys. Rev.* **144** (Apr, 1966) 1087–1093.

[135] B. Koch, M. Bleicher and H. Stoecker, *"Black Holes at LHC?"*, *J. Phys.* **G34** (2007) S535–542 `arXiv:hep-ph/0702187 [HEP-PH]`.

[136] Energy Loss Distribution of charged particles in silicon layers

`http://meroli.web.cern.ch/meroli/lecture_stragglingfunction.html`, retrieved: August 02, 2017.

[137] A. C. Kraan *"Interactions of heavy stable hadronizing particles"*, *Eur. Phys. J.* **C37** (2004) 91–104 `arXiv:hep-ex/0404001 [hep-ex]`.

[138] R. Mackeprang and A. Rizzi, *"Interactions of Coloured Heavy Stable Particles in Matter"*, *Eur. Phys. J.* **C50** (2007) 353–362 `arXiv:hep-ph/0612161 [hep-ph]`.

[139] A. Kalinovskii, N. Mokhov and Y. Nikitin, *Passage of High-Energy Particles through Matter*. American Institute of Physics 1989. Translation Series.

[140] A. Policicchio *"Searches for highly ionizing particles in ATLAS and CMS"*, Tech. Rep. ATL-PHYS-PROC-2015-084 CERN Geneva Sep, 2015.

[141] **ATLAS** Collaboration G. Aad *et. al.* *"Search for magnetic monopoles and stable particles with high electric charges in 8 TeV pp collisions with the ATLAS detector"*, *Phys. Rev.* **D93** (2016) 5, 052009 `arXiv:1509.08059 [hep-ex]`.

[142] M. Drees and X. Tata, *"Signals for heavy exotics at hadron colliders and supercolliders"*, *Phys. Lett. B* **252** (Jul, 1990) 695–702. 18 p.

[143] U. Sarid and S. D. Thomas, *"Mesino - anti-mesino oscillations"*, *Phys. Rev. Lett.* **85** (2000) 1178–1181 `arXiv:hep-ph/9909349 [hep-ph]`.

[144] **SUSY Working Group** Collaboration R. L. Culbertson *et. al.* *"Low scale and gauge mediated supersymmetry breaking at the Fermilab Tevatron Run II"*, `arXiv:hep-ph/0008070 [hep-ph]`.

[145] R. Mackeprang and D. Milstead, *"An Updated Description of Heavy-Hadron Interactions in GEANT-4"*, *Eur. Phys. J.* **C66** (2010) 493–501 `arXiv:0908.1868 [hep-ph]`.

[146] Y. R. de Boer, A. B. Kaidalov, D. A. Milstead and O. I. Piskounova, *"Interactions of Heavy Hadrons using Regge Phenomenology and the Quark Gluon String Model"*, *J. Phys.* **G35** (2008) 075009 `arXiv:0710.3930 [hep-ph]`.

[147] A. Mafi and S. Raby, *"An Analysis of a heavy gluino LSP at CDF: The Heavy gluino window"*, *Phys. Rev.* **D62** (2000) 035003 `arXiv:hep-ph/9912436 [hep-ph]`.

[148] **ATLAS** Collaboration *"Search for long-lived stopped R-hadrons decaying out-of-time with pp collisions using the ATLAS detector"*, *Phys. Rev.* **D88** (2013) 11, 112003 `arXiv:1310.6584 [hep-ex]`.

[149] **CMS** Collaboration V. Khachatryan *et. al.* *"Search for Stopped Gluinos in pp collisions at $\sqrt{s} = 7$ TeV"*, *Phys. Rev. Lett.* **106** (2011) 011801 `arXiv:1011.5861 [hep-ex]`.

[150] A. Arvanitaki, S. Dimopoulos, A. Pierce, S. Rajendran and J. G. Wacker, *"Stopping gluinos"*, *Phys. Rev.* **D76** (2007) 055007 `arXiv:hep-ph/0506242 [hep-ph]`.

[151] A. Arvanitaki, C. Davis, P. W. Graham, A. Pierce and J. G. Wacker, *"Limits on split supersymmetry from gluino cosmology"*, *Phys. Rev.* **D72** (2005) 075011 `arXiv:hep-ph/0504210 [hep-ph]`.

[152] K. Jedamzik *"Big bang nucleosynthesis constraints on hadronically and electromagnetically decaying relic neutral particles"*, *Phys. Rev.* **D74** (2006) 103509 `arXiv:hep-ph/0604251 [hep-ph]`.

[153] W. Buchmuller, K. Hamaguchi, M. Ibe and T. T. Yanagida, *"Eluding the BBN constraints on the stable gravitino"*, *Phys. Lett.* **B643** (2006) 124–126 `arXiv:hep-ph/0605164 [hep-ph]`.

[154] F. D. Steffen *"Gravitino dark matter and cosmological constraints"*, *JCAP* **0609** (2006) 001 `arXiv:hep-ph/0605306 [hep-ph]`.

[155] W. Hu and J. Silk, *"Thermalization constraints and spectral distortions for massive unstable relic particles"*, *Phys. Rev. Lett.* **70** (1993) 2661–2664.

[156] **ALEPH** Collaboration *"Search for sleptons in e^+e^- collisions at centre-of-mass energies up to 184 GeV"*, *Phys. Lett. B* **433** (May, 1998) 176. 18 p.

[157] **DELPHI** Collaboration *"Search for Heavy Stable and Long-Lived Particles in e^+e^- Collisions at $\sqrt{s}$=189 GeV"*, *Phys. Lett. B* **478** (Jan, 2000) 65–72. 9 p.

[158] **L3** Collaboration M. Acciarri *et. al.* *"Search for scalar leptons in e+ e- collisions at $\sqrt{s}$=183 GeV"*, *Phys. Lett.* **B456** (1999) 283–296.

[159] **OPAL** Collaboration *"Search for stable and long-lived massive charged particles in e+ e- collisions at $\sqrt{s}$=130 GeV to 209 GeV"*, *Phys. Lett.* **B572** (2003) 8–20 `arXiv:hep-ex/0305031 [hep-ex]`.

[160] **ATLAS** Collaboration G. Aad *et. al.* *"Searches for heavy long-lived charged particles with the ATLAS detector in proton-proton collisions at $\sqrt{s} = 8$ TeV"*, *JHEP* **01** (2015) 068 `arXiv:1411.6795 [hep-ex]`.

[161] **CMS** Collaboration V. Khachatryan *et. al.* *"Search for long-lived charged particles in proton-proton collisions at $\sqrt{s}$=13 TeV"*, *Phys. Rev.* **D94** (2016) 11, 112004 `arXiv:1609.08382 [hep-ex]`.

[162] **LHCb** Collaboration R. Aaij *et. al.* *"Search for long-lived heavy charged particles using a ring imaging Cherenkov technique at LHCb"*, *Eur. Phys. J.* **C75** (2015) 12, 595 `arXiv:1506.09173 [hep-ex]`.

[163] **D0** Collaboration *"Search for charged massive long-lived particles at $\sqrt{s} = 1.96$ TeV"*, *Phys. Rev.* **D87** (2013) 5, 052011 `arXiv:1211.2466 [hep-ex]`.

[164] **ALEPH** Collaboration *"Search for stable hadronizing squarks and gluinos in e^+e^- collisions up to $\sqrt{s}$ = 209 GeV"*, *Eur. Phys. J. C* **31** (May, 2003) 327–342. 30 p.

[165] **DELPHI** Collaboration *"Search for an LSP gluino at LEP with the DELPHI detector"*, *Eur. Phys. J. C* **26** (Aug, 2002) 505–525. 33 p. 36 pages, 19 figures Report-no: CERN-EP/2002-076 Journal-ref: Eur. Phys. J. C 26 (2003) 505-525.

[166] **CDF** Collaboration T. Aaltonen *et. al.* *"Search for Long-Lived Massive Charged Particles in 1.96 TeV $\bar{p}p$ Collisions"*, *Phys. Rev. Lett.* **103** (2009) 021802 `arXiv:0902.1266 [hep-ex]`.

[167] **ATLAS** Collaboration *"Search for metastable heavy charged particles with large ionization energy loss in pp collisions at $\sqrt{s} = 13$ TeV using the ATLAS experiment"*, *Phys. Rev.* **D93** (2016) 11, 112015 `arXiv:1604.04520 [hep-ex]`.

[168] **ATLAS** Collaboration *"Search for metastable heavy charged particles with large ionisation energy loss in pp collisions at $\sqrt{s} = 8$ TeV using the ATLAS experiment"*, *Eur. Phys. J.* **C75** (2015) 9, 407 `arXiv:1506.05332 [hep-ex]`.

[169] **CMS** Collaboration S. Chatrchyan *et. al.* *"Searches for long-lived charged particles in pp collisions at $\sqrt{s}$=7 and 8 TeV"*, *JHEP* **07** (2013) 122 `arXiv:1305.0491 [hep-ex]`.

[170] **CMS** Collaboration *"Search for Decays of Stopped Long-Lived Particles Produced in Proton–Proton Collisions at $\sqrt{s} = 8$ TeV"*, *Eur. Phys. J.* **C75** (2015) 4, 151 `arXiv:1501.05603 [hep-ex]`.

[171] **DELPHI** Collaboration P. Abreu *et. al.* *"Update of the search for charginos nearly mass-degenerate with the lightest neutralino"*, *Phys. Lett.* **B485** (2000) 95–106 `arXiv:hep-ex/0103035 [hep-ex]`.

[172] **L3** Collaboration M. Acciarri *et. al.* *"Search for charginos with a small mass difference with the lightest supersymmetric particle at $\sqrt{S}$ = 189-GeV"*, *Phys. Lett.* **B482** (2000) 31–42 `arXiv:hep-ex/0002043 [hep-ex]`.

[173] **D0** Collaboration V. M. Abazov *et. al.* *"Search for Long-Lived Charged Massive Particles with the D0 Detector"*, *Phys. Rev. Lett.* **102** (2009) 161802 `arXiv:0809.4472 [hep-ex]`.

[174] **CMS** Collaboration V. Khachatryan *et. al.* *"Constraints on the pMSSM, AMSB model and on other models from the search for long-lived charged particles in proton-proton collisions at sqrt(s) = 8 TeV"*, *Eur. Phys. J.* **C75** (2015) 7, 325 `arXiv:1502.02522 [hep-ex]`.

[175] P. Verkerk, G. Grynberg, B. Pichard, M. Spiro, S. Zylberajch, M. E. Goldberg and P. Fayet, *"Search for superheavy hydrogen in sea water"*, *Phys. Rev. Lett.* **68** (Feb, 1992) 1116–1119.

[176] T. Yamagata, Y. Takamori and H. Utsunomiya, *"Search for anomalously heavy hydrogen in deep sea water at 4000 m"*, *Phys. Rev. D* **47** (Feb, 1993) 1231–1234.

[177] R. Boyd and M. Caffee, *"A search for stable strangelets in helium"*, *Nuclear Physics B - Proceedings Supplements* **24** (1991) 2 195 – 198.

[178] C. M. Stevens, J. P. Schiffer and W. Chupka, *"Search for fractionally charged particles in lunar soil"*, *Phys. Rev. D* **14** (Aug, 1976) 716–727.

[179] K. Han, J. Ashenfelter, A. Chikanian, W. Emmet, L. E. Finch, A. Heinz, J. Madsen, R. D. Majka, B. Monreal and J. Sandweiss, *"Search for stable Strange Quark Matter in lunar soil"*, *Phys. Rev. Lett.* **103** (2009) 092302 `arXiv:0903.5055 [nucl-ex]`.

[180] W. G. Jones *et. al. "Searches for fractional electric charge in meteorite samples"*, *Zeitschrift für Physik C Particles and Fields* **43** (Sep, 1989) 349–355.

[181] S. Burdin, M. Fairbairn, P. Mermod, D. Milstead, J. Pinfold, T. Sloan and W. Taylor, *"Non-collider searches for stable massive particles"*, *Phys. Rept.* **582** (2015) 1–52 `arXiv:1410.1374 [hep-ph]`.

[182] T. Saito, Y. Hatano, Y. Fukada and H. Oda, *"Is there strange-quark matter in galactic cosmic rays?"*, *Phys. Rev. Lett.* **65** (Oct, 1990) 2094–2097.

[183] `http://images.techtimes.com/data/images/full/206669/cern-lhc.jpg`, retrieved: June 23, 2017.

[184] O. S. Brüning, P. Collier, P. Lebrun, S. Myers, R. Ostojic, J. Poole and P. Proudlock, *LHC Design Report: Vol. I The LHC Main Ring*. CERN Geneva 2004.

[185] O. S. Brüning, P. Collier, P. Lebrun, S. Myers, R. Ostojic, J. Poole and P. Proudlock, *LHC Design Report: Vol. II The LHC Infrastructure and General Services*. CERN Geneva 2004.

[186] O. S. Brüning, P. Collier, P. Lebrun, S. Myers, R. Ostojic, J. Poole and P. Proudlock, *LHC Design Report: Vol. III The LHC Injector Chain*. CERN Geneva 2004.

[187] *LEP design report*. CERN Geneva 1983. By the LEP Injector Study Group.

[188] CERN *ECFA-CERN Workshop on Large Hadron Collider in the LEP Tunnel* , Geneva, CERN 1984.

[189] M. Srednicki *Quantum Field Theory*. Cambridge University Press 2007. sixth edition.

[190] S. Holmes, R. S. Moore and V. Shiltsev, *"Overview of the Tevatron Collider Complex: Goals, Operations and Performance"*, *JINST* **6** (2011) T08001, `arXiv:1106.0909 [physics.acc-ph]`.

[191] *"Interim Summary Report on the Analysis of the 19 September 2008 Incident at the LHC"*, EDMS 973073 2008.

[192] L. Rosselet *"The Heavy-Ion Physics Programme with the ATLAS Detector"*, *J. Phys.: Conf. Ser.* **110** (2008) 032015.

[193] **ATLAS** Collaboration *"The ATLAS Experiment at the CERN Large Hadron Collider"*, *JINST* 3 (2008) S08003.

[194] **CMS** Collaboration *"The CMS experiment at the CERN LHC. The Compact Muon Solenoid experiment"*, *JINST* 3 (2008) S08004. 361 p. Also published by CERN Geneva in 2010.

[195] **ALICE** Collaboration *"The ALICE experiment at the CERN LHC. A Large Ion Collider Experiment"*, *JINST* 3 (2008) S08002. 259 p. Also published by CERN Geneva in 2010.

[196] **LHCb** Collaboration *"The LHCb Detector at the LHC"*, *JINST* 3 (2008) LHCb-DP-2008-001. CERN-LHCb-DP-2008-001 S08005. Also published by CERN Geneva in 2010.

[197] **LHCf** Collaboration O. Adriani *et. al. "The LHCf detector at the CERN Large Hadron Collider"*, *JINST* 3 (2008) S08006.

[198] **TOTEM** Collaboration G. Anelli *et. al. "The TOTEM experiment at the CERN Large Hadron Collider"*, *JINST* 3 (2008) S08007.

[199] J. L. Pinfold *"The MoEDAL Experiment at the LHC"*, *EPJ Web Conf.* **71** (2014) 00111.

[200] F. Fayette *"Strategies for precision measurements of the charge asymmetry of the W boson mass at the LHC within the ATLAS experiment"*. PhD thesis Paris U., VI-VII 2009.

[201] M. Wing *"Measurements of Deep Inelastic Scattering at HERA"*, `arXiv:1301.7572 [hep-ex]`.

[202] S. White *Determination of the absolute luminosity at the LHC*. PhD thesis University of Paris-Sud 2010.

[203] F. L. Sterzo *Search for the Standard Model Higgs Boson in the* $H \to ZZ^* \to l^+l^-q\bar{q}$ *final state with the ATLAS detector at the LHC*. PhD thesis University of Rome 2012.

[204] `https://twiki.cern.ch/twiki/bin/view/AtlasPublic/LuminosityPublicResultsRun2`, retrieved: June 24, 2017.

[205] *"LHC smashes luminosity record"*, *Physics World* **29** (2016) 12.

[206] B. Mikulec, A. Blas, C. Carli, A. Findlay, K. Hanke, G. Rumolo and J. Tan, *"LHC beams from the CERN PS Booster"*, *Proceedings of PAC09, Vancouver, BC, Canada* (2009).

[207] L. Baulieu *et. al. Theoretical Physics to Face the Challenge of LHC*. Oxford University Press Oxford, OX2 6DP 2015.

[208] L. Evans and P. Bryant, *"LHC Machine"*, *Journal of Instrumentation* **3** (2008) 08 S08001.

[209] W. Herr *"Effects of PACMAN bunches in the LHC"*, Tech. Rep. LHC-Project-Report-39. CERN-LHC-Project-Report-39 CERN Geneva Jul, 1996.

[210] W. Bartmann, M. Barnes, G. Kotzian, L. Stoel, F. M. Velotti, V. Vlachodimitropoulos and C. Wiesner, *"Measurement report on the LHC injection kicker ripple denition and maximum pulse length (MD 1268)"*, .

[211] R. Bruce *et. al. "LHC RUN 2: RESULTS AND CHALLENGES"*, in *Proceedings of HB2016, Malmö, Sweden Pre-Release Snapshot* 2016.

[212] R. Bailey and P. Collier, *"Standard Filling Schemes for Various LHC Operation Modes"*, Tech. Rep. LHC-PROJECT-NOTE-323 CERN Geneva Sep, 2003.

[213] S. Claudet *"Operation of the LHC Cryogenics system and interface with beam & machine operation"*, Presentation slides, Workshop on Accelerator Operations August, 2012 `http://www-conf.slac.stanford.edu/wao2012/talks/Wed_Aug8/Claudet_LHCCryo_WAO_2012_final.pdf`.

[214] **LHC Study Group** Collaboration T. S. Pettersson and P. Lefèvre, *"The Large Hadron Collider: conceptual design"*, Tech. Rep. CERN-AC-95-05-LHC Oct, 1995.

[215] M. Lamont *"LHC Performance in Run 2 and Beyond"*, *PoS* **LeptonPhoton2015** (2016) 001. 8 p.

[216] M. Lamont *"LHC Status and Outlook"*, Presentation slides, Charged 2016 October, 2016 `https://indico.cern.ch/event/497135/contributions/1176387/attachments/1347061/2031612/LHC-status-CHARGED16.pdf`.

[217] **ATLAS** Collaboration *ATLAS detector and physics performance: Technical Design Report Volume I*. Technical Design Report ATLAS. CERN Geneva 1999.

[218] **ATLAS** Collaboration *ATLAS detector and physics performance: Technical Design Report Volume II*. Technical Design Report ATLAS. CERN Geneva 1999.

[219] Homepage of the ATLAS Experiment: `http://www.atlas.ch`, retrieved: November 08, 2013.

[220] **ATLAS** Collaboration *ATLAS magnet system: Technical Design Report*. Technical Design Report ATLAS. CERN Geneva 1997.

[221] The ATLAS magnet system `http://atlas-magnet-dfs.web.cern.ch/atlas-magnet-dfs/`, retrieved: June 27, 2017.

[222] **ATLAS** Collaboration *ATLAS central solenoid: Technical Design Report*. Technical Design Report ATLAS. CERN Geneva 1997.

[223] **ATLAS** Collaboration *ATLAS barrel toroid: Technical Design Report*. Technical Design Report ATLAS. CERN Geneva 1997.

[224] **ATLAS** Collaboration *ATLAS end-cap toroids: Technical Design Report*. Technical Design Report ATLAS. CERN Geneva 1997.

[225] U. Egede *"The search for a standard model Higgs at the LHC and electron identification using transition radiation in the ATLAS tracker"*. PhD thesis Department of Physics, Lund University 1998.

[226] `https://en.wikipedia.org/wiki/Pseudorapidity`, retrieved: June 29, 2017.

[227] **ATLAS** Collaboration *ATLAS inner detector: Technical Design Report, 1*. Technical Design Report ATLAS. CERN Geneva 1997.

[228] **ATLAS** Collaboration *ATLAS inner detector: Technical Design Report, 2*. Technical Design Report ATLAS. CERN Geneva 1997.

[229] *"Track Reconstruction Performance of the ATLAS Inner Detector at $\sqrt{s} = 13$ TeV"*, Tech. Rep. ATL-PHYS-PUB-2015-018 CERN Geneva Jul, 2015.

[230] **ATLAS** Collaboration *Expected performance of the ATLAS experiment: detector, trigger and physics*. CERN Geneva 2009.

[231] **ATLAS** Collaboration *ATLAS pixel detector: Technical Design Report*. Technical Design Report ATLAS. CERN Geneva 1998.

[232] M. Capeans, G. Darbo, K. Einsweiller, M. Elsing, T. Flick, M. Garcia-Sciveres, C. Gemme, H. Pernegger, O. Rohne and R. Vuillermet, *"ATLAS Insertable B-Layer Technical Design Report"*, Tech. Rep. CERN-LHCC-2010-013. ATLAS-TDR-19 Sep, 2010.

[233] **ATLAS** Collaboration A. La Rosa *"The ATLAS Insertable B-Layer: from construction to operation"*, Tech. Rep. ATL-INDET-PROC-2016-004 CERN Geneva Oct, 2016.

[234] S. Tsuno *"Physics performance of the ATLAS pixel detector"*, *Journal of Instrumentation* **12** (2017) 01 C01025.

[235] F. Huegging *"The ATLAS Pixel Detector"*, *IEEE Trans.Nucl.Sci.* **53** (2006) 1732-1736, `arXiv:physics/0412138v2 [physics.ins-det]`.

[236] G. Aad *et. al. "ATLAS pixel detector electronics and sensors"*, *Journal of Instrumentation* **3** (2008) 07 P07007.

[237] **ATLAS** Collaboration *"dE/dx measurement in the ATLAS Pixel Detector and its use for particle identification"*, Tech. Rep. ATLAS-CONF-2011-016 CERN Geneva Mar, 2011.

[238] A. Ahmad, Z. Albrechtskirchinger, P. Allport *et. al. "The Silicon Microstrip Sensors of the ATLAS SemiConductor Tracker"*, Tech. Rep. ATL-INDET-PUB-2007-007. ATL-COM-INDET-2007-008. CERN-ATL-COM-INDET-2007-008. 1 CERN Geneva Mar, 2007.

[239] Y. Unno *"ATLAS silicon microstrip detector system (SCT)"*, *Nucl. Ins. a. Meth. in Phys. Res. A* **511** (2003) 58-63.

[240] **ATLAS TRT** Collaboration E. Abat, T. N. Addy, T. P. A. Akesson *et. al. "The ATLAS Transition Radiation Tracker (TRT) proportional drift tube: design and performance"*, *J. Instrum.* **3** (2008) P02013.

[241] **ATLAS TRT** Collaboration *"The ATLAS TRT electronics"*, *Journal of Instrumentation* **3** (2008) 06 P06007.

[242] K. Potamianos *"The upgraded Pixel detector and the commissioning of the Inner Detector tracking of the ATLAS experiment for Run-2 at the Large Hadron Collider"*, *PoS* **EPS-HEP2015** (2015) 261 `arXiv:1608.07850 [physics.ins-det]`.

[243] **ATLAS** Collaboration *ATLAS calorimeter performance: Technical Design Report*. Technical Design Report ATLAS. CERN Geneva 1996.

[244] **ATLAS** Collaboration *ATLAS liquid-argon calorimeter: Technical Design Report*. Technical Design Report ATLAS. CERN Geneva 1996.

[245] **ATLAS** Collaboration *ATLAS tile calorimeter: Technical Design Report*. Technical Design Report ATLAS. CERN Geneva 1996.

[246] S. Tavernier *Experimental Techniques in Nuclear and Particle Physics*. Springer-Verlag Berlin Heidelberg 2010.

[247] **ATLAS** Collaboration *"Readiness of the ATLAS Liquid Argon Calorimeter for LHC Collisions"*, *Eur. Phys. J.* **C70** (2010) 723-753, `arXiv:0912.2642 [physics.ins-det]`.

[248] A. Solodkov *"Performance of the ATLAS Tile Calorimeter"*, Tech. Rep. ATL-TILECAL-PROC-2015-024 CERN Geneva Dec, 2015.

[249] A. M. Henriques Correia *"The ATLAS Tile Calorimeter"*, Tech. Rep. ATL-TILECAL-PROC-2015-002 CERN Geneva Mar, 2015.

[250] B. Dowler, J. L. Pinfold *et. al.* *"Performance of the ATLAS Hadronic End-Cap Calorimeter in Beam Tests"*, Tech. Rep. ATL-LARG-2001-019 Max-Planck Inst. München Oct, 2001.

[251] **ATLAS** Collaboration G. Aad *et. al.* *"Commissioning of the ATLAS Muon Spectrometer with Cosmic Rays"*, *Eur. Phys. J.* **C70** (2010) 875–916 `arXiv:1006.4384 [physics.ins-det]`.

[252] **ATLAS** Collaboration *ATLAS muon spectrometer: Technical Design Report*. Technical Design Report ATLAS. CERN Geneva 1997. distribution.

[253] **ATLAS** Collaboration G. Aad *et. al.* *"Standalone vertex finding in the ATLAS muon spectrometer"*, *JINST* **9** (2014) P02001 `arXiv:1311.7070 [physics.ins-det]`.

[254] Y. Arai, B. Ball *et. al.* *"ATLAS Muon Drift Tube Electronics"*, *Journal of Instrumentation* **3** (2008) 09 P09001.

[255] **ATLAS Muon Group** Collaboration M. Livan *"Monitored drift tubes in ATLAS"*, Tech. Rep. ATL-M-PN-129 CERN Geneva Sep, 1996.

[256] F. Bauer, U. Bratzler *et. al.* *"Construction and Test of MDT Chambers for the ATLAS Muon Spectrometer"*, *Nucl. Instrum. Methods Phys. Res., A* **461** (Apr, 2016) 17–20. 5 p.

[257] J. Chapman, Y. Arai, R. Ball, G. Brandenburg, E. Hazen, J. Oliver and C. Posch, *"On-chamber readout system for the ATLAS MDT Muon Spectrometer"*, *IEEE Trans. Nucl. Sci.* **51** (2004) 2196–2200.

[258] G. Cattani and the RPC group, *"The Resistive Plate Chambers of the ATLAS experiment: performance studies"*, *Journal of Physics: Conference Series* **280** (2011) 1 012001.

[259] D. Boscherini *"Performance and operation of the ATLAS Resistive Plate Chamber system in LHC Run-1"*, Tech. Rep. ATL-MUON-PROC-2014-005. 12 CERN Geneva Sep, 2014.

[260] A. Aloisio, V. Bocci *et. al.* *"The RPC Level-1 Muon Trigger of the ATLAS Experiment at the LHC"*, Tech. Rep. ATL-DAQ-CONF-2006-004. ATL-COM-DAQ-2006-011 CERN Geneva Mar, 2006.

[261] J. Wotschack *"ATLAS Muon Chamber Construction Parameters for CSC, MDT, and RPC chambers"*, Tech. Rep. ATL-MUON-PUB-2008-006. ATL-COM-MUON-2008-008 CERN Geneva Apr, 2008.

[262] J. Stelzer and the ATLAS collaboration, *"The ATLAS High Level Trigger Configuration and Steering: Experience with the First 7 TeV Collision Data"*, *Journal of Physics: Conference Series* **331** (2011) 2 022026.

[263] **ATLAS** Collaboration P. Jenni, M. Nessi, M. Nordberg and K. Smith, *ATLAS high-level trigger, data-acquisition and controls: Technical Design Report*. Technical Design Report ATLAS. CERN Geneva 2003.

[264] W. Buttinger *"The ATLAS Level-1 Trigger System"*, *Journal of Physics: Conference Series* **396** (2012) 1 012010.

[265] S. Ask, D. Berge *et. al.* *"The ATLAS central level-1 trigger logic and TTC system"*, *Journal of Instrumentation* **3** (2008) 08 P08002.

[266] **ATLAS** Collaboration *"Performance of the ATLAS Trigger System in 2015"*, *Eur. Phys. J. C* **77** (Nov, 2016) 317. 76 p.

[267] **The ATLAS TDAQ** Collaboration *"The ATLAS Data Acquisition and High Level Trigger system"*, *Journal of Instrumentation* **11** (2016) 06 P06008.

[268] K. Nagano and the Atlas Collaboration, *"Algorithms, performance, development of the ATLAS High-Level trigger"*, *Journal of Physics: Conference Series* **513** (2014) 1 012026.

[269] J. Catmore, P. Laycock *et. al.* *"A New Petabyte-scale Data Derivation Framework for ATLAS"*, Tech. Rep. ATL-SOFT-PROC-2015-041. 7 CERN Geneva May, 2015.

[270] A. Buckley, T. Eifert, M. Elsing, D. Gillberg, K. Koeneke, A. Krasznahorkay, E. Moyse, M. Nowak, S. Snyder and P. van Gemmeren, *"Implementation of the ATLAS Run 2 event data model"*, *Journal of Physics: Conference Series* **664** (2015) 7 072045.

[271] P. F. Akesson and E. Moyse, *"Event Data Model in ATLAS"*, .

[272] Updated ATLAS Resource Request for 2014 and 2015 `https://indico.in2p3.fr/event/8870/contribution/10/material/1/0.pdf`, retrieved: August 14, 2017.

[273] T. Sjöstrand *"Monte Carlo Generators"*, *CERN-LCGAPP-2006-06* (2006) `arXiv:hep-ph/0611247 [hep-ph]`.

[274] A. Buckley, J. Butterworth *et. al.* *"General-purpose event generators for LHC physics"*, *CERN-PH-TH-2010-298* (2011) `arXiv:1101.2599 [hep-ph]`.

[275] E. Barberio, J. Boudreau *et. al.* *"Fast Simulation of Electromagnetic Showers in the ATLAS calorimeter: Frozen Showers"*, *J. Phys.: Conf. Ser.* **160** (2009) 012082.

[276] `https://www.britannica.com/biography/Carl-Friedrich-Gauss`, retrieved: October 17, 2017.

[277] G. Chiodini, N. Orlando and S. Spagnolo, *"ATLAS RPC time-of-flight performance"*, Tech. Rep. ATL-MUON-PROC-2012-002 CERN Geneva Apr, 2012.

[278] G. Chiodini *"ATLAS RPC time-of-flight performance"*, Presentation slides, Workshop on Resistive Plate Chambers and Related Detectors February, 2012 `https://cds.cern.ch/record/1422725/files/ATL-MUON-SLIDE-2012-027.pdf`.

[279] M. Corradi *"Procedure for L1 Barrel time alignment in Run-2"*, unpublished internal documentation 2016.

[280] M. Corradi. personal communication.

[281] S. Baron, T. Mastoridis, J. Troska and P. Baudrenghien, *"Jitter impact on clock distribution in LHC experiments"*, *Journal of Instrumentation* **7** (2012) 12 C12023.

[282] **RD12 Project** Collaboration B. G. Taylor *"TTC distribution for LHC detectors"*, *IEEE Trans. Nucl. Sci.* **45** (1998) 821–828.

[283] B. Taylor *et. al.* *"Timing, Trigger and Control Systems for LHC Detectors"*, tech. rep. CERN Geneva Jan, 2000.

[284] M. Corradi *"Performance of ATLAS RPC Level-1 Muon trigger during the 2015 data taking"*, .

[285] S. Frixione, P. Nason and C. Oleari, *"Matching NLO QCD computations with Parton Shower simulations: the POWHEG method"*, *JHEP* **11** (2007) 070 `arXiv:0709.2092 [hep-ph]`.

[286] S. Alioli, P. Nason, C. Oleari and E. Re, *"A general framework for implementing NLO calculations in shower Monte Carlo programs: the POWHEG BOX"*, *JHEP* **06** (2010) 043 `arXiv:1002.2581 [hep-ph]`.

[287] T. Sjostrand, S. Mrenna and P. Z. Skands, *"A Brief Introduction to PYTHIA 8.1"*, *Comput. Phys. Commun.* **178** (2008) 852–867 `arXiv:0710.3820 [hep-ph]`.

[288] D. J. Lange *"The EvtGen particle decay simulation package"*, *Nuclear Instruments and Methods in Physics Research Section A: Accelerators, Spectrometers, Detectors and Associated Equipment* **462** (2001) 1 152 – 155. BEAUTY2000, Proceedings of the 7th Int. Conf. on B-Physics at Hadron Machines.

[289] J. Pumplin, D. R. Stump, J. Huston, H. L. Lai, P. M. Nadolsky and W. K. Tung, *"New generation of parton distributions with uncertainties from global QCD analysis"*, *JHEP* **07** (2002) 012 `arXiv:hep-ph/0201195 [hep-ph]`.

[290] N. Davidson, T. Przedzinski and Z. Was, *"PHOTOS interface in C++: Technical and Physics Documentation"*, *Comput. Phys. Commun.* **199** (2016) 86–101 `arXiv:1011.0937 [hep-ph]`.

[291] **ATLAS** Collaboration G. Aad *et. al.* *"The ATLAS Simulation Infrastructure"*, *Eur. Phys. J.* **C70** (2010) 823–874 `arXiv:1005.4568 [physics.ins-det]`.

[292] **GEANT4** Collaboration S. Agostinelli *et. al.* *"GEANT4: A Simulation toolkit"*, *Nucl. Instrum. Meth.* **A506** (2003) 250–303.

[293] V. Blobel *"Unfolding Methods in High-energy Physics Experiments"*, in *Proceedings, CERN School of Computing: Aiguablava, Spain, September 9-22 1984* 1984.

[294] V. Blobel *"An Unfolding method for high-energy physics experiments"*, in *Advanced Statistical Techniques in Particle Physics. Proceedings, Conference, Durham, UK, March 18-22, 2002* pp. 258–267 2002. `arXiv:hep-ex/0208022 [hep-ex]`.

[295] A. Hocker and V. Kartvelishvili, *"SVD approach to data unfolding"*, *Nucl. Instrum. Meth.* **A372** (1996) 469–481 `arXiv:hep-ph/9509307 [hep-ph]`.

[296] R. Brun and F. Rademakers, *"ROOT: An object oriented data analysis framework"*, *Nucl. Instrum. Meth.* **A389** (1997) 81–86.

[297] T. Sjostrand, S. Mrenna and P. Z. Skands, *"PYTHIA 6.4 Physics and Manual"*, *JHEP* **05** (2006) 026 `arXiv:hep-ph/0603175 [hep-ph]`.

[298] R. Mackeprang *Stable Heavy Hadrons in ATLAS.* PhD thesis Niels Bohr Inst. 2007.

[299] A. J. Barr, C. G. Lester, M. A. Parker, B. C. Allanach and P. Richardson, *"Discovering anomaly mediated supersymmetry at the LHC"*, *JHEP* **03** (2003) 045 `arXiv:hep-ph/0208214 [hep-ph]`.

[300] J. Alwall, R. Frederix, S. Frixione, V. Hirschi, F. Maltoni, O. Mattelaer, H. S. Shao, T. Stelzer, P. Torrielli and M. Zaro, *"The automated computation of tree-level and next-to-leading order differential cross sections, and their matching to parton shower simulations"*, *JHEP* **07** (2014) 079 `arXiv:1405.0301 [hep-ph]`.

[301] *"ATLAS Run 1 Pythia8 tunes"*, Tech. Rep. ATL-PHYS-PUB-2014-021 CERN Geneva Nov, 2014.

[302] R. D. Ball *et. al.* *"Parton distributions with LHC data"*, *Nucl. Phys.* **B867** (2013) 244–289 `arXiv:1207.1303 [hep-ph]`.

[303] J. H. Friedman *"Data Analysis Techniques for High-Energy Particle Physics"*, in *1974 CERN School of Computing, Godoysund, Norway, 11-24 Aug 1974: Proceedings* p. 271 1974.

[304] **ATLAS** Collaboration M. Aaboud *et. al.* *"Performance of the ATLAS Track Reconstruction Algorithms in Dense Environments in LHC run 2"*, *Eur. Phys. J.* **C77** (2017) 10, 673 `arXiv:1704.07983 [hep-ex]`.

[305] T. Cornelissen, M. Elsing, I. Gavrilenko, W. Liebig, E. Moyse and A. Salzburger, *"The new ATLAS track reconstruction (NEWT)"*, *Journal of Physics: Conference Series* **119** (2008) 3 032014.

[306] **ATLAS** Collaboration *"Muon reconstruction efficiency in reprocessed 2010 LHC proton-proton collision data recorded with the ATLAS detector"*, Tech. Rep. ATLAS-CONF-2011-063 CERN Geneva Apr, 2011.

[307] S. Tarem, Z. Tarem, N. Panikashvili and O. Belkind, *"MuGirl – Muon identification in the ATLAS detector from the inside out"*, in *2006 IEEE Nuclear Science Symposium Conference Record* vol. 1 pp. 617–621 Oct, 2006.

[308] S. Tarem, S. Bressler, H. Nomoto and A. Di Mattia, *"Trigger and reconstruction for heavy long-lived charged particles with the ATLAS detector"*, *Eur. Phys. J.* **C62** (2009) 281–292.

[309] **ATLAS** Collaboration G. Aad *et. al.* *"Searches for heavy long-lived sleptons and R-Hadrons with the ATLAS detector in pp collisions at $\sqrt{s} = 7$ TeV"*, *Phys. Lett.* **B720** (2013) 277–308 `arXiv:1211.1597 [hep-ex]`.

[310] E. Fullana *et. al.* *"Optimal Filtering in the ATLAS Hadronic Tile Calorimeter"*, Tech. Rep. ATL-TILECAL-2005-001. ATL-COM-TILECAL-2005-001. CERN-ATL-TILECAL-2005-001 CERN Geneva 2005.

[311] *"2015 start-up trigger menu and initial performance assessment of the ATLAS trigger using Run-2 data"*, Tech. Rep. ATL-DAQ-PUB-2016-001 CERN Geneva Mar, 2016.

[312] **ATLAS** Collaboration *"Trigger Menu in 2016"*, Tech. Rep. ATL-DAQ-PUB-2017-001 CERN Geneva Jan, 2017.

[313] Y. L. Dokshitzer, V. A. Khoze and S. I. Troian, *"On specific QCD properties of heavy quark fragmentation ('dead cone')"*, *J. Phys.* **G17** (1991) 1602–1604.

[314] **ATLAS** Collaboration M. Aaboud *et. al.* *"Performance of the ATLAS Trigger System in 2015"*, *Eur. Phys. J.* **C77** (2017) 5, 317 `arXiv:1611.09661 [hep-ex]`.

[315] O. Bulekov, D. Ponomarenko, A. Romaniouk and Y. Smirnov, *"Search for heavy long-lived multi-charged particles in pp collisions at* $\sqrt{s} = 13$ *TeV using the ATLAS detector"*, Tech. Rep. ATL-COM-PHYS-2017-690 CERN Geneva Jun, 2017.

[316] **ATLAS** Collaboration Y. Suzuki *et. al.* *"Precise Timing Adjustment for the ATLAS Level1 Endcap Muon Trigger System"*, Tech. Rep. ATL-DAQ-PROC-2009-035 CERN Geneva Nov, 2009.

[317] K. Hasuko, S. Matsuura and O. Sasaki, *"Strategy for timing adjustment of ATLAS endcap / forward muon trigger system"*, in *Fifth Workshop on electronics for LHC experiments, Snowmass, CO, USA, 20-24 Sep 1999: Proceedings* pp. 331–335 1999.

[318] *"Selection of jets produced in 13TeV proton-proton collisions with the ATLAS detector"*, Tech. Rep. ATLAS-CONF-2015-029 CERN Geneva Jul, 2015.

[319] G. Borissov, D. W. Casper, K. Grimm, S. Pagan Griso, L. E. Pedersen, K. Prokofiev, M. S. Rudolph and A. M. Wharton, *"ATLAS strategy for primary vertex reconstruction during Run-2 of the LHC"*, Tech. Rep. ATL-SOFT-PROC-2015-016. 7 CERN Geneva May, 2015.

[320] S. Kazama *"Search for Charginos Nearly Mass-Degenerate with the Lightest Neutralino"*. PhD thesis The University of Tokyo 2016.

[321] W. Beenakker, M. Kramer, T. Plehn, M. Spira and P. M. Zerwas, *"Stop production at hadron colliders"*, *Nucl. Phys.* **B515** (1998) 3–14 `arXiv:hep-ph/9710451 [hep-ph]`.

[322] W. Beenakker, S. Brensing, M. Kramer, A. Kulesza, E. Laenen and I. Niessen, *"Supersymmetric top and bottom squark production at hadron colliders"*, *JHEP* **08** (2010) 098 `arXiv:1006.4771 [hep-ph]`.

[323] W. Beenakker, S. Brensing, M. n. Kramer, A. Kulesza, E. Laenen, L. Motyka and I. Niessen, *"Squark and Gluino Hadroproduction"*, *Int. J. Mod. Phys.* **A26** (2011) 2637–2664 `arXiv:1105.1110 [hep-ph]`.

[324] M. Kramer, A. Kulesza, R. van der Leeuw, M. Mangano, S. Padhi, T. Plehn and X. Portell, *"Supersymmetry production cross sections in pp collisions at* $\sqrt{s} = 7$ *TeV"*, `arXiv:1206.2892 [hep-ph]`.

[325] A. D. Martin, W. J. Stirling, R. S. Thorne and G. Watt, *"Parton distributions for the LHC"*, *Eur. Phys. J.* **C63** (2009) 189–285 `arXiv:0901.0002 [hep-ph]`.

[326] P. M. Nadolsky *et. al.* *"Implications of CTEQ global analysis for collider observables"*, *Phys. Rev.* **D78** (2008) 013004 `arXiv:0802.0007 [hep-ph]`.

[327] M. Botje *et. al.* *"The PDF4LHC Working Group Interim Recommendations"*, `arXiv:1101.0538 [hep-ph]`.

[328] N. Lavesson and L. Lonnblad, *"Merging parton showers and matrix elements: Back to basics"*, *JHEP* **04** (2008) 085 `arXiv:0712.2966 [hep-ph]`.

[329] S. van der Meer *"Calibration of the effective beam height in the ISR"*, Tech. Rep. CERN-ISR-PO-68-31. ISR-PO-68-31 CERN Geneva 1968.

[330] **ATLAS** Collaboration M. Aaboud *et. al.* *"Luminosity determination in pp collisions at* $\sqrt{s}$ *= 8 TeV using the ATLAS detector at the LHC"*, *Eur. Phys. J.* **C76** (2016) 12, 653 `arXiv:1608.03953 [hep-ex]`.

[331] A. L. Read *"Presentation of search results: The CL(s) technique"*, *J. Phys.* **G28** (2002) 2693–2704. [,11(2002)].

[332] `https://www.ppd.stfc.ac.uk/Gallery/ATLAS_L1Calo_C-side.JPG`, retrieved: November 23, 2017.

[333] E. Simioni *"The Topological Processor for the future ATLAS Level-1 Trigger: from design to commissioning"*, `arXiv:1406.4316 [physics.ins-det]`.

[334] C. Kourkoumelis and S. Vourakis, *"HYPATIA - an online tool for ATLAS event visualization"*, *Physics Education* **49** (2014) 1 21.

[335] D. Berge, N. Ellis, P. Farthouat, S. Haas, P. Klofver, A. Krasznahorkay, A. Messina, T. Pauly, G. Schuler, R. Spiwoks and T. Wengler, *"The ATLAS Level-1 Muon to Central Trigger Processor Interface"*, .

[336] **ATLAS** Collaboration *"Trigger monitoring and rate predictions using Enhanced Bias data from the ATLAS Detector at the LHC"*, Tech. Rep. ATL-DAQ-PUB-2016-002 CERN Geneva Oct, 2016.

[337] P. Gambino, G. F. Giudice and P. Slavich, *"Gluino decays in split supersymmetry"*, *Nucl. Phys.* **B726** (2005) 35–52 `arXiv:hep-ph/0506214 [hep-ph]`.

[338] E. Bagnaschi, G. F. Giudice, P. Slavich and A. Strumia, *"Higgs Mass and Unnatural Supersymmetry"*, *JHEP* **09** (2014) 092 `arXiv:1407.4081 [hep-ph]`.

[339] **ATLAS** Collaboration *"Search for heavy long-lived multi-charged particles in pp collisions at $\sqrt{s} = 8$ TeV using the ATLAS detector"*, *Eur. Phys. J.* **C75** (2015) 362 `arXiv:1504.04188 [hep-ex]`.

[340] **ATLAS** Collaboration M. Corradi *"Performance of ATLAS RPC Level-1 muon trigger during the 2015 data taking"*, Tech. Rep. ATL-MUON-PROC-2016-003 CERN Geneva Jun, 2016.